



# Governance of Alteration of the Deformation Field of Fractal Quasi-Two-Dimensional Structures in Nanosystems

Olga P. Abramova, Sergey V. Abramov

Donetsk National University, Ukraine

E-mail: [oabramova@ua.fm](mailto:oabramova@ua.fm)

**Abstract:** A model nanosystem is investigated: a sample in the form of a rectangular parallelepiped of finite size with volumetric discrete lattice. It is shown that a separate nodal plane of a model nanosystem can be in different structural states: stochastic state of the deformation field on the whole rectangular lattice; the state with the linear fractal dislocation of different orientations; quasi-two-dimensional structures of the type of fractal elliptical, hyperbolic dislocations and fractal quantum dot. Using the numerical modelling method, the behaviour of the deformation field and a possibility of the alteration of these structures is investigated. The analysis of the behavior of the averaged functions allows to determine the critical values of the governing parameters.

**Keywords:** fractal quasi-two-dimensional structures, nanosystem, stochastic deformation field, numerical modeling, averaged functions, alteration of the structure.

## 1. Introduction

Investigation of fundamental properties of nanosystems and nanomaterials of a new generation [1, 2] is actual for modern areas of science and nanotechnology. Among the real nanomaterials the active nanostructural elements are clusters, porous, quantum dots, wells, corrals, surface superlattices. The physical properties of these elements can demonstrate chaotic behavior [3]. The active nanostructural elements can find their application in the quantum nanoelectronics, quantum informations [4], quantum optics. Previously in paper [5] fractons – vibrational excitations on fractals – were introduced. Fractal dislocation [6, 7] is one of the non-classical active nanostructural objects. For the theoretical descriptions of fractal objects it has been proposed [6, 7] to use the theory of fractional calculations [8] and the concept of fractals [9]. The new structural states [10-13] of fractal dislocation were investigated on the basis of fractional calculation theory and Hamilton operators. The purpose of the paper is to research a possibility of governing the alteration of the deformation field of fractal quasi-two-dimensional structures in model nanosystems.

## 2. Basic nonlinear equations

A model nanosystem is investigated: a sample in the form of a rectangular parallelepiped of a finite size with volumetric discrete lattice  $N_1 \times N_2 \times N_3$ , whose nodes are given integers  $n, m, j$  ( $n = \overline{1, N_1}; m = \overline{1, N_2}; j = \overline{1, N_3}$ ). In papers [11] the dimensionless variable displacement  $u$  of the lattice nodes is described by function



$$u = (1 - \alpha) \left( 1 - 2 \operatorname{sn}^2(u - u_0, k) \right) / Q, \quad Q = p_{01} - p_1 n - p_2 m - p_3 j. \quad (1)$$

Here  $\alpha$  is the fractal dimension of the deformation field  $u$  along the  $Oz$ -axis ( $\alpha \in [0, 1]$ );  $u_0$  is the constant (critical) displacement;  $k$  is the modulus of the elliptic sine; governing parameters  $p_{01}, p_1, p_2, p_3$  do not depend on the integers  $n, m, j$ . This paper takes into account the parameters  $p_{01}, p_1, p_2, p_3$  depending on the integers  $n, m, j$ . While modeling deformation fields of stochastic fractal quasi-two-dimensional structures, this allowed to obtain the basic non-linear equations that take into account the interaction of nodes in the plane of the discrete rectangular lattice  $N_1 \times N_2$ . The structure of these equations is similar to the expression (1), but with a different value of the function  $Q$ . For a linear fractal dislocation the function  $Q$  has the form

$$Q = p_0 - b_1 \left( (n - n_0) / n_c \right) - b_2 \left( (m - m_0) / m_c \right); \quad (2)$$

$$b_1 = \cos(\pi / 2 + \varphi(j)); \quad b_2 = \cos \varphi(j). \quad (3)$$

For other fractal quasi-two-dimensional structures the function  $Q$  has the form

$$Q = p_0 - b_1 \left( (n - n_0) / n_c \right)^2 - b_2 \left( (m - m_0) / m_c \right)^2, \quad (4)$$

where for the elliptic dislocation and fractal quantum dot

$$b_1 = b_2 = \cos \varphi(j) \quad (5)$$

and in the case of fractal hyperbolic dislocation

$$b_1 = \cos \varphi(j); \quad b_2 = \cos(\pi + \varphi(j)). \quad (6)$$

Now here the governing parameters are  $p_0, n_0, n_c, m_0, m_c, \varphi(j)$ . Varying these parameters both a structural state of the self-fractal dislocation and the type of dislocation (for example, the transition from fractal elliptical dislocation to fractal quantum dot) can be governed. In general case the governing parameters can be changed from one node plane to another, which may be connected not only with external governance (for example, when a parameter  $p_0$  is changed), but also with internal governance (the process of self-organization of structures when  $\varphi(j)$  is changed). To investigate the behavior of the stochastic deformation field of fractal quasi-two-dimensional structure in terms of the statistical approach, averaged functions are introduced [11]. The necessity of averaging is connected with the fact that the elements of the lattice nodes displacement matrix are in general case random real functions. The average is taken only on nodes in the plane of the discrete rectangular lattice  $N_1 \times N_2$ . For this the operators fields of displacement  $\hat{u}$  and density of states  $\hat{\rho}$  are introduced. These operators are coincided to the matrix with the elements of  $u_{nm}; \rho_{mn} = 1 / N_2 N_1$ . Rectangular matrices  $\hat{u}$  and  $\hat{\rho}$  have the dimensions of  $N_1 \times N_2; N_2 \times N_1$ , respectively. For a homogeneous distribution the operator  $\hat{\rho}$  is given by



$$\hat{\rho} = \hat{\xi}_{N2}^T \hat{\xi}_{N1} / N_2 N_1, \quad (7)$$

where « $T$ » denotes transposition;  $\hat{\xi}_{N1}$ ,  $\hat{\xi}_{N2}$  are row-vectors with elements equal to one. The averaged function  $M$  has the form [11]

$$M = Sp(\hat{\rho}\hat{u}) = M' + iM''; \quad M' = \text{Re}M; \quad M'' = \text{Im}M. \quad (8)$$

Here  $Sp$  is an operation of calculating the trace of a square matrix;  $\text{Re}$ ,  $\text{Im}$  represent an allocation of real and imaginary parts of the complex function  $M$ ;  $i$  is an imaginary unit. Averaged function  $M$  depends on the governing parameters  $p_0(j)$ ,  $\varphi(j)$ . In general case  $M = M(j)$  is a random function, as an average over the index  $j$  is not made. This means that there are some critical values  $p_0(j)$ ,  $\varphi(j)$ , during the transition through which the behavior of function  $M$  can vary from regular to stochastic. Therefore there is a problem of finding the critical values of these governing parameters.

### 3. Numerical simulation and the analysis of results

Solution of the nonlinear equation (1) with the value of function  $Q$  in the form (3) is constructed by the iteration method [11] for fixed values  $\alpha = 0,5$ ;  $k = 0,5$ ;  $u_0 = 29,537$ . The iterative procedure on the index  $m$  simulates a stochastic process on a rectangular discrete lattice with a size  $N_1 \times N_2 = 30 \times 40$ . The initial parameters were the following:  $n_0 = 14,3267$ ;  $n_c = 9,4793$ ;  $m_0 = 19,1471$ ;  $m_c = 14,7295$ . In the simulation it was assumed that  $\varphi(j) = (j-1)\pi/10$ . A separate nodal plane of a model nanosystem can be in different structural states: the state with the linear fractal dislocation of different orientations (Fig. 1); stochastic state of the deformation field on the whole rectangular lattice (Fig. 2. b, Fig. 3. b); quasi-two-dimensional structures of the type of fractal elliptical (Fig. 2. a), hyperbolic dislocations (Fig. 3. a. c) and fractal quantum dot (Fig. 2. c). Governance of alteration (Fig. 1-Fig. 3) of the deformation field is achieved by changing the internal parameters  $b_1, b_2$ . At the same time the external parameter  $p_0 = 0.1453$  has been fixed and is chosen from the field of stochastic behavior of the averaged function  $M$  (Fig. 4-Fig. 6). Rotation of a linear dislocation (Fig. 1) is achieved by governing the internal parameters  $b_1, b_2$  (3) by changing the angle  $\varphi(j)$ . At rotation there is a change of the structural state of the dislocation and substructures appear, which is related to the influence of the stochastic iteration process along the axis  $Om$ . If  $\cos\varphi(j) > 0$  the quasi-two-dimensional structure (4), (5) is a structure of the type of fractal elliptical dislocation, for which the location of the singular points is typical for real ellipse. If  $\cos\varphi(j) < 0$  the quasi-two-dimensional structure is a structure of the type of the fractal quantum dot [12], for which the location of the singular points is typical for an imaginary ellipse. Fig. 2 show the transition from the elliptic dislocation to the quantum dot through the stochastic state of the whole lattice.

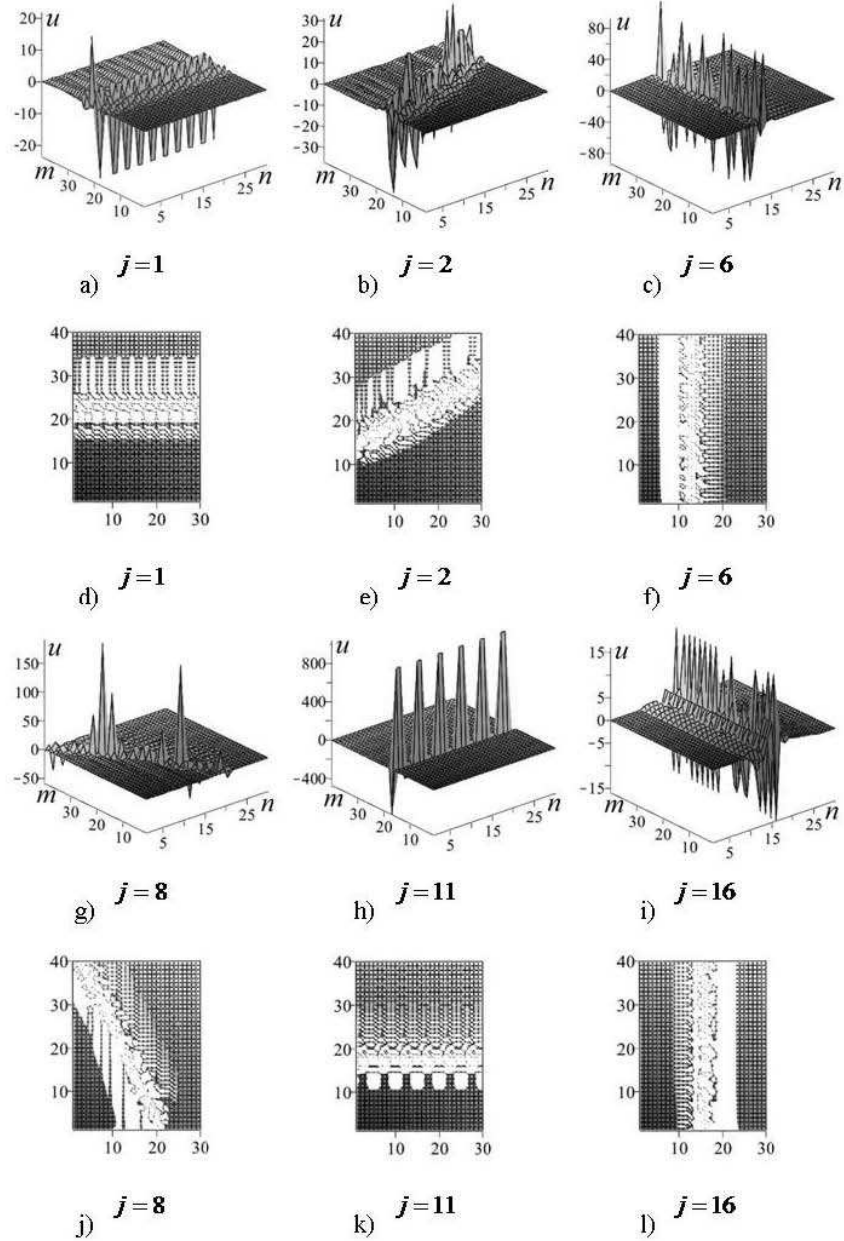


Fig. 1. The behavior of functions  $u$  (a,b,c,g,h,i) and their cuts (d,e,f,j,k,l) at  $u \in [-0.5, 0.5]$  (top view) depending on the lattice index  $n$  and  $m$  for linear fractal dislocation

This transition is realized when governing the internal parameters of  $b_1, b_2$  (5) by changing the angle  $\varphi(j)$ . At the same time a reorientation of the peaks, a change of the substructure, an expansion (at  $j \in [1,5]$ ) and a restriction (at  $j \in [17,21]$ ) of the area of the elliptical dislocation; a restriction (at  $j \in [7,11]$ ) and an expansion (at  $j \in [12,15]$ ) of the area of the quantum dot are observed.

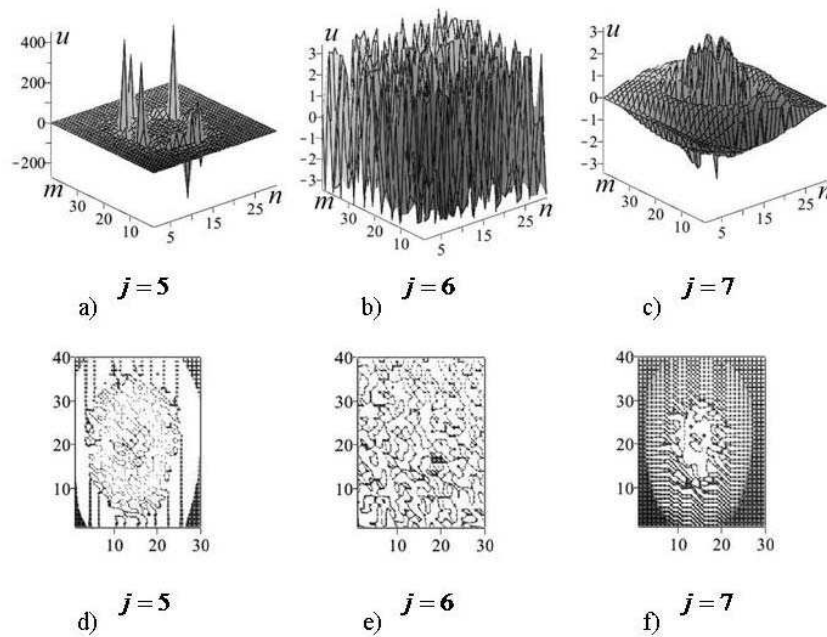


Fig. 2. The transition from the elliptical dislocation to the quantum dot. The behavior of the functions  $u$  (a,b,c) and their cuts (d,e,f) at  $u \in [-0.5, 0.5]$  (top view) depending on the lattice index  $n$  and  $m$

The reorientation of the branches of the fractal hyperbolic dislocation through the stochastic state of the whole lattice is achieved by governing the internal parameters  $b_1, b_2$  from (6) by changing the angle  $\varphi(j)$  (Fig. 3). Strongly pronounced stochastic behavior of the deformation field and the substructure can be observed for the region between the branches of the hyperbolic dislocation. The analysis of the behavior of the averaged functions allows to determine the critical values of the governing parameters. In our case, the parameter  $p_0$  is a parameter of the external governance, averaged function  $M$  is a real random function. The behavior of function  $M$  for the fractal elliptical dislocation ( $p_0 > 0$ ,  $b_1 = b_2 = 1$ ) is shown in Fig. 4. In the interval of  $p_0 \in [0; 5]$  a base peak (Fig. 4. a) and a stochastic behavior with smaller amplitudes (Fig. 4. b) are observed. The presence of several features (such as

local resonance dispersion) allows us to determine the critical values of  $p_0$ , during the transition through which the stochastic behavior of  $M$  is changed to a regular one (Fig. 4. c). These features allow us to study the mechanism of alteration of fractal quasi-two-dimensional structures of the type of elliptical dislocation. With a further increase in  $p_0$  function  $M$  is regular and asymptotically approach to zero from negative values.

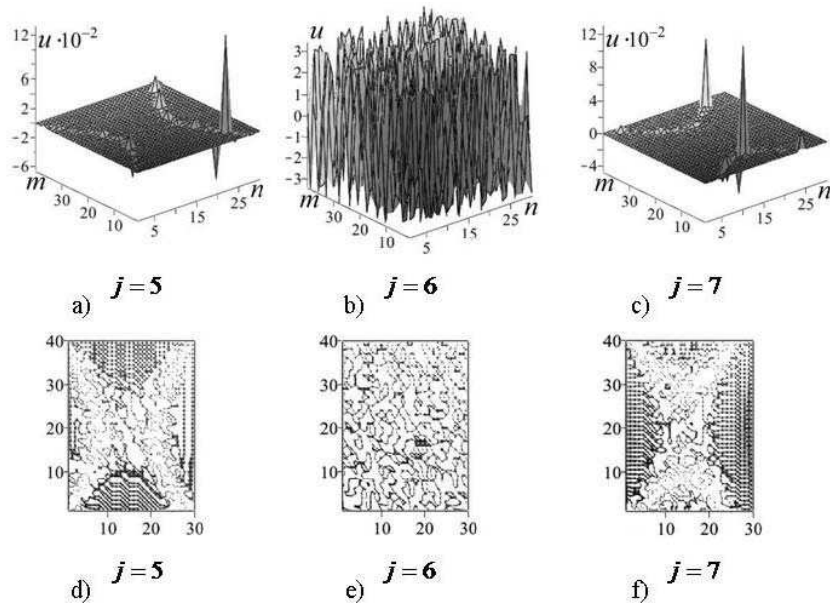


Fig. 3. The reorientation of the branches of the hyperbolic dislocation through the stochastic state. The behavior of the functions  $u$  (a,b,c) and their cuts (d,e,f) at  $u \in [-0.5, 0.5]$  (top view) depending on the lattice index  $n$  and  $m$

The behavior of  $M$  for the fractal quantum dot ( $p_0 < 0, b_1 = b_2 = 1$ ) is shown in Fig. 5. When changing  $p_0$  the regular behavior of function  $M$  (Fig. 5. a) goes into pronounced stochastic (Fig. 5. b). The presence of such features as inflection points, local maxima and minima allows to determine the critical values of the parameter  $p_0$  (Fig. 5. c). The behavior of the function  $M$  of the parameter  $p_0$  at  $b_1 = -1, b_2 = 1$  ( $j = 11$ ) for the fractal hyperbolic dislocation (4), (6) is shown in Fig. 6. By changing  $p_0$  a base peak and two additional peaks (Fig. 6. a) are observed, as well as a pronounced stochastic behavior with smaller amplitudes (Fig. 6. b). The features of the function behavior are given by a type of local inflection points, maxima and minima (as in the quantum dot of Fig. 5. c). This allows to determine the critical value of the parameter  $p_0$ , across which the regular behavior of the function  $M$  changes to stochastic (Fig. 6. c).

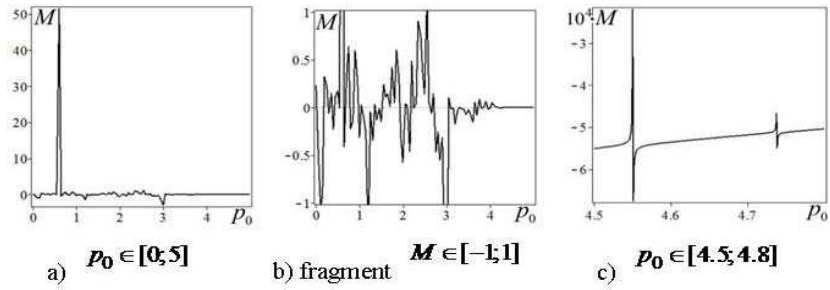


Fig. 4. The behavior of  $M$  of  $p_0$  for the elliptic dislocation at  $j = 1$

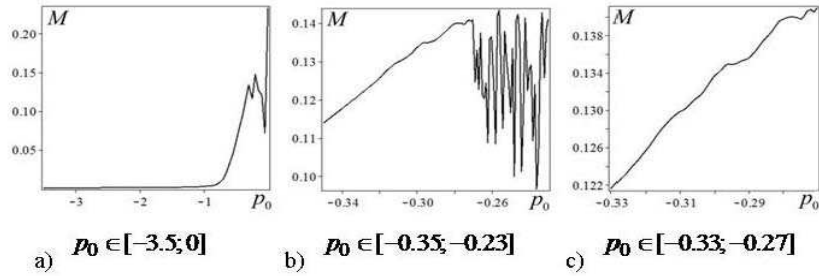


Fig. 5. The behavior of  $M$  of  $p_0$  for the fractal quantum dot at  $j = 1$

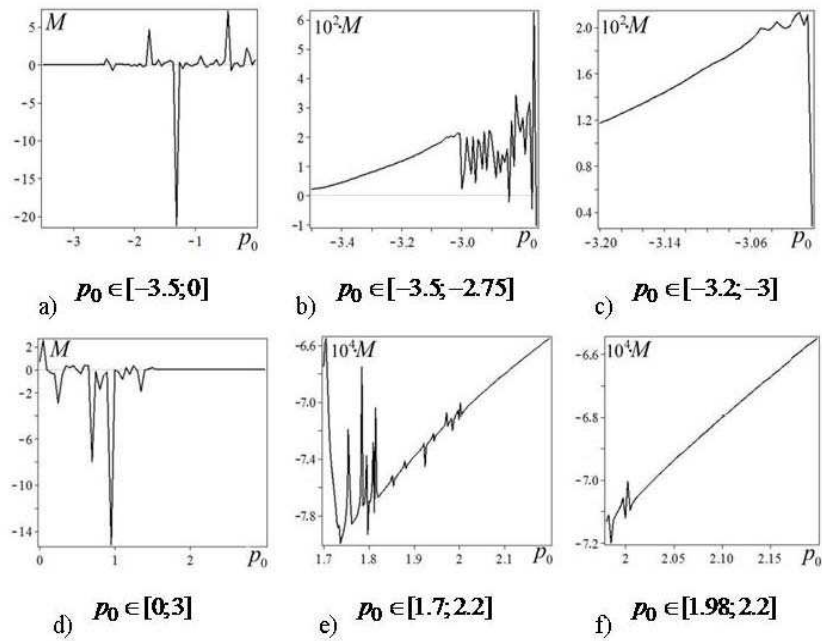


Fig. 6. The behavior of  $M$  of  $p_0$  for the hyperbolic dislocation at  $j = 11$



By changing the sign of  $p_0$  (Fig. 6. d) there is a change in the orientation of the branches of the fractal hyperbolic dislocation. In this case the features of  $M$  have the form of a resonance dispersion type (Fig. 6. e) against the background of the step (Fig. 6. f). This allows to determine the critical value of the parameter  $p_0$ , across which the stochastic behavior of  $M$  changes to regular.

#### 4. Conclusions

In order to describe stochastic deformation fields of fractal quasi-two-dimensional structures the basic non-linear equations taking into account the interaction of nodes in the plane of the discrete rectangular lattice were obtained. The alteration of the deformation field of fractal quasi-two-dimensional structures is achieved by changing internal and external governing parameters. It is shown that in this case both the structural state of the self-structure and the type of structure vary. The behavior of the averaged functions when changing the governing parameters correlates with the behavior of the deformation field and is related to the mechanisms of alteration of fractal quasi-two-dimensional structures.

#### References

1. A. Castro Neto, F. Guinea, N. Peres, K. Novoselov, A. Geim. The electronic properties of graphene. *Rev. Mod. Phys.* **81**: 109-162, 2009.
2. L. Tarruell, D. Greif, T. Uehlinger, G. Jotzu, T. Esslinger. Creating, moving and merging Dirac points with a Fermi gas in a tunable honeycomb lattice. *Nature* **483**, 7389: 302-305, 2012.
3. H.-J. Stockmann. *Quantum Chaos. An Introduction*. Cambridge Univers. Press, 1999.
4. M.A Nielsen, I.L. Chuang. *Quantum Computation and Quantum Information*. Cambridge: Cambridge Univ. Press, 2000.
5. S. Alexander, O. Entin-Wohlman, R. Orbach. Relaxation and nonradiative decay in disordered systems. I. One-fracton emission. *Phys. Rev. B*, **32**, 10: 6447-6455, 1985.
6. V.S. Abramov. Fractal dislocation as one of non-classical structural objects in the nano-dimensional systems. *Metallofiz. i Noveishie Tekhnologii*. **33**, 2: 247-251, 2011.
7. O.P. Abramova, S.V. Abramov. Alteration of the structure of the stochastic dislocation deformation field under the change of governing parameters. *Metallofiz. i Noveishie Tekhnologii*. **33**, 4: 519-524, 2011.
8. S.G. Samko, A. Kilbas O. Marichev. *Fractional Integrals and Derivatives. Theory and Applications*. Gordon and Breach Sci. Publ., New York et alibi, 1990.
9. B.B. Mandelbrot. *The Fractal Geometry of Nature*. Freeman, New York, 1982.
10. V.S. Abramov. Behavior of the deformation field of fractal dislocation in the presence of bifurcations. *Bul. of Donetsk Nat. Univers. Ser. A*, 2: 23-29, 2011.
11. O.P. Abramova, S.V. Abramov. Deterministic and stochastic governance of the alteration of the fractal dislocation structure. *Bul. of Donetsk Nat. Univers. Ser. A*, 2: 30-35, 2011.
12. V.S. Abramov. Inverse structural states of the deformation field of a fractal quantum dot. *Book of Abstracts CHAOS 2012 «5th Chaotic Modeling and Simulation International Conference», 12-15 June 2012 Athens, Greece*. p. 11-12, Greece, 2012.
13. O.P. Abramova, S.V. Abramov. Governing the behaviour of the deformation fields of fractal quasi-two-dimensional structures. *Book of Abstracts CHAOS 2012 «5th Chaotic Modeling and Simulation International Conference», 12-15 June 2012 Athens, Greece*. p. 12-13, Greece, 2012.



## Correlation relations and statistical properties of the deformation field of fractal dislocation in a model nanosystem

Valeriy S. Abramov

Donetsk Institute for Physics and Engineering named after A.A. Galkin,  
National Academy of Sciences of Ukraine, Ukraine  
E-mail: [vsabramov@mail.ru](mailto:vsabramov@mail.ru)

**Abstract:** A model sample of a finite nanosize with the volumetric lattice in the form of a rectangular parallelepiped is considered. On the basis of the previously proposed one-point model, a two-point model is constructed, which uses the theory of fractional calculus and the concept of fractal. The features of the behavior of the deformation field of fractal dislocation and possible correlation connections are investigated. It is shown that complex correlation connections have negative, positive and sign changing correlation coefficients. The strongly pronounced stochastic behaviour of amplitudes and phases of average functions is established. The change of the statistics from Fermi-Dirac type to the statistics of Bose-Einstein type for separate internal nodal planes is shown by the method of numerical modeling.

**Keywords:** fractal dislocation, nanosystem, stochastic deformation field, numerical modeling, distribution functions, correlation connections.

### 1. Introduction

For experimental studies of the physical properties of individual atoms (electrons, photons) and the quantum measurement it is necessary to create special traps: nanosystem - trapped particles (or group of particles) in a trap. These traps can be useful for realization of optical quantum computation with quantum information processing, measurement in quantum optics [1]. In his Nobel lecture in Physics in 1989 W. Paul [2] considered electromagnetic traps for charged and neutral particles. For the observation of Bose-Einstein condensation phenomenon [3] the magnetic traps were used. Serge Haroche and David Wineland, 2012 Nobel laureates in Physics, proposed experimental methods that made it real to measure individual quantum systems and govern them [4, 5]. The experimental studies of the features of the statistical properties of individual quantum systems in neutron spin measurements [6], with the observation of Bose-Einstein condensation [7] showed the presence of correlations in the measured values. Near singular points (Dirac points) Dirac fermions in molecular graphene show quantum and statistical features of behavior [8].

Fractal dislocation is one of the structural objects in nanostructured materials [9, 10]. The core of a linear dislocation is a set of singular points. The deformation field of fractal dislocation has unusual quantum and statistical properties [11 - 13] and shows the presence of quantum chaos [14]. Earlier a



one-point model was used to describe the structural states of the deformation field of fractal dislocation [10, 12] (fractal dimension was an effective coordinate). In this model, the elements of the displacement of the lattice nodes are real random functions and were determined without the effect of bifurcation of solutions of a nonlinear equation. However, consideration of the effect of bifurcation of solutions [11] leads to the four branches of the lattice nodes displacement function. Elements of the lattice nodes displacement matrix become complex random functions. In order to describe possible correlation effects and statistical properties of the deformation field of fractal dislocation of net structural states a two-point model was proposed [15] in which the theory of fractional calculus [16] and the concept of fractal [17] are used. It is necessary to investigate the mixed states, the description of which requires introducing the density of states and accounting for the distribution of this density of states on nodes of the volumetric lattice.

The purpose of this paper is to generalize the two-point model to the case of mixed state and investigate correlation connections and the statistical properties of the deformation field of fractal dislocation in the model nanosystem.

## 2. Description of mixed states in the two-point model

A model nanosystem [15] is considered: a sample in the form of a rectangular parallelepiped of finite size with volumetric discrete lattice  $N_1 \times N_2 \times N_3$ . Deviations of the lattice nodes from the state of equilibrium in a separate plane  $N_1 \times N_2$  for two different points of  $z_1(j)$  and  $z_2(j)$  are described by non-hermitian displacements operators  $\hat{u}(z_1)$  and  $\hat{u}(z_2)$ , corresponding to the rectangular matrix with dimensions  $N_1 \times N_2$ ,  $j \in [1, N_3]$ .

For the description of mixed states the effective composite operators of displacements for the states  $p = 1, 2, \dots, 8$  are introduced, respectively,

$$\hat{u}_1 = \hat{\rho}_{12} \hat{u}^+(z_1); \quad \hat{u}_3 = \hat{\rho}_{12} \hat{u}^+(z_2); \quad \hat{u}_5 = \hat{u}(z_1) \hat{\rho}_{12}^T; \quad \hat{u}_7 = \hat{u}(z_2) \hat{\rho}_{12}^T; \quad (1)$$

$$\hat{u}_2 = \hat{\rho}_{21} \hat{u}(z_1); \quad \hat{u}_4 = \hat{\rho}_{21} \hat{u}(z_2); \quad \hat{u}_6 = \hat{u}^+(z_1) \hat{\rho}_{21}^T; \quad \hat{u}_8 = \hat{u}^+(z_2) \hat{\rho}_{21}^T. \quad (2)$$

Here the symbols «+» and «T» mean the operation of hermitian conjugation and transposition. The square matrices with sizes  $N_1 \times N_1$  for  $p = 1, 3, 5, 7$  and  $N_2 \times N_2$  for  $p = 2, 4, 6, 8$  correspond to the introduced operators  $\hat{u}_p$ ; so that  $\hat{u}_5 = \hat{u}_1^+$ ,  $\hat{u}_7 = \hat{u}_3^+$ ,  $\hat{u}_6 = \hat{u}_2^+$ ,  $\hat{u}_8 = \hat{u}_4^+$ . The density state operators  $\hat{\rho}_{12}, \hat{\rho}_{12}^T, \hat{\rho}_{21}, \hat{\rho}_{21}^T$  are represented by

$$\hat{\rho}_{12} = \hat{\xi}_{N_1}^T \hat{\xi}_{N_2} / N_1 N_2; \quad \hat{\rho}_{12}^T = \hat{\xi}_{N_2}^T \hat{\xi}_{N_1} / N_1 N_2; \quad \hat{\rho}_{21} = \hat{\rho}_{12}^T; \quad \hat{\rho}_{21}^T = \hat{\rho}_{12}, \quad (3)$$

where  $\hat{\xi}_{N_1}, \hat{\xi}_{N_2}$  are row-vectors of dimensions  $1 \times N_1, 1 \times N_2$ , with elements equal to one. The rectangular matrices  $\hat{\rho}_{12}, \hat{\rho}_{21}$  have dimensions  $N_1 \times N_2, N_2 \times N_1$ . For the operators in (3) the normalization conditions are fulfilled



$$\hat{\xi}_{N1} \hat{\rho}_{12} \hat{\xi}_{N2}^T = 1; \quad \hat{\xi}_{N2} \hat{\rho}_{21} \hat{\xi}_{N1}^T = 1. \quad (4)$$

Having performed an averaging over the index nodes  $n, m$  by calculating trace  $Sp$  of square matrices (1), (2), the averaged functions  $u_p, |u_p|, tg\varphi_p$  for states with  $p = 1, 2, \dots, 8$  are obtained

$$u_p = Sp\hat{u}_p = u'_p + iu''_p = |u_p| \exp(i\varphi_p); \quad u_p^* = Sp\hat{u}_p^+; \quad tg\varphi_p = u''_p / u'_p, \quad (5)$$

where  $u'_p = \text{Re}u_p, u''_p = \text{Im}u_p$ ; the symbol «\*» means the operation of complex conjugation;  $|u_p|, \varphi_p$  are a module, a phase of the complex averaged functions  $u_p$ . Here the averaging across an index  $j$  is not made.

Then we find the correlation function of the first order. For  $p, q = 1, 3, 5, 7$  we obtain

$$\begin{aligned} K_{pq} &= S_{pq} - H_{pq} = K'_{pq} + iK''_{pq} = |K_{pq}| \exp(i\theta_{pq}); \\ S_{pq} &= Sp\hat{S}_{pq} = S'_{pq} + iS''_{pq} = |S_{pq}| \exp(i\psi_{pq}); \quad \hat{S}_{pq} = \hat{u}_p \hat{u}_q^+; \quad \hat{S}_{pq}^+ \neq \hat{S}_{pq}; \\ H_{pq} &= (Sp\hat{u}_p)(Sp\hat{u}_q^+) = u_p u_q^* = H'_{pq} + iH''_{pq} = |H_{pq}| \exp(i\delta_{pq}); \\ &|H_{pq}| = |u_p| \cdot |u_q|; \quad \delta_{pq} = \varphi_p - \varphi_q. \end{aligned} \quad (6)$$

In the case  $p, q = 2, 4, 6, 8$  we obtain

$$\begin{aligned} C_{pq} &= A_{pq} - B_{pq} = C'_{pq} + iC''_{pq} = |C_{pq}| \exp(i\beta_{pq}); \\ A_{pq} &= Sp\hat{A}_{pq} = A'_{pq} + iA''_{pq} = |A_{pq}| \exp(i\chi_{pq}); \quad \hat{A}_{pq} = \hat{u}_p \hat{u}_q^+; \quad \hat{A}_{pq}^+ \neq \hat{A}_{pq}; \\ B_{pq} &= (Sp\hat{u}_p)(Sp\hat{u}_q^+) = B'_{pq} + iB''_{pq} = |B_{pq}| \exp(i\gamma_{pq}); \\ &|B_{pq}| = |u_p| \cdot |u_q|; \quad \gamma_{pq} = \varphi_p - \varphi_q. \end{aligned} \quad (7)$$

From (6) at  $p = q$  we have  $\delta_{pp} = 0, H_{pp} = |H_{pp}| = |u_p|^2$ ; operators  $\hat{S}_{pp} = \hat{S}_{pp}^+$  are hermitian,  $S''_{pp} = 0, S_{pp} = S'_{pp}$  and

$$K_{pp} = S'_{pp} - |H_{pp}| = |K_{pp}| \exp(i\theta_{pp}). \quad (8)$$

From (8) it follows that  $\theta_{pp} = \pi k$ , where  $k = 0, \pm 1, \pm 2, \dots$  and autocorrelation function can be either positive ( $k = 0, \pm 2, \pm 4, \dots$ ) or negative ( $k = \pm 1, \pm 3, \dots$ ).

From (7) at  $p = q$  we obtain  $\gamma_{pp} = 0, B_{pp} = |B_{pp}| = |u_p|^2$ ; then operators  $\hat{A}_{pp} = \hat{A}_{pp}^+$  are hermitian,  $A''_{pp} = 0, A_{pp} = A'_{pp}$  and

$$C_{pp} = A'_{pp} - |B_{pp}| = |C_{pp}| \exp(i\beta_{pp}). \quad (9)$$

From (9) it follows that  $\beta_{pp} = \pi l$ , where  $l = 0, \pm 1, \pm 2, \dots$  and autocorrelation



function can be either positive ( $l = 0, \pm 2, \pm 4, \dots$ ) or negative ( $l = \pm 1, \pm 3, \dots$ ). Having done the normalization of the above functions, we obtain the distribution function of mixed states of Bose-Einstein type and Fermi-Dirac type for  $p = 1, 3, 5, 7$  in form

$$f'_{pp} - f_{pp} = 1; \quad f'_{pp} = S_{pp} / H_{pp}; \quad f_{pp} = K_{pp} / H_{pp}; \quad (10)$$

$$F'_{pp} + F_{pp} = 1; \quad F_{pp} = H_{pp} / S_{pp}; \quad F'_{pp} = K_{pp} / S_{pp}, \quad (11)$$

and for  $p = 2, 4, 6, 8$  in form

$$f'_{pp} - f_{pp} = 1; \quad f'_{pp} = A_{pp} / B_{pp}; \quad f_{pp} = C_{pp} / B_{pp}; \quad (12)$$

$$F'_{pp} + F_{pp} = 1; \quad F_{pp} = B_{pp} / A_{pp}; \quad F'_{pp} = C_{pp} / A_{pp}. \quad (13)$$

By numerical simulation it will be shown that for mixed states all autocorrelation functions  $K_{pp}(j), C_{pp}(j)$  are positive in the interval  $j \in [1; N_3]$ . Earlier in [15] it was shown that for pure states similar autocorrelation functions are negative.

At  $p \neq q$  from (6), (7) it follows that the functions  $K_{pq}, C_{pq}$  are complex. For some values  $p, q$  these functions have a sense of cross-correlated functions (for a pair of different points  $z_1, z_2$ ). In this case, to investigate the correlations it is necessary to introduce second-order correlation functions. For  $p, q = 1, 3, 5, 7$  we have

$$G_{pq} = V_{pq} - W_{pq}; \quad V_{pq} = Sp\hat{V}_{pq}; \quad \hat{V}_{pq} = \hat{S}_{pq}\hat{S}_{pq}^+; \quad \hat{V}_{pq}^+ = \hat{V}_{pq}; \\ W_{pq} = (Sp\hat{S}_{pq})(Sp\hat{S}_{pq}^+) = S_{pq}S_{pq}^* = |S_{pq}|^2. \quad (14)$$

Using (6), we find a representation for

$$|S_{pq}|^2 = (|K_{pq}| - |u_p| \cdot |u_q|)^2 + 2|u_p| \cdot |u_q| \cdot |K_{pq}| (1 + \cos \Phi_{pq}), \quad (15)$$

where  $\Phi_{pq} = \delta_{pq} - \theta_{pq}$ . For  $p, q = 2, 4, 6, 8$  we obtain

$$g_{pq} = v_{pq} - w_{pq}; \quad v_{pq} = Sp\hat{v}_{pq}; \quad \hat{v}_{pq} = \hat{A}_{pq}\hat{A}_{pq}^+; \quad \hat{v}_{pq}^+ = \hat{v}_{pq}; \\ w_{pq} = (Sp\hat{A}_{pq})(Sp\hat{A}_{pq}^+) = A_{pq}A_{pq}^* = |A_{pq}|^2. \quad (16)$$

Using (7), we find a representation for

$$|A_{pq}|^2 = (|C_{pq}| - |u_p| \cdot |u_q|)^2 + 2|u_p| \cdot |u_q| \cdot |C_{pq}| (1 + \cos \Psi_{pq}), \quad (17)$$

where  $\Psi_{pq} = \gamma_{pq} - \beta_{pq}$ . At some points  $j \in [1; N_3]$  changes sign at second order correlation functions  $G_{pq}(j), g_{pq}(j)$  from the expressions (14) - (17) which confirms the presence of a mixed statistics.

When describing pure states [15] of the deformation field of fractal dislocation in the two-point model, the following operators and functions were introduced



$$\begin{aligned}\hat{M}_7 &= \hat{u}(z_2) \hat{u}^+(z_1); \quad \hat{M}_8 = \hat{u}^+(z_1) \hat{u}(z_2); \quad \hat{S}_r = \hat{M}_r \hat{M}_r^+; \\ S_r &= Sp \hat{S}_r; \quad H_r = (Sp \hat{M}_r)(Sp \hat{M}_r^+); \quad K_r = S_r - H_r; \\ f_r' - f_r &= 1; \quad f_r = -K_r / S_r; \quad f_r' = H_r / S_r; \quad r = 7, 8.\end{aligned}\quad (18)$$

Correlation functions  $K_r$  are sign changing within the interval  $j \in [1; N_3]$  and describe the states with mixed statistics.

### 3. Numerical simulation and the analysis of results

The original rectangular matrix displacement  $\hat{u}(z_1)$  and  $\hat{u}(z_2)$  with elements  $u_{nm}(z_1) = u_{\varepsilon 1}(z_1)$ ,  $u_{nm}(z_2) = u_{\varepsilon 1}(z_2)$  in bulk lattice  $N_1 \times N_2 \times N_3 = 30 \times 40 \times 67$  were obtained by the method of iterations on an index  $m$  for the first branch of the dimensionless complex function displacement  $u(z) = u_{\varepsilon 1}(z)$  by the formulas in [15] under the same input parameters and initial conditions. In the calculations it should be:  $z_1 = 0.053 + 0.1(j-1)$ ;  $z_2 = 6.653 - 0.1(j-1)$ , which corresponds to the forward and backward waves of displacements  $u_{nm}(z_1), u_{nm}(z_2)$ ;  $n = \overline{1, 30}$ ;  $m = \overline{1, 40}$ ;  $j = \overline{1, 67}$ . The choice of the model parameters determines the state of a discrete rectangular sublattice  $N_1 \times N_2$  with fractal dislocation, localized within this region parallel to the axis  $Om$ .

The analysis of the results of the numerical simulation for the mixed states (Fig. 1) shows that all of the first-order correlation functions  $K_{pp}$  are positively defined on the whole interval  $j \in [1, 67]$ . This means that for states  $pp$  there are correlation relations with positive correlation coefficients. The distribution function of the Fermi-Dirac type  $F_{55}(j)$  with increasing  $j$  (Fig. 1, a) varies randomly around the value of 0.1, goes to the stochastic peak at  $j = 26$  with the value  $F_{55}(26) = 0.3315$  and then again randomly changed by another law near the value of 0.1. The distribution function of the  $F_{77}(j)$  with increasing  $j$  (Fig. 1, c) also varies randomly near the value of 0.1, comes to a peak at the other stochastic value of  $j = 42$  with the same value of  $F_{77}(42) = 0.3315$  and then again changes randomly by another law near the value of 0.1. In this case the values of the functions of  $F_{55}(j)$ ,  $F_{77}(j)$  in the peaks do not exceed the value of 0.5, which is typical for the ground state Fermi-system. The distribution functions of Bose-Einstein type  $f_{55}(j)$ ,  $f_{77}(j)$  (Fig. 1, b, d) randomly change with increasing  $j$  near the population number equal to 10, in separate planes the peaks with large population numbers are observed. Such a behavior of functions  $f_{55}(j)$ ,  $f_{77}(j)$  indicates that the ground state of a Bose-system is populated (the population number greater than 1). The global minima

with the values  $f_{55}(26) = f_{77}(42) = 2.0162$  are observed in the points at which the main peaks of the functions  $F_{55}(j)$ ,  $F_{77}(j)$  are observed. The above values of the functions in global minima and main peaks indicate that the correlations in both ground and excited states of both Bose- and Fermi-systems are taken into account.

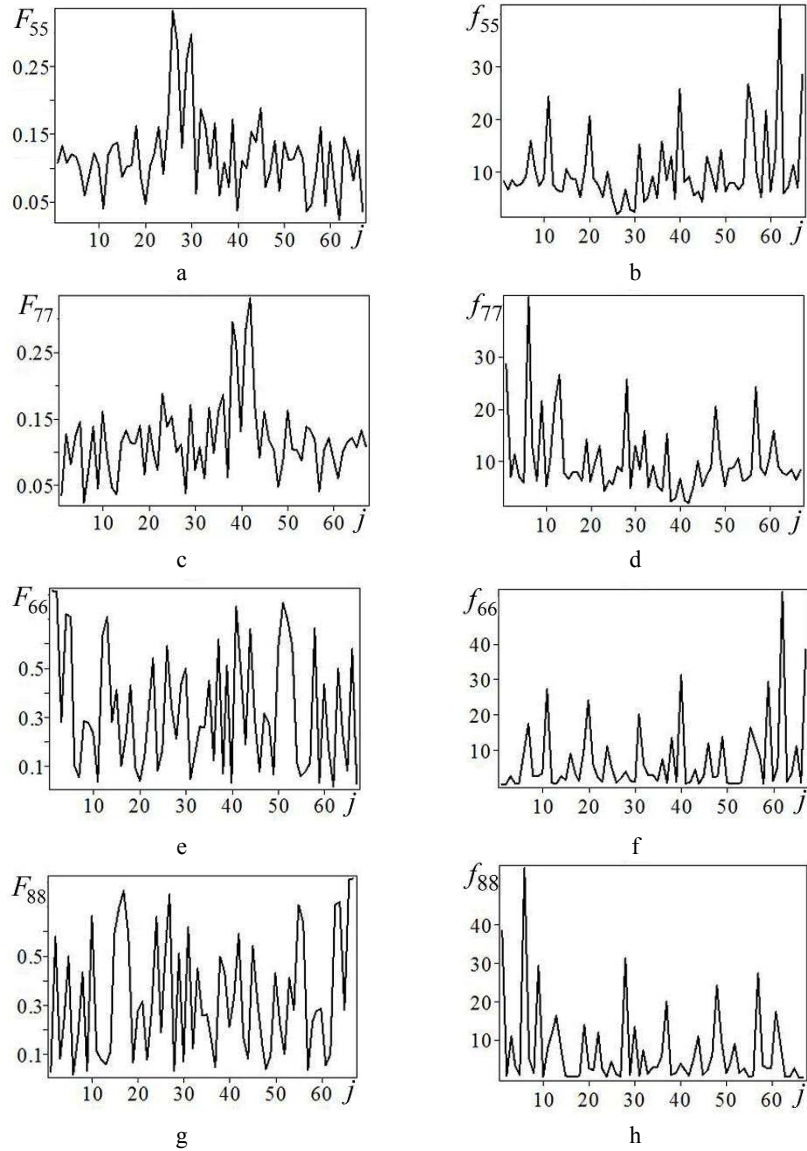


Fig. 1. Dependencies of the distribution functions of the Fermi-Dirac type (a, c, e, g) and Bose-Einstein type (b, d, f, h) on  $j$  for mixed states  $pp$

In this case, the autocorrelation function  $K_{55}$  describes a forward wave, and the autocorrelation function  $K_{77}$  describes a backward wave. The distribution functions of the Fermi-Dirac type  $F_{66}(j), F_{88}(j)$  with increasing  $j$  (Fig. 1,e,g) vary randomly around 0.5. The values of the functions in individual peaks are higher than 0.5, which is typical for inverted states of Fermi-systems. The distribution functions of Bose-Einstein type  $f_{66}(j), f_{88}(j)$  (Fig. 1,f,h) randomly change with increasing  $j$  near the occupation numbers from 0 to 10, in separate planes the peaks with large population numbers are observed. Accounting ordering pair operators in (1), (2) (the displacement and density of states of the lattice nodes) in the correlation function (6) - (9) leads to different distribution functions (10) - (13), as confirmed by numerical simulations (Fig. 1).

The dependencies of the distribution functions with mixed statistics (18) on an integer index  $j$  of a nodal plane for pure states at  $r = 7, 8$  are shown in Fig. 2.

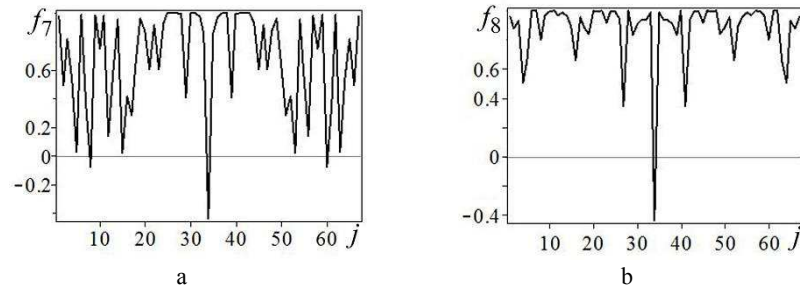


Fig. 2. Dependencies of the distribution functions with mixed statistics on  $j$  for pure states

At some points  $j$  changes sign at functions  $f_7, f_8$ , which confirms the presence of a mixed statistics. In this case functions  $f_r$  and  $f'_r$  may be interpreted as Fermi-Dirac type distribution functions for those areas of changes for  $j$ , where  $K_r > 0$ , and at  $K_r < 0$  as Bose-Einstein type distribution functions in the main and excited states, respectively. Note the pronounced stochastic behavior of the amplitudes  $|M_r|$  and phases  $\mu_r$  have of averaged functions

$$M_r = Sp\hat{M}_r = |M_r| \exp(i\mu_r).$$

The possibility of changing the sign of real parts of the first order complex correlation functions  $K_{pq}(j), C_{pq}(j)$  (6), (7) and second order correlation functions  $G_{pq}(j), g_{pq}(j)$  (14), (16) is also confirmed by the results of the numerical simulations.

#### 4. Conclusions

The numerical simulation has confirmed the theoretical conclusion of the



presence of a mixed statistics: the change of the statistics from Fermi-Dirac type to the statistics of Bose-Einstein type for separate internal nodal planes of the bulk lattice. The analysis of the distribution functions of the occupation numbers for mixed states shows that particular nodal planes may be in inverse structural states.

Based on the analysis of the correlation functions of the first and second order a possibility of changing the sign of real parts of the correlation functions is shown. This indicates a possible change in the nature of the interaction (attraction or repulsion) between lattice nodes within a single nodal plane as well as between different planes.

Accounting ordering pair operators (displacement and density of states the lattice nodes) in the correlation function has the effect of deviations of the initial distribution function.

### References

1. M.O Scully, M.S. Zubairy. *Quantum Optics*. Cambridge: Cambridge Univ. Press, 1997.
2. W. Paul. Electromagnetic traps for charged and neutral particles. *Rev. of Modern Physics* **62**, 3: 531-543, 1990.
3. M.H. Anderson, J.R. Ensher, M.R. Matthews et al. Observation of Bose-Einstein condensation in a dilute atomic vapor. *Science* **269**, 5221: 198-201, 1995.
4. S. Gleyzes, S. Kuhr, C. Guerlin et al. Quantum jumps of light recording the birth and death of a photon in a cavity. *Nature* **446**: 297-300, 2007.
5. C.W. Chou, D.B. Hume, T. Rosenband, D.J. Wineland. Optical clocks and relativity. *Science* **329**: 1630-1633, 2010.
6. J. Erhart, S. Sponar, G. Sulyok. Experimental demonstration of a universally valid error-disturbance uncertainty relation in spin measurements. *Nature Physics* **8**: 185-189, 2012.
7. A. Perrin, R. Bücker, S. Manz. Hanbury Brown and Twiss correlations across the Bose-Einstein condensation threshold. *Nature Physics* **8**: 195-198, 2012.
8. K.K. Gomes, W. Mar, W. Ko, F. Guinea et al. Designer Dirac fermions and topological phases in molecular graphene. *Nature* **483**, 7389: 306-310, 2012.
9. V.S. Abramov. Fractal dislocation as one of non-classical structural objects in the nano-dimensional systems. *Metallofiz. i Noveishie Tekhnologii* **33**, 2: 247-251, 2011.
10. O.P. Abramova, S.V. Abramov. Alteration of the structure of the stochastic dislocation deformation field under the change of governing parameters. *Metallofiz. i Noveishie Tekhnologii* **33**, 4: 519-524, 2011.
11. V.S. Abramov. Behavior of the deformation field of fractal dislocation in the presence of bifurcations. *Bul. of Donetsk Nat. Univers. Ser. A*, 2: 23-29, 2011.
12. O.P. Abramova, S.V. Abramov. Deterministic and stochastic governance of the alteration of the fractal dislocation structure. *Bul. of Donetsk Nat. Univers. Ser. A*, 2: 30-35, 2011.
13. V.S. Abramov. Inverse structural states of the stochastic deformation field of fractal dislocation. *Book of Abstracts 4th Chaotic Modeling and Simulation International Conference (CHAOS 2011), May 31 - June 3, 2011, Agios Nikolaos, Crete Greece*. p. 10, Greece, 2011.
14. H.-J. Stockmann. *Quantum Chaos. An Introduction*. Cambridge Univers. Press, 1999.
15. V.S. Abramov. Features of statistical properties of the deformation field of the fractal dislocation. *Bul. of Donetsk Nat. Univers. Ser. A*, 1: 105-113, 2012.
16. S.G. Samko, A. Kilbas O. Marichev. *Fractional Integrals and Derivatives. Theory and Applications*. Gordon and Breach Sci. Publ., New York et alibi, 1990.
17. B.B. Mandelbrot. *The Fractal Geometry of Nature*. Freeman, New York, 1982.



## New Criteria for Generalized Synchronization Preserving the Chaos Type

M. U. Akhmet<sup>1</sup> and M. O. Fen<sup>2</sup>

<sup>1</sup> Department of Mathematics, Middle East Technical University, 06800, Ankara, Turkey

(E-mail: marat@metu.edu.tr)

<sup>2</sup> Department of Mathematics, Middle East Technical University, 06800, Ankara, Turkey

(E-mail: ofen@metu.edu.tr)

**Abstract.** We provide new conditions for the presence of generalized synchronization in unidirectionally coupled systems. One of the main results in the paper is the preservation of the chaos type of the drive system. The analysis is based on the Devaney definition of chaos. Appropriate simulations which illustrate the generalized synchronization are depicted.

**Keywords:** Generalized synchronization, Devaney chaos, Chaotic set of functions.

### 1 Introduction

The most general ideas about the synchronization of different chaotic systems with an unrestricted form of coupling can be found in paper [1]. Rulkov et al. [2] realized this proposal by introducing the concept of generalized synchronization (GS) for unidirectionally coupled systems. The concept of GS [2]-[5] characterizes the dynamics of a response system that is driven by the output of a chaotic driving one.

In the present paper, the drive system will be considered in the following form

$$x' = F(x), \quad (1)$$

where  $F : \mathbb{R}^m \rightarrow \mathbb{R}^m$  is a continuous function, and the response is assumed to have the form

$$y' = Ay + g(x, y), \quad (2)$$

where  $g : \mathbb{R}^m \times \mathbb{R}^n \rightarrow \mathbb{R}^n$  is a continuous function in all its arguments and the constant  $n \times n$  real valued matrix  $A$  has real parts of eigenvalues all negative. We assume that system (1) admits a chaotic attractor.

GS is said to occur if there exist sets  $I_x, I_y$  of initial conditions and a transformation  $\varphi : \mathbb{R}^m \rightarrow \mathbb{R}^n$ , defined on the chaotic attractor of the drive system, such that for all  $x(0) \in I_x, y(0) \in I_y$  the relation  $\lim_{t \rightarrow \infty} \|y(t) - \varphi(x(t))\| = 0$  holds. In this case, a motion which starts on  $I_x \times I_y$  collapses onto a manifold  $M \subset I_x \times I_y$  of synchronized motions. The transformation  $\varphi$  is not required to exist for the transient trajectories [2,3].

According to the results of [3], GS occurs if and only if for all  $x_0 \in I_x, y_{10}, y_{20} \in I_y$ , the following criterion holds:



$$(A) \lim_{t \rightarrow \infty} \|y(t, x_0, y_{10}) - y(t, x_0, y_{20})\| = 0,$$

where  $y(t, x_0, y_{10}), y(t, x_0, y_{20})$  denote the solutions of (2) corresponding to the initial data  $y(0, x_0, y_{10}) = y_{10}, y(0, x_0, y_{20}) = y_{20}$  with the same  $x(t), x(0) = x_0$ .

A consequence of GS is the ability to predict the behavior of  $y(t)$ , based on the knowledge of  $x(t)$  and  $\varphi$  only. If  $\varphi$  is invertible  $x(t)$  is also predictable from  $y(t)$ . The usage of statistical estimations of predictability [2], analysis of conditional Lyapunov exponents [3] and the auxiliary system approach [4] are the main approaches to the observation of GS.

Let us introduce the ingredients of Devaney chaos [6] for continuous time dynamics. Denote by

$$\mathcal{B} = \{\psi(t) \mid \psi : \mathbb{R} \rightarrow K \text{ is continuous}\}$$

a collection of functions, where  $K \subset \mathbb{R}^q$  is a bounded region.

We say that  $\mathcal{B}$  is sensitive if there exist positive numbers  $\epsilon$  and  $\Delta$  such that for every  $\psi(t) \in \mathcal{B}$  and for arbitrary  $\delta > 0$  there exist  $\bar{\psi}(t) \in \mathcal{B}, t_0 \in \mathbb{R}$  and an interval  $J \subset [t_0, \infty)$ , with length not less than  $\Delta$ , such that  $\|\psi(t_0) - \bar{\psi}(t_0)\| < \delta$  and  $\|\psi(t) - \bar{\psi}(t)\| > \epsilon$ , for all  $t \in J$ .

On the other hand, the collection  $\mathcal{B}$  is said to possess a dense function  $\psi^*(t) \in \mathcal{B}$  if for every  $\psi(t) \in \mathcal{B}$ , arbitrary small  $\epsilon > 0$  and arbitrary large  $E > 0$ , there exist a number  $\xi > 0$  and an interval  $J \subset \mathbb{R}$ , with length  $E$ , such that  $\|\psi(t) - \psi^*(t + \xi)\| < \epsilon$ , for all  $t \in J$ . We say that  $\mathcal{B}$  is transitive if it possesses a dense function.

Furthermore,  $\mathcal{B}$  admits a dense collection  $\mathcal{G} \subset \mathcal{B}$  of periodic functions if for every function  $\psi(t) \in \mathcal{B}$ , arbitrary small  $\epsilon > 0$  and arbitrary large  $E > 0$ , there exist  $\tilde{\psi}(t) \in \mathcal{G}$  and an interval  $J \subset \mathbb{R}$ , with length  $E$ , such that  $\|\psi(t) - \tilde{\psi}(t)\| < \epsilon$ , for all  $t \in J$ .

The collection  $\mathcal{B}$  is called a Devaney chaotic set if: (i)  $\mathcal{B}$  is sensitive; (ii)  $\mathcal{B}$  is transitive; (iii)  $\mathcal{B}$  admits a dense collection of periodic functions.

We present two main results in the paper. The first one is the the occurrence of GS in system (1)+(2), and the second one is the preservation of the chaos type of the drive system. The GS is verified in the next section by means of the criterion (A). The third section is devoted for the presence of Devaney chaos in the response system.

## 2 Preliminaries

Throughout the paper, the uniform norm  $\|F\| = \sup_{\|v\|=1} \|Fv\|$  for matrices will be used.

Since the matrix  $A$ , which is aforementioned in system (2), is supposed to admit eigenvalues all with negative real parts, there exist positive real numbers  $N$  and  $\omega$  such that  $\|e^{At}\| \leq Ne^{-\omega t}, t \geq 0$ . These numbers will be used in the last condition below.

The following assumptions on systems (1) and (2) are needed throughout the paper:



- (A1) There exists a number  $H_0 > 0$  such that  $\sup \|F(x)\| \leq H_0$ ;
- (A2) There exists a number  $L_0 > 0$  such that  $\|F(x_1) - F(x_2)\| \leq L_0 \|x_1 - x_2\|$ ,  
for all  $x_1, x_2 \in \mathbb{R}^m$ ;
- (A3) There exists a number  $M_0 > 0$  such that  $\sup_{x \in \mathbb{R}^m, y \in \mathbb{R}^n} \|g(x, y)\| \leq M_0$ ;
- (A4) There exist numbers  $L_1 > 0$  and  $L_2 > 0$  such that
- $$L_1 \|x_1 - x_2\| \leq \|g(x_1, y) - g(x_2, y)\| \leq L_2 \|x_1 - x_2\|,$$
- for all  $x_1, x_2 \in \mathbb{R}^m, y \in \mathbb{R}^n$ ;
- (A5) There exists a number  $L_3 > 0$  such that
- $$\|g(x, y_1) - g(x, y_2)\| \leq L_3 \|y_1 - y_2\|,$$
- for all  $x \in \mathbb{R}^m, y_1, y_2 \in \mathbb{R}^n$ ;
- (A6)  $NL_3 - \omega < 0$ .

Using the theory of quasilinear equations [7], for a given solution  $x(t)$  of system (1), one can verify the existence of a unique bounded on  $\mathbb{R}$  solution  $\phi_{x(t)}(t)$  of the system  $y' = Ay + g(x(t), y)$ , which satisfies the following integral equation

$$\phi_{x(t)}(t) = \int_{-\infty}^t e^{A(t-s)} g(x(s), \phi_{x(t)}(s)) ds. \quad (3)$$

Our main assumption is the existence of a nonempty set  $\mathcal{A}_x$  of all solutions of system (1), uniformly bounded on  $\mathbb{R}$ . That is, there exists a positive real number  $H$  such that  $\sup_{t \in \mathbb{R}} \|x(t)\| \leq H$ , for all  $x(t) \in \mathcal{A}_x$ .

Let us introduce the following set of functions

$$\mathcal{A}_y = \{\phi_{x(t)}(t) \mid x(t) \in \mathcal{A}_x\}.$$

We note that for all  $y(t) \in \mathcal{A}_y$  one has  $\sup_{t \in \mathbb{R}} \|y(t)\| \leq M$ , where  $M = NM_0/\omega$ . Moreover, if  $x(t) \in \mathcal{A}_x$  is periodic then  $\phi_{x(t)}(t) \in \mathcal{A}_y$  is periodic with the same period, and vice versa.

Next, we will reveal that if the set  $\mathcal{A}_x$  is an attractor with basin  $\mathcal{U}_x$ , that is, for each  $x(t) \in \mathcal{U}_x$  there exists  $\bar{x}(t) \in \mathcal{A}_x$  such that  $\|x(t) - \bar{x}(t)\| \rightarrow 0$  as  $t \rightarrow \infty$ , then the set  $\mathcal{A}_y$  is also an attractor in the same sense. In the following lemma we specify the basin of attraction of  $\mathcal{A}_y$ .

Suppose that the set  $\mathcal{U}_y$  consists of solutions of the system  $y' = Ay + g(x(t), y)$ , where  $x(t)$  belongs to  $\mathcal{U}_x$ .

**Lemma 1.**  $\mathcal{U}_y$  is a basin of  $\mathcal{A}_y$ .

*Proof.* Fix an arbitrary  $\epsilon > 0$  and let  $y(t) \in \mathcal{U}_y$ . There exists  $\bar{x}(t) \in \mathcal{A}_x$  such that  $\|x(t) - \bar{x}(t)\| \rightarrow 0$  as  $t \rightarrow \infty$ . Set  $\alpha = \frac{\omega - NL_3}{\omega - NL_3 + NL_2}$  and  $\bar{y}(t) = \phi_{\bar{x}(t)}(t)$ . One can find  $R_0 = R_0(\epsilon) > 0$  such that if  $t \geq R_0$  then  $\|x(t) - \bar{x}(t)\| < \alpha\epsilon$  and  $N\|y(R_0) - \bar{y}(R_0)\| e^{(NL_3 - \omega)t} < \alpha\epsilon$ . Using the equation

$$\begin{aligned} y(t) - \bar{y}(t) &= e^{A(t-R_0)}(y(R_0) - \bar{y}(R_0)) \\ &+ \int_{R_0}^t e^{A(t-s)} [g(x(s), y(s)) - g(x(s), \bar{y}(s))] ds \\ &+ \int_{R_0}^t e^{A(t-s)} [g(x(s), \bar{y}(s)) - g(\bar{x}(s), \bar{y}(s))] ds, \end{aligned}$$



we obtain for  $t \geq R_0$  that

$$e^{\omega t} \|y(t) - \bar{y}(t)\| \leq N e^{\omega R_0} \|y(R_0) - \bar{y}(R_0)\| + \frac{NL_2\alpha\epsilon}{\omega} (e^{\omega t} - e^{\omega R_0}) \\ + NL_3 \int_{R_0}^t e^{\omega s} \|y(s) - \bar{y}(s)\| ds.$$

Applying Gronwall's inequality we attain that

$$e^{\omega t} \|y(t) - \bar{y}(t)\| \leq \frac{NL_2\alpha\epsilon}{\omega} e^{\omega t} + N \|y(R_0) - \bar{y}(R_0)\| e^{\omega R_0} e^{NL_3(t-R_0)} \\ - \frac{NL_2\alpha\epsilon}{\omega} e^{\omega R_0} e^{NL_3(t-R_0)} + \frac{N^2 L_2 L_3 \alpha \epsilon}{\omega(\omega - NL_3)} e^{\omega t} \left(1 - e^{(NL_3 - \omega)(t-R_0)}\right).$$

Thus, we have

$$\|y(t) - \bar{y}(t)\| < N \|y(R_0) - \bar{y}(R_0)\| e^{(NL_3 - \omega)(t-R_0)} + \frac{NL_2\alpha\epsilon}{\omega - NL_3}, \quad t \geq R_0.$$

For  $t \geq 2R_0$ , one can show that  $\|y(t) - \bar{y}(t)\| < \left(1 + \frac{NL_2}{\omega - NL_3}\right) \alpha\epsilon = \epsilon$ . Consequently,  $\|y(t) - \bar{y}(t)\| \rightarrow 0$  as  $t \rightarrow \infty$ .  $\square$

One can verify using Lemma 1 that for a fixed  $x(t) \in \mathcal{U}_x$ , any two solutions  $y(t), \bar{y}(t)$  of the system  $y' = Ay + g(x(t), y)$  satisfy the criterion (A). Therefore, we have the following corollary.

**Corollary 1.** *GS occurs in the coupled system (1)+(2).*

### 3 The chaotic dynamics

We will prove that if the drive system (1) is Devaney chaotic then the response system (2) is also chaotic in the same sense. The three ingredients of Devaney chaos will be considered individually. We start with sensitivity in the next lemma.

**Lemma 2.** *Sensitivity of the set  $\mathcal{A}_x$  implies the same feature for the set  $\mathcal{A}_y$ .*

*Proof.* Fix an arbitrary  $\delta > 0$  and  $y(t) \in \mathcal{A}_y$ . There exists  $x(t) \in \mathcal{A}_x$  such that  $y(t) = \phi_{x(t)}(t)$ . Choose a sufficiently small number  $\bar{\epsilon} = \bar{\epsilon}(\delta) > 0$  such that  $\left(1 + \frac{NL_2}{\omega - NL_3}\right) \bar{\epsilon} < \delta$ , and take  $R = R(\bar{\epsilon}) < 0$  sufficiently large in absolute value such that  $\frac{2M_0N}{\omega} e^{(\omega - NL_3)R} < \bar{\epsilon}$ . Set  $\delta_1 = \delta_1(\bar{\epsilon}, R) = \bar{\epsilon} e^{L_0 R}$ . Since  $\mathcal{A}_x$  is sensitive, there exist  $\epsilon_0 > 0$ ,  $\Delta > 0$  such that  $\|x(t_0) - \bar{x}(t_0)\| < \delta_1$  and  $\|x(t) - \bar{x}(t)\| > \epsilon_0$ ,  $t \in J$ , for some  $\bar{x}(t) \in \mathcal{A}_x$ ,  $t_0 \in \mathbb{R}$  and for some interval  $J \subset [t_0, \infty)$  whose length is not less than  $\Delta$ .

By means of continuous dependence on initial conditions, one can verify that  $\|x(t) - \bar{x}(t)\| < \bar{\epsilon}$ ,  $t \in [t_0 + R, t_0]$ . Denote  $\bar{y}(t) = \phi_{\bar{x}(t)}(t)$ . Using the relation (3) for both  $y(t)$  and  $\bar{y}(t)$ , we obtain for  $t \in [t_0 + R, t_0]$  that

$$e^{\omega t} \|y(t) - \bar{y}(t)\| \leq NL_3 \int_{t_0+R}^t e^{\omega s} \|y(s) - \bar{y}(s)\| ds \\ + \frac{NL_2\bar{\epsilon}}{\omega} (e^{\omega t} - e^{\omega(t_0+R)}) + \frac{2M_0N}{\omega} e^{\omega(t_0+R)}.$$



Applying Gronwall's Lemma to the last inequality we attain that

$$\|y(t) - \bar{y}(t)\| \leq \frac{NL_2\bar{\epsilon}}{\omega - NL_3} + \frac{2M_0N}{\omega} e^{(NL_3 - \omega)(t - t_0 - R)}, \quad t \in [t_0 + R, t_0].$$

Consequently, we have  $\|y(t_0) - \bar{y}(t_0)\| \leq \frac{NL_2\bar{\epsilon}}{\omega - NL_3} + \frac{2M_0N}{\omega} e^{(\omega - NL_3)R} < \delta$ .

Next, we will show the existence of a positive numbers  $\epsilon_1$ ,  $\bar{\Delta}$  and an interval  $J^1 \subset J$  with length  $\bar{\Delta}$  such that the inequality  $\|y(t) - \bar{y}(t)\| > \epsilon_1$  holds for all  $t \in J^1$ .

Suppose that  $g(x, y) = (g_1(x, y), g_2(x, y), \dots, g_n(x, y))$ , where each  $g_j$ ,  $1 \leq j \leq n$ , is a real valued function.

Since  $\mathcal{A}_x$  and  $\mathcal{A}_y$  are both equicontinuous on  $\mathbb{R}$ , and the function  $\bar{g}: \mathbb{R}^m \times \mathbb{R}^m \times \mathbb{R}^n \rightarrow \mathbb{R}^n$  defined as  $\bar{g}(x_1, x_2, x_3) = g(x_1, x_3) - g(x_2, x_3)$  is uniformly continuous on the compact region

$$\mathcal{D} = \{(x_1, x_2, x_3) \in \mathbb{R}^m \times \mathbb{R}^m \times \mathbb{R}^n \mid \|x_1\| \leq H, \|x_2\| \leq H, \|x_3\| \leq M\},$$

the set  $\mathcal{F}$  with elements of the form  $g_j(x(t), \phi_{x(t)}(t)) - g_j(\bar{x}(t), \phi_{x(t)}(t))$ ,  $1 \leq j \leq n$ , where  $x(t), \bar{x}(t) \in \mathcal{A}_x$ , is an equicontinuous family on  $\mathbb{R}$ . Therefore, there exists a positive number  $\tau < \Delta$ , independent of  $x(t), \bar{x}(t) \in \mathcal{A}_x$ ,  $y(t), \bar{y}(t) \in \mathcal{A}_y$ , such that for any  $t_1, t_2 \in \mathbb{R}$  with  $|t_1 - t_2| < \tau$  the inequality

$$\begin{aligned} & |(g_j(x(t_1), y(t_1)) - g_j(\bar{x}(t_1), y(t_1))) - (g_j(x(t_2), y(t_2)) - g_j(\bar{x}(t_2), y(t_2)))| \\ & < \frac{L_1\epsilon_0}{2n} \end{aligned} \quad (4)$$

holds, for all  $1 \leq j \leq n$ .

Condition (A4) implies that for each  $t \in J$ , there exists an integer  $j_0 = j_0(t)$ ,  $1 \leq j_0 \leq n$ , such that  $|g_{j_0}(x(t), y(t)) - g_{j_0}(\bar{x}(t), y(t))| \geq \frac{L_1}{n} \|x(t) - \bar{x}(t)\|$ .

Let  $s_0$  be the midpoint of the interval  $J$  and  $\theta = s_0 - \tau/2$ . One can find an integer  $j_0 = j_0(s_0)$ ,  $1 \leq j_0 \leq n$ , such that

$$|g_{j_0}(x(s_0), y(s_0)) - g_{j_0}(\bar{x}(s_0), y(s_0))| \geq \frac{L_1}{n} \|x(s_0) - \bar{x}(s_0)\| > \frac{L_1\epsilon_0}{n}. \quad (5)$$

According to (4), for all  $t \in [\theta, \theta + \tau]$  we obtain that

$$|g_{j_0}(x(s_0), y(s_0)) - g_{j_0}(\bar{x}(s_0), y(s_0))| - |g_{j_0}(x(t), y(t)) - g_{j_0}(\bar{x}(t), y(t))| < \frac{L_1\epsilon_0}{2n}$$

and therefore by means of (5), the following inequality:

$$|g_{j_0}(x(t), y(t)) - g_{j_0}(\bar{x}(t), y(t))| > \frac{L_1\epsilon_0}{2n}, \quad t \in [\theta, \theta + \tau].$$

The last inequality implies that

$$\left\| \int_{\theta}^{\theta + \tau} [g(x(s), y(s)) - g(\bar{x}(s), y(s))] ds \right\| > \frac{\tau L_1\epsilon_0}{2n}.$$



Therefore, we have

$$\begin{aligned} & \max_{t \in [\theta, \theta + \tau]} \|y(t) - \bar{y}(t)\| \geq \|y(\theta + \tau) - \bar{y}(\theta + \tau)\| \\ & > \frac{\tau L_1 \epsilon_0}{2n} - [1 + \tau(L_3 + \|A\|)] \max_{t \in [\theta, \theta + \tau]} \|y(t) - \bar{y}(t)\|, \end{aligned}$$

$$\text{and hence, } \max_{t \in [\theta, \theta + \tau]} \|y(t) - \bar{y}(t)\| > \frac{\tau L_1 \epsilon_0}{2n[2 + \tau(L_3 + \|A\|)]}.$$

Now, suppose that at the point  $\eta \in [\theta, \theta + \tau]$ , the function  $\|y(t) - \bar{y}(t)\|$  takes its maximum. Define  $\bar{\Delta} = \min \left\{ \frac{\tau}{2}, \frac{\tau L_1 \epsilon_0}{8n(M\|A\| + M_0)[2 + \tau(L_3 + \|A\|)]} \right\}$

and  $\theta^1 = \begin{cases} \eta, & \text{if } \eta \leq \theta + \tau/2 \\ \eta - \bar{\Delta}, & \text{if } \eta > \theta + \tau/2 \end{cases}$ . For  $t \in J^1 = [\theta^1, \theta^1 + \bar{\Delta}]$ , we have

$$\begin{aligned} & \|y(t) - \bar{y}(t)\| \geq \|y(\eta) - \bar{y}(\eta)\| - \left| \int_{\eta}^t \|A\| \|y(s) - \bar{y}(s)\| ds \right| \\ & - \left| \int_{\eta}^t \|g(x(s), y(s)) - g(\bar{x}(s), \bar{y}(s))\| ds \right| \\ & > \frac{\tau L_1 \epsilon_0}{4n[2 + \tau(L_3 + \|A\|)]}. \end{aligned}$$

Consequently,  $\|y(t) - \bar{y}(t)\| > \epsilon_1$ ,  $t \in J^1$ , where  $\epsilon_1 = \frac{\tau L_1 \epsilon_0}{4n[2 + \tau(L_3 + \|A\|)]}$  and the length of the interval  $J^1$  does not depend on the functions  $y(t), \bar{y}(t) \in \mathcal{A}_y$ .  $\square$

**Lemma 3.** *Transitivity of  $\mathcal{A}_x$  implies the same feature for  $\mathcal{A}_y$ .*

*Proof.* Fix arbitrary numbers  $\epsilon > 0$ ,  $E > 0$ , and  $y(t) \in \mathcal{A}_y$ . There exists a function  $x(t) \in \mathcal{A}_x$  such that  $y(t) = \phi_{x(t)}(t)$ . Let  $\gamma = \frac{\omega(\omega - NL_3)}{2M_0N(\omega - NL_3) + NL_2\omega}$ . Since there exists a dense solution  $x^*(t) \in \mathcal{A}_x$ , one can find  $\xi > 0$  and an interval  $J \subset \mathbb{R}$  with length  $E$  such that  $\|x(t) - x^*(t + \xi)\| < \gamma\epsilon$ , for all  $t \in J$ . Without loss of generality, assume that  $J$  is a closed interval, that is,  $J = [a, a + E]$  for some real number  $a$ . Denote  $y^*(t) = \phi_{x^*(t)}(t)$ .

Making use of the integral equation (3) for both  $y(t)$  and  $y^*(t)$ , one can verify for  $t \in J$  that

$$\begin{aligned} e^{\omega t} \|y(t) - y^*(t + \xi)\| & \leq \frac{2M_0N}{\omega} e^{\omega a} + \frac{NL_2\gamma\epsilon}{\omega} (e^{\omega t} - e^{\omega a}) \\ & + NL_3 \int_a^t e^{\omega s} \|y(s) - y^*(s + \xi)\| ds. \end{aligned}$$

Application of Gronwall's Lemma to the last inequality implies that

$$\|y(t) - y^*(t + \xi)\| \leq \frac{2M_0N}{\omega} e^{(NL_3 - \omega)(t-a)} + \frac{NL_2\gamma\epsilon}{\omega - NL_3} (1 - e^{(NL_3 - \omega)(t-a)}).$$

Suppose that  $E > \frac{2}{\omega - NL_3} \ln\left(\frac{1}{\gamma\epsilon}\right)$ . If  $t \in J_1 = [a + \frac{E}{2}, a + E]$ , then it is true that  $e^{(NL_3 - \omega)(t-a)} < \gamma\epsilon$ . Consequently, we have  $\|y(t) - y^*(t + \xi)\| < \left[ \frac{2M_0N}{\omega} + \frac{NL_2}{\omega - NL_3} \right] \gamma\epsilon = \epsilon$ , for  $t \in J_1$ . Thus, the set  $\mathcal{A}_y$  is transitive.  $\square$



In a similar way to Lemma 3 one can prove the following assertion.

**Lemma 4.** *If  $\mathcal{A}_x$  admits a dense collection of periodic functions, then the same is true for  $\mathcal{A}_y$ .*

The following theorem can be proved using Lemmas 2-4.

**Theorem 1.** *If the set  $\mathcal{A}_x$  is Devaney's chaotic, then the same is true for the set  $\mathcal{A}_y$ .*

In the next part, we will present an example which supports our theoretical discussions. The usual Euclidean norm for vectors and the norm induced by the Euclidean norm for square matrices will be used.

## 4 An example

We consider the Lorenz equations [8]

$$\begin{aligned}x'_1 &= 10(-x_1 + x_2) \\x'_2 &= -x_2 + 28x_1 - x_1x_3 \\x'_3 &= -\frac{8}{3}x_3 + x_1x_2,\end{aligned}\tag{6}$$

as the drive system. It is known that system (6) admits sensitivity and possesses infinitely many unstable periodic solutions [8]. The equations for the response system are chosen as

$$\begin{aligned}y'_1 &= -2y_1 - y_3 + 0.003y_2^2 + x_2 - \frac{1}{2}\cos x_2 \\y'_2 &= -y_1 - 2y_2 + 5x_1 + 0.01x_1^3 \\y'_3 &= y_1 - y_2 - 3y_3 + 2 \tan\left(\frac{x_3 + y_2}{120}\right).\end{aligned}\tag{7}$$

System (7) is in the form of (2), where  $A = \begin{pmatrix} -2 & 0 & -1 \\ 1 & -1 & -3 \\ 0 & 0 & 0 \end{pmatrix}$ . The inequality

$\|e^{At}\| \leq Ne^{-\omega t}$  is valid, where  $N = 4.829$  and  $\omega = 2$ . One verify that conditions (A4) – (A6) are satisfied with constants  $L_1 = \sqrt{3}/180$ ,  $L_2 = 17\sqrt{3}$  and  $L_3 = 16\sqrt{3}/75$ .

According to the results of the present paper, system (7) exhibits GS, saving the sensitivity feature of the drive and the existence of infinitely many unstable periodic solutions. Consider a trajectory of system (6)+(7) with  $x_1(0) = 0.11$ ,  $x_2(0) = 0.96$ ,  $x_3(0) = 18.98$ ,  $y_1(0) = -0.69$ ,  $y_2(0) = -11.09$ ,  $y_3(0) = 1.96$ . Figure 1 shows the projections of this trajectory on the  $y_1 - y_2 - y_3$  space, and supports the theoretical results such that the response system (7) possesses chaotic motions. According to the GS, the attractor shown in Figure 1, (a) is a nonlinear image of the chaotic attractor of system (6). Figure 1, (b), on the other hand, depicts the projection on the  $x_2 - y_2$  plane, and reveals that the systems are not synchronized in the sense of identical synchronization [9].

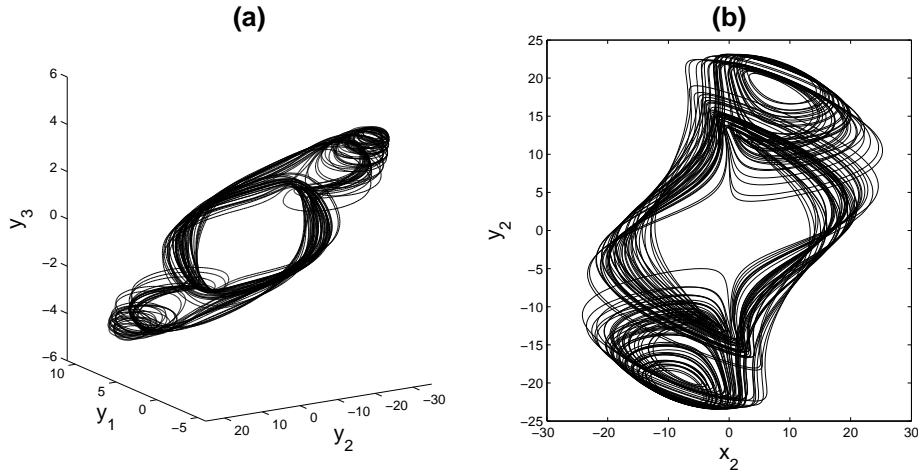


**Fig. 1.** The projections of the chaotic attractor generated by the coupled system (6)+(7). (a) Projection on the  $y_1 - y_2 - y_3$  space; (b) Projection on the  $x_2 - y_2$  plane. The pictures represent the synchronized behavior.

## References

- 1.V.S. Afraimovich, N.N. Verichev and M.I. Rabinovich. Stochastic synchronization of oscillation in dissipative systems. Radiophys. Quantum Electron., 29:795-803, 1986.
- 2.N.F. Rulkov, M.M. Sushchik, L.S. Tsimring and H.D.I. Abarbanel. Generalized synchronization of chaos in directionally coupled chaotic systems. Phys. Rev. E, 51:980-994, 1995.
- 3.L. Kocarev and U. Parlitz. Generalized synchronization, predictability, and equivalence of unidirectionally coupled dynamical systems. Phys. Rev. Lett., 76:1816-1819, 1996.
- 4.H.D.I. Abarbanel, N.F. Rulkov and M.M. Sushchik. Generalized synchronization of chaos: The auxiliary system approach. Phys. Rev. E, 53:4528-4535, 1996.
- 5.J.M. Gonzales-Miranda. Synchronization and Control of Chaos. Imperial College Press, London, 2004.
- 6.R. Devaney. An Introduction to Chaotic Dynamical Systems. Addison-Wesley, United States of America, 1987.
- 7.J.K. Hale. Ordinary Differential Equations. Krieger Publishing Company, Malabar, Florida, 1980.
- 8.E.N. Lorenz. Deterministic nonperiodic flow. J. Atmos. Sci, 20:130-141, 1963.
- 9.L.M. Pecora and T.L. Carroll. Synchronization in chaotic systems. Phys. Rev. Lett., 64:821-825, 1990.



## Replication of Discrete Chaos

M. U. Akhmet<sup>1</sup> and M. O. Fen<sup>2</sup>

<sup>1</sup> Department of Mathematics, Middle East Technical University, 06800, Ankara, Turkey  
(E-mail: marat@metu.edu.tr)

<sup>2</sup> Department of Mathematics, Middle East Technical University, 06800, Ankara, Turkey  
(E-mail: ofen@metu.edu.tr)

**Abstract.** We provide extension of chaos by implementing chaotic perturbations to exponentially stable difference equations with arbitrarily high dimensions. Our analysis is based on the Li-Yorke definition of chaos. The results are supported with the aid of simulations.

**Keywords:** Chaos extension, Li-Yorke chaos, Generalized synchronization, Chaotic set of sequences.

### 1 Introduction

Discrete equations are popular systems to provide a wide range of chaos and important to approve the existence rigorously [1]-[6]. We propose in the present paper the extension of chaos from known chaotic systems to systems with arbitrarily high dimensions.

Throughout the paper,  $\mathbb{R}$ ,  $\mathbb{Z}$  and  $\mathbb{N}$  will denote the sets of real numbers, integers and natural numbers, respectively.

We consider the discrete equations

$$x_{n+1} = F(x_n), \quad (1)$$

and

$$y_{n+1} = Ay_n + f(y_n) + g(x_n), \quad (2)$$

where  $n \in \mathbb{Z}$ ,  $A$  is a nonsingular, constant  $q \times q$  real valued matrix, and the functions  $F : \mathbb{R}^p \rightarrow \mathbb{R}^p$ ,  $f : \mathbb{R}^q \rightarrow \mathbb{R}^q$  and  $g : \mathbb{R}^p \rightarrow \mathbb{R}^q$  are continuous in all their arguments. We suppose that the map  $F$  admits the chaos and possesses an invariant set  $A \subset \mathbb{R}^p$ .

A concept which is related to our theory of chaos extension is the generalized synchronization [7]-[10]. According to the results of [9], generalized synchronization occurs in system (1)+(2) if and only if there exist sets  $B_x \subset \mathbb{R}^p$ ,  $B_y \subset \mathbb{R}^q$  such that the criterion

$$(A) \quad \lim_{n \rightarrow \infty} \|y_n - \bar{y}_n\| = 0,$$

holds, for all  $(x_0, y_0), (x_0, \bar{y}_0) \in B_x \times B_y$ , where  $\{y_n\}$  and  $\{\bar{y}_n\}$  are solutions of equation (2) with the same solution  $\{x_n\}$  of (1). Taking advantage of the



criterion (A), in the next section, we will show that generalized synchronization occurs in the dynamics of equation (1)+(2).

The first mathematically rigorous definition of chaos for one dimensional difference equations is introduced by Li and Yorke [1]. Generalizations of Li-Yorke chaos to high dimensional difference equations are provided in [2,4]. In the present paper, besides the presence of generalized synchronization, we show that if equation (1) is chaotic in the sense of Li-Yorke then the same is true for (2). In other words, equation (2) preserves the chaos type of equation (1). This is the main difference between the papers [9,10] and the present one. Moreover, we will show, by an example, the convenience of our method to equations which possess Neimark-Sacker bifurcation resulting in a stable closed curve.

Let us describe the ingredients of Li-Yorke chaos [1]-[4]. Consider a set of uniformly bounded sequences

$$\mathcal{B} = \left\{ \{\eta_n\} : \sup_{n \in \mathbb{Z}} \|\eta_n\| \leq M_{\mathcal{B}} \right\},$$

where  $M_{\mathcal{B}}$  is a positive real number.

We say that a pair of sequences  $(\{\eta_n^1\}, \{\eta_n^2\}) \in \mathcal{B} \times \mathcal{B}$  is proximal if for an arbitrary small real number  $\epsilon > 0$  and an arbitrary large natural number  $E$ , there exists an increasing sequence  $\{m_j\}$ ,  $j \in \mathbb{N}$ , of integers satisfying  $m_{2j} - m_{2j-1} \geq E$  such that for each  $j$  we have  $\|\eta_n^1 - \eta_n^2\| < \epsilon$ , for  $m_{2j-1} \leq n \leq m_{2j}$ .

It is mentioned in [3,5] that a pair of sequences  $(\{\eta_n^1\}, \{\eta_n^2\})$  is proximal if  $\liminf_{n \rightarrow \infty} \|\eta_n^1 - \eta_n^2\| = 0$ . It is worth saying that our definition for proximality, which is adapted to the collection  $\mathcal{B}$  and needed for our extension purposes, is, in general, stronger than the one mentioned in the classical sense. Nevertheless, one can achieve the equivalence of both definitions for equations of the form (1), for example, by requesting a Lipschitz condition on the function  $F$ .

Another feature of Li-Yorke chaos is the following one. A pair of sequences  $(\{\eta_n^1\}, \{\eta_n^2\}) \in \mathcal{B} \times \mathcal{B}$  is called not asymptotic if  $\limsup_{n \rightarrow \infty} \|\eta_n^1 - \eta_n^2\| > 0$ .

We call a pair of sequences  $(\{\eta_n^1\}, \{\eta_n^2\}) \in \mathcal{B} \times \mathcal{B}$  as a Li-Yorke pair, if they are proximal and not asymptotic. On the other hand, a subset  $\mathcal{C} \subset \mathcal{B}$  is called a scrambled set if it does not contain any periodic sequences and for any distinct sequences  $\{\eta_n^1\}, \{\eta_n^2\} \in \mathcal{C}$ , the pair  $(\{\eta_n^1\}, \{\eta_n^2\})$  is a Li-Yorke pair.

The set  $\mathcal{B}$  is called a Li-Yorke chaotic set if: (i)  $\mathcal{B}$  admits a periodic sequence of period  $k$ , for any  $k \in \mathbb{N}$ ; (ii)  $\mathcal{B}$  possesses an uncountable scrambled set  $\mathcal{C}$ ; (iii) For any sequence  $\{\eta_n\} \in \mathcal{C}$  and any periodic sequence  $\{\xi_n\} \in \mathcal{B}$ , we have  $\limsup_{n \rightarrow \infty} \|\eta_n - \xi_n\| > 0$ .

## 2 Preliminaries

In the following parts, we will use the uniform norm  $\|F\| = \sup_{\|v\|=1} \|Fv\|$  for matrices.

The following assumptions will be needed in the paper:

(A1) There exist positive numbers  $L_1$  and  $L_2$  such that

$$L_1 \|x - \bar{x}\| \leq \|g(x) - g(\bar{x})\| \leq L_2 \|x - \bar{x}\|,$$



for all  $x, \bar{x} \in \mathbb{R}^p$ ;

(A2) There exists a positive number  $L_3$  such that

$$\|f(y) - f(\bar{y})\| \leq L_3 \|y - \bar{y}\|,$$

for all  $y, \bar{y} \in \mathbb{R}^q$ ;

(A3) There exist positive real numbers  $M_f$  and  $M_g$  such that  $\sup_{y \in \mathbb{R}^q} \|f(y)\| \leq M_f$  and  $\sup_{x \in \mathbb{R}^p} \|g(x)\| \leq M_g$ ;

(A4)  $\|A\| + L_3 < 1$ .

For a given solution  $x = \{x_n\}$  of equation (1), using the standard technique for maps [11], one can verify that there exists a unique bounded solution  $\{\phi_n^x\}$  of equation (2). In the notation  $\{\phi_n^x\}$ , the symbol “ $x$ ” is devoted to indicate the dependence of the bounded solution on the chosen solution  $x = \{x_n\}$  of equation (1). Moreover, the unique bounded solution  $\{\phi_n^x\}$ , satisfies the following relation

$$\phi_n^x = \sum_{j=-\infty}^n A^{n-j} [f(\phi_{j-1}^x) + g(x_{j-1})], \quad n \in \mathbb{Z}. \quad (3)$$

Let us denote by  $\mathcal{A}_x$  the set of all uniformly bounded solutions of equation (1) with initial data from the set  $\Lambda$ . Set  $\mathcal{A}_y = \{\{\phi_n^x\} : x = \{x_n\} \in \mathcal{A}_x\}$ . Equation (3) implies that for any  $\{y_n\} \in \mathcal{A}_y$  the inequality  $\sup_{n \in \mathbb{Z}} \|y_n\| \leq H$  holds, where  $H = \frac{M_f + M_g}{1 - \|A\|}$ .

We say that  $\mathcal{A}_y$  is an attractor if for each solution  $\{y_n\}$  of equation (2), there exists a solution  $\{\tilde{y}_n\} \in \mathcal{A}_y$  such that  $\|y_n - \tilde{y}_n\| \rightarrow 0$  as  $n \rightarrow \infty$ . We will verify in the next lemma that the set  $\mathcal{A}_y$  is an attractor.

**Lemma 1.**  $\mathcal{A}_y$  is an attractor.

*Proof.* Consider an arbitrary solution  $\{y_n\}$  of equation (2) with a fixed solution  $\{x_n\}$  of equation (1). The relations

$$y_n = A^n y_0 + \sum_{j=1}^n A^{n-j} [f(y_{j-1}) + g(x_{j-1})],$$

$$\phi_n^x = A^n \phi_0^x + \sum_{j=1}^n A^{n-j} [f(\phi_{j-1}^x) + g(x_{j-1})],$$

imply for each  $n \geq 1$  the following inequality:

$$\|A\|^{-n} \|y_n - \phi_n^x\| \leq \|y_0 - \phi_0^x\| + \frac{L_3}{\|A\|} \sum_{j=0}^{n-1} \|A\|^{-j} \|y_j - \phi_j^x\|.$$

Applying Gronwall inequality, one can obtain that

$$\|y_n - \phi_n^x\| \leq \|y_0 - \phi_0^x\| (\|A\| + L_3)^n.$$

According to condition (A4), we have  $\|y_n - \phi_n^x\| \rightarrow 0$  as  $n \rightarrow \infty$ .  $\square$



One can verify using Lemma 1 that any two solutions  $\{y_n\}, \{\bar{y}_n\}$  of equation (2) with the same  $\{x_n\}$  satisfy the criterion (A). Therefore, generalized synchronization occurs in equation (1)+(2).

Extension of chaos in the sense of Li-Yorke will be handled in the next section.

### 3 Extension of Li-Yorke chaos

The following lemma can be proved using equation (3).

**Lemma 2.** *If a pair of sequences  $(\{x_n\}, \{\bar{x}_n\}) \in \mathcal{A}_x \times \mathcal{A}_x$  is proximal, then the pair  $(\{\phi_n^x\}, \{\phi_n^{\bar{x}}\}) \in \mathcal{A}_y \times \mathcal{A}_y$  is also proximal.*

By means of equation (2) one can show for a pair  $(\{x_n\}, \{\bar{x}_n\}) \in \mathcal{A}_x \times \mathcal{A}_x$  that

$$\|\phi_{n+1}^x - \phi_{n+1}^{\bar{x}}\| \geq \|x_n - \bar{x}_n\| - (\|A\| + L_3) \|\phi_n^x - \phi_n^{\bar{x}}\|, \quad n \in \mathbb{Z}. \quad (4)$$

Inequality (4) can be used to verify the following lemma.

**Lemma 3.** *If a pair of sequences  $(\{x_n\}, \{\bar{x}_n\}) \in \mathcal{A}_x \times \mathcal{A}_x$  is not asymptotic, then the same is true for the pair  $(\{\phi_n^x\}, \{\phi_n^{\bar{x}}\}) \in \mathcal{A}_y \times \mathcal{A}_y$ .*

The main theorem of the present paper is the following one.

**Theorem 1.** *If  $\mathcal{A}_x$  is a Li-Yorke chaotic set, then the same is true for  $\mathcal{A}_y$ .*

*Proof.* Assume that the set  $\mathcal{A}_x$  is Li-Yorke chaotic. One can show that for any  $k \in \mathbb{N}$ , the sequence  $x = \{x_n\} \in \mathcal{P}_x$  is  $k$ -periodic if and only if  $\{\phi_n^x\}$  is  $k$ -periodic. Therefore, the set  $\mathcal{A}_y$  admits a  $k$ -periodic sequence for any  $k \in \mathbb{N}$ . Denote by  $\mathcal{P}_x$  the set of periodic solutions of (1), and let  $\mathcal{P}_y = \{\{\phi_n^x\} : x = \{x_n\} \in \mathcal{P}_x\}$ .

Suppose that the set  $\mathcal{C}_x$  is an uncountable scrambled set inside  $\mathcal{A}_x$ . Define the set  $\mathcal{C}_y = \{\{\phi_n^x\} : x = \{x_n\} \in \mathcal{C}_x\}$ . Condition (A1) implies that there is a one-to-one correspondence between the elements of  $\mathcal{C}_x$  and  $\mathcal{C}_y$ . Therefore,  $\mathcal{C}_y$  is uncountable. Moreover, using the same condition one can show that no periodic sequences exist inside  $\mathcal{C}_y$ , since no such sequences take place inside  $\mathcal{C}_x$ .

Since the collection  $\mathcal{A}_x$  is assumed to be chaotic in the sense of Li-Yorke, each pair of sequences inside  $\mathcal{C}_x \times \mathcal{C}_x$  is proximal. Lemma 2 implies that the same feature is valid for each pair inside  $\mathcal{C}_y \times \mathcal{C}_y$ . On the other hand, according to Lemma 3, any couple  $(\{y_n\}, \{\bar{y}_n\}) \in \mathcal{C}_y \times \mathcal{C}_y$  satisfies the property that  $\limsup_{n \rightarrow \infty} \|y_n - \bar{y}_n\| > 0$ . Hence, the set  $\mathcal{C}_y$  is an uncountable scrambled set inside  $\mathcal{A}_y$ . Moreover, each pair inside  $\mathcal{C}_y \times \mathcal{P}_y$  is also not asymptotic, since the same is true for each pair inside  $\mathcal{C}_x \times \mathcal{P}_x$ . Consequently,  $\mathcal{A}_y$  is Li-Yorke chaotic.  $\square$



## 4 Examples

In the following two examples, as the source of chaotic perturbations, we will consider the logistic map

$$x_{n+1} = \mu x_n(1 - x_n), \quad (5)$$

where  $\mu$  is a parameter and  $x_0 \in \Lambda = [0, 1]$ . If  $0 < \mu \leq 4$  then the set  $\Lambda$  is invariant under the iterations of equation (5) [12]. For the parameter value  $\mu = 3.9$ , Li-Yorke chaos takes place in the dynamics of the logistic map [1].

*Example 1.* In this example, we consider the map

$$\begin{aligned} y_{n+1} &= -\frac{1}{4}y_n + \frac{1}{6}z_n + \frac{1}{3}y_n^3, \\ z_{n+1} &= \frac{1}{5}y_n + \frac{1}{10}z_n. \end{aligned} \quad (6)$$

Equation (6) possesses a stable equilibrium point, and does not admit chaos.

We perturb equation (6) by the solutions of (5) with the parameter value  $\mu = 3.9$ , and set up the following equation:

$$\begin{aligned} y_{n+1} &= -\frac{1}{4}y_n + \frac{1}{6}z_n + \frac{1}{3}y_n^3 + \tan\left(\frac{x_n}{4}\right), \\ z_{n+1} &= \frac{1}{5}y_n + \frac{1}{10}z_n + \frac{1}{2}e^{x_n}. \end{aligned} \quad (7)$$

Equation (7) is in the form of (2), where  $A = \begin{pmatrix} -1/4 & 1/6 \\ 1/5 & 1/10 \end{pmatrix}$ . The conditions (A1), (A2) are satisfied with  $L_1 = 3\sqrt{2}/8$ ,  $L_2 = (e + 1)/2$  and  $L_3 = 0.16$ . One can verify that condition (A4) holds for equation (7).

In compliance with Theorem 1, the chaos of the logistic map (5) is extended through equation (7). Moreover, the dynamics of equation (5)+(7) exhibits generalized synchronization.

Let us consider a solution of equation (5)+(7) with  $x_0 = 0.46$ ,  $y_0 = 0.35$  and  $z_0 = 1.23$ . Figure 1, (a) and (b), depict the  $y$  and  $z$  coordinates of the solution. Both pictures show that the solution behaves chaotically.

*Example 2.* Consider the delayed logistic map [12,13], which is represented by the following equation:

$$\begin{aligned} y_{n+1} &= z_n, \\ z_{n+1} &= \lambda z_n(1 - y_n), \end{aligned} \quad (8)$$

where  $\lambda$  is a positive real parameter.

Equation (8) describes a population dynamics model, where  $z_n$  is the density of a population at time  $n$ , and  $\lambda$  is the growth rate. In this model, the growth is determined not only by the current population but also by its density in the past [13].

According to the results mentioned in [12,13], for the parameter value  $\lambda = \lambda_0 \equiv 2$ , the fixed point  $(1/2, 1/2)$  of equation (8) undergoes a supercritical

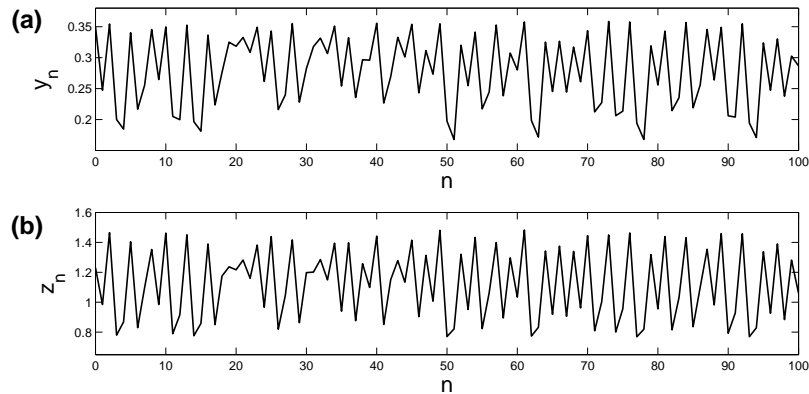


**Fig. 1.** The extension of chaos in equation (7). (a) The graph of y-coordinate; (b) The graph of z-coordinate. The parameter value  $\mu = 3.9$  is used in the map (5) such that Li-Yorke chaos takes place. The presented pictures support the theoretical results such that the chaos of the logistic map is extended.

Neimark-Sacker bifurcation. In other words, for  $\lambda > 2$  and  $\lambda - 2$  sufficiently small, the delayed logistic map has a unique attracting closed invariant curve encircling the fixed point  $(1 - 1/\lambda, 1 - 1/\lambda)$ .

We use the value  $\lambda = 2.01$  from the book [12], and perturb equation (8) by the solutions of the logistic map (5) with the parameter value  $\mu = 3.9$  to set up the following equation:

$$\begin{aligned} y_{n+1} &= z_n + 0.0045x_n, \\ z_{n+1} &= 2.01z_n(1 - y_n). \end{aligned} \quad (9)$$

Consider the trajectory of equation (5)+(9) with  $x_0 = 0.4209$ ,  $y_0 = 0.4316$  and  $z_0 = 0.4717$ . Figure 2 depicts the projection of this trajectory for  $0 \leq n \leq 10000$  on the  $y - z$  plane. One can see in the figure that the solution behaves chaotically around the stable invariant curve of equation (8). This picture reveals that our theoretical results can be used not only for systems with stable equilibrium points but also with attracting closed curves.

## References

- 1.T.Y. Li and J.A. Yorke. Period three implies chaos. *The American Mathematical Monthly*, 82:985-992, 1975.
- 2.F.R. Marotto, Snap-back repellers imply chaos in  $\mathbb{R}^n$ , *J. Math. Anal. Appl.*, 63:199-223, 1978.
- 3.M. Ciklová. Li-Yorke sensitive minimal maps. *Nonlinearity*, 19:517-529, 2006.
- 4.P. Kloeden and Z. Li. Li-Yorke chaos in higher dimensions: a review. *J. Diff. Equ. Appl.*, 12:247-269, 2006.
- 5.E. Akin and S. Kolyada. Li-Yorke sensitivity. *Nonlinearity*, 16:1421-1433, 2003.
- 6.R. Devaney. *An Introduction to Chaotic Dynamical Systems*. Addison-Wesley, United States of America, 1987.

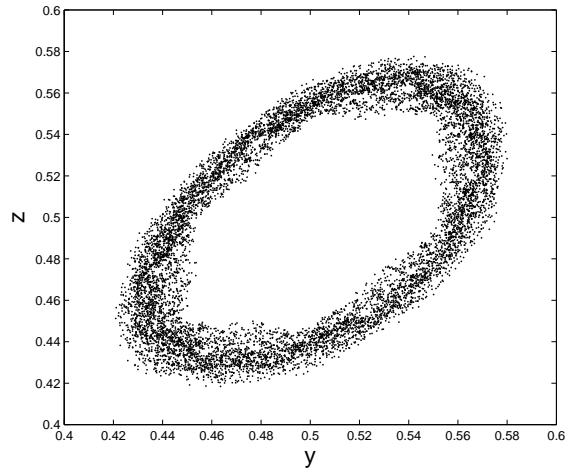


**Fig. 2.** Chaotic behavior in the perturbed delayed logistic equation (9).

- 7.N.F. Rulkov, M.M. Sushchik, L.S. Tsimring and H.D.I. Abarbanel. Generalized synchronization of chaos in directionally coupled chaotic systems. *Phys. Rev. E*, 51:980-994, 1995.
- 8.L. Kocarev and U. Parlitz. Generalized synchronization, predictability, and equivalence of unidirectionally coupled dynamical systems. *Phys. Rev. Lett.*, 76:1816-1819, 1996.
- 9.V. Afraimovich, J.-R. Chazottes and A. Cordonet. Nonsmooth functions in generalized synchronization of chaos. *Physics Letters A*, 283:109-112, 2001.
- 10.A.A. Koronovskii, O.I. Moskalenko, S.A. Shurygina and A.E. Hramov. Generalized synchronization in discrete maps. New point of view on weak and strong synchronization. *Chaos, Solitons & Fractals* 46:1218, 2013.
- 11.V. Lakshmikantham and D. Trigante. *Theory of Difference Equations: Numerical Methods and Applications*. Marcel Dekker, United States of America, 2002.
- 12.J. Hale and H. Koçak. *Dynamics and Bifurcations*. Springer-Verlag, New York, 1991.
- 13.Y.A. Kuznetsov. *Elements of Applied Bifurcation Theory*. Springer, New York, 1998.





## Model Order Reduction for Nonlinear Schrödinger Equation

Canan Akkoyunlu<sup>1</sup>, Murat Uzunca<sup>2</sup>, and Bülent Karasözen<sup>3</sup>

<sup>1</sup> Department of Mathematics and Computer Sciences, Istanbul Kültür University, 34156, Istanbul, Turkey

(E-mail: [c.kaya@iku.edu.tr](mailto:c.kaya@iku.edu.tr) )

<sup>2</sup> Department of Mathematics, Middle East Technical University, 06800 Ankara, Turkey

(E-mail: [uzunca@metu.edu.tr](mailto:uzunca@metu.edu.tr) )

<sup>3</sup> Department of Mathematics and Institute of Applied Mathematics, Middle East Technical University, 06800 Ankara, Turkey

(E-mail: [bulent@metu.edu.tr](mailto:bulent@metu.edu.tr) )

**Abstract.** Proper orthogonal decomposition (POD) is a method for deriving reduced order models of dynamical systems. In this paper, the POD is applied to the nonlinear Schrödinger equation (NLS). The NLS equation is discretized in space by finite differences and is solved in time either by structure preserving symplectic or energy preserving average vector field (AVF) integrators. Numerical results for one dimensional NLS equation with soliton solutions show that the low-dimensional approximations obtained by POD reproduce very well the characteristic dynamics of the system, such as preservation of energy and phase space structure of the NLS equation.

**Keywords:** Nonlinear Schrödinger equation, model order reduction, periodic solutions .

### 1 Introduction

The nonlinear Schrödinger (NLS) equation arises as the model equation with second order dispersion and cubic nonlinearity describing the dynamics of slowly varying wave packets in nonlinear optics and fluid dynamics and it appears in Bose-Einstein condensate theory. We consider in this paper the NLS equation

$$\psi_t = i\psi_{xx} + i\gamma |\psi|^2 \psi \quad (1)$$

with the periodic boundary conditions  $\psi(x + L, t) = \psi(x, t)$ . Here  $\psi = \psi(x, t)$  is a complex valued function,  $\gamma$  is a parameter and  $i^2 = -1$ . The NLS equation is called focusing if  $\gamma > 0$  and defocusing if  $\gamma < 0$ ; for  $\gamma = 0$ , it reduces to the linear Schrödinger equation. In last two decades various numerical methods were applied for solving NLS equation, among them are the well-known symplectic and multisymplectic integrators, discontinuous Galerkin methods.

There is a strong need for model reduction techniques to reduce the computational costs and storage requirements in large scale simulations. They should yield low-dimensional approximations for the full high-dimensional dynamical system, which reproduce the characteristic dynamics of the system.



Among the model order reduction techniques the proper orthogonal decomposition (POD) is one of the most widely used method. Surprisingly good approximation properties are reported for POD based model order reduction techniques in the literature. It has been successfully used in different fields including signal analysis and pattern recognition Fukunaga[3], fluid dynamics and coherent structures Berkooz *et al.*[2] and more recently in control theory Kunisch and Volkwein[4]. The POD is applied mostly to linear and nonlinear parabolic equations Kunisch and Volkwein[5]. In this paper, we apply the POD to the NLS equation. To the best of our knowledge, there is only one paper where POD is applied to NLS equation Schlizerman *et al.*[7], where the authors use only one and two modes approximations of the NLS equation. In this paper, the NLS equation is discretized in space and time by preserving the symplectic structure and the energy. Then, from the snapshots of the fully discretized dynamical system, the POD basis are computed using the singular value decomposition (SVD). It turns out that most of the energy of the system can be accurately approximated by using few POD modes. Numerical results for a NLS equation with soliton solutions confirm the energy and phase space preserving properties of the POD.

The paper is organized as follows. Section 2 and Section 3 are devoted to reviewing the POD method and its application to semi-linear dynamical systems. Numerical solution of the semi-discrete NLS equation and the POD reduced form are described in Section 4. In the last section, Section 5, the numerical results for the reduced order models of one-dimensional NLS equation are presented.

## 2 The Proper Orthogonal Decomposition

Let  $X$  be a real Hilbert space endowed with inner product  $\langle \cdot, \cdot \rangle_X$  and norm  $\|\cdot\|_X$ . For  $y_1, \dots, y_n \in X$  we set

$$V = \text{span} \{y_1, \dots, y_n\},$$

and refer to  $V$  as the ensemble consisting of the snapshots  $\{y_j\}_{j=1}^n$ . Let  $\{\psi_k\}_{k=1}^d$  denote an orthonormal basis of  $V$  with  $d = \dim V$ . Then each member of the ensemble can be expressed as

$$y_j = \sum_{k=1}^d \langle y_j, \psi_k \rangle_X \psi_k, \quad j = 1, \dots, n \quad (2)$$

The POD is constructed by choosing the orthonormal basis such that for every  $l \in \{1, \dots, d\}$  the mean square error between the elements  $y_j$ ,  $1 \leq j \leq n$ , and the corresponding  $l$ -th partial sum of (2) is minimized on average:

$$\min_{\{\psi_k\}_{k=1}^l} \frac{1}{n} \sum_{j=1}^n \left\| y_j - \sum_{k=1}^l \langle y_j, \psi_k \rangle_X \psi_k \right\|_X^2 \quad (3)$$

$$\langle \psi_i, \psi_j \rangle_X = \delta_{ij}, \quad 1 \leq i \leq l, \quad 1 \leq j \leq l$$



A solution  $\{\psi_k\}_{k=1}^l$  to (3) is called a POD-basis of rank  $l$ . We introduce the correlation matrix  $K = \{K_{ij}\} \in \mathbb{R}^{n \times n}$  corresponding to the snapshots  $\{y_j\}_{j=1}^n$  by

$$K_{ij} = \frac{1}{n} \langle y_j, y_i \rangle_X$$

The matrix  $K$  is positive semi-definite and has rank  $d$ . Let  $\lambda_1 \geq \dots \geq \lambda_d > 0$  denote the positive eigenvalues of  $K$  and  $v_1, \dots, v_d \in \mathbb{R}^n$  the associated eigenvectors. Then a POD basis of rank  $l \leq d$  is given by

$$\psi_k = \frac{1}{\sqrt{\lambda_k}} \sum_{j=1}^n (v_k)_j y_j$$

where  $(v_k)_j$  is the  $j$ -th component of the eigenvector  $v_k$ . Moreover, we have the error formula

$$\frac{1}{n} \sum_{j=1}^n \left\| y_j - \sum_{k=1}^l \langle y_j, \psi_k \rangle_X \psi_k \right\|_X^2 = \sum_{j=l+1}^d \lambda_j$$

The choice of  $l$  is based on heuristic considerations combined with observing the ratio of the modeled to the total energy contained in the system  $Y$  which is expressed by

$$\epsilon(l) = \frac{\sum_{i=1}^l \lambda_i}{\sum_{i=1}^d \lambda_i}$$

## 2.1 POD and SVD

There is a strong connection between POD and singular value decomposition (SVD) for rectangular matrices.

Let  $Y$  be a real-valued  $m \times n$  matrix of rank  $d \leq \min\{m, n\}$  with columns  $y_j \in \mathbb{R}^m$ ,  $1 \leq j \leq n$ . In the context of POD, it will be useful to think of the columns  $\{Y_{\cdot j}\}_{j=1}^n$  of  $Y$  as the spatial coordinates vectors of a dynamical system at time  $t_j$ . Similarly, we consider the rows  $\{Y_{i \cdot}\}_{i=1}^m$  of  $Y$  as the time trajectories of the dynamical system evaluated at the locations  $x_i$ .

SVD guarantees the existence of real numbers  $\sigma_1 \geq \sigma_2 \geq \dots \geq \sigma_d > 0$  and orthogonal matrices  $U \in \mathbb{R}^{m \times m}$  with columns  $\{u_i\}_{i=1}^m$  and  $V \in \mathbb{R}^{n \times n}$  with columns  $\{v_i\}_{i=1}^n$  such that

$$U^T Y V = \begin{pmatrix} D & 0 \\ 0 & 0 \end{pmatrix} := \Sigma \in \mathbb{R}^{m \times n} \quad (4)$$

where  $D = \text{diag}(\sigma_1, \sigma_2, \dots, \sigma_d) \in \mathbb{R}^{d \times d}$  and the zeros in (4) denote the matrices of appropriate dimensions. Moreover, the vectors  $\{u_i\}_{i=1}^d$  and  $\{v_i\}_{i=1}^d$  satisfy

$$Y v_i = \sigma_i u_i, \quad Y^T u_i = \sigma_i v_i, \quad i = 1, \dots, d.$$



One of the central issues of POD is the reduction of the data expressing their essential information by means of a few basis vectors. Let us now interpret SVD in terms of POD by the following theorem.

**Theorem :** (Kunisch and Volkwein[5]) Let  $Y = [y_1, \dots, y_n] \in \mathbb{R}^{m \times n}$  be a given matrix with rank  $d \leq \min\{m, n\}$ . Further, let  $Y = U\Sigma V^T$  be the SVD of  $Y$ , where  $U = [u_1, \dots, u_m] \in \mathbb{R}^{m \times m}$ ,  $V = [v_1, \dots, v_n] \in \mathbb{R}^{n \times n}$  are orthogonal matrices and the matrix  $\Sigma \in \mathbb{R}^{m \times n}$  has the form (4). Then, for any  $l \in \{1, \dots, d\}$  the solution to

$$\max_{\tilde{u}_1, \dots, \tilde{u}_l \in \mathbb{R}^m} \sum_{i=1}^l \sum_{j=1}^n |\langle y_j, \tilde{u}_i \rangle_{\mathbb{R}^m}|^2, \quad \langle \tilde{u}_i, \tilde{u}_j \rangle_{\mathbb{R}^m} = \delta_{ij}, \quad 1 \leq i, j \leq l \quad (5)$$

is given by the singular vectors  $\{u_i\}_{i=1}^l$ . A necessary optimality condition for (5) is given by the eigenvalue problem  $YY^T u_i = \lambda_i u_i$ .

### 3 Application to Semi-linear Time Dependent Systems

We consider the semi-linear initial value problem

$$\dot{y}(t) = Ay(t) + f(t, y(t)), \quad t \in [0, T], \quad y(0) = y_0, \quad (6)$$

where  $f : [0, T] \times \mathbb{R}^m \rightarrow \mathbb{R}^m$  is continuous in both arguments and locally Lipschitz-continuous with respect to the second argument. The NLS equation (1) is a semi-linear equation, where the cubic nonlinear part is locally Lipschitz continuous.

Suppose that we have determined a POD basis  $\{u_j\}_{j=1}^l$  of rank  $l \in \{1, \dots, m\}$  in  $\mathbb{R}^m$ . Then we make the ansatz

$$y^l(t) = \sum_{j=1}^l \underbrace{\langle y^l(t), u_j \rangle}_{=: y_j^l(t)} u_j, \quad t \in [0, T], \quad (7)$$

where the Fourier coefficients  $y_j^l$ ,  $1 \leq j \leq l$ , are functions mapping  $[0, T]$  into  $\mathbb{R}^m$ , and the inner product  $\langle \cdot, \cdot \rangle$  represents the Euclidean inner product  $\langle \cdot, \cdot \rangle_{\mathbb{R}^m}$  to make the notation simple. Since

$$y(t) = \sum_{j=1}^m \langle y(t), u_j \rangle u_j, \quad t \in [0, T]$$

holds,  $y^l(t)$  is an approximation for  $y(t)$  provided  $l < m$ . Inserting (7) into (6) yields

$$\sum_{j=1}^l \dot{y}_j^l(t) u_j = \sum_{j=1}^l y_j^l(t) A u_j + f(t, y^l(t)), \quad t \in [0, T], \quad \sum_{j=1}^l y_j^l(0) u_j = y_0 \quad (8)$$



Note that (8) is an initial-value problem in  $\mathbb{R}^m$  for  $l \leq m$  coefficient functions  $y_j^l(t)$ ,  $1 \leq j \leq l$  and  $t \in [0, T]$ , so that the coefficients are overdetermined. Therefore, we assume that (8) holds after projection on the  $l$  dimensional subspace  $V^l = span \{u_j\}_{j=1}^l$ . From (8) and  $\langle u_j, u_i \rangle = \delta_{ij}$  we infer that

$$\dot{y}_i^l(t) = \sum_{j=1}^l y_j^l(t) \langle Au_j, u_i \rangle + \langle f(t, y^l(t)), u_i \rangle \quad (9)$$

for  $1 \leq i \leq l$  and  $t \in (0, T]$ . Let us introduce the matrix

$$B = \{b_{ij}\} \in \mathbb{R}^{l \times l}, \quad b_{ij} = \langle Au_j, u_i \rangle$$

and the non-linearity  $F = (F_1, \dots, F_l)^T : [0, T] \times \mathbb{R}^l \rightarrow \mathbb{R}^l$  by

$$F_i(t, y) = \left\langle f(t, \sum_{j=1}^l y_j u_j), u_i \right\rangle, \quad t \in [0, T], \quad y = (y_1, \dots, y_l) \in \mathbb{R}^l$$

Then, (9) can be expressed as

$$\dot{y}^l(t) = B y^l(t) + F(t, y^l(t)), \quad t \in (0, T] \quad (10)$$

For initial condition, we derive  $y^l(0) = y_0$  where

$$y_0 = (\langle y_0, u_1 \rangle, \dots, \langle y_0, u_l \rangle)^T \in \mathbb{R}^l$$

This system is called the POD-Galerkin projection for (6). In case of  $l \ll m$  the  $l$ -dimensional system is a low-dimensional approximation for (6). Therefore, it is the reduced-order model for (6).

#### 4 Numerical solution of NLS equation

One dimensional NLS equation (1) can be written by decomposing  $\psi = p + iq$  in real and imaginary components

$$p_t = -q_{xx} - \gamma(p^2 + q^2)q, \quad q_t = p_{xx} + \gamma(p^2 + q^2)p \quad (11)$$

as an infinite dimensional Hamiltonian pde in the phase space  $u = (p, q)^T$

$$\dot{u} = \mathcal{D} \frac{\delta \mathcal{H}}{\delta u}, \quad \mathcal{H} = \int \frac{1}{2} (p_x^2 + q_x^2 - \frac{\gamma}{2} (p^2 + q^2)^2) dx, \quad \mathcal{D} = \begin{pmatrix} 0 & 1 \\ -1 & 0 \end{pmatrix}.$$

After discretizing the Hamiltonian in space

$$H = \frac{1}{2\Delta x^2} \sum_{j=1}^n ((p_{j+1} - p_j)^2 + (q_{j+1} - q_j)^2) - \frac{\gamma}{4} \sum_{j=1}^n (p_j^2 + q_j^2)^2.$$

we obtain the semi-discretized Hamiltonian ode's

$$p_t = -Aq - \gamma q(p^2 + q^2), \quad q_t = Ap + \gamma p(p^2 + q^2), \quad (12)$$

where  $A$  is a circulant matrix.

To solve (12) we apply the second order Strang split-step method by adapting the linear, non-linear splitting

$$u_t = \mathcal{N}u + \mathcal{L}u, \quad \mathcal{L}u = iu_{xx}, \quad \mathcal{N}u = i\gamma|u|^2u.$$



#### 4.1 POD Basis for NLS equation

Suppose that we have determined POD bases  $\{u_j\}_{j=1}^l$  and  $\{v_j\}_{j=1}^l$  of rank  $l = \{1, \dots, m\}$  in  $\mathbb{R}^m$ . Then we make the ansatz

$$p^l = \sum_{j=1}^l \alpha_j u_j(x), \quad q^l = \sum_{j=1}^l \beta_j v_j(x) \quad (13)$$

where  $\alpha_j = \langle p^l, u_j \rangle$ ,  $\beta_j = \langle q^l, v_j \rangle$  and  $p^l$ ,  $q^l$  are approximations for  $p$  and  $q$ , respectively. Inserting (13) into (12), and using that  $\langle u_i, u_j \rangle = \delta_{ij}$  and  $\langle v_i, v_j \rangle = \delta_{ij}$ ,  $i, j = 1, \dots, l$ , we obtain

$$\begin{aligned} \dot{\alpha}_i &= -\sum_{j=1}^l \beta_j \langle Av_j, u_i \rangle - \gamma \left\langle \left( \sum_{j=1}^l \beta_j v_j \right) \left( \sum_{j=1}^l \alpha_j u_j \right)^2, u_i \right\rangle - \gamma \left\langle \left( \sum_{j=1}^l \beta_j v_j \right)^3, u_i \right\rangle \\ \dot{\beta}_i &= \sum_{j=1}^l \alpha_j \langle Au_j, v_i \rangle + \gamma \left\langle \left( \sum_{j=1}^l \alpha_j u_j \right) \left( \sum_{j=1}^l \beta_j v_j \right)^2, v_i \right\rangle + \gamma \left\langle \left( \sum_{j=1}^l \alpha_j u_j \right)^3, v_i \right\rangle \end{aligned}$$

As defining  $V = [v_1, v_2, \dots, v_l] \in \mathbb{R}^{m \times l}$ ,  $\beta \in \mathbb{R}^l$ ,  $U = [u_1, u_2, \dots, u_l] \in \mathbb{R}^{m \times l}$ ,  $\alpha \in \mathbb{R}^l$ ,  $B = \{b_{ij}\}$ ,  $b_{ij} = \langle Av_j, u_i \rangle$ ,  $B^T = \{c_{ij}\}$ ,  $c_{ij} = \langle Au_j, v_i \rangle$ , we obtain

$$\begin{aligned} \dot{\alpha} &= -B\beta - \gamma U^T ((V\beta) \cdot (U\alpha)^2) - \gamma U^T ((V\beta)^3) \\ \dot{\beta} &= B^T \alpha + \gamma V^T ((U\alpha) \cdot (V\beta)^2) + \gamma V^T ((U\alpha)^3) \end{aligned} \quad (14)$$

with both the operation  $\cdot$  and the powers are hold elementwise.

The reduced order system (14) is solved, as the unreduced one (1), with the energy preserving AVF method and symplectic midpoint method applying linear-nonlinear Strang splitting Weideman and Herbst[8]. The nonlinear parts of the equations are solved by Newton-Raphson method. For solving the linear system of equations, we have used the Matlab toolbox **smt** Redivo-Zaglia and Rodriguez[6], which is designed for solving linear systems with a structured coefficient matrix like the circulant and Toeplitz matrices. It reduces the number of floating point operations for matrix factorization to  $O(n \log n)$ .

## 5 Numerical Results

For the one dimensional NLS equation we have taken the example in Celledoni *et al.*[1] with  $\gamma = 1$ , and the periodic boundary conditions in the interval  $[-20, 20]$ . The initial conditions are given as  $p(x, 0) = \exp(-(x - 1)^2/2)$ ,  $q(x, 0) = \exp(-x^2/2)$ . As mesh sizes in space and time we have used  $dx = 40/20$  and  $dt = 0.1$ , respectively.



We compare the energy error and the norm error with ROM-AVF and ROM-MID using with and without difference quotients in Table 1. With increasing number of POD basis  $l$ , the errors in the energy and discrete solutions of the fully discretized NLS equation and the reduced order model decreases. The singular values of the snapshot matrix are rapidly decaying (Figure 4) so that the only few POD modes would be sufficient to approximate the fully discretized NLS equation. For POD basis with  $l = 3$  (Figure 3), hence, the energy is well preserved as for the fully discretized form (Figure 2) and more accurate solutions are obtained with increasing number of POD modes (Figure 4).

**Table 1.**  $L_\infty$ -errors of the energy and solutions

POD	Energy (ROM-AVF)	Energy (ROM-MID)	Solution (ROM-AVF)	Solution (ROM-MID)
2	6.125e-002	6.107e-002	2.164e-001	2.159e-001
3	5.529e-002	5.528e-002	2.010e-001	2.011e-001
4	4.612e-002	4.609e-002	1.847e-001	1.835e-001
5	4.100e-002	4.095e-002	1.838e-001	1.817e-001

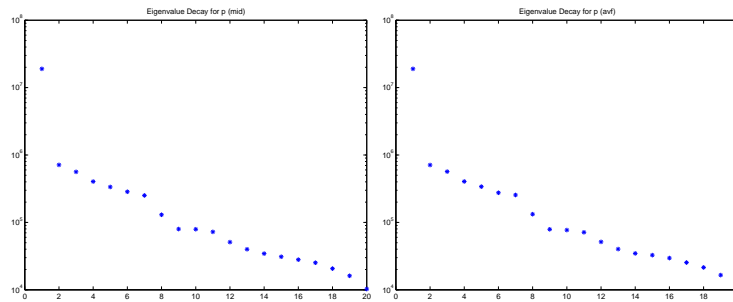


**Fig. 1.** Singular values: left: mid-point, right: AVF

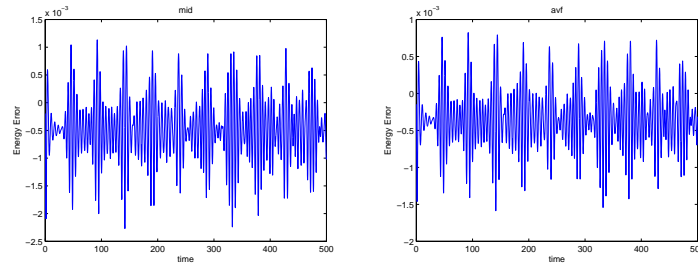


**Fig. 2.** Energy (full discretization): left: mid-point, right: AVF

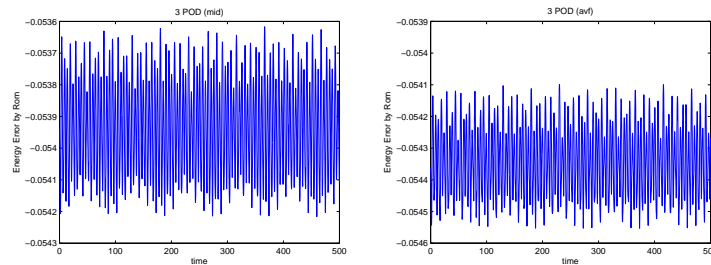


Fig. 3. Energy (POD,  $l=3$ ) : left: mid-point, right: AVF

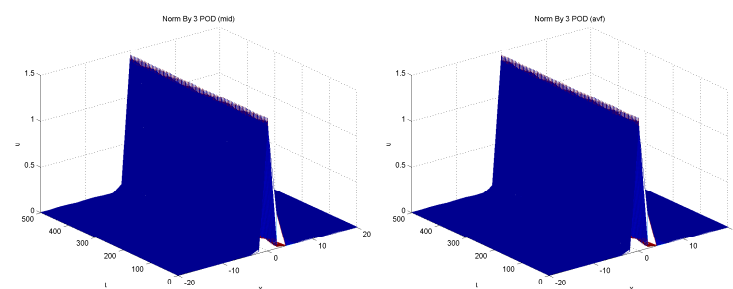


Fig. 4. ROM solutions with 3 POD modes: left: mid-point, right: AVF

## References

- 1.E. Celledoni, V. Grimm, R. I. McLachlan, D. I. McLaren, D. O’Neale, B. Owren and G.R.W. Quispel. : Preserving energy resp. dissipation in numerical PDEs using the "Average Vector Field" method, *Journal of Computational Physics*, 231:6770-6789, 2012.
- 2.G. Berkooz, P. Holmes and J.L. Lumley. *Turbulence, Coherent Structures, Dynamical Systems and Symmetry*, Cambridge University Press: Cambridge Monographs on Mechanics, 1996.
- 3.K. Fukunaga. *Introduction to statistical pattern recognition*. Computer Science and Scientific Computing. Academic Press Inc., Boston, MA, second edition, 1990.
- 4.K. Kunisch and S. Volkwein. Control of Burgers’ equation by a reduced order approach using proper orthogonal decomposition, *J. Optimization Theory and Applications* 102:345-371, 1999.
- 5.K. Kunisch and S. Volkwein. Galerkin proper orthogonal decomposition methods for parabolic problems. *Numer. Math.*, 90:117-148, 2001.
- 6.M. Redivo-Zaglia and G. Rodriguez, SMT: a Matlab structured matrices toolbox. *Numer. Algorithm*, 59:639-659, 2012.
- 7.E. Schlizerman, E. Ding, O.M. Williams and J.N. Kutz. The Proper Orthogonal Decomposition for Dimensionality Reduction in Mode-Locked Lasers and Optical Systems, *International Journal of Optics*, 831604, 2012.
- 8.J.A.C. Weideman and B.M. Herbst : Split-step methods for the solution of the nonlinear Schrödinger equation. *SIAM J. Numer. Anal.* 23:485-507, 1986.



## MPC based switching control method for PWL systems

Veysel G. Anık, Leyla Gören Sümer

Istanbul Technical University, Istanbul, Turkey  
E-mail: [anik@itu.edu.tr](mailto:anik@itu.edu.tr), [leyla.goren@itu.edu.tr](mailto:leyla.goren@itu.edu.tr)

**Abstract:** Mostly, control methods developed for nonlinear systems are used to control hybrid systems. These control methods are based on Mixed Integer Linear Programming (MILP) techniques which have computational complexity. In this study, a new Model Predictive Control (MPC) based switching control technique for Piecewise Linear systems (PWL) -a sub-class of hybrid systems- is developed to get rid of disadvantage of existing control methods.

**Keywords:** Hybrid systems, Piecewise Linear Systems, MPC.

### 1. Introduction

Nonlinear Model predictive control techniques are used in order to control Piecewise Linear systems, [9-12]. Most of these control techniques are based on Mixed Integer Linear Programming (MILP) techniques. Because of usage of MILP techniques, these control techniques have computational complexity, so the control rules must be calculated offline and some tables are generated for using online control.

In this study, a new Model Predictive Control (MPC) based switching control technique for PWL systems is developed to get rid of MILP based control techniques' disadvantages.

In the second section of this paper, Piecewise Linear systems and model predictive control technique for linear systems with polytopic uncertainties are briefly presented. It will be shown that piecewise affine system can be modeled as linear system with polytopic uncertainties which play a key role in control technique proposed here. In the last section, the control technique will be given in detail and be compared with other widely used MPC based control technique in the literature over numerical experiments.

### 2. Piecewise Linear Systems

Linear (PWL) systems are defined as [4],

$$\begin{aligned} x(k+1) &= A_i x(k) + B_i u(k) \\ y(k) &= C_i x(k) + D_i u(k) \end{aligned} \quad \text{for } \begin{bmatrix} x(k) \\ u(k) \end{bmatrix} \in \Omega_i \quad (1)$$

where  $\Omega_i$  is defined as a convex polyhedral. This convex polyhedral  $\Omega_i$  is given as equalities and/or inequalities of inputs and states. Linear systems with polytopic uncertainties are defined as,



$$x(k+1) = Ax(k) + Bu(k)$$

$$A = \sum_{i=1}^n \lambda_i A_i \quad B = \sum_{i=1}^n \lambda_i B_i \quad \sum_{i=1}^n \lambda_i = 1 \quad (2)$$

where  $\lambda_i \geq 0$  are nonnegative.

The main idea of MPC method is to calculate a series control rule which is calculated using predicted output signals for a finite horizon  $N_p$  making the considered objective function minimum for each sampling time. Then only the first control rule in this series is used to control process and data and calculations are updated at each step, [2]. In MPC method, the objective function is as follows,

$$J = J_{out} + \lambda J_m$$

$$= \sum_{j=1}^{N_p} \|\hat{y}(k+j|k) - r(k+j)\|^2 + \lambda \sum_{j=1}^{N_p} \|u(k+j-1)\|^2 \quad (3)$$

where  $\hat{y}(k)$  is estimated future output vector and  $N_p$  is prediction horizon and  $r(k)$  is reference input. MPC can be easily adapted to limitations on the control signal where these limitations can be written as

$$E(k)\tilde{u}(k) + F(k)\tilde{y}(k) \leq h(k) \quad (4)$$

In order to get a more smooth response, the control input sequence out of control horizon is defined as,

$$u(k+j) = u(k+N_c-1) \quad \text{for } j = N_c, N_{c+1}, \dots \quad (5)$$

Briefly, in model predictive control algorithm, the following steps are executed at every sampling time,

- i. Update the data
- ii. Calculate future input series which minimizes the performance index given in (3)
- iii. Apply the first control rule of this input series to the system

### 3. Main Result

The control method developed for PWL systems is based on the fact that a PWL system has always a linear system representation with polytopic uncertainty. PWL system can be rewritten as,

$$x(k+1) = Ax(k) + Bu(k)$$

$$A = \sum_{i=1}^2 \lambda_i A_i \quad B = \sum_{i=1}^2 \lambda_i B_i \quad \lambda_i = \begin{cases} 1 & \begin{bmatrix} x(k) \\ u(k) \end{bmatrix} \in \Omega_i \\ 0 & \begin{bmatrix} x(k) \\ u(k) \end{bmatrix} \notin \Omega_i \end{cases} \quad (6)$$

By comparing the PWL system model in (6) and linear system with polytopic uncertainties in (2) it can easily be seen that PWL systems can be represented as linear systems with polytopic uncertainties.



### 3.1. Model Predictive Control of linear systems with polytopic uncertainties (RMPC)

The problem of finding the control rule in the form of  $u(k+i|k) = F \cdot x(k+i|k)$  such that minimizing the upper bound of  $V(x(k/k))$  on  $J_\infty(k|k)$  can be formulated as

$$\min \max_{(A_i, B_i)} \sum_{i=0}^{\infty} x(k+i|k)^T Q_1 x(k+i|k) + u(k+i|k)^T R u(k+i|k)$$

$$s.t. \quad x(k+i|k) = A_i x(k+i-1|k) + B_i u(k+i-1|k) \quad \text{for} \quad \begin{bmatrix} x(k|k) \\ u(k|k) \end{bmatrix} \in \Omega_i \quad (7)$$

and the following theorem is taken from [5] for the solution of this problem .

*Theorem 2.1.* Let  $x(k) = x(k/k)$  be the state of the uncertain polytopic system measured at sampling time  $k$ . Then, in the absence of input and output constraints, the state-feedback matrix  $F$  which minimizes the upper bound  $V(x(k|k))$  on  $J_\infty(k|k)$

$$J = \sum_{i=0}^{\infty} x^T(k|k) Q_1 x(k|k) + u^T(k|k) R u(k|k) \quad (8)$$

at sampling time  $k$  is given by,

$$F = YQ^{-1} \quad (9)$$

where  $Q > 0$  and  $Y$  are the solutions (if they exist) to the following eigenvalue problem :

$$\min_{\gamma, Q, Y} \gamma$$

$$s.t. \quad \begin{bmatrix} 1 & x(k|k)^T \\ x(k|k) & Q \end{bmatrix} \geq 0$$

$$s.t. \quad \begin{bmatrix} Q & QA_j^T + Y^T B_j^T & QQ_1^{1/2} & Y^T R^{1/2} \\ A_j Q + B_j Y & Q & 0 & 0 \\ Q_1^{1/2} Q & 0 & \gamma I & 0 \\ R^{1/2} Y & 0 & 0 & \gamma I \end{bmatrix} \geq 0 \quad j=1, 2, \dots, n \quad (10)$$

### 3.3. Control method for PWL systems

The following procedure is given for the control method proposed in this study,

- i. Calculate the intersection points between the trajectory of the system and the border of sub-regions. The first boundary point is denoted by  $x_h$ .
- ii. For each region, find the control rule which drives the system from the initial point to these points using linear MPC technique as

$$u = \begin{cases} \min_{u=F_1x(k+1|k)} J & \text{s.t. } \dot{x} = A_1x + B_1u & \text{if } x \in X_1 \\ \vdots & & \vdots \\ \min_{u=F_nx(k+1|k)} J & \text{s.t. } \dot{x} = A_nx + B_nu & \text{if } x \in X_n \end{cases}$$

- iii. Repeat the procedure as long as the trajectory of the system until it reaches origin.

### 3.4. Numerical Experiments

In this study, the developed control method will be compared with the following switching control rule proposed in [6-8],

$$u = \begin{cases} \min_{u=F_1x(k+1|k)} J & \text{s.t. } \dot{x} = A_1x + B_1u & \text{if } x \in X_1 \\ \vdots & & \vdots \\ \min_{u=F_nx(k+1|k)} J & \text{s.t. } \dot{x} = A_nx + B_nu & \text{if } x \in X_n \end{cases} \quad (11)$$

where the control rule  $u = F_i \cdot x(k+1|k)$  is MPC rule designed for  $i^{\text{th}}$  sub-region to drive the related linear system to origin.

For the first numerical experiment, consider the following bimodal system,

$$\dot{x} = \begin{cases} \begin{bmatrix} -1 & 0.5 \\ 1 & 0 \end{bmatrix} x + \begin{bmatrix} 0 \\ 1 \end{bmatrix} u & \text{if } x_1 \geq 5 \\ \begin{bmatrix} -1 & 0.3 \\ 1 & 0 \end{bmatrix} x + \begin{bmatrix} 0 \\ 1 \end{bmatrix} u & \text{otherwise} \end{cases} \quad (12)$$

and the objective function given in the form,

$$\min \int x^T(t) \begin{bmatrix} 1 & 0 \\ 0 & 1 \end{bmatrix} x(t) + 1.5u^2(t) dt$$

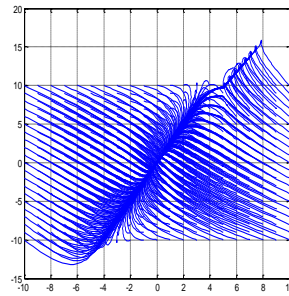


Fig. 1. The phase portrait of the closed loop system controlled by switching controller proposed in [6,7,8]

Using MPC based switching control method proposed in [6]; the phase portrait of the system is shown in the Figure 1. As stated in [6], the switching control

rule  $u(k+i|k) = F_i \cdot x(k+1|k)$  can cause stability problems at the sub-region borders.

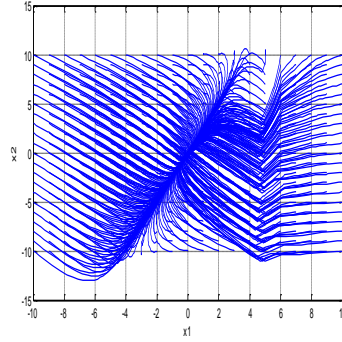


Fig. 2. The phase portrait of the closed loop system controlled by control method proposed in the study

Using MPC based switching control method proposed in this study; the phase portrait of the system is shown in the Figure 2. Since the intersection points between the trajectory of the system and the border of sub-regions ultimately converge to the origin, the control method given in Section 3.3 guarantees the stability of the closed loop system. Initial condition is set as  $x = [6 \ 6]^T$  and closed loop system trajectories are shown in the Figure 3. The convenient comparison of control methods can be given in terms of objective function value in Table 1.

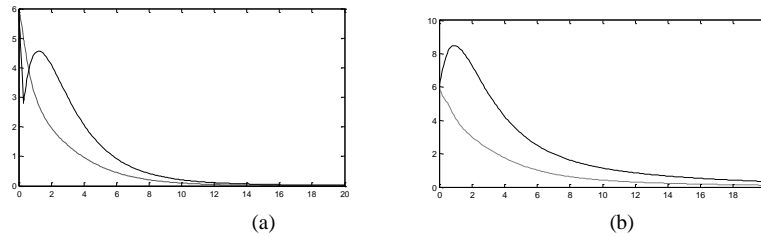


Fig. 3. Closed loop system trajectory controlled by control method proposed here (a) and by switching control rule developed in [6-8] (b) for the given initial point

Table 1. Objective function's values

Control method proposed in [6]	Developed control method
$J=2.1048$	$J=2.8059$

In the second experiment, control rules are calculated for the following PWL system,

$$\dot{x}(t) = \begin{cases} \begin{bmatrix} -1 & 0.5 \\ 1 & 0 \end{bmatrix} x + \begin{bmatrix} 0 \\ 1 \end{bmatrix} u & \text{for } x_1 \leq -5 \\ \begin{bmatrix} -1 & 0.3 \\ 1 & 0 \end{bmatrix} x + \begin{bmatrix} 0 \\ 1 \end{bmatrix} u & \text{for } -5 < x_1 \leq 5 \\ \begin{bmatrix} -1 & 0.2 \\ 1 & -2 \end{bmatrix} x + \begin{bmatrix} 0 \\ 1 \end{bmatrix} u & \text{for } x_1 > 5 \end{cases}$$

and the objective function is given in the form of,

$$\min \int x^T(t) \begin{bmatrix} 1 & 0 \\ 0 & 1 \end{bmatrix} x(t) + 1.5u^2(t) dt$$

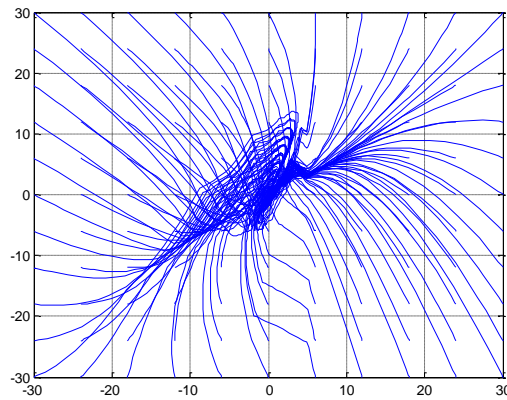


Fig. 4. Phase portrait of the closed loop system controlled by switching controller developed in [6]

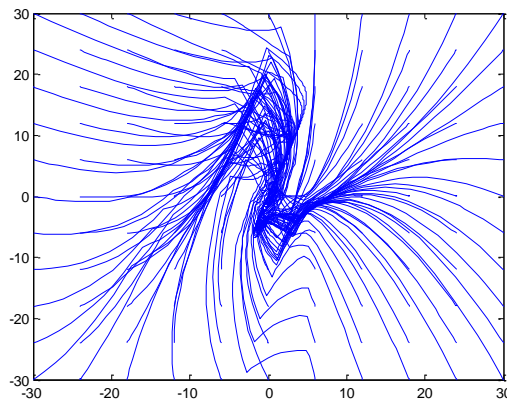


Fig. 5. The phase portrait of the closed loop system controlled by control method proposed in the study

For a more convenient comparison of control methods in terms of objective function value, initial condition is set as  $x = [20 \ 20]^T$ . Obtained closed loop system trajectories are shown in Figure 6.

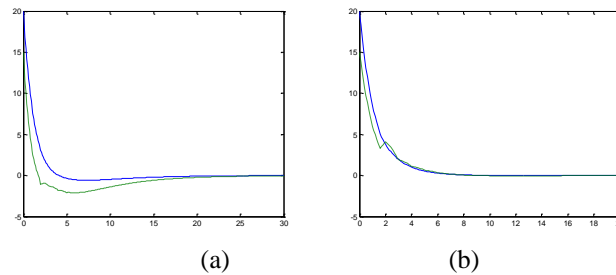


Fig. 6. Closed loop system trajectory controlled by control method proposed here (a) and by switching control rule developed in [6-8] (b) for the given initial point

Table 2. Objective Function's value

Control method proposed in [6]	Developed control method
$J=0.6659$	$J=0.2977$

#### 4. Results

In this study, using the representation of bimodal system as linear system with polytopic uncertainties, a switching control method is developed which guarantees the stability of the closed loop system. Proposed control method is compared with the switching control method given in [6] in the sense of stability and objective function values.

Even the switching control method proposed in [6-8] has good performance index value; it cannot guarantee the stability of the closed loop system. The proposed control method guarantees the stability of the closed loop system, since the intersection points between the trajectory of the system and the border of sub-regions ultimately converge to the origin. It could be argued that developed control method is a better control method for PWL systems than the existing control methods in the literature considering guaranteed stability and good objective function values.

#### References

1. E. F. Camacho and C. Bordons, Model predictive control, 2nd ed., Springer-Verlag, 2004
2. D. Mayne, J. Rawlings, C. Rao and P. Sokaert, "Constrained model predictive control: Stability and optimality", Automatica, No: 36, s: 789-814, 2000.
3. M. Baotic, F. J. Christophersen and M. Morari, "Constrained optimal control of hybrid systems with a linear performance index," IEEE Transactions on Automatic Control, no. 51, 2006.



4. E.D. Sontag, "Nonlinear regulation: the piecewise linear approach", IEEE Transection on Automatic Control, vol:26, No: 2, p: 346-358,1981
5. M.V. Kothare, V. Balakrishnan and M. Morari,"Robust Constrained Model Predictive Control using Linear Matrix Inequalities",IFA-Report No.95-02, March 1995
6. D. Mignone, G. Ferrari-Trecate and M. Morari, "Stability and Stabilization of Piecewise Affine and Hybrid Systems: An LMI Approach", Proceedings of the 39th IEEE Conference on Decision and Control, p. 504-509, 2000.
7. B. De Schutter and M. Heemels, Modelling and Control of Hybrid Systems, Ders notlari, July 2007
8. M. Johansson, "Piecewise Linear Control Systems", Lecture Notes in Control and Information Sciences, vol: 284, Springer, Berlin, Almanya, 2003.
9. M. Rubagotti, S. Trimboli, D. Bernardini and A. Bemporad, "Stability and Invariance Analysis of Approximate Explicit MPC based on PWA Lyapunov Functions", IFAC World Congress, p. 5712-5717, 2011.
10. A. Bemporad, "Hybrid Toolbox – User's Guide," Aralık 2003, <http://www.dii.unisi.it/hybrid/toolbox>
11. F.D. Torrisi and A. Bemporad, "HYSDEL - A tool for generating computational hybrid models," IEEE Transactions on Control Systems Technology, vol: 12, no: 2, p. 235-249, March 2004
12. A. Bemporad and M. Morari, "Control of systems integrating logic, dynamics, and constraints," Automatica, cilt: 35, no: 3, s. 407-427, March 1999.



## Bifurcation Phenomena Observed in an Interrupted Electric Circuit with Two Switches

Hiroyuki Asahara<sup>1</sup>, Yutaka Izumi<sup>2</sup>, and Takuji Kousaka<sup>2</sup>

<sup>1</sup> Dept. of Electrical Engineering, Fukuoka University,  
19-1, Nanakuma 8, Jonan-ku, Fukuoka, Japan.  
(E-mail: asahara@bifurcation.jp)

<sup>2</sup> Dept. of Mechanical and Energy Systems Engineering, Oita University,  
700 Dannoharu, Oita, Japan.  
(E-mail: yutaka@bifurcation.jp, takuji@oita-u.ac.jp)

**Abstract.** In this study, we analyze a simple interrupted electric circuit with two switches. First, we show the circuit model and then we explain its dynamics. Next, we define the sampled data model. Using the sampled data model, we derive the 1- and 2-parameter bifurcation diagrams. Finally, we discuss the characteristic of the circuit. The proposed circuit is the simplest interrupted electric circuit with two switches; the switching action is dependent on the state and a periodic interval. Therefore, the qualitative characteristic may be same for the real circuit, which has two interrupted switches, i.e., such as the parallel-connected DC/DC converters.

**Keywords:** Bifurcation, Interrupted electric circuit, Poincaré map.

### 1 Introduction

..An electric circuit, which has the switch depending on the state and a periodic interval, has the interrupted characteristics. We call this class of the circuit as the interrupted electric circuit, eg., DC/DC converters are the typical example of the interrupted electric circuit. It is known that the interrupted electric circuit has two or more subsystems. Also, the discrete map of the interrupted electric circuit is categorized as the piecewise smooth map. There are rich nonlinear dynamics in the interrupted electric circuit upon varying the circuit parameter such as the input voltage and control gain [1,2]. It is important to analyze the nonlinear dynamics in the interrupted electric circuit not only for understanding circuit characteristics but also for providing a useful information to the practical application. So, many researchers have analyzed nonlinear dynamics of the interrupted electric circuit since decades ago [3–6]. We have also proposed an interrupted electric circuit, which simulates switching dynamics of the current mode controlled DC/DC converter, for rigorously understanding nonlinear phenomena of the this class of the circuit [7].

The nonlinear phenomena in a simple class of the interrupted electric circuit, such as the DC/DC buck, boost, and buck-boost converters, have been completely analyzed in the previous works [8, 9]. But, detailed analysis of the parallel connected DC/DC converters or resonate type converters are insufficient because of their complicated behavior. Especially, for understanding fundamental characteristic of the parallel connected DC/DC converters in detail, we have proposed a simple interrupted electric circuit with two switches [10]. The switching action of the circuit simulates that of the parallel connected DC/DC converters. Thus, we consider is is important to analyze nonlinear phenomena of the circuit for rigorously understanding characteristics of the

parallel connected DC/DC converters. But, the analysis of the circuit is insufficient yet.

In this study, we analyze the nonlinear phenomena of the circuit proposed in Ref. [10]. First, we show the circuit model and then we explain behavior of the waveform. Next, we define the Poincaré map. Using the Poincaré map, we derive the 1- and 2-parameter bifurcation diagrams. Finally, we discuss the characteristic of the circuit.

## 2 Circuit dynamics

Figure 1 shows the circuit model. If the clock pulse is impressed at every period of  $2T$ , the switch-1 and switch-2 change from B's side to A's side. Note that the clock pulse for switch-2 delays time  $T$  compared with that for switch-1. The circuit parameters are follows:

$$R = 10[\text{k}\Omega], C = 0.33[\mu\text{F}], E = 3.0[\text{V}], T = 1.0[\text{ms}] \quad (1)$$

The circuit has four subsystems depending on the switching state. We call each subsystems as Case-1, Case-2, Case-3 and Case-4 as follows:

- Case-1:** The switch-1 and the switch-2 are in state-A.
- Case-2:** The switch-1 is in state-A and the switch-2 is in state-B.
- Case-3:** The switch-1 is in state-B and the switch-2 is in state-A.
- Case-4:** The switch-1 and the switch-2 are in state-B.

We can easily derive the circuit equations for each subsystems. By solving the circuit equation, we get

$$v(t) = \begin{cases} \varphi_1(t, kT, v_k, \lambda, \lambda_1) , & \text{for state 1} \\ \varphi_2(t, kT, v_k, \lambda, \lambda_2) , & \text{for state 2,} \\ \varphi_3(t, kT, v_r, \lambda, \lambda_3) , & \text{for state 3} \end{cases} \quad (2)$$

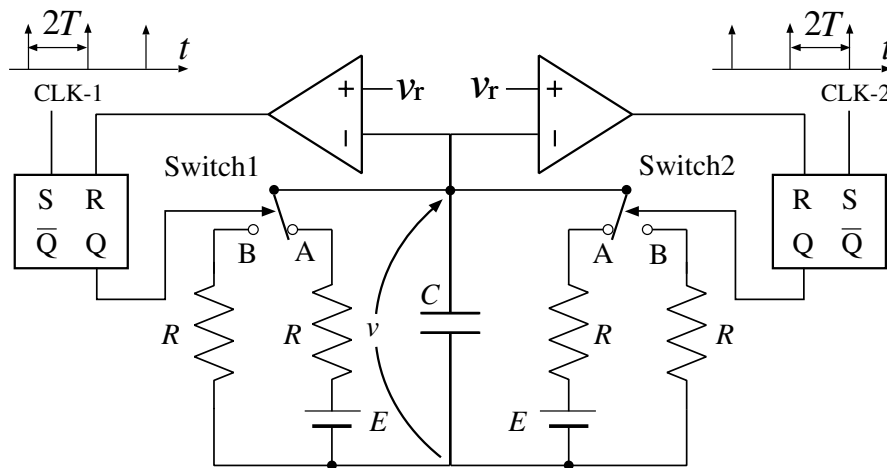


Fig. 1. Circuit model.





where  $\Pi$  denotes the reference value. After that the waveform reaches to  $v_{k+1}$  at  $t = (k + 1)T$ . So, we define the following map  $M_{2B}$ :

$$\begin{aligned} M_{2B} : \Pi &\rightarrow \mathbf{R} \\ v_r &\mapsto v_{k+1} = \varphi_3(T - t_A, kT + t_A, v_r, \lambda, \lambda_3). \end{aligned} \quad (7)$$

Thus, the discrete map is defined as follows:

$$\begin{aligned} M_2 : \mathbf{R} &\rightarrow \mathbf{R} \\ v_k &\mapsto v_{k+1} = M_{2B} \circ M_{2A}. \end{aligned} \quad (8)$$

Likewise, the subsystem keeps state-2 during the clock interval if  $v_k \leq D'$  is satisfied. Thus, the discrete map  $M'_1$  is defined as follows:

$$\begin{aligned} M'_1 : \mathbf{R} &\rightarrow \mathbf{R} \\ v_k &\mapsto v_{k+1} = \varphi_2(T, kT, v_k, \lambda, \lambda_2). \end{aligned} \quad (9)$$

The waveform reaches to the reference value  $v_r$  at  $t = kT + t'_A$  if  $v_k > D'$  is satisfied. Thus, we define the following map  $M'_{2A}$ :

$$\begin{aligned} M'_{2A} : \mathbf{R} &\rightarrow \Pi \\ v_k &\mapsto v_r = \varphi_2(t'_A, kT, v_k, \lambda, \lambda_2). \end{aligned} \quad (10)$$

Then, the waveform is sampled at  $t = (k + 1)T$ :

$$\begin{aligned} M'_{2B} : \Pi &\rightarrow \mathbf{R} \\ v_r &\mapsto v_{k+1} = \varphi_3(T - t'_A, kT + t'_A, v_r, \lambda, \lambda_3). \end{aligned} \quad (11)$$

Thus, the discrete map is defined as follows:

$$\begin{aligned} M'_2 : \mathbf{R} &\rightarrow \mathbf{R} \\ v_k &\mapsto v_{k+1} = M'_{2B} \circ M'_{2A}. \end{aligned} \quad (12)$$

Using the discrete maps, we derive the bifurcation diagrams and discuss the fundamental characteristic of the circuit in the following analysis.

## 4 Fundamental characteristics of the circuit

First, we discuss the bifurcation phenomena of the circuit. Figure 3 shows an example of the 1-parameter bifurcation diagrams upon varying the bifurcation parameter  $v_r$  from  $v_r = 0.5[\text{V}]$  to  $v_r = 2.0[\text{V}]$ . Note that we have calculated the 1 parameter bifurcation diagram in the circuit with single switch for comparing the bifurcation point and bifurcation structure. Moreover, Fig. 4 shows the waveforms and the Poincaré maps. Here, (a) and (b) in Fig. 4 correspond to the parameters (a) and (b) in Fig. 3. Note that we have numerically calculated Figs. 3 and 4 using Eqs. (5), (8), (9), (12). We observe the bifurcation phenomena in the 1-parameter bifurcation diagram. For example, the period-1 solution bifurcates to the period-2 solution around  $v_r = 0.8[\text{V}]$ . After that the period-2 solution bifurcates to the period-3 solution around  $v_r = 1.9[\text{V}]$ . Moreover, it is clear that there are various kinds of the periodic solution and the chaotic attractors in the circuit.

Figure 5 shows examples of the 2-parameter bifurcation diagrams of  $v_r$ - $T$  plane. In the figure, we express the existence region of the period- $m$  solution as  $mP$ , where  $m = 1, 2, 3$ . There is the period-doubling bifurcation in the circuit. The condition of the period-doubling bifurcation is defined as follows:

$$\left(\frac{dM_1}{dv_k}\right)^{n-2} \frac{dM_2}{dv_k} \frac{dM'_1}{dv_k} + 1 = 0 \quad (n \geq 2). \quad (13)$$

Using Eq. (13), for example, we can define the bifurcation sets of the period-1 solution as follows:

$$\frac{dM'_2}{dv_k} + 1 = 0. \quad (14)$$

The solid lines in Fig. 5 are the bifurcation sets of the period doubling bifurcation.

Tables 1 and 2 show the characteristic multiplier of the period-1 solution. In the following analysis, we compare the characteristic multipliers, between the circuit with two switches and the circuit with single switch, and discuss the fundamental characteristic of the circuit with two switches. The tables say that two interrupted switches

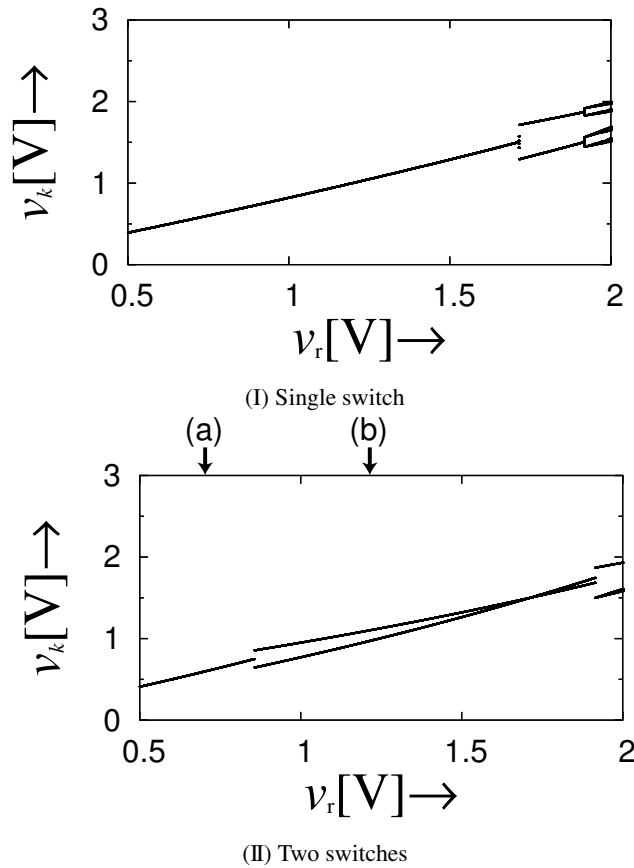
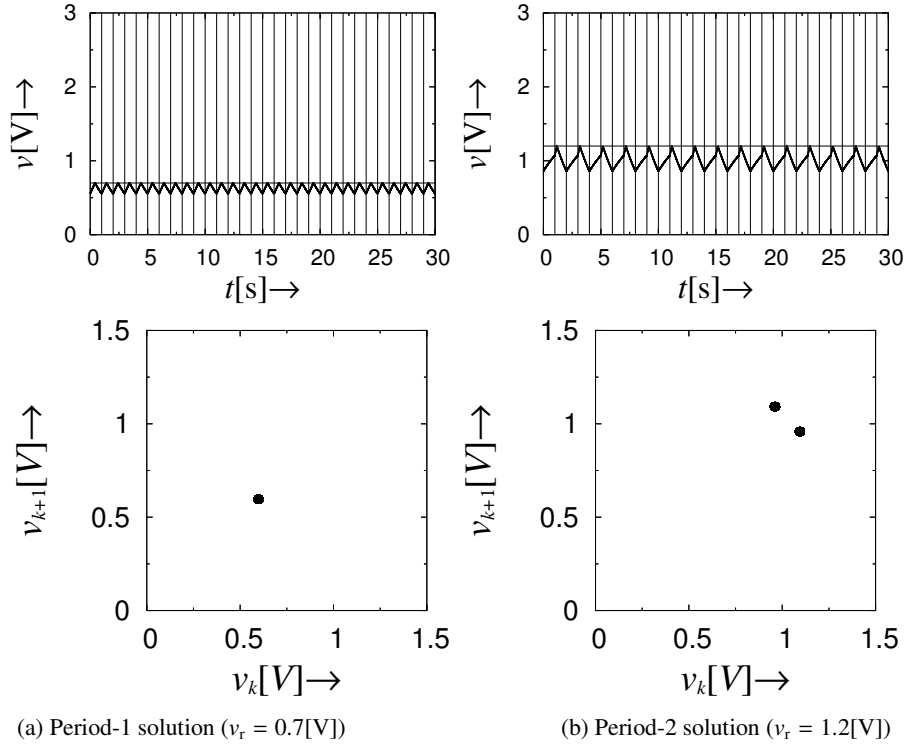


Fig. 3. Example of the 1-parameter bifurcation diagram.



**Fig. 4.** Examples of the waveform and the discrete map.

make the existence region of the period-1 solution small. This result will be same in the practical system, i.e., parallel-connected DC/DC converters, because both of our simple model and the parallel-connected DC/DC converters have the two interrupted switches.

## 5 Conclusion

In this study, we have studied characteristic of an interrupted electric circuit with two switches. First, we showed the circuit model and its behavior. Next, we defined the Poincaré map. Using the Poincaré map, we calculated the 1- and 2-parameter bifurcation diagrams. Finally, we discussed the characteristics the circuit using the bifurcation diagrams. We found that the two interrupted switches affect the existing region of the periodic solution. Especially, we remarked that the two interrupted switches makes the existence region of the period-1 solution small. We consider that above result will be apply for the parallel-connected DC/DC converters because our circuit simulates switching action of the parallel-connected DC/DC converters. In future, we will clarify the characteristics of the circuit in detail and also will analyze the nonlinear phenomena in the parallel-connected DC/DC converter for understanding fundamental characteristic of it.

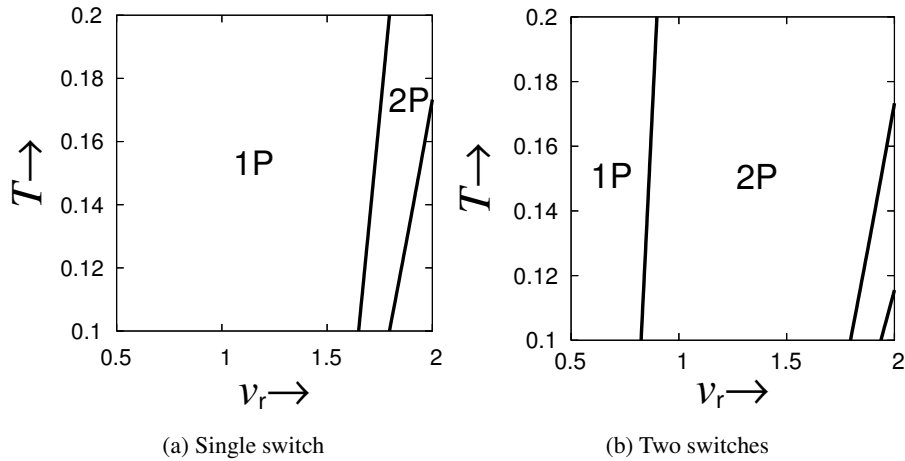


Fig. 5. Example of the 2-parameter bifurcation diagrams.

Table 1. Stability of the circuit with single switch.

Bifurcation parameter $v_r$	Characteristic multiplier	Remark
1.6056	-0.99962	Stable
1.6057	-0.99975	Stable
1.6058	-0.99989	Stable
1.6059	-1.00002	Period doubling bifurcation
1.6060	-1.00016	Unstable
1.6061	-1.00029	Unstable
1.6062	-1.00042	Unstable

Table 2. Stability of the circuit with two switches.

Bifurcation parameter $v_r$	Characteristic multiplier	Remark
0.855100	-0.999295	Stable
0.855200	-0.999567	Stable
0.855300	-0.999839	Stable
0.855400	-1.000111	Period doubling bifurcation
0.855500	-1.000383	Unstable
0.855600	-1.000655	Unstable
0.855700	-1.000928	Unstable

## References

- 1.S. Banerjee, G. C. Verghese, eds., "Nonlinear Phenomena in Power Electronics: Attractors, Bifurcations, Chaos, and Nonlinear Control." IEEE Press 2001.
- 2.C. K. Tse, "Complex Behavior of Switching Power Converters." New York: CRC, 2003.
- 3.G. Yuan, S. Banerjee, E. Ott, J.A. Yorke, "Border-Collision Bifurcations in the Buck Converter." IEEE Transaction on Circuits and Systems I, Vol. 45, No. 7, Pp. 707-716, 1998. piecewise linear map



- 4.A. El. Aroudi, G. Olivar, L. Benadero, T. Toribio, "Hopf bifurcation and chaos from torus breakdown in a PWM voltage-controlled DC-DC boost converter." IEEE Transaction on Circuits and Systems I, Vol. 46, Pp. 1374–1382, 1999.
- 5.T. Kabe, S. Parui, H. Torikai, S. Banerjee, and T. Saito, "Analysis of Piecewise Constant Models of Current Mode Controlled DC-DC Converters." IEICE TRANS. FUNDAMENTALS, vol.E90-A, no.2, 2007.
- 6.D. Fournier-Prunaret, P. Charge, L. Gardini, "Border collision bifurcations and chaotic sets in a two-dimensional." Communications in Nonlinear Science and Numerical Simulation, Vol. 16, No. 2, Pp. 916-927, 2011.
- 7.T. Kousaka, T. Ueta, S. Tahara and H. Kawakami, "Implementation and Analysis of a Simple Circuit Causing Border-Collision Bifurcation." IEE Japan, Vol.122-C, No.11, pp.1908–1916, 2002. (In Japanese)
- 8.H. H. C. Iu et al., "Comparative Study of Bifurcation in Single and Parallel-Connected Buck Converters Under Current-Mode Control: Disappearance of Period-Doubling." Circuits Systems Signal Processing Vol. 24, No. 2, 2005, Pp. 201–219.
- 9.Y. Huang, C.K. Tse, "Circuit theory of paralleling switching converters." International Journal of Circuit Theory and Applications Vol. 37, No. (1), Pp. 109–135, 2009
- 10.H. Asahara, T. Kousaka, "FUNDAMENTAL CHARACTERISTICS OF AN ELECTRIC CIRCUIT WITH TWO STATE- AND TIME-DEPENDENT INTERRUPTED SWITCHES." Proc. ITC-CSCC 2012, B-T3-01, 2012.



## Mathematical Modeling of Chaotic Vibrations of Strongly Non-Linear Continuous Structures

A.V. Krysko<sup>1</sup>, J. Awrejcewicz<sup>2</sup>, T.V. Yakovleva<sup>3</sup>, V. Dobriyan<sup>4</sup>,  
I.V. Papkova<sup>5</sup>, V.A. Krysko<sup>6</sup>

<sup>1</sup> Department of Higher Mathematics and Mechanics Engels Institute of Technology (Branch) Saratov State Technical University, Russian Federation, 413100 Engels, Saratov region, Ploschad Svobodi 17, [anton.krysko@gmail.com](mailto:anton.krysko@gmail.com)

<sup>2</sup> Department of Automation and Biomechanics, Lodz University of Technology, 90-924 Lodz, 1/15 Stefanowski Str. and Institute of Vehicles, Warsaw University of Technology, Poland; [awrejcew@p.lodz.pl](mailto:awrejcew@p.lodz.pl)

<sup>3</sup> Department of Mathematics and Modeling, Saratov State Technical University, Russian Federation, 410054 Saratov, Politehnicheskaya 77; [Yan-tan1987@mail.ru](mailto:Yan-tan1987@mail.ru)

<sup>4</sup> Department of Mathematics and Modeling, Saratov State Technical University, Russian Federation, 410054 Saratov, Politehnicheskaya 77; [Dobriy88@yandex.ru](mailto:Dobriy88@yandex.ru)

<sup>5</sup> Department of Mathematics and Modeling, Saratov State Technical University, Russian Federation, 410054 Saratov, Politehnicheskaya 77; [ikravzova@mail.ru](mailto:ikravzova@mail.ru)

<sup>6</sup> Department of Mathematics and Modeling Saratov State Technical University, Russian Federation, 410054 Saratov, Politehnicheskaya 77; [tak@san.ru](mailto:tak@san.ru)

**Abstracts:** We study the interaction of multi-layer packets consisting of beams, plates and shells, where there are gaps between the mentioned structural members. The proposed mathematical model takes into account various types of non-linearity: (i) geometrical (in the Kármán form); (ii) physical (layer material properties depend on the space co-ordinates, deformation intensity and time); (iii) design (it either switches on or off a contact between layers). Physical properties of the material can be different. The governing partial differential equations, boundary and initial conditions are obtained using Hamilton's variation principle. The so far obtained boundary value problem is then reduced to the Cauchy problem by the following methods: FDM (Finite Difference Method) and the hybrid method matching FEM (Finite Element Method) and the Bubnov-Galerkin method with high order approximations. The obtained initial value problem is solved using the 4th, 6th and 8th Runge-Kutta techniques. It will be shown that those approaches are necessary to get the reliable results of our problem exhibiting strong non-linearity effects and chaotic vibrations. It should be emphasized that the obtained results are studied for all engineering required intervals of changes of the input load parameters, i.e. its amplitude and frequency (charts of vibration-type are constructed). Each output signal is analyzed via phase and modal portraits, Poincaré maps, auto-correlation functions, Fourier spectra as well as wavelets. In the latter case the efficiency of different wavelets is illustrated and discussed. Furthermore, we propose a novel approach to quantify regular and chaotic vibrations via signs estimation of the Lyapunov exponents. Different scenarios of transition from regular to chaotic dynamics exhibited by the studied objects for the mentioned types of non-linearity are illustrated and discussed. We show how the non-linearity type leads to a dramatic change of the transition from regular to chaotic vibrations. In addition, the influence on the non-linear vibrations of the studied multi-layer continuous systems of the non-linearity type, layer



number, boundary conditions, layer thickness as well as magnitude of the gap between layers is investigated and reported.

**Keywords:** chaos, beam, plate, shell, Lyapunov exponents.

### 1. Introduction

It is well known that in the classical mechanics its two branches have been separated over decades, i.e. the fluid mechanics and the solid mechanics. However, we show that in some cases the same/similar phenomena can be found in those two distinguished parts of our matter. Since fluid mechanics phenomena are governed by partial differential equations (PDEs) it is tempting to consider the dynamics of infinite systems represented by fluid/gas composed of the moving infinite sets of particles with the mechanical continuous systems governed by PDEs such as beams, plates shells and panels treated either as separated or linked objects.

In particular, one of the challenging key problems in the fluid mechanics is associated with the explanation of turbulence and a route from laminar to turbulent dynamics via an increase of the Reynolds number  $Re$ .

It is rather expected that the so called fully developed turbulence in fluids associated with a high  $Re$  cannot be found in the mentioned solid structural members. However, there is a way to simplify the turbulent behavior preserving its main features but simplifying the problem by the relaxation of some assumption within the framework of the so called *weak turbulence* [1]. This idea not only allows us to explain the origin of turbulence through an analytical treatment of the simplified closed *kinetic equations*, but also opens the door for finding a similar type turbulent dynamics exhibited by other physical systems including plasmas [2], optics [3] and magneto-hydrodynamics [4]. The weak turbulence theory relies on the movement of the energy flux through small and large length scales being measured, and identified by the broad band Kolmogorov turbulence spectrum.

Our results indicate that the turbulence exhibited by the mentioned structural members with large amplitude dynamics and with the geometric/design non-linearity being externally driven periodically may not only reveal the turbulent behavior quantified through a broad band Fourier component of the power spectrum, but also (in some cases) may give rise to the intermittency, thus violating the strong simplification introduced via weak turbulence theory. In other words, the obtained results indicate a possible correspondence between turbulent dynamics in solids and the classical turbulent dynamics in fluids governed by the Navier-Stokes equations.

The transition from periodic/laminar to chaotic/turbulent behavior of continuous solid mechanical systems (beams, plates, cylindrical shells, panels, sector-type spherical shells) was illustrated and discussed in the series of papers [5-12], where various classical and non-classical scenarios were detected using different numerical approaches (FDM - Finite Difference Method, FEM - Finite Element Method, the Bubnov-Galerkin approach, the modified Ritz method).



Circular cylindrical shells and doubly-curved panels have been analyzed by Amabili [13-14].

On the other hand, there is a series of works devoted to laboratory/experimental investigation of turbulent dynamics in plates. The Föppl-von Kármán model of a thin elastic plate was studied in references [15-18], where various Fourier power spectra of the plate deformations were analyzed. Despite qualitative good agreement with the kinetic weak turbulent phenomena, the experimental form of energy spectrum was not confirmed by theoretically obtained results.

One of the challenging problems of non-linear dynamics is that devoted to mathematical modeling and analysis of the temporal-space (turbulent) chaotic vibrations of the multi-layer structural systems taking into account their contact interactions [19]. Once the contact problem appears, it is necessary to study the phase synchronization of a construction [20]. It is clear that the knowledge of loading of the structure members plays a key role in the estimation of dynamical behavior of the whole studied construction. The system dynamical regime depends strongly on the parameters of exciting load as well as dispersion properties of the surrounding environment. This work aims at a mathematical modeling of the structural systems consisting of beams and plates with small gaps between them. It means that the system dynamics is changed when the contact between the structural members is activated. In addition, we study the phase chaotic synchronization of the multi-layer mechanical systems composed of beams and plates being coupled only through the boundary conditions. Since we consider small gaps, the contact problem should be solved on each of the iteration step in time.

## 2. Method of Phase Chaotic Synchronization

The method of phase synchronization belongs to important branches of the today non-linear dynamics. Phase synchronization is observed experimentally in various radio generators, electrochemical oscillators, lasers, cardiac arrhythmia, and many others. In this work we study the phase chaotic synchronization exhibited by the mechanical structural members: multilayer beams and plates coupled through the boundary conditions.

The wavelet based analysis allows us to study the oscillation type behavior on an arbitrary chosen scale. It characterizes frequency and time localization. Although there are different wavelet transformations [21,22], the most useful for engineering purposes are the Morlet wavelets.

Phase synchronization means that the phase locking phenomenon occurs though both signals remain chaotic. Phase locking yields overlapping of the frequencies. The frequency of a chaotic signal is defined as the average velocity of the phase variation. The wavelet surface  $W(s, t_0) = \|W(s, t_0)\| \exp[j\phi_s(t_0)]$  characterizes the system dynamics on each time interval at an arbitrary time instant  $t_0$ . The integral energy distribution of a wavelet spectrum with respect to the time scales  $E(s) = \int \|W(s, t_0)\|^2 dt_0$  is introduced. The phase is defined as



$\phi_s(t_0) = \arg W(s, t)$  for each time interval  $s$ , which yields a possibility of monitoring each interval  $s$  with the help of the associated phase  $\phi_s(t)$ . Particular attention was paid to the synchronization of vibrations of the studied structural systems with the help of the Morlet wavelets.

### 3. Algorithm for Computation of the Lyapunov Exponents

In order to investigate chaotic vibrations of the design-nonlinear structures we apply the qualitative theory of differential equations and nonlinear dynamics: analysis of the signals, Fourier power spectra, phase and modal portraits, and Lyapunov exponents versus time for each of the studied structures. Various wavelet transforms are applied.

Below, we describe briefly the algorithms devoted to the computation of the Lyapunov exponents. The estimation of Lyapunov exponents spectrum with the use of one co-ordinate and within the frame of neural networks includes the following steps. Assume that we have the reconstructed series

$$x_i = (x(i), x(i - \tau), \dots, x(i - (m - 1)\tau)) = (x_1(i), x_2(i), \dots, x_m(i)), \quad (3.1)$$

where  $i = \overline{((m - 1)\tau + 1), N}$ ,  $m$  – dimension of the embedding space,  $\tau$  – time delay,  $N$  – length of the time series. The following tasks are solved:

1. Appropriate delays  $\tau$  are chosen.
2. Dimension of an embedding space is estimated.
3. Pseudo-phase reconstruction of a trajectory is carried out using the time delays method. Next the  $m$ -dimensional vectors are chosen, having dimension of a lesser order than the initial choice.
4. First, an approximating neural net is constructed, which essentially improves the convergence of the iteration process.
5. Neural network is taught to compute a successive vector of the reconstructed series through the previously estimated vector.
6. Next we applied the already trained network in the generalized Benettin algorithm to estimate the Lyapunov exponents.

The generalized Benettin algorithm is as follows: let  $r_0$  be an arbitrary point of the system attractor. We first fix a small, comparing to the linear attractor dimension, positive value of  $\varepsilon$ , and we choose the perturbed points  $x_0, y_0$  and  $z_0$  in the way to keep the perturbation vectors length  $\Delta x_0 = x_0 - r_0$ ,  $\Delta y_0 = y_0 - r_0$  and  $\Delta z_0 = z_0 - r_0$  equal to  $\varepsilon$ , and to preserve their orthogonal property. The points  $r_0, x_0, y_0$  and  $z_0$  are transited into points  $x_1, y_1$  and  $z_1$ , respectively, after a certain small time interval  $T$ . Let us consider the new perturbation vectors:  $\Delta x_1 = x_1 - r_1$ ,  $\Delta y_1 = y_1 - r_1$  and  $\Delta z_1 = z_1 - r_1$ . The Gram-Schmidt orthogonalization method is further applied:



$$\begin{aligned}\Delta x_1' &= \Delta x_1, \quad \Delta x_1'' = \frac{\Delta x_1'}{\|\Delta x_1'\|}, \\ \Delta y_1' &= \Delta y_1 - (\Delta y_1, \Delta x_1'') \Delta x_1'', \quad \Delta y_1'' = \frac{\Delta y_1'}{\|\Delta y_1'\|}, \\ \Delta z_1' &= \Delta z_1 - (\Delta z_1, \Delta x_1'') \Delta x_1'' - (\Delta z_1, \Delta y_1'') \Delta y_1'', \quad \Delta z_1'' = \frac{\Delta z_1'}{\|\Delta z_1'\|}.\end{aligned}\quad (3.2)$$

The orthogonalization procedure yields unit perturbation vectors. Next we transform these vectors to the corresponding ones with the length  $\varepsilon$ :  $\Delta x_1''' = \Delta x_1'' \cdot \varepsilon$ ,  $\Delta y_1''' = \Delta y_1'' \cdot \varepsilon$  and  $\Delta z_1''' = \Delta z_1'' \cdot \varepsilon$ . Then we take into account the new choice of the perturbation points  $x_1' = x_1 + \Delta x_1'''$ ,  $y_1' = y_1 + \Delta y_1'''$  and  $z_1' = z_1 + \Delta z_1'''$ . The so far described process is repeated with respect to the points  $r_1, x_1', y_1'$ , and  $z_1'$ . Repeating this algorithm  $M$  times, the following sums are computed:

$$S_1 = \sum_{k=1}^M \|\Delta x_k'\|, \quad S_2 = \sum_{k=1}^M \|\Delta y_k'\|, \quad S_3 = \sum_{k=1}^M \|\Delta z_k'\|. \quad (3.3)$$

The Lyapunov spectrum  $\Lambda = \{\lambda_1, \lambda_2, \lambda_3\}$  is estimated via the following formula:

$$\lambda_i = \frac{S_i}{MT}, \quad i = 1, 2, 3. \quad (3.4)$$

#### 4. Two-Layer Packets of Plates-Plates, Plates-Beams, Beams-Beams

We consider the mathematical models of non-linear two-layer plates (Fig. 4.1), two-layer beams (Fig. 4.3) and plate-beam construction (Fig. 4.2), all of them being coupled through the boundary conditions and transversally loaded in a time periodic manner. We solve the so far stated dynamical non-linear problems in chaotic regimes via the Bubnov-Galerkin method in higher approximations within the approach proposed by Vlasov with respect to spatial co-ordinates, and using the fourth Runge-Kutta method with respect to the time co-ordinate.

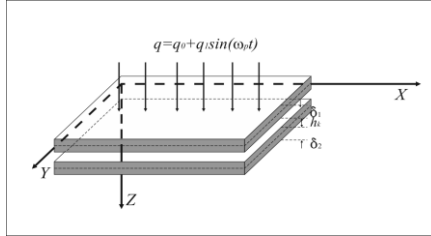


Fig. 4.1. Plate-plate model

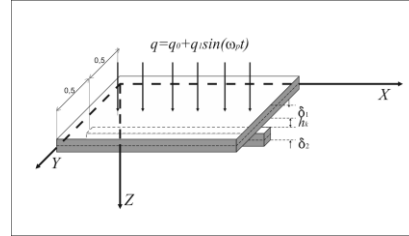


Fig. 4.2. Plate-beam model

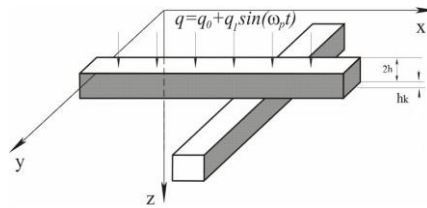


Fig. 4.3. Beam-beam model

The following Germain-Lagrange type PDEs govern dynamics of the two-layer elastic plates packet shown in Fig. 4.1:

$$\begin{cases} \frac{1}{12(1-\mu^2)} (\nabla_\lambda^4 w_1) + \frac{\partial^2 w_1}{\partial t^2} + \varepsilon \frac{\partial w_1}{\partial t} - q(t) - K(w_1 - w_2 - h_k) \Psi = 0, \\ \frac{1}{12(1-\mu^2)} (\nabla_\lambda^4 w_2) + \frac{\partial^2 w_2}{\partial t^2} + \varepsilon \frac{\partial w_2}{\partial t} + K(w_1 - w_2 - h_k) \Psi = 0, \end{cases} \quad (4.1)$$

$$w_m = \sum_{i=1}^N \sum_{j=1}^N A_{ij}^{(m)}(t) \sin(i\pi x) \sin(j\pi y), \quad m = 1, 2$$

We take the following boundary conditions:

$$w_m = 0; \quad w_m''|_x = 0; \quad \text{for } x = 0; 1; \quad w_m = 0; \quad w_m''|_y = 0; \quad \text{for } y = 0; 1; \quad m=1, 2,$$

whereas the initial conditions follow

$$w_m(x, y)|_{t=0} = 0, \quad \dot{w}_m|_{t=0} = 0, \quad m=1, 2.$$

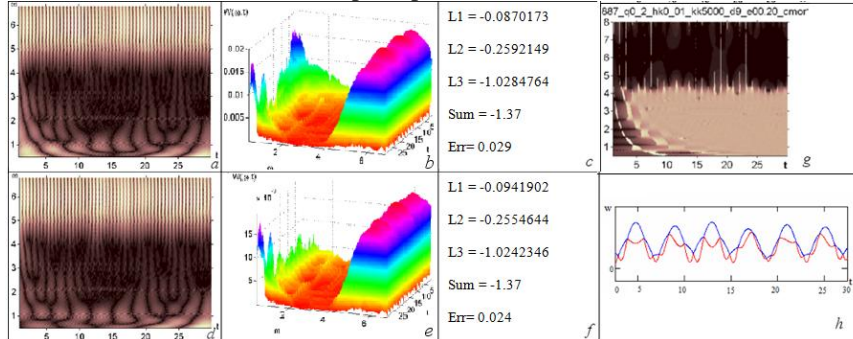
Here  $\Psi = \frac{1}{2} [1 + \text{sign}(w_1 - h_k - w_2)]$ , if  $w_1 > w_2 + h_k$  we take  $\Psi = 1$ , and the contact between plates occurs, otherwise  $\Psi = 0$ ;  $w_1, w_2$  deflection functions of

the upper and lower plate, respectively,  $K$  - stiffness coefficient of the transversal contact zone,  $h_k$  - clearance between the plates.

Let us consider the following example. We take the uniform time-independent load and the following system parameters:  $q = q_0 = const = 0.2$ ,  $K = 5000$ ,  $h_k = 0.01$ ,  $\varepsilon = 0$ ,  $\omega_0 = 5.9887$  - frequency of the associated linear vibrations. Table 4.1 reports 2D (a, d) and 3D (b,e) Morlet wavelets spectra, Lyapunov exponent values, their sum and the corresponding errors (c, f) for each of the plates, domain of frequencies synchronization (g), as well as the interacting vibrations in the centers of each plate (h) (upper (lower) plate vibration corresponds to red (blue) color).

This example exhibits the phase synchronization in the neighborhood of the natural vibration frequencies  $\omega_0$ . In the phase difference graph (g) the frequency interval  $\omega \in [4, 8]$ , where the phase synchronization takes place, is marked by the dark color. The vibrations take place at the frequency  $\omega_0$ , i.e. that of the natural frequency of two-layer plates structure, which is approved by the Morlet wavelet spectrum (a,d) consisting of the energy component of each of the frequencies studied in a given time instant. Analysis of the Lyapunov exponent signs allows us to conclude that the vibrations are out of chaos and the vibration process yields the full phase locking of the amplitudes of the upper and lower plates.

Table 4.1. Characteristics of the plate/plate vibration



Next, we present PDEs of the two-layer packet consisting of a plate and beam (Fig. 4.2). The upper plate is governed by the Germain-Lagrange equation, whereas the beam is described via the Euler-Bernoulli equation:



$$\begin{cases}
 \frac{1}{12(1-\mu^2)} \left( \frac{1}{\lambda^2} \frac{\partial^4 w_1}{\partial x^4} + \lambda^2 \frac{\partial^4 w_1}{\partial y^4} + 2 \frac{\partial^4 w_1}{\partial x^2 \partial y^2} \right) + \frac{\partial^2 w_1}{\partial t^2} + \\
 \quad + \varepsilon \frac{\partial w_1}{\partial t} - q(t) - K(w_1 - w_2 - h_k) \Psi = 0, \\
 \frac{1}{12} \frac{\partial^4 w_2}{\partial x^4} + \frac{\partial^2 w_2}{\partial t^2} + \varepsilon \frac{\partial w_2}{\partial t} + K(w_1 - w_2 - h_k) \Psi = 0,
 \end{cases} \quad (4.2)$$

$$w_1 = \sum_{i=1}^N \sum_{j=1}^N A_{ij}^1(t) \sin(i\pi x) \sin(j\pi y), \quad w_2 = \sum_{i=1}^N A_i^2(t) \sin(i\pi x)$$

We take the following boundary conditions:

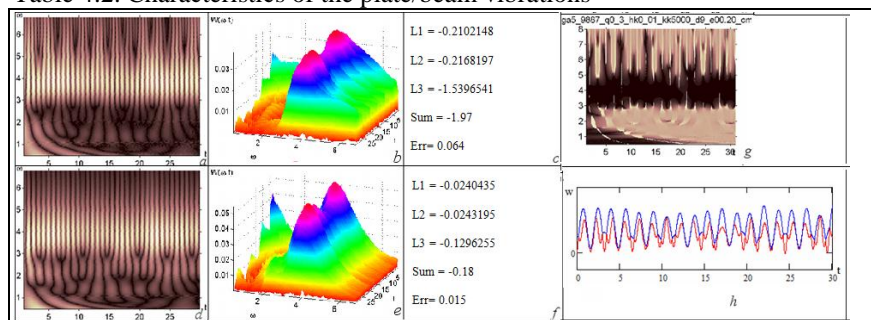
$$\begin{aligned}
 w_1 = 0; \quad w_1''|_x = 0; \quad \text{for } x = 0; 1; \quad w_1 = 0; \quad w_1''|_y = 0; \quad \text{for } y = 0; 1; \\
 w_2 = 0; \quad w_2''|_x = 0; \quad \text{for } x = 0; 1; \quad w_2 = 0; \quad \text{for } y = 0; 1,
 \end{aligned}$$

and the initial conditions:

$$w_1(x, y)|_{t=0} = 0, \quad w_2(x)|_{t=0} = 0, \quad \dot{w}_m|_t = 0, \quad m=1, 2.$$

We consider the vibration process of the plate and the beam by taking  $q_0 = const$  and  $t_0 = 0$ , and fixing the following parameters:  $K = 5000$ ,  $q = q_0 = const = 1$ ,  $h_k = 0.01$ ,  $\varepsilon = 0.5$ ,  $\omega_0^{(1)} = 5.9887$ ,  $\omega_0^{(2)} = 2.84$  - frequencies of the linear vibrations. We observe the damped vibrations on the packet frequency. A decrease in the system clearance causes the overlapping of amplitudes, i.e. a full synchronization with regard to both amplitude and frequency is observed, and the system locking occurs for small values of the load amplitude  $q_0$ . Therefore, a decrease of the clearance implies the synchronization increase.

Table 4.2. Characteristics of the plate/beam vibrations





We have studied the influence of the damping coefficient  $\varepsilon$  on the packet vibration character. A decrease of the damping up to  $\varepsilon = 0.25$  causes an increase of the system chaotization, but both amplitude and frequency synchronization is increased, which finally implies the full synchronization of the structural members. Then, we take the conservative system into consideration, i.e. for  $\varepsilon = 0$ . We observe intermittency character of switching on and switching off the synchronization zones. The Lyapunov exponents indicate that we have regular vibrations, though noisy components appear. The full synchronization of both structural members occurs. Tables 4.2 2D (a, d) and 3D (b,e) give wavelet spectra, Lyapunov exponents, their sum and the estimated errors (c, f) for the plate and beam, respectively, frequencies synchronization graph (g), as well as the graph of simultaneous vibrations in the center point of a plate and beam (h) with the following fixed parameters:  $q = q_0 = const = 0.3$ ,  $h_k = 0.01$ ,  $\varepsilon = 0$ ,  $\omega_0^{(1)} = 5.9887$ ,  $\omega_0^{(2)} = 2.84$ . An increase of the load amplitude yields a synchronization increase (g). Vibrations take place at the packet natural frequency and the Hopf bifurcation. The phase and amplitude locking in some time instants is observed. A further increase of the loading implies the full synchronization regarding both frequencies and amplitudes (h).

The governing equations of the cross-located two layer beams are as follows (Fig. 4.3):

$$\begin{cases} \frac{1}{12} \frac{\partial^4 w_1}{\partial x^4} - \frac{\partial^2 w_1}{\partial t^2} - \varepsilon \frac{\partial w_1}{\partial t} - q(t) + K(w_1 - w_2 - h_k) \Psi = 0, \\ \frac{1}{12} \frac{\partial^4 w_2}{\partial y^4} - \frac{\partial^2 w_2}{\partial t^2} - \varepsilon \frac{\partial w_2}{\partial t} - K(w_1 - w_2 - h_k) \Psi = 0, \end{cases} \quad (4.3)$$

$$w_m = \sum_{i=1}^N \sum_{j=1}^N A_{ij}^{(m)}(t) \sin(i\pi x) \sin(j\pi y), \quad m = 1, 2.$$

We applied the following boundary conditions:

$$w_m = 0; \quad w_m''|_x = 0; \quad \text{for } x = 0; 1; \quad w_m = 0; \quad w_m''|_y = 0; \quad \text{for } y = 0; 1; \quad m=1, 2,$$

and the following initial conditions:

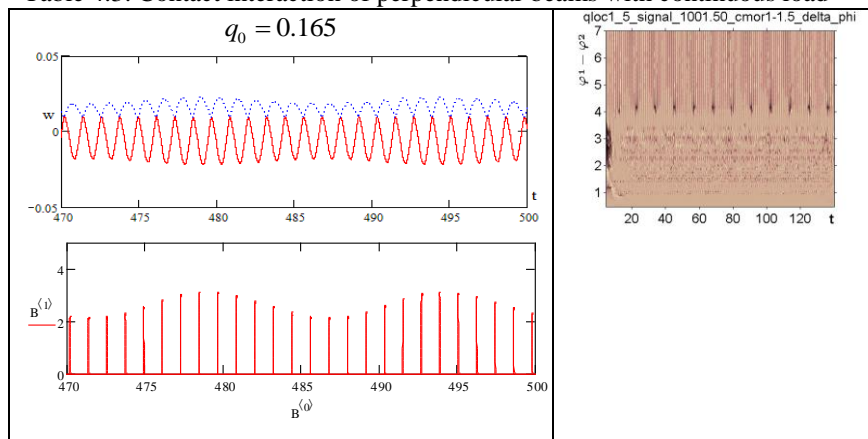
$$w_m(x, y)|_{t=0} = 0, \quad \dot{w}_m|_{t=0} = 0, \quad m=1, 2.$$

In the case of parallel located beams the governing equations have the following form:

$$\begin{cases} \frac{1}{12} \frac{\partial^4 w_1}{\partial x^4} - \frac{\partial^2 w_1}{\partial t^2} - \varepsilon \frac{\partial w_1}{\partial t} - q(t) + K(w_1 - w_2 - h_k) \Psi = 0, \\ \frac{1}{12} \frac{\partial^4 w_2}{\partial x^4} - \frac{\partial^2 w_2}{\partial t^2} - \varepsilon \frac{\partial w_2}{\partial t} - K(w_1 - w_2 - h_k) \Psi = 0. \end{cases} \quad (4.4)$$

We have studied the contact interaction of two perpendicular beams with different types of the external transversal harmonic excitation of the form  $q = q_0 \sin(\omega_p t)$ .

Table 4.3. Contact interaction of perpendicular beams with continuous load



In the case of load distributed on the whole upper beam (Table 4.1) the Ruelle-Takens-Newhouse scenario has been detected. Table 4.3 gives time histories of the simultaneous vibrations of two beams monitored in their centers, their contact pressure as well as their phase difference for the fixed clearance  $h_k = 0.01$ .

## 5. Conclusions

It has been shown that depending on the construction design the phase synchronization can be different, it may appear or not. In the case of design of non-linear two-layer plate-plate packet, the phase synchronization takes place with the frequencies interval  $\omega \in [4, 8]$ . There are separated time intervals with the lack of the phase synchronization (bright parts on the phase difference diagrams), but the phase locking sources appear. In the case of the non-linear design of two-layer plate=beam packet the phase synchronization takes place within a narrow frequencies interval  $\omega \in [3, 5]$ , but the phase synchronization occurs also on the separated time intervals with activation of other frequencies (dark parts on the phase difference diagrams), and also the amplitude locking



phenomenon appears. In the case of design of non-linear two-layer beam-beam packet the phase synchronization takes place on the separated time intervals only on the frequency  $\omega \in [4]$ .

### Acknowledgements

This work has been supported by the National Centre of Science under the grant MAESTRO 2, No. 2012/04/A/ST8/00738 for the years 2012-2015 (Poland). J. Awrejcewicz acknowledges a support by the Alexander von Humboldt Award.

### References

1. V.E. Zakharov, V.S. Lvov, G. Falkovich. *Kolmogorov Spectra of Turbulence*, Springer Verlag, Berlin, 1992.
2. S.L. Musher, A.M. Rubenchik, V.E. Zakharov. Weak Langmuir turbulence, *Physics Reports* 252(4): 177-274, 1995.
3. S. Dyachenko, A.C. Newell, A. Pushkarev, V.E. Zakharov. Optical turbulence: weak turbulence, condensates and collapsing filaments in the nonlinear Schrödinger equation, *Physica D*, 57(1-2): 96-160, 1992.
4. S.V. Nazarenko, A.C. Newell, S. Galtier. Non-local MHD turbulence, *Physica D*, 152-153: 646-652, 2001.
5. J. Awrejcewicz, A.V. Krysko. Analysis of complex parametric vibrations of plates and shells using Bubnov-Galerkin approach, *Archive of Applied Mechanics*, 73: 495-504, 2003.
6. J. Awrejcewicz, V.A. Krysko, A.V. Krysko. Complex parametric vibrations of flexible rectangular plates, *Meccanica*, 39(3):221-244, 2004.
7. V.A. Krysko, J. Awrejcewicz, T.V. Shchekaturova. Chaotic vibrations of spherical and conical axially-symmetric shells, *Archive of Applied Mechanics*, 74(5-6): 338-358, 2005.
8. J. Awrejcewicz, V.A. Krysko, T.V. Shchekaturova. Transitions from regular to chaotic vibrations of spherical and conical axially-symmetric shells, *International Journal of Structural Stability and Dynamics*, 5(3): 1-27, 2005.
9. V.A. Krysko, J. Awrejcewicz, N.E. Saveleva, A.V. Krysko. Dynamics of flexible shells and Sharkovskiy's periodicity, *Differential Equations and Nonlinear Mechanics*, 2006, 8 pages (DOI: 10.1155/DENM/2006/59709).
10. J. Awrejcewicz, V.A. Krysko, V. Nazar'iantz. Chaotic vibrations of flexible infinite length cylindrical panels using the Kirchhoff-Love model, *Communications in Nonlinear Science and Numerical Simulation*, 12(4): 519-542, 2007.
11. A.V. Krysko, J. Awrejcewicz, E.S. Kuznetsova, V.A. Krysko. Chaotic vibrations of closed cylindrical shells in a temperature field, *Shock and Vibration*, 15(3-4): 335-343, 2008.
12. J. Awrejcewicz, A.V. Krysko, M.V. Zhigalov, O.A. Saltykova, V.A. Krysko. Chaotic vibrations in flexible multi-layered Bernoulli-Euler and Timoshenko type beams, *Latin American Journal of Solids and Structures*, 5(4): 319-363, 2008.



13. M. Amabili, A. Sarkar, M.P. Paidoussis. Chaotic vibrations of circular cylindrical shells: Galerkin versus reduced-order models via the proper orthogonal decomposition method, *Journal of Sound and Vibration*, 290(3-5): 736-762, 2006.
14. M. Amabili. Non-linear vibrations of doubly-curved shallow shells, *International Journal of Non-linear Mechanics*, 40(5): 683-710, 2005.
15. N. Mordant. Fourier analysis of wave turbulence in a thin elastic plate, *European Physics Journal B*, 76: 537-545, 2010.
16. C. Connaughton. Numerical solutions of the isotropic 3-wave kinetic equation, *Physica D*, 238(23-24): 2282-2297, 2009.
17. A. Boudaoud, O. Cadot, B. Odille, C. Touzé. Observation of wave turbulence in vibrating plates, *Physical Review Letters*, 100: 234504-1 – 234504-4, 2008.
18. N. Mordant. Are There Waves in Elastic Wave Turbulence? *Physical Review Letters*, 100(23): 234505-1 – 234505-4, 2008.
19. A.V. Krysko, M.I. Koch, T.V. Yakovleva, U. Nackenhorst, V.A. Krysko. Chaotic nonlinear dynamics of cantilever beams under the action of signs-variables loads, *PAMM, Special Issue: 82nd Annual Meeting of the International Association of Applied Mathematics and Mechanics (GAMM)*, 11(1): 327-328, 2011.
20. J. Awrejcewicz, A. Krysko, T. Yakovleva, D. Zelenchuk, V. Krysko. Chaotic synchronization of vibrations of a coupled mechanical system consisting of a plate and beams, *Dynamical Systems, Analytical/Numerical Methods, Stability, Bifurcation and Chaos*, Łódź, 129-140, 2011.
21. X. Chen, J. Xiang, B. Li, Z. He. A study of multiscale wavelet-based elements for adaptive finite elements analysis. *Advances in Engineering Software*, 41: 196-205, 2010.
22. U. Lepik. Solving integral and differential equations by the aid of non-uniform Haar wavelets, *Applied Mathematical Computations*, 198: 326-332, 2008.



## Kinetics Complexity in Physical Ageing of Chalcogenide Glassy Semiconductors

V. Balitska<sup>1,2</sup>, O. Shpotyuk<sup>1,3</sup>, R. Golovchak<sup>1,4</sup>, A. Kozdras<sup>5</sup>

<sup>1</sup> Lviv Scientific Research Institute of Materials of SRC “Carat”, Lviv, Ukraine

E-mail: [shpotyuk@novas.lviv.ua](mailto:shpotyuk@novas.lviv.ua)

<sup>2</sup> Lviv State University of Vital Activity Safety, Lviv, Ukraine

<sup>3</sup> Institute of Physics of Jan Dlugosz University, Czestochowa, Poland

<sup>4</sup> Department of Materials Science and Engineering, Lehigh University,  
Bethlehem, USA

<sup>5</sup> Institute of Physics, Mathematics and Chemistry of Opole Technical  
University, Opole, Poland

**Abstract:** Long-term kinetics of natural physical ageing lasting from several days to more than twenty years at the ambient temperature is analysed at the example of  $As_{10}Se_{90}$  glass. Non-monotonic character of this kinetics is registered, which reveals subsequent saturation plateaus and steep regions (growing step-wise kinetics) owing to multiple alignment-shrinkage stages reaped in the in network structure of glass.

**Keywords:** Glassy Semiconductors, Physical Ageing, Enthalpy, Relaxation, Kinetics.

### 1. Introduction

Chalcogenide glassy semiconductors (ChGS) possessing unique glass-forming networks with fully saturated covalent bonds are widely used in modern energy conversion technologies, information storage, IR transmitting devices, optical and thermal imaging, IR telecommunication, low-cost reliable optics, etc. [1-3]. However, these solids are characterized by a metastability associated with their disordered structure and, therefore, are subject to physical ageing (PhA) [3,4]. The latter leads to changes in ChGS physical-chemical properties during their prolonged use/storage [4,5]. So, ChGS kept below the glass transition temperature ( $T_g$ ) losses with time their excess of configurational entropy, enthalpy or free volume gained during synthesis to reach a more favorable thermodynamic state. The most unlike for practical application is the natural PhA occurring at normal ambient conditions, because this effect leads to unwanted, spontaneous and highly unpredictable drift in main exploitation characteristics of ChGS [5].

The purpose of this work is to analyze the kinetics of enthalpy losses induced by prolonged dark storage under natural conditions of  $As_{10}Se_{90}$  glass as typical representatives of Se-rich ChGS.

### 2. The Model and Simulations

The  $As_{10}Se_{90}$  glassy samples were prepared by conventional melt quenching route in evacuated quartz ampoules from a mixture of high purity precursors.

Amorphous state and chemical composition of as-prepared glasses were controlled visually by a characteristic conch-like fracture, data of X-ray diffraction and X-ray photoelectron spectroscopy.

In order to establish the kinetics of enthalpy losses  $\Delta H$ , the differential scanning calorimetry (DSC) measurements were performed on NETZSCH 404/3/F microcalorimeter precalibrated with a set of standard elements. The DSC traces were recorded in the ambient atmosphere with 5 K/min heating rate. The same calibration procedure was repeated each time during routine measurements. Three independent DSC measurements with samples of close masses were performed to confirm the reproducibility of the results.

With a purpose of adequate mathematical description of the kinetics of enthalpy losses, the numerical values of fitting parameters of corresponding relaxation function (RF), were calculated in such a way to minimize the mean-square deviation of experimentally measured points from the RF.

Typical kinetics of enthalpy losses  $\Delta H$  caused by long-term dark storage of  $As_{10}Se_{90}$  ChGS is shown in Figure 1.

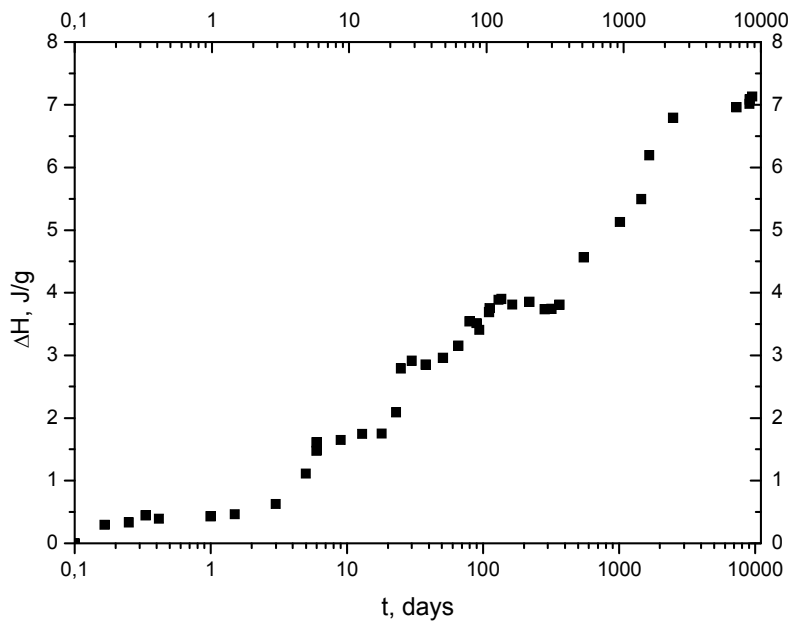


Fig. 1. Kinetics of enthalpy losses  $\Delta H$  caused by long-term dark storage of  $As_{10}Se_{90}$  ChGS.



In order to describe this relaxation kinetics, two typical models are often used. The first is the parameterization via known stretched-exponential or Kohlrausch relaxation function (non-exponential function) [6], established for different relaxation processes in complex electronic and molecular systems:

$$\Delta H(t) = \exp\left(-\left(\frac{t}{\tau}\right)^\beta\right), \quad (1)$$

where  $\tau$  is effective time constant and  $\beta$  is a so-called fractional exponent (the stretching parameter also known as non-exponentially or dispersivity index).

The mechanisms of degradation processes, leading to stretched-exponential relaxation kinetics, are quite different. In general, they can be divided into two main groups. The first group explores the mechanisms of dispersive transport in disordered structures [7]. Within such consideration, the characteristic defects responsible for deviation from any equilibrium participate in multiple trapping-recombination acts before being finally stabilized due course of time. The model of hierarchically limited relaxation dynamics [8] forms the basis for second group of mechanisms. Within this model, each subsequent relaxation event in disordered solid is possible only after successful realization of the previous relaxation act, which forms preconditions for it to happen. Other approach for the characterization of relaxation phenomena in ChGS can be developed on the basis of the mechanism proposed in [9] for PhA of silicate glasses. It was supposed, that structural relaxation originates from a superposition of slow and fast relaxation processes, which can be well described by a sum of simple exponential-like Debye components with individual relaxation times  $\tau_i$ .

Structural data obtained for a number of Se-rich As-Se glasses suggest that the mechanism of PhA in ChG is based on the elementary relaxation acts (twisting) of inner Se atoms within double-well potentials (DWP) associated with high flexibility of bridge-type chalcogen Se-Se bonds [10].

Let's consider the process of twisting of Se atoms within DWP in more details. Three possible DWP can be assumed for Se atoms owing to their immediate surrounding -Se-Se-Se-, =As-Se-Se- and =As-Se-As= (Figure 2).

Obviously, these states differ by energetic parameters, which are determined by type of surrounding atoms (As or Se). Owing to a magnitude of PhA in the investigated  $As_xSe_{100-x}$  ChGS [11], the lowest barrier for Se twisting should be expected for homoatomic Se-Se-Se DWP, while the highest one corresponds to heteropolar As-Se-As surrounding.

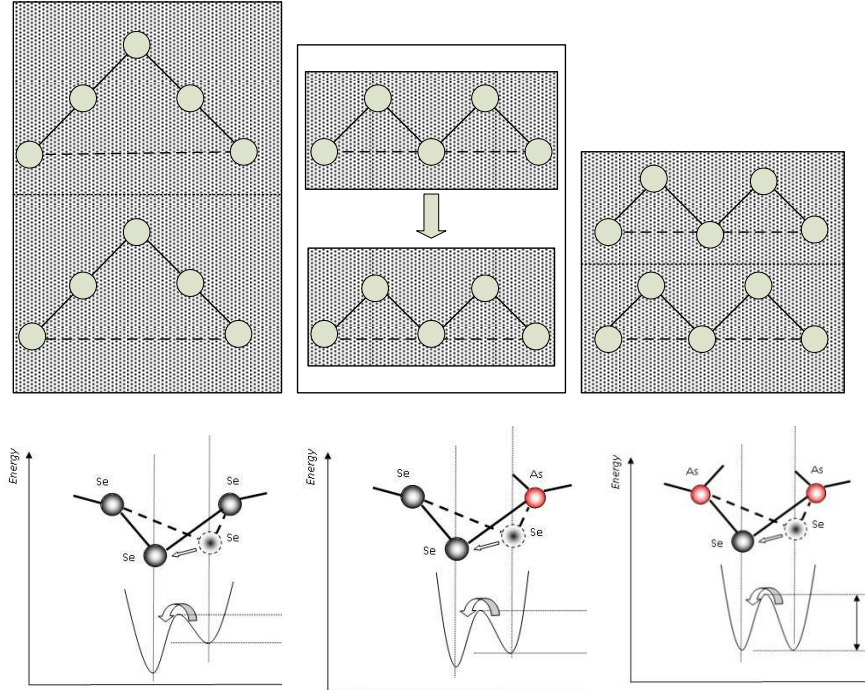
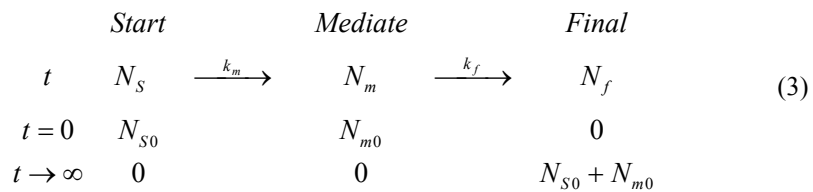


Fig. 2. Schematic illustration showing main features of PhA mechanism in Se-rich ChGS according in respect to double-well potential concept.

Let's denote an average relative probability of Se atom twisting within corresponding DWP (the alignment rate) as  $k_m$  and probability of further atomic shrinkage (the shrinkage rate) as  $k_f$ . If these rates are independent on time  $t$ , then the overall process of PhA can be presented by following scheme:



where  $N_S$  denotes concentration of atomic sites described by DWP as precursors for Se twisting ( $N_{S0}$  is their initial concentration);  $N_m$  is the concentration of precursors for shrinkage, which originate from preliminary stage of DWP twisting ( $N_{m0}$  is the initial concentration of twisted Se atoms);  $N_f$  is the



concentration of atomic sites, affected by general shrinkage of the network;  $k_m$  is the relative probably of Se atom twisting within DWP and  $k_f$  is the probability of further atomic shrinkage.

It is obvious that at each time the overall amount of inter-balanced sites is held:

$$N_s + N_m + N_f = N_{s0} + N_{m0} \quad (4)$$

Then, for considered glassy network the classic first order differential rate equations, which govern changes in the concentration of twisted (the mediate alignment stage) and densified (the final shrinkage stage) atomic sites, can be composed as:

$$\begin{cases} \frac{dN_m}{dt} = k_m N_s - k_f N_m \\ \frac{dN_f}{dt} = k_f N_m \end{cases} \quad (5)$$

Solutions of rate equations (5) can be considered in terms of microstructural mechanism for PhA illustrated in Figure 2.

In case the measured property (the enthalpy losses  $\Delta H$ ) is sensitive to both stages of PhA in Figure 2 (mediate and final), the next equation should be used to describe PhA kinetics:

$$F(t) = N_m(t) + N_f(t) = N_{m0} + N_{s0}(1 - e^{-k_m t}) \quad (6)$$

We believe, this is the case for  $\Delta H(t)$  kinetics obtained from DSC data, which is supposed to reflect the overall mechanism of PhA.

If the measured quantity is sensitive to one of the stages in Figure 2, then each component of the equation (6) should be considered separately:

$$N_m(t) = \frac{N_{s0}k_m}{k_f - k_m} e^{-k_m t} - \left( \frac{N_{s0}k_m}{k_f - k_m} - N_{m0} \right) e^{-k_f t} \quad (7)$$

$$N_f(t) = (N_{s0} + N_{m0}) - \frac{N_{s0}k_f}{k_f - k_m} N_{s0} e^{-k_m t} + \left( \frac{N_{s0}k_m}{k_f - k_m} - N_{m0} \right) e^{-k_f t} \quad (8)$$

Two different possibilities in view of the above solutions are to be analyzed:

1) the mechanism in Figure 2 happens once during overall PhA with  $k_m$  and  $k_f$  rates dependent on time  $t$  (reflecting statistical distribution of atomic sites involved into alignment-shrinkage process);



2) the processes in Figure 2 are routinely repeated in such a way that final stage in Figure 4 becomes the initial one for subsequent alignment-shrinkage process of newly formed glassy network (the serial relaxation processes), or, alternatively, the independent relaxation processes in Figure 2 with different  $k_m$  and  $k_f$  rates occur simultaneously (the parallel relaxation processes).

The protocol used for present enthalpy losses  $\Delta H$  measurements in  $As_{10}Se_{90}$  glass allows us to identify at least four quite distinguishable steps in the corresponding relaxation kinetics (see Figure 1): the first (the quickest) step lasting  $\sim 0$ -1.5 days, the second step from  $\sim 1.5$  to 23 days, the third step from  $\sim 23$  to 365 days and the fourth (the slowest) step starting at  $\sim 365$  days onwards. The kinetics of each step  $i$  was modelled by single exponential function in full respect to (6):

$$\Delta H_i(t) = a + b \left( 1 - \exp \left( - \frac{t - \Delta t}{\tau} \right) \right), \quad (9)$$

where  $a$  and  $b$  are materials-related parameters connected with amplitude of the relaxation process,  $\tau$  is effective time constant (the relaxation time) and  $\Delta t$  is a so-called retardation time (the parameter giving time delaying of the next step of PhA in respect to the previous one).

The straightforward fitting of the experimentally measured enthalpy losses  $\Delta H(t)$  curve as shown in Figure 1 with equation (9) are summarized in Table 1, where all parameters are fitted with a quite high goodness  $r^2$  (the mean square deviations of experimentally measured points from theoretical exponent).

Table 1. Fitting parameters describing PhA kinetics in  $As_{10}Se_{90}$  ChGS with respect to equation (9).

Step No (duration)	Fitting goodness $r^2$	$a$	$b$	$\tau$	$\Delta t$
1 (0÷1.5 days)	0.008	0	0.46	0.2	0
2 (1.5÷23 days)	0.022	0.46	1.52	5.3	1.7
3 (23÷365 days)	0.038	1.98	1.82	35.0	16.5
4 (365÷9500 days)	0.034	3.80	3.27	1173	337

It can be seen that the further we are from completeness of PhA, the smaller is effective time constant  $\tau$ , this parameter being increased by over  $\sim 5$  orders of magnitude with PhA duration changing from several days to approximately twenty years. The amplitude of each relaxation step  $b$ , as well as overall relaxation process  $a$  reveal similar behaviour, showing steady increase from 0.46 to 3.27 and from 0 to 3.80 for  $b$  and  $a$  parameters, respectively, throughout PhA duration.

In general, by accepting the growing tendency in the experimental enthalpy losses  $\Delta H$  in ChGS, we can express the observed step-wise PhA kinetics in a more compact (generalized) form:



$$\Delta H_i(t) = \sum_{i=1}^n \theta(t - \Delta t_i) \left[ a_i + b_i \left( 1 - \exp\left(-\frac{t - \Delta t_i}{\tau_i}\right) \right) \right], \quad (10)$$

where  $\theta(t - \Delta t_i)$  is Heaviside step function, whose value is accepted to be 0 for negative arguments ( $t < \Delta t_i$ ) and 1 for positive arguments ( $t \geq \Delta t_i$ ), and  $n$  is the number of steps distinguished in the relaxation kinetics (in our case  $n=4$ ).

### 3. Conclusions

Long-term kinetics of enthalpy losses occurring during natural PhA at the ambient temperature is analysed at the example of  $As_{10}Se_{90}$  glass. This kinetics is shown to have non-monotonic character, revealing some kind of subsequent plateaus and steep regions (step-wise kinetics) owing to multiple alignment-shrinkage stages. This complexity in the PhA kinetics is treated through corresponding changes in structural relaxation parameters occurred during glass-to-supercooled liquid transition in a heating mode.

Complex phenomenology of natural PhA in the investigated  $As_{10}Se_{90}$  ChGS allows consideration of chalcogen-rich glasses as nonlinear disordered systems exhibiting significant chaotic behaviour.

### References

1. X. Zhang, H. Ma and J. Lucas. Application of chalcogenide glass bulks and fibers, *J. Optoelectronics Adv Mat*, vol. 5, 1327-1333, 2003.
2. J. S. Sanghera and I. D. Aggarwal. Active and passive chalcogenide glass optical fibers for IR applications: a review, *J. Non-Cryst Sol*, vol. 256-257, 6-16, 1999.
3. A. Feltz. *Amorphous and Vitreous Inorganic Solids*, Moscow, Mir, 1986.
4. L. C. E. Struik, *Physical ageing in amorphous polymers and other materials*, Eslevier, New York, NY, 1978.
5. D. J. McEnroe and W. C. LaCourse. Tensile strength of Se,  $As_2S_3$ ,  $As_2Se_3$ , and  $Ge_{30}As_{15}Se_{55}$  glass fibers, *J Am Ceram Soc*, vol. 72, 1491-1494, 1989.
6. F. Kohlrausch. *Pogg. Ann.*, vol. 119, 337. 1863.
7. E. V. Emelianova, P. Hertogen, V. I. Arkhipov and G. I. Adriaenssens. A model of photoinduced anisotropy in chalcogenide glasses. *J Non-Cryst Sol*, vol. 954, 266-269, 2000.
8. A. I. Gusarov, A. K. Dmytrjuk and A. N. Kononov. Long-term kinetics of activation spectra of post-irradiation relaxation in glasses, *Zh Eksp Teor Fiziki (Rus.)*, vol. 97, 525-540, 1990.
9. S.V. Nemilov. Physical ageing of silicate glasses at room temperature: general regularities as a basis for the theory and the possibility of *a priory* calculation of the ageing rate. *Glass Physics and Chemistry*, vol. 26, no 6, 511-530, 2000.
10. R. Golovchak, O. Shpotyuk, A. Kozdras, B. Bureau, M. Vlcek, A. Ganjoo and H. Jain. Atomistic model of physical ageing in Se-rich As-Se glasses *Philosophical Magazine* vol. 87, no. 28, 4323-4334, 2007.
11. R. Golovchak, Gz. Gorecki, A. Kozdras and O. Shpotyuk. Physical ageing effects in vitreous arsenic selenides. *Soid. State Communication*, vol. 137, 67-69, 2006.





# Comprehensive Chaotic Description of Heartbeat Dynamics Using Scale Index and Lyapunov Exponent

Sohrab Behnia<sup>1</sup>, Javid Ziaei<sup>1</sup>, Marjan Ghiassi<sup>1</sup>, and Mohammad Yahyavi<sup>2</sup>

<sup>1</sup> Department of Physics, Urmia University of Technology, Urmia, Iran  
(E-mail: s.behnia@sci.uut.ac.ir, j.ziaei@uut.ac.ir,  
marjanghiassi@yahoo.com)

<sup>2</sup> Department of Physics, Bilkent University, Ankara, Turkey  
(E-mail: yahyavi.mohamad@yahoo.com)

**Abstract.** Since cardiac system is capable of exhibiting chaotic behaviors, many works have been carried out to study its dynamics. In this paper, based on Grudziński and Żebrowski's model, the impacts of external periodic stimuli on cardiac impulses were studied using the scale index and Lyapunov exponent. Obtained results revealed that the scale index can detect special behaviors in the action potential whereas the Lyapunov exponent is not capable of uncovering them. Furthermore, it was found that the non-periodicity of pacemaker rhythms in the presence of external factors is not high, but the restoration of the heart to normal conditions requires medical attentions.

**Keywords:** Chaos, Scale index, Lyapunov exponent, Cardiac system, Action potential.

## 1 Introduction

One of the pioneering mathematical models describing heartbeat dynamics has been established by Van der Pol and Van der Mark [1]. Important similarities between their oscillator behavior and cardiac impulses such as oscillation at rates, without effecting the amplitude of oscillation motivated other researches to extend this topic [2,3]. Recently, Grudziński and Żebrowski [4] have proposed a modification of the original Van der Pol oscillator as a more complete model of pacemaker rhythms by considering effective biological factors in generation of an action potential.

There are several researches focusing on the evidences of nonlinear characteristics and chaotic characteristics in cardiac system dynamics [5,6]. Two basic indicators of chaotic motion is: sensitive dependence on initial conditions and non-periodic long-term behavior [7]. So, if a given dynamical deterministic nonlinear system exhibit two above mentioned characteristics, then it is said to be chaotic. The Lyapunov exponent can be an indicator of sensitive dependence on initial conditions, albeit it cannot specify non-periodicity [8]. Hence, for proper investigation of the chaos, there is a need to a new scale to determine non-periodicity. The scale index proposed in [8], can meet our requirement. It can complement the Lyapunov exponent to an exact discussion about the chaotic behavior. Our innovation is the use of the scale index to comprehensive



study about cardiac impulses.

After the introduction, the mathematical model of the heart pacemaker [4] is reviewed in Section 2. Then a brief discussion about the Lyapunov exponent and the scale index are presented in Section 3. Section 4 includes the obtained results. Finally, conclusions are discussed in Section 5.

## 2 Mathematical Model

In this paper the model proposed by Grudziński and Żebrowski [4] was employed. Periodic and chaotic behaviors of their model correspond to the normal and pathological functioning of the cardiac conducting system, respectively [9]. Their model is as follow:

$$\frac{d^2x}{dt^2} + \alpha(x - v_1)(x - v_2)\frac{dx}{dt} + \frac{x(x + e)(x + d)}{ed} = F(t)$$

$$A, \alpha, e, d > 0, \quad v_1 v_2 < 0.$$

where  $\alpha$  changes the refractory time, the  $(v_1, v_2)$  pair modify the frequency of the action potential or the value of the resting potential,  $e$  together with  $d$  control the diastolic period [4] and  $F(t) = A \sin(\omega t)$  is an external driving which is available for external adjustments [9].

For the sake of simplicity the above equation was transformed to a set of two coupled first-order ordinary differential equations (ODE) [9]:

$$\dot{x} = y$$

$$\dot{y} = F(t) - \alpha(x - v_1)(x - v_2)y - \frac{x(x + e)(x + d)}{ed}$$

Table I illustrates parameter values which was used in this paper to reproduce the normal action potential carrying the main properties of the natural action potential in the absence of external driving. Under this condition, the system can represent periodic behaviors as well as chaotic ones under different values of  $A$  with the same initial condition:  $[x_0, y_0] = [-0.1, 0.025]$ .

$A$	$\in [0, 12]$
$\alpha$	15
$v_1$	0.5
$v_2$	-0.3
$e$	1.4
$d$	1.5
$\omega$	1.9

**Table 1.** Parameter Values

The aim of [4] was to reproduce the normal rhythms of the cardiac system. Moreover, in [9] the authors have demonstrated that different initial conditions



may exhibit the various behaviors of the action potential which may be related to the abnormal functioning of the cardiac pacemaker. However, neither [4] nor [9] have investigated the effects of external periodic forcing on the pacemaker impulses.

### 3 Methods

#### 3.1 Lyapunov Exponent

The Lyapunov exponent measures the rate of the convergence/divergence of the trajectories of a given dynamical system in the phase space [10]. Indeed, it is a quantitative measure to indicate sensitive dependence on initial conditions. A typical  $m$ -dimensional dynamical system has  $m$  Lyapunov exponent which can be negative, positive or zero. The existence of a positive Lyapunov exponent indicates chaos [10–12]. So, Lyapunov exponents are usually used to determine whether the system is chaotic or not.

Generally, the Lyapunov exponents can be estimated from either the differential equations that govern underlying dynamics or the observed time series [13,14]. In this paper, the Wolf's algorithm in which the Lyapunov exponent in the  $i$ th direction is computed as follow:

$$\lambda_i = \lim_{t \rightarrow \infty} \frac{1}{t} \ln \frac{\|\delta x_i(t)\|}{\|\delta x_i(0)\|}.$$

was used. Where  $p_i(0)$  represents initial distance between two nearly orbits and  $p_i(t)$  distance between them after time  $t$  in the  $i$ th direction.

First, the Lyapunov exponent was computed for a given control parameter,  $A$ , then the amplitude of periodic force was increased by 0.01, and the new Lyapunov exponent was computed versus the new  $A$ . This process was continued until the whole range of the interval  $[0, 12]$  was covered.

#### 3.2 Scale Index

Non-periodic behavior means that there are trajectories that do not settle down to periodic or quasi periodic orbits as  $t \rightarrow \infty$  [7]. Although the Fourier transforms can be used for studying the periodicity of a given signal in frequency domain, it has a limitation, namely, that the signal must be stationary. Therefore, to study the periodicity of a non-stationary signal, the wavelet transforms must be replaced. Recently, the scale index was proposed in the basis of the wavelet transforms as a measure to investigate the degree of non-periodicity [8]. The summarized definition of the scale index is introduced as follows.

The CWT of the signal  $f$  at time  $u$  and scale  $s$  is defined as:

$$W_\psi f(u, s) = \int_{-\infty}^{+\infty} f(t) \psi_{u,s}^*(t) dt.$$

where

$$\psi_{u,s}(t) = \frac{1}{\sqrt{s}} \psi\left(\frac{t-u}{s}\right).$$



The inner scalogram  $\bar{S}^{inner}$  of  $f$  is defined as:

$$\bar{S}^{inner}(s) = \left( \frac{\int_{c(s)}^{d(s)} |W_\psi f(u, s)|^2 du}{d(s) - c(s)} \right)^{\frac{1}{2}}.$$

Indeed, the inner scalogram is the normalized energy of the CWT of  $f$  on interval  $[c(s), d(s)]$  at scale  $s$ . In practice, the inner scalogram is studied on a finite interval  $[s_0, s_1]$ . The scale  $s_{max}$  is a scale for which the inner scalogram reaches its maximum and  $s_{min}$  is the smallest ones, i.e.,  $\bar{S}^{inner}(s_{min}) \leq \bar{S}^{inner}(s)$  for all  $s$  such that  $s_{max} \leq s \leq s_1$ . So, the scale index,  $i_{scale}$ , of  $f$  on the scale interval  $[s_0, s_1]$  is computed as follow:

$$i_{scale} = \frac{\bar{S}^{inner}(s_{min})}{\bar{S}^{inner}(s_{max})}.$$

The scale index,  $i_{scale}$ , is defined such that  $0 \leq i_{scale} \leq 1$ : Highly non-periodic orbits correspond to the values close to 1 and periodic orbits to the values close to 0. In contrast with the Lyapunov exponent, the bounded feature of the scale index makes it as a much sensible tool in the sense of chaoticity and non-periodicity measures.

In this paper the Daubechies eight-wavelet (db8) function and the scale parameter from  $s_0 = 1$  to  $s_1 = 512$ , with  $\Delta s = 1$  were considered in the computation of the  $i_{scale}$  for a given control parameter. Increasing control parameter by 0.01, the new  $i_{scale}$  was computed for new parameter and this procedure was continued until the whole range of the control parameter was covered.

## 4 Results

In this section the effects of changing the amplitude of external stimuli on action potential are discussed.

In order to investigate different states of the model, the bifurcation analysis method was applied. For do, the amplitude of external forcing was taken as a control parameter. To show the global structure of the model, the amplitude of external forcing  $A$ , was restricted to vary on a finite interval  $[0, 12]$ . Figure 1 shows the bifurcation diagram. Both the local maximum and minimum values of the  $x$ -variable were plotted in the bifurcation diagram. It is clear that both kinds of orbits (periodic and non-periodic) can be achieved with changing  $A$ .

Accordingly, for the each value of control parameter, the action potential was generated. Figure 1 shows the action potential and related phase spaces in the absence ( $A = 0$ ) and presence of the external forcing. In the absence of any external stimuli, it can be recognized that the heart behaves as a periodic oscillator [15]. Pan et al. [16] have showed that the external stimuli may accelerate the action potential generation in cardiac pacemaker cells. Accordingly, generated action potentials in the presence of external force (e.g.  $A = 1.42$  and  $A = 4.49$ ) depicted increase in the heartbeat rhythms generation. This acceleration of the rhythms generation can lead to tachycardia [17]. In addition,

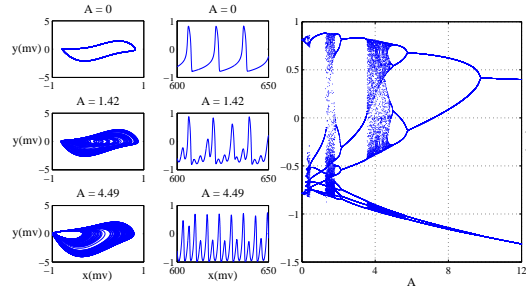


**Fig. 1.** Bifurcation diagram and phase spaces for different values of  $A$  and related action potentials.

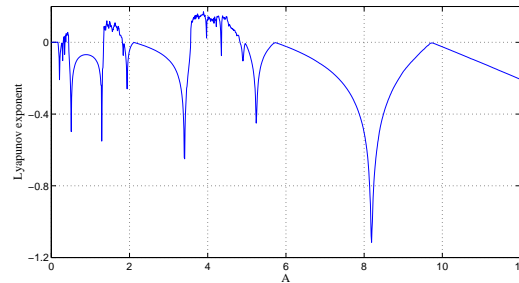


**Fig. 2.** Lyapunov exponent vs.  $A$ .

these figures showed abnormalities in the action potential. Abnormalities may be caused by strong interrelation between inward and outward ion currents. Especially, it is evident from Figure 1 that changing the amplitude of external periodic driving has been resulted in appearing delayed after depolarization in the action potential. Briefly, these diagrams demonstrated that:

1. The parameter sensitivity of the action potential compared to the amplitude of external forcing was very high [18]. This parameter sensitivity of the action potential confirmed the previous works [19,20] proving the existence of the chaos in the cardiac system.
2. External stimuli may accelerate action potential generation in cardiac pacemaker cells [16].
3. There were three distinct regions defined as  $A \in [0.31, 0.44]$ ,  $[1.34, 1.81]$  and  $[3.57, 4.82]$  for which the behavior of the system was non-periodic. The region defined as  $A \in [1.34, 1.81]$  was more non-periodic in comparison with two others, since the space between two branches of the bifurcation diagram had been filled thoroughly. In this region the functioning of the cardiac pacemaker was more abnormal and no regular patterns in the action potential were observed.

After these recognitions, the Lyapunov exponent need to be computed by considering the different values of control parameter for identifying chaotic regions. Figure 2 shows the Lyapunov exponent versus control parameter  $A$ . Regions

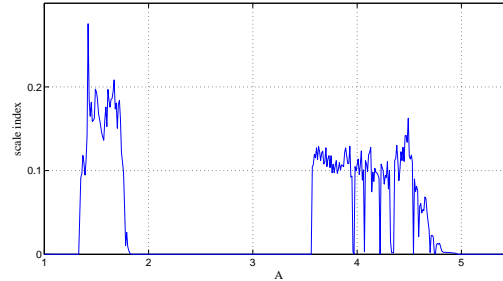


**Fig. 3.** Scale index vs.  $A$ .

associated with the negative values of the Lyapunov exponent indicated that the system was in stable states and cardiac pacemaker functioning was normal. It is clear from Figure 2 that the value of the Lyapunov exponent for  $A \in [0.31, 0.44]$ ,  $[1.34, 1.81]$  and  $[3.57, 4.82]$  was positive and cardiac pacemaker functioning was abnormal. These results were in accordance with previous works [19,20] showing the pathological states have positive Lyapunov exponents and hence chaotic nature. Especially, it was found that The variation range of the Lyapunov exponent in the region defined as  $A \in [1.34, 1.81]$  was low than the  $A \in [3.57, 4.82]$ . In terms of the Lyapunov exponent this means that the latter region was more chaotic, whereas the bifurcation diagram showed that the non-periodicity in the latter's was low. This perceived shortcoming of the Lyapunov exponent in addressing whether the system's behavior was more non-periodic or low demands a new measure for properly identifying chaos in the cardiac system. Accordingly, it was illustrated how the scale index  $i_{scale}$  can detect the non-periodic orbits of cardiac pacemaker.

In order to show the effectiveness of the scale index,  $i_{scale}$ , its diagram was compared with the Lyapunov exponent and bifurcation. Figure 3 depicts the variation of  $i_{scale}$  versus to  $A$ . Due to better resolution,  $A$  was restricted to vary on a finite interval  $[1,5.5]$ . It was shown that:

1. There was a good agreement among the chaotic regions of the bifurcation diagram, regions where the Lyapunov exponent were positive and regions where  $i_{scale}$  was much greater than 0. The values of  $A$  for which the Lyapunov exponent was negative were also the values for which  $i_{scale} \approx 0$ . It is noteworthy that the high value of the scale index associates with the chaotic regions [8]. Since pacemaker cells generate periodic impulses in normal conditions and these impulses are responsible for controlling the rate and rhythm of the heartbeats, the high value of the scale index displayed disturbance in the periodicity of the action potential which has been caused by changes in the rate and rhythm of heartbeats.
2. It is significant to know that the relative maximum in the  $i_{scale}$  and the sudden expansion of the size of the attractor at  $A = 1.42$  were simultaneous. This point is in agreement with overlapping the main branches of the bifurcation diagram which was not detected by the Lyapunov exponent. Also, the same overlapping was occurred for the sudden contraction of the



size of the attractor at  $A = 4.49$ . As mentioned before, the appearance of two relative maximums indicates the acceleration in the rhythms generation and alternation in the amplitude of the action potential related to the abnormal functioning of the cardiac pacemaker, like arrhythmia.

3. The values range of the scale index on the region defined as  $A \in [1.34, 1.81]$  was greater than the region defined as  $A \in [3.57, 4.82]$ , the result that had previously been expected from the bifurcation diagram.
4. It is also noticeable that the numerical computations resulted that  $(i_{scale})_{max} \approx 0.28$ , expressing the measure of chaoticity and non-periodicity in the cardiac action potential was not high, but the restoration of the heart to normal conditions requires medical attentions.

## 5 Conclusions

Focusing on the model of Grudziński and Żebrowski, the effects of changing the amplitude of external forcing on pacemaker rhythm were examined and the deficiency of the Lyapunov exponent in detecting non-periodic behaviors in the action potential was shown. Then the ability of the scale index in overcoming the shortcoming of the Lyapunov exponent was explored. Furthermore, it was shown that the measure of the chaos in the action potential was not high. Finally, it was found that the scale index can provide a non-invasive assessment of the heart in real-life conditions.

Next thing to be mentioned is that the results of this study can be improved by analyzing the models that can more accurately represent the natural conditions of the heart dynamics under external factors. Furthermore, the findings of this study provide new perspectives into the new methods should be applied to control of abnormal heartbeats in order to avoid chaotic behaviors in the action potential.

## References

- 1.V. der Pol B. and V. der Mark J. The heartbeat considered as a relaxation oscillation and an electrical model of the heart *Philosophical Magazine Supplement*, 6:763–775, 1928.
- 2.J. M. T. Thompson and H. B. Steward. Nonlinear dynamics and chaos. John Wiley and Sons, 2002.
- 3.C. R. Katholi, F. Urthaler, J. Macy Jr, and James T. N. A mathematical model of automaticity in the sinus node and av junction based on weakly coupled relaxation oscillators *Computers and Biomedical Research*, 10:529–543, 1977.
- 4.K. Grudziński and J. J. Żebrowski. Modeling cardiac pacemakers with relaxation oscillators *Physica A: Statistical Mechanics and its Applications*, 336:153–162, 2004.
- 5.F. X. Witkowski, K. M. Kavanagh, P. A. Penkoske, R. Plonsey, M. L. Spano, W. L. Ditto, and D. T. Kaplan. Evidence for determinism in ventricular fibrillation *Physical Review Letters*, 75:1230–1233, 1995.
- 6.S. Behnia, A. Akhshani, H. Mahmodi, and H. Hobbenagi. On the calculation of chaotic features for nonlinear time series *Chinese Journal of Physics*, 46:394–404, 2008.



- 7.S. H. Strogatz. Nonlinear dynamics and chaos: with applications to physics, biology, chemistry and engineering. Addison-Wesley, 1994.
- 8.R. Benítez, V. J. Bolós, and M. E. Ramírez. A wavelet-based tool for studying non-periodicity *Computers and Mathematics with Applications*, 60:634–641, 2010.
- 9.B. B. Ferreira, A. S. de Paula, and M. A. Savi. Chaos control applied to heart rhythm dynamics *Chaos, Solitons and Fractals*, 44:587–599, 2011.
- 10.R. Brown, P. Bryant, and H. D. I. Abarbanel. Computing the lyapunov spectrum of a dynamical system from an observed time series *Physical Review A*, 43:2787–2806, 1991.
- 11.M. Casdagli. Nonlinear prediction of chaotic time series *Physica D: Nonlinear Phenomena*, 35:335–356, 1989.
- 12.J.-P. Eckmann, S. O. Kamphorst, D. Ruelle, and S. Ciliberto. Liapunov exponents from time series *Physical Review A*, 34:4971–4979, 1986.
- 13.A. Wolf, B. J. Swift, H. L. Swinney, and J. A. Vastano. Determining Lyapunov exponents from a time series *Physica D: Nonlinear Phenomena*, 16:285–317, 1985.
- 14.M. T. Rosenstein, J. J. Collins, and C. J. de Luca. A practical method for calculating largest Lyapunov exponents from small data sets *Physica D: Nonlinear Phenomena*, 65:117–134, 1993.
- 15.J. Keener and J. Sneyd. Mathematical physiology. Springer, 1996.
- 16.Zh. Pan, R. Yamaguchi, and Sh. Doi. Bifurcation analysis and effects of changing ionic conductances on pacemaker rhythm in a sinoatrial node cell model *Biosystems*, 106:9–18, 2011.
- 17.M. S. Lipsky, M. Mendelson, S. Havas, and M. Miller. Guide to preventing and treating heart disease. John Wiley and Sons, 2008.
- 18.P. K. C. Wang and B. Y. Kogan. Parametric study of the noble’s action potential model for cardiac purkinje fibers *Chaos, Solitons and Fractals*, 33:1048–1063, 2007.
- 19.E. D. Übeyli. Recurrent neural networks employing Lyapunov exponents for analysis of ECG signals *Expert Systems with Applications*, 37:1192–1199, 2010.
- 20.E. D. Übeyli. Adaptive neuro-fuzzy inference system for classification of ECG signals using Lyapunov exponents *Computer Methods and Programs in Biomedicine*, 93:313–321, 2009.



# CHAOTIC SOLUTIONS IN NON LINEAR ECONOMIC- FINANCIAL MODELS

Giovanni Bella,\*Paolo Mattana,†Betrice Venturi‡

July 31, 2013

## Abstract

Techniques from dynamical systems, specifically from bifurcation theory, are used to investigate the occurrence of cycle and chaotic solutions in non linear economic-financial models. In particular, we consider a general class of endogenous growth models as formalized by Mulligan and Sala-i-Martin (1993), reducible in the form of a non linear three-dimensional system.

The Lucas model can be considered as particular example of this general class. We found that Smale horseshoe chaotic behavior will be exhibited in the neighborhood of parameter space of our economic model where a homoclinic Shilnikov orbits occur.

*Keywords:* homoclinic Shilnikov bifurcation, Smale horseshoe chaos.

*JEL classification:* C61, C62, E32

## 1 Introduction

The study of homoclinic orbits and chaotic phenomena in nonlinear dynamical systems has attracted much attention in economics (see i.e. Lorenz H.W., (1989), Benhabib J., (1992), Jarsulic M., (1993), Benhabib J. and Perli R., (1994), Mattana P. and Venturi B. (1999), Boldrin Michele, Nishimura Kazuo, Shigoka Tadashi, Yano Makoto (2000), Mattana P. (2004), Neri U. and Venturi B. (2007), Mattana P., Nishimura K., Shigoka T. (2008), Bella G. Mattana P. and Venturi B. (2013). It has been showed that the concept of cycles and chaos are perfectly compatible with a lot of standard equilibrium models that incorporate the assumption of stationary motion, preference and technology.

In this paper we prove analytically the existence of a homoclinic Shilnikov orbit and horseshoe chaos in a model of a classe of nonlinear economic-financial models.

---

\*Department of Economics and Business, University of Cagliari, Italy. Email: bella@unica.it

†Department of Economics and Business, University of Cagliari, Italy. Email: mattana@unica.it

‡*Corresponding Author.* Department of Economics and Business, University of Cagliari, Italy. Email: venturi@unica.it



Under Shilnikov Theorem assumptions, we found that the Smale horseshoe chaos occurs both theoretically and numerically in a particular system of a generalized class of one equilibrium point, two sector models of endogenous growth, as formulated by Mulligan B.- Sala-I-Martin X.,1993.

As described by Guckenheimer J. - Holmes P.,1983, and Wiggins S.,1990, usually a chaotic attractor has two or more equilibrium points: one determines the location and structure of the attractor, and another is used to build a suspended flow which forms the spine of the attractor. However, as reported in recently papers one equilibrium point is still possible to form a chaotic attractor.

The work develops as follows. The second Section introduces the considered class of generalized two sector models of endogenous growth, as a dynamical system.

The third Section studies the long-run properties of the equilibrium of a particular example of this general class: the Lucas Model.

We refer to the original paper of Mulligan B.- Sala-I-Martin X.,1993 and Lucas 1988 for an appropriate economic description of the system. The last Section is devoted to give a rigorous proof of the conditions leading to the emergence of a homoclinic Shilnikov orbit.

Finally, chaos is obtained for the existence of Smale horseshoes in the discrete dynamics of the Shilnikov map defined near the homoclinic orbit.

In the last section we show optimality for paths starting in the homoclinic Shilnikov orbit and chaotic solutions very closed to the homoclinic orbit (their satisfy the transversality conditions).

Some economic implications of this analysis are discussed.

## 2 The Generalized Class of Two Sector Models of Endogenous Growth

We review the generalized class of two sector models of endogenous growth, with externalities, as formulated by Mulligan B.- Sala-I-Martin X.,1993. The model deal with the maximization of a standard utility function:

$$\int_0^{\infty} \frac{c^{1-\sigma} - 1}{1-\sigma} e^{-\rho t} dt \quad (1.1)$$

where  $c$  is per-capita consumption,  $\rho$  is a positive discount factor and  $\sigma$  is the inverse of the intertemporal elasticity of substitution. The constraints to the growth process are represented by the following equations

$$\dot{k} = A((h(t)^{\alpha_h} u(t)^{\alpha_u})(\nu(t)^{\alpha_\nu} k(t)^{\alpha_k}) \hat{h}(t)^{\alpha_{\hat{h}}} k(t)^{\alpha_{\hat{k}}} - \tau_k k(t) - c(t) \quad (1.2)$$

$$\dot{h} = B((h(t)^{\beta_h} (1 - u(t)^{\beta_u}))((1 - \nu(t)^{\beta_\nu} k(t)^{\beta_k}) \hat{h}(t)^{\beta_{\hat{h}}} k(t)^{\beta_{\hat{k}}} - \tau_h h(t)$$

where  $k$  is physical capital,  $h$  is human capital,  $\alpha_k$  and  $\alpha_h$  being the private share of physical and the human capital in the output sector,  $\beta_k$  and  $\beta_h$  being the corresponding shares share in the education sector,  $u$  and  $v$  are the fraction of aggregate human and physical capital used in the final output sector at instant  $t$



( and conversely,  $(1-u)$  and  $(1-v)$  are the fractions used in the education sector),  $A$  and  $B$  are the level of the technology in each sector,  $\tau$  is a discount factor,  $\alpha_k^\wedge$  is a positive externality parameter in the production of physical capital,  $\alpha_h^\wedge$  is a positive externality parameter in the production of human capital.

The equalities  $\alpha_k + \alpha_h = 1$  and  $\beta_k + \beta_h = 1$  ensure that there are constant returns to scale at the private level. At the social level, however, there may be increasing, constant or decreasing returns depending on the signs of the externality parameters.

All other parameters  $\omega = (\alpha_k, \alpha_k^\wedge, \alpha_h, \alpha_h^\wedge, \beta_k, \beta_k^\wedge, \beta_h, \beta_h^\wedge, \sigma, \gamma, \delta, \rho)$  live inside the following set  $\Omega \subset (0, 1) \times \mathbb{R}_+^4$ .

The representative agent's problem (1.1)-(1.2) is solved by defining the current value Hamiltonian.

$$H = \frac{c^{1-\sigma}-1}{1-\sigma} + \lambda_1 (A((h(t))^{\alpha_h} u(t)^{\alpha_u}) (\nu(t)^{\alpha_\nu} k(t)^{\alpha_k}) \hat{h}(t)^{\alpha_h^\wedge} k(t)^{\alpha_k^\wedge} - \tau_k k(t) - c(t)) + \lambda_2 (B((h(t))^{\beta_h} (1-u(t)^{\beta_u})) ((1-\nu(t)^{\beta_\nu} k(t)^{\beta_k}) \hat{h}(t)^{\beta_h^\wedge} k(t)^{\beta_k^\wedge} - \tau_h h(t)) (1.3)$$

where  $\lambda_1$  and  $\lambda_2$  are co-state variables which can be interpreted as shadow prices of the accumulation. The solution candidate comes from the first-order necessary conditions (for an interior solution) obtained from the Maximum Principle, with the usual transversality condition:

$$\lim_{t \rightarrow \infty} [e^{-\rho t} (\lambda_1 k + \lambda_2 h)] = 0 \quad (1.4)$$

We call the solution of this optimal control problem from (1.1) to (1.3) a Balance Growth Path (B.G.P). The maximized Hamiltonian is jointly concave in  $(k, h)$ ; this fact is a sufficient condition for a solution of the first-order conditions (see Mulligan B.-Sala-I-Martin X.,1993, Benhabib J. - Pearli R., 1994, (BP), Mattana P. Venturi B.1999,(MV)).

We consider only the competitive equilibrium solution.

After eliminating  $v(t)$  the rest of the first order conditions and accumulation constraints entail four first order non linear differential equations in four variables: two controls ( $c$  and  $u$ ) and two states ( $k$  and  $h$ ).

By using new variables, since  $h, k$  and  $c$  grow at a constant rate and  $u$  is a constant, Mulligan B.-Sala-I-Martin X.,1993, have transformed a system of ordinary differential equations for  $c, u, k$  and  $h$ , into a system of three first order ordinary differential equations.

Setting ,

$$x_1 = h^{\frac{\alpha_h^\wedge}{(\alpha_h^\wedge - 1)}} k ; \quad x_2 = u; \quad x_3 = \frac{c}{k} \quad (1.5)$$

and

$$A = B = 1$$

we get:

$$\begin{aligned} \dot{x}_1 &= \phi_1(x_1, x_2, x_3, \alpha_k, \alpha_k^\wedge, \alpha_h, \alpha_h^\wedge, \beta_k, \beta_k^\wedge, \beta_h, \beta_h^\wedge, \sigma, \gamma, \delta, \rho) \\ \dot{x}_2 &= \phi_2(x_1, x_2, x_3, \alpha_k, \alpha_k^\wedge, \alpha_h, \alpha_h^\wedge, \beta_k, \beta_k^\wedge, \beta_h, \beta_h^\wedge, \sigma, \gamma, \delta, \rho) \\ \dot{x}_3 &= \phi_3(x_1, x_2, x_3, \alpha_k, \alpha_k^\wedge, \alpha_h, \alpha_h^\wedge, \beta_k, \beta_k^\wedge, \beta_h, \beta_h^\wedge, \sigma, \gamma, \delta, \rho) \end{aligned} \quad (1.6)$$



where the  $\phi_i$  with  $i = 1, 2, 3$  are complicated nonlinear functions ; which depend of the parameters  $(x_1, x_2, x_3, \alpha_k, \alpha_k^\wedge, \alpha_h, \alpha_h^\wedge, \beta_k, \beta_k^\wedge, \beta_h, \beta_h^\wedge, \sigma, \gamma, \delta, \rho)$  of the model.

Mulligan B. - Sala-I-Martin X.,1993, have also shown that for the new model (1.6), under phisical economic assumptions, exist only one stationary point  $P^*(x_1^*, x_2^*, x_3^*)$ .

### 3 The Lucas Model

The general model just presented collapses to Lucas's model (1988) that is analyzed by Benhabib and Perli (1994), Mattana and Venturi (1999) and Mattana (2004).when depreciation is neglected and the following restrictions are imposed

$$\alpha_\nu = \alpha_k^\wedge = 0; \beta_k^\wedge = \beta_h^\wedge = \beta_\nu = \beta_k = 0; \alpha_\nu = \alpha_h = 1 - \alpha_k; \beta_u = \beta_h \quad (2.1)$$

The equations of the Lucas's model can be formalized in  $R^3$  in the following form

$$\begin{aligned} \dot{x}_1 &= x_1^\beta x_2^{\beta-1} - x_1 x_3 + \psi \frac{(\beta-1)}{\beta} (1 - x_2) \\ \dot{x}_2 &= \eta x_2^2 + \psi \frac{(\beta-1)}{\beta} x_2 + x_1 x_3 \\ \dot{x}_3 &= \phi x_2^{1-\beta} x_1^{\beta-1} x_3 - \frac{\rho}{\sigma} x_3 + x_3^2 \end{aligned} \quad (2.2)$$

as a system of three first order differential equations where

$$\phi = \frac{\beta-\sigma}{\sigma} \quad \eta = \frac{\delta(\beta-1)}{\beta} \quad \psi = \frac{\delta(1-\beta+\gamma)}{\beta-1} \quad \xi = \frac{\rho}{\sigma} \quad (2.3)$$

A stationary (equilibrium) point  $P^*$  of the system is any solution of

$$\begin{aligned} x_1^{*1-\beta} x_2^{*\beta-1} - x_1^* x_3^* + \psi(1 - x_2^*) x_1^* &= 0 \\ \eta x_2^{*2} + \psi \frac{(\beta-1)}{\beta} x_2^* - x_2^* x_3^* &= 0 \\ \phi x_2^{*1-\beta} x_1^{*\beta-1} x_3^* - \xi x_3^* + x_3^{*2} &= 0 \end{aligned} \quad (2.4)$$

.Then, we solved the system in (2.4) and we get the following steady state values

$$x_1^* = x_2^* \left[ \frac{\beta\rho - \delta\sigma(1-u^*) + \delta(\beta-\gamma)}{\beta(\beta-\sigma)} \right]^{1/(\beta-1)} \quad (2.5a)$$

$$x_2^* = \frac{(1-\beta)(\rho-\delta)}{\delta - [\gamma - \sigma(1-\beta+\gamma)]} \quad (2.5b)$$

$$x_3^* = \eta x_2^* + \delta \frac{(1-\beta+\gamma)}{\beta} \quad (2.5c)$$

where  $\phi = \frac{\beta-\sigma}{\sigma}$  simplifies the notation.

The system (2.2) possesses an interior steady-state characterized by the stationary values in (2.5.a), (2.5.b) and (2.5.c) for  $x_1^*$ ,  $x_2^*$  and  $x_3^*$ .It is well-known that many theoretical result relating to the system depend upon the eigenvalues of the Jacobian matrix evaluated at the stationary point in some values of the parameters.

Let  $J$  be the Jacobian matrix and  $P^*(x_1^*, x_2^*, x_3^*)$  the stationary point ( $J(P^*) = J^*$ , see appendix A).

The "feasible" restrictions in the parameters are satisfied if and only if the parameters lie in one of the following subsets of  $\Omega$  :



- i) if  $\omega \in \Omega^1$ ,  $J^*$  has one negative eigenvalue and two eigenvalues with positive real parts. (This means that the competitive equilibrium path is locally unique).
- ii)  $\omega \in \Omega^2$ ,  $J^*$  has one positive eigenvalue and two eigenvalues with negative real parts.
- iii)  $\omega \in \Omega^3$  there exist two subsets  $\Omega_3^A$  and  $\Omega_3^B$ , and such that:

- a) if  $\omega \in \Omega_3^A$   $J^*$  has one eigenvalue with a positive real part and two eigenvalues with negative real parts.

$$\Omega_3^A = \left\{ \rho \in (\delta, -\psi), \sigma \in (0.1, \rho/\psi), \gamma \in \left( \frac{(1-\beta)(\rho-\delta)}{\delta}, \tilde{\gamma} \right) \right\}$$

where  $\tilde{\gamma}$  is the Hopf bifurcation value found in MV (Mattana P. and Venturi B.1999)

- b) if  $\omega \in \Omega_3^B$   $J^*$  has three eigenvalues with positive real parts:

$$\Omega_3^B = \left\{ \rho \in (\delta, -\psi), \sigma \in (0.1, \rho/\psi), \gamma \in (\tilde{\gamma}, \beta) \right\}.$$

So, there is either a continuum of equilibria converging towards the steady-state or no stable transitional paths at all.

In order to prove the existence of homoclinic Shilnikov orbit analitically, in the next section, we focus our attention in the set  $\Omega_3^A$ .

## 4 The Emergence of a Homoclinic Orbit.

We remember that a homoclinic orbit is a transversal intersection between the stable manifold with the unstable manifold of a hyperbolic point (connects a saddle to itself). In general is not easy to prove the existence of a homoclinic orbit for a dynamical system.

We rigorously prove that our system satisfies all conditions stated in the Shilnikov Theorem.

In the first, we translate the equilibrium point  $P^*$  in the origin  $W^*$  and we make use of the normal form( see Appendix B and MV 1999), in the new variables the system becomes:

$$\frac{dw_i}{dt} = f_i(w_1, w_2, w_3) \text{ with } i = 1, 2, 3 \quad (3.1).$$

**Lemma 1** If  $\omega \in \Omega_3^A$  the equilibrium point  $W^*(0, 0, 0)$  is a saddle focus

The jacobian  $J^*$  in  $\Omega_3^A$  has one positive real and two complex conjugate eigenvalues whose real parts is negative: then the equilibrium point  $P^*$  in  $\Omega_3^A$  is a saddle focus and the real eigenvalue is bigger than the absolute value of the real part of the complex conjugate eigenvalues.

**Lemma 2** In  $\Omega_3^A$  the system (2.2) has an homoclinic Shilnikov orbit.

**Proof.** See Appendix B. ■

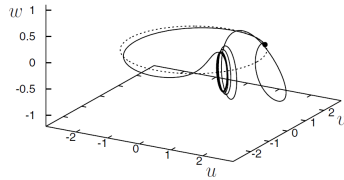


Figure 1

In Figure 1. we have the graph of the Homoclinic Shilnikov Orbit with:  
 $w_1 = w, w_2 = u, w_3 = v$

**Remark 1** In the set  $\Omega_3^B$  the jacobian  $J^*$  has one positive real and two complex conjugate eigenvalues whose real parts is positive. In this situation the model is expanding and thus it cannot have homoclinic orbits .

**Theorem 2** 1.If the third-order autonomous system (2.2) has a saddle-focus (of index 2) in the unique equilibrium points,  $P^*$  with eigenvalues associated to  $J^*$  given by  $r \in \mathbb{R}$  and  $\alpha + i\beta \in \mathbb{C}$ , such that  $r\alpha > 0$ . with a further constraint  $|r| > |\alpha|$ , and there exists a homoclinic orbit, connecting  $W^*$  then

(a) The Shilnikov map, defined in a neighborhood of the homoclinic orbit of the system, possesses a countable number of Smale horseshoes in its discrete dynamics.

(b) For any sufficiently small  $C^1$ -perturbation  $\mathbf{g}$  of  $\mathbf{f}$  the perturbed system  $\frac{dw_i}{dt} = g_i(w_1, w_2, w_3)$  with  $i = 1, 2, 3$  (3.2) exhibits a Smale horseshoe type of chaos has at least a finite number of Smale horseshoes in the discrete dynamics of the Shilnikov map defined near the homoclinic orbit.

(c) Both the original system (2,2) and the perturbed system (3.1) exhibit horseshoe chaos.

**Proof.** Theorem 1 is a direct application of the Shilnikov Theorem (see Guckenheim-Holmes 1983, pp.151-152). We only have to verify that the assumptions of Shilnikov theorem are satisfied.



By lemma1 the equilibrium point  $W^*$  is a saddle focus when  $\omega \in \Omega_3^A$  and the real eigenvalue is bigger than the real part of the complex conjugate eigenvalues.  
By lemma 2 the system has a homoclinic Shilnikov orbit.  
This covers completely the assumptions of Shilnikov theorem. ■

(Q.E.D.)

## 5 Transversality Conditions

**Proposition 1** *The transversality conditions are satisfied on the homoclinic orbit.*

As shown in BP the transversality conditions are satisfied on the balanced growth paths. Let  $W^*$   $(\beta, \delta, \rho, \sigma, \gamma^*)$  be the only steady state in  $\Omega_3^A$ . Let  $U$  in  $R^3$  be a small open neighborhood of  $W^*$ . So for each  $(\beta, \delta, \rho, \sigma, \bar{\gamma}) \in \Omega_3^A$ , if we choose  $U$  sufficiently small, each path inside, starting from a point in the homoclinic orbit, satisfies the transversality conditions.

It follows directly from continuity arguments (the theorem of the permanence of the sign for continuous functions).

**Proposition 2** *The transversality conditions hold near the homoclinic orbit where the Shilnikov Theorem is true.*

**Proof.** Let  $g_i$  be a  $C^1$  perturbation of  $f_i$  where the Shilnikov Theorem is true near the homoclinic orbit.

Then for each  $(\beta, \delta, \rho, \sigma, \bar{\gamma}) \in \Omega_3^A$  there exists a constant  $\mathbf{L}$  such that

$$|\mathbf{f}(\bar{w}(t)) - \mathbf{g}(\mathbf{w}(t))| < \mathbf{L} |\bar{w}(t) - \mathbf{w}(t)| \quad (3.3)$$

( we consider (3.3) in vectorial form) the distance between a path starting in the homoclinic Shilnikov orbit and a Smale horseshoe chaotic path of  $\mathbf{g}$  can be arbitrary small.

From proposition 1 the transversality conditions are satisfied on the homoclinic orbit of (3.1) then their are satisfied also in the chaotic solutions. We can choose an arbitrary small open set  $U$  of  $f$  a path starting in the homoclinic orbits in which there is a path that exhibits a Smale horseshoe chaos.

But the Shilnikov Theorem stated that for any sufficiently small  $C^1$ -perturbation  $g$  of  $f$ , the perturbed system exhibits a Smale horseshoe chaos.

Then the transversality condition are satisfies. ■

## 6 Conclusions

This paper aims to give a contribution of research to conditions which determine a chaotic behavior in the long-run properties of an economic model . Investigations of this kind are important in economic theory since help mapping the regions of the parameters space in correspondence of which the capacity of the models to produce indications on future economic outcomes starting from given



fundamentals is drastically impaired. The aim of the present paper is to point out some basic ideas that may be useful to prove the transition to bounded and complex behavior, and to explain how the presence of an Homoclinic Shilnikov orbit and chaos in a model of a general class of economic-financial models can be interesting from an economic and dynamic point of view.

## References

- [1] C. Azariadis, R. Guesnerie, Sunspot and cycles, *Review of Economic Studies* 53 (1986) 725-736.
- [2] G. Bella, P. Mattana, B. Venturi, The double scroll chaotic attractor in the dynamics of a fixed-price IS-LM model, *Int. J. Mathematical Modelling and Numerical Optimisation*, Vol. 4, No. 1, (2013), 1-13.
- [3] J. Benhabib, K. Nishimura, T. Shigoka, Bifurcation and sunspots in the continuous time equilibrium model with capacity utilization, *International Journal of Economic Theory* 4 (2008) 337-355.
- [4] J. Benhabib, R. Perli, Uniqueness and indeterminacy: on the dynamics of endogenous growth. *Journal of Economic Theory* 63, (1994), 113-142.
- [5] J. Benhabib, S. Schmitt-Grohé, M. Uribe, The perils of Taylor rules, *Journal of Economic Theory* 96 (2001) 40-69.
- [6] J.B. Bullard, A Two-Headed Dragon for Monetary Policy, *Business Economics* 44 (2009) 73-79.
- [7] J.B. Bullard, S.H. Russel, An Empirically Plausible Model of Low Real Interest Rates and Unbaked Government Debt, *Journal of Monetary Economics* 44 (1999) 477-508.
- [8] D. Fiaschi, S. Sordi, Real business cycle models, endogenous growth models and cyclical growth: A critical survey," *Computing in Economics and Finance* Real business cycle models, 16, (2002), 306-329.
- [9] G. Gandolfo, *Economic dynamics*, Springer-Verlag, Berlin, 1997.
- [10] J.M. Grandmond, On endogenous business cycles, *Econometrica* 53 (1985) 995-1046.
- [11] N. Kopell, L.N. Howard, Bifurcations and trajectories joining critical points, *Advances in Mathematics* 18 (1975) 306-358.R.
- [12] E. Lucas, On the mechanics of economic development. *Journal of Monetary Economics* 22, (1998), 3-42.
- [13] P. Mattana, B. Venturi, Existence and Stability of Periodic Solutions in the Dynamics of Endogenous Growth. *RISEC, International Review of Economics*, vol. 46, fas. 2, (1999), 259-284.



- [14] C.B. Mulligan, X. Sala-i-Martin, Transitional dynamics in two-sector models of endogenous growth. *Quarterly Journal of Economics* 103, (1993), 739-773.
- [15] P. Mattana, K. Nishimura, T. Shigoka, Homoclinic bifurcation and global indeterminacy of equilibrium in a two-sector endogenous growth model, *International Journal of Economic Theory* 5 (2009) 1-23.
- [16] M. Neamtu, D. Opris, C. Chilarescu, Hopf bifurcation in a dynamic IS-LM model with time delay, *Chaos, Solitons and Fractals* 34 (2007) 519-530.
- [17] U. Neri, B. Venturi, Stability and Bifurcations in IS-LM economic models, *International Review of Economics* 54 (2007) 53-65.
- [18] D. Shang , M. Han., The existence of homoclinic orbits to saddle-focus, *Applied Mathematics and Computation* 163, (2005), 621–631.

## 7 Appendix A

As shown in the text, Lucas model gives rise to the following system of first-

$$\begin{aligned} \dot{x}_1 &= x_1^\beta x_2^{1-\beta} - x_1 x_3 + \psi(1-x_2)x_1; \\ \dot{x}_2 &= \eta x_2^2 + \psi \frac{(\beta-1)}{\beta} x_2 - x_2 x_3; \end{aligned} \quad (\text{A.1})$$

order differential equations

$$\dot{x}_3 = \phi x_2^{1-\beta} x_1^{\beta-1} x_3 - \xi x_3 + x_3^2;$$

where:

$$\phi = \frac{\beta-\sigma}{\sigma} \quad \eta = \frac{\delta(\beta-\gamma)}{\beta} \quad \psi = \frac{\delta(1-\beta+\gamma)}{\beta-1} \quad \xi = \frac{\rho}{\sigma};$$

The system has the single equilibrium point:  $P^*(x_1^*, x_2^*, x_3^*)$

$$\begin{aligned} x_1^* &= x_2^* \left[ \frac{\beta\xi - \delta(1-\beta+\gamma) + \delta(\beta-\gamma)x_2^*}{\beta\phi} \right]^{1/(\beta-1)} \\ x_2^* &= \frac{(1-\beta)(\rho-\delta)}{\delta - [\gamma - \sigma(1-\beta+\gamma)]} \\ x_3^* &= \eta x_2^* + \delta \frac{(1-\beta+\gamma)}{\beta} \end{aligned} \quad (\text{A.2})$$

The jacobian matrix  $J$  associated with the system (A.1) evaluated at the unique equilibrium point  $P^*$  is given by  $J(P^*)$ :

$$J(P^*) = \begin{bmatrix} J_{11}^* & \frac{x_1^*}{x_2^*} (J_{11} + \psi x_2^*) & -x_1^* \\ 0 & -\eta x_2^* & x_2^* \\ \frac{J_{11} \phi x_3^*}{x_1^*} & \frac{J_{11} \phi x_3^*}{x_2^*} & x_3^* \end{bmatrix} \quad (\text{A.3})$$

where

$$J_{11}^* = \frac{(\beta-1)[\gamma\rho - \delta\sigma(1-\beta+\gamma)]}{\beta[\gamma - \sigma(1-\beta+\gamma)]}; \quad (\text{A.4})$$

and



$$Tr(J^*) = 3\lambda_1 - J_{11}^* - J_{22}^* - J_{33}^* = \frac{\delta(2\beta - \gamma)}{\beta} x_2^*; \quad (A.5)$$

$$Det(J^*) = J_{11}^* x_2^* x_3^* \frac{\delta(\gamma - \sigma(1 - \beta + \gamma))}{\sigma(\beta - 1)}; \quad (A.6)$$

$$B(J^*) = J_{11}^* x_3^* + \frac{\delta^2(\beta - \gamma)}{\beta} x_2^{*2} \quad (A.7)$$

## 8 Appendix B.

### The Shilnikov type homoclinic orbit in an analitic style.

To apply the Shilnikov theorem to the system (A.1), we have to prove that the system has a homoclinic Shilnikov orbit at the equilibrium point  $P^*$ . If the parameters lie in the following subsets:

$$\Omega_3^A = \left\{ \rho \in (\delta, -\psi), \sigma \in (0.1, \rho/\psi), \gamma \in \left( \frac{(1-\beta)(\rho-\delta)}{\delta}, \tilde{\gamma} \right) \right\}$$

where  $\tilde{\gamma}$  is the Hopf bifurcation value found in Mattana and Venturi1999 (MV) then the singular equilibrium point  $P^* \in \Omega_3^A$  is a hyperbolic saddle focus.

In other words, the eigenvalues of (A.3) the Jacobian matrix of the system (A.1) evaluated in  $P^*$  are of the form  $\lambda_1 = r$  and  $\lambda_{2/3} = -p \pm iq$ : a saddle focus, with  $r > 0, p > 0, q \neq 0$  and  $r > p > 0$ .

We remember that a homoclinic orbit joining the **equilibrium point**  $P^*$  of system (A.1) is **doubly asymptotic** with respect to time  $t$  along the solution manifold.

We translate the system in the origin and we put the system (A.1) in normal form and we get:

$$\begin{aligned} \dot{w}_1 &= r w_1 + F_{1a} w_1 w_2 + F_{1b} w_1 w_3 + F_{1c} w_2 w_3 + F_{1d} w_1^2 + F_{1e} w_2^2 + F_{1f} w_3^2; \\ \dot{w}_2 &= p w_2 - q w_3 + F_{2a} w_1 w_2 + F_{2b} w_1 w_3 + F_{2c} w_2 w_3 + F_{2d} w_1^2 + F_{2e} w_2^2 + F_{2f} w_3^2 \\ \dot{w}_3 &= q w_2 + p w_3 + F_{3a} w_1 w_2 + F_{3b} w_1 w_3 + F_{3c} w_2 w_3 + F_{3d} w_1^2 + F_{3e} w_2^2 + F_{3f} w_3^2 \end{aligned} \quad (B.1)$$

where

$$q = \sqrt[2]{B\tilde{J}}.$$

We compute the stable and unstable manifolds of the saddle focus equilibrium point to construct the Shilnikov type homoclinic orbit in an analitic style. So let's begin with the **analitic expression** of the **one-dimensional unstable manifold** associated with **the real eigenvalue**  $r$  where  $a_m, b_m, c_m$  are undetermined coefficients such that

$$\begin{aligned} w_1(t) &= a_0 + \sum_{k=1}^{\infty} a_k e^{k\lambda t}, \quad (B.2) \\ w_2(t) &= b_0 + \sum_{k=1}^{\infty} b_k e^{k\lambda t}, \\ w_3(t) &= c_0 + \sum_{k=1}^{\infty} c_k e^{k\lambda t} \end{aligned}$$



$$\begin{aligned}
 w_1(t) &= a_0 + a_1 e^{\lambda t} + a_2 e^{2\lambda t} + a_3 e^{3\lambda t} + a_4 e^{4\lambda t} \dots \\
 w_2(t) &= b_0 + b_1 e^{\lambda t} + b_2 e^{2\lambda t} + b_3 e^{3\lambda t} + b_4 e^{4\lambda t} \dots \\
 w_3(t) &= c_0 + c_1 e^{\lambda t} + c_2 e^{2\lambda t} + c_3 e^{3\lambda t} + c_4 e^{4\lambda t} \dots \\
 \begin{bmatrix} a_0 \\ b_0 \\ c_0 \end{bmatrix} &= \begin{bmatrix} w_1^* \\ w_2^* \\ w_3^* \end{bmatrix} = \begin{bmatrix} 0 \\ 0 \\ 0 \end{bmatrix}; \quad I = \begin{bmatrix} 1 & 0 & 0 \\ 0 & 1 & 0 \\ 0 & 0 & 1 \end{bmatrix} \quad (B.3)
 \end{aligned}$$

The Jacobian of the system (B.1) evaluated in unique steady state  $W^*(w_1^*, w_2^*, w_3^*) = (0, 0, 0)$ , the origin, is given by

$$A(w^*) = \begin{pmatrix} r & 0 & 0 \\ 0 & p & -q \\ 0 & q & p \end{pmatrix}, (B.4)$$

$$\text{Det}A(w^*) = r(p^2 + q^2).$$

For  $k=1$  substituting (B.2) in the system.(A.1) and matching the coefficients

of  $e^{k\lambda t}$  on both side of the resultant equations, we get  $(\lambda I - A(W^*)) \begin{bmatrix} a_1 \\ b_1 \\ c_1 \end{bmatrix} =$

$$\begin{pmatrix} \lambda - r & 0 & 0 \\ 0 & \lambda - p & -q \\ 0 & q & \lambda - p \end{pmatrix} \begin{pmatrix} a_1 \\ b_1 \\ c_1 \end{pmatrix} = \begin{pmatrix} -a_1(r - \lambda) \\ -qc_1 - b_1(p - \lambda) \\ qb_1 - c_1(p - \lambda) \end{pmatrix} =$$

Let be  $\lambda = r$  the real eigenvalues, we known that:

$$\det(\lambda I - A(W^*)) = 0$$

so:

$$\begin{aligned}
 &\begin{pmatrix} -a_1(r - r) \\ -qc_1 - b_1(p - r) \\ qb_1 - c_1(p - r) \end{pmatrix} = 0 \\
 &-a_1(r - r) = 0 \\
 &-qc_1 - b_1(p - r) = 0 \implies a_1 \neq 0, b_1 = 0, c_1 = 0 \\
 &qb_1 - c_1(p - r) = 0
 \end{aligned}$$

$$\begin{bmatrix} a_1 \\ b_1 \\ c_1 \end{bmatrix} = \begin{bmatrix} \xi \\ 0 \\ 0 \end{bmatrix}$$

and  $a_1 = \xi$  can be expressed with an arbitrary parameter as  $\xi$ .

For  $k=2$  substituting (B.2) in the system.(A.1) and matching the coefficients of  $e^{k\lambda t}$  on both side of the resultant equations, we get

$$\begin{pmatrix} 2\lambda - r & 0 & 0 \\ 0 & 2\lambda - (-p) & -q \\ 0 & q & 2\lambda - (-p) \end{pmatrix} \begin{bmatrix} a_2 \\ b_2 \\ c_2 \end{bmatrix} = \begin{pmatrix} F_1 \\ F_2 \\ F_3 \end{pmatrix}$$

$$\begin{aligned}
 \begin{bmatrix} a_2 \\ b_2 \\ c_2 \end{bmatrix} &= \begin{pmatrix} \frac{1}{r} & 0 & 0 \\ 0 & \frac{p+2r}{p^2+4pr+q^2+4r^2} & \frac{q}{p^2+4pr+q^2+4r^2} \\ 0 & -\frac{q}{p^2+4pr+q^2+4r^2} & \frac{p+2r}{p^2+4pr+q^2+4r^2} \end{pmatrix} \begin{pmatrix} F_{1d}a_1^2 \\ F_{2d}a_1^2 \\ F_{3d}a_1^2 \end{pmatrix} = \\
 &= \begin{pmatrix} \frac{1}{r}a_1^2 F_d \\ a_1^2 F_{2d} \frac{p+2r}{p^2+4pr+q^2+4r^2} + qa_1^2 \frac{F_{3d}}{p^2+4pr+q^2+4r^2} \\ a_1^2 F_{3d} \frac{p+2r}{p^2+4pr+q^2+4r^2} - qa_1^2 \frac{F_{2d}}{p^2+4pr+q^2+4r^2} \end{pmatrix} = \begin{pmatrix} \frac{1}{r}a_1^2 F_d \\ a_1^2 \frac{F_{3d}}{4pr+p^2+q^2+4r^2} q + a_1^2 \frac{F_{2d}(p+2r)}{4pr+p^2+q^2+4r^2} \\ -qa_1^2 \frac{F_{2d}}{4pr+p^2+q^2+4r^2} + a_1^2 (p+2r) \frac{F_{3d}}{4pr+p^2+q^2+4r^2} \end{pmatrix}
 \end{aligned}$$



=

$$\begin{bmatrix} a_2 \\ b_2 \\ c_2 \end{bmatrix} = \begin{pmatrix} \frac{F_{1d}a_1^2}{r} \\ \frac{(F_{2d}(2r+p)+F_{3d}q)a_1^2}{[(2r+p)^2+q^2]} \\ -\frac{(F_{2d}q^2+(2r+p)^2F_{3d})a_1^2}{[(2r+p)^2+q^2]} \end{pmatrix}$$

For  $k=3$  substituting (B.2) in the system.(A.1) and matching the coefficients of  $e^{krt}$  on both side of the resultant equations, we get:

$$\begin{bmatrix} a_3 \\ b_3 \\ c_3 \end{bmatrix} = \begin{pmatrix} \frac{1}{3r-r} & 0 & 0 \\ 0 & \frac{3r+p}{[(3r+p)^2+q^2]} & \frac{q}{[(3r+p)^2+q^2]} \\ 0 & -\frac{q}{[(3r+p)^2+q^2]} & -\frac{p+3r}{[(3r+p)^2+q^2]} \end{pmatrix} \begin{pmatrix} F_{1d}a_2^2 \\ F_{2d}a_2^2 \\ F_{3d}a_2^2 \end{pmatrix}$$

$$\begin{bmatrix} a_3 \\ b_3 \\ c_3 \end{bmatrix} = \begin{pmatrix} \frac{F_{1d}a_2^2}{2r} \\ \frac{(F_{2d}q+(3r+p)F_{3d})a_2^2}{[(3r+p)^2+q^2]} \\ -\frac{(F_{2d}q+(3r+p)F_{3d})a_2^2}{[(3r+p)^2+q^2]} \end{pmatrix} =$$

$$\begin{bmatrix} a_3 \\ b_3 \\ c_3 \end{bmatrix} = \begin{pmatrix} \frac{F_{1d}}{2r} \left( \frac{F_{1d}a_1^2}{r} \right)^2 \\ \frac{(F_{2d}q+(3r+p)F_{3d})}{[(3r+p)^2+q^2]} \left( \frac{(F_{2d}q+(2r+p)F_{3d})a_1^2}{[(2r+p)^2+q^2]} \right)^2 \\ -\frac{(F_{2d}q+(3r+p)F_{3d})}{[(3r+p)^2+q^2]} \left( -\frac{(F_{2d}q+(2r+p)F_{3d})a_1^2}{[(2r+p)^2+q^2]} \right)^2 \end{pmatrix}$$

$$\begin{bmatrix} a_3 \\ b_3 \\ c_3 \end{bmatrix} = \begin{pmatrix} \frac{F_{1d}^3}{2r^3} a_1^4 \\ \frac{(F_{2d}q+(3r+p)F_{3d})}{[(3r+p)^2+q^2]} \left( \frac{(F_{2d}q+(2r+p)F_{3d})}{[(2r+p)^2+q^2]} \right)^2 a_1^4 \\ -\frac{(F_{2d}q+(3r+p)F_{3d})}{[(3r+p)^2+q^2]} \left( -\frac{(F_{2d}q+(2r+p)F_{3d})}{[(2r+p)^2+q^2]} \right)^2 a_1^4 \end{pmatrix}$$

For  $k=4$  substituting (B.2) in the system.(A.1) and matching the coefficients of  $e^{krt}$  on both side of the resultant equations, we get:

$$\begin{bmatrix} a_4 \\ b_4 \\ c_4 \end{bmatrix} = \begin{pmatrix} -\frac{1}{r-4r} & 0 & 0 \\ 0 & \frac{4r+p}{[(4r+p)^2+q^2]} & \frac{q}{[(4r+p)^2+q^2]} \\ 0 & -\frac{q}{[(4r+p)^2+q^2]} & -\frac{4r-p}{[(4r+p)^2+q^2]} \end{pmatrix} \begin{pmatrix} F_{1d}a_3^2 \\ F_{2d}a_3^2 \\ F_{3d}a_3^2 \end{pmatrix}$$

$$\begin{bmatrix} a_4 \\ b_4 \\ c_4 \end{bmatrix} = \begin{pmatrix} \frac{F_{1d}a_3^2}{3r} \\ \frac{(F_{2d}q+(4r+p)F_{3d})a_3^2}{[(4r+p)^2+q^2]} \\ -\frac{(F_{2d}q+(4r+p)F_{3d})a_3^2}{[(4r+p)^2+q^2]} \end{pmatrix}$$

$$\begin{bmatrix} a_4 \\ b_4 \\ c_4 \end{bmatrix} = \begin{pmatrix} \frac{F_{1d}}{3r} \left( \frac{F_{1d}^3}{2r^3} \right)^2 (a_1)^8 \\ \frac{(F_{2d}q+(4r+p)F_{3d})}{[(4r+p)^2+q^2]} \left\{ \left[ \frac{(F_{2d}q+(3r+p)F_{3d})}{[(3r+p)^2+q^2]} \right] \left( \frac{(F_{2d}q+(2r+p)F_{3d})}{[(2r+p)^2+q^2]} \right)^2 \right\}^2 (a_1)^8 \\ -\frac{(F_{2d}q+(4r+p)F_{3d})}{[(4r+p)^2+q^2]} \left\{ \left[ \frac{(F_{2d}q+(3r+p)F_{3d})}{[(3r+p)^2+q^2]} \right]^2 \right\} (a_1)^8 \end{pmatrix}$$

We evaluate the analytic expression of the **two-dimensional stable manifold** associated with the complex eigenvalues  $-p \pm iq$  where  $a_m . b_m . c_m .$  are undetermined coefficients such that

Let  $k=1$  be and  $\lambda = -p + iq$  the complex eigenvalues, we known that:

$$\det(\lambda I - A(W^*)) = 0$$

so:



$$\begin{pmatrix} -p + iq - r & 0 & 0 \\ 0 & -p + iq + p & -q \\ 0 & q & -p + iq + p \end{pmatrix} \begin{bmatrix} a_1 \\ b_1 \\ c_1 \end{bmatrix} = 0,$$

We get the following homogenous system:

$$\begin{aligned} -a_1(-p + iq - r) &= 0 \\ -b_1(-p + iq + p) - qc_1 &= 0 \implies a_1 = 0, b_1 = -\varsigma + i\eta, c_1 = -\eta + i\varsigma \\ qb_1 - c_1(-p + iq + p) &= 0 \end{aligned}$$

$$\begin{bmatrix} a_1 \\ b_1 \\ c_1 \end{bmatrix} = \begin{bmatrix} a_1 \\ b_1 \\ c_1 \end{bmatrix} = \begin{bmatrix} 0 \\ -\varsigma + i\eta \\ -\eta + i\varsigma \end{bmatrix}$$

$$\begin{aligned} \begin{bmatrix} a_2 \\ b_2 \\ c_2 \end{bmatrix} &= \\ &= \begin{pmatrix} \frac{1}{2(-p+iq)-r} & 0 & 0 \\ 0 & \frac{(2(-p+iq)+p)}{[(2(-p+iq)+p)^2+q^2]} & \frac{q}{[(2(-p+iq)+p)^2+q^2]} \\ 0 & -\frac{q}{[(2(-p+iq)+p)^2+q^2]} & \frac{(2(-p+iq)+p)}{[(2(-p+iq)+p)^2+q^2]} \end{pmatrix} \begin{pmatrix} F_{1c}b_1c_1 + F_{1e}b_1^2 + F_{1f}c_1^2 \\ F_{2c}b_1c_1 + F_{2e}b_1^2 + F_{2f}c_1^2 \\ F_{3c}b_1c_1 + F_{3e}b_1^2 + F_{3f}c_1^2 \end{pmatrix} \end{aligned}$$

$$\begin{bmatrix} a_2 \\ b_2 \\ c_2 \end{bmatrix} = \begin{pmatrix} \frac{F_{1c}b_1c_1 + F_{1e}b_1^2 + F_{1f}c_1^2}{2(-p+iq)-r} \\ \frac{(2(-p+iq)+p)(F_{2c}b_1c_1 + F_{2e}b_1^2 + F_{2f}c_1^2) + (F_{3c}b_1c_1 + F_{3e}b_1^2 + F_{3f}c_1^2)q}{[(2(-p+iq)+p)^2+q^2]} \\ -\frac{q(F_{3c}b_1c_1 + F_{3e}b_1^2 + F_{3f}c_1^2) + (2(-p+iq)+p)(F_{2c}b_1c_1 + F_{2e}b_1^2 + F_{2f}c_1^2)}{[(2(-p+iq)+p)^2+q^2]} \end{pmatrix}.$$





## Influence of densimetric Froude number on sharp-edged orifice jets

Luigi A. Besalduch, Maria G. Badas, Simone Ferrari & Giorgio Querzoli

DICAAR (Dipartimento di Ingegneria Civile, Ambientale e Architettura),  
University of Cagliari, Italy  
E-mail: [besalduch@unica.it](mailto:besalduch@unica.it)

**Abstract:** We have performed an experimental study on the influence of the densimetric Froude number on the statistics of the velocity fields of jets issuing from a round, sharp-edged orifice, by means of a novel technique, namely Feature Tracking Velocimetry (FTV). The velocity and turbulent kinetic energy profiles orthogonal to the jet axis, the mean streamwise centreline velocity decay, and the integral turbulent kinetic energy along the jet axis have been measured and analyzed.

**Keywords:** simple jet, negatively buoyant jet, velocity measurement, turbulence.

### 1. Introduction

The mixing properties of simple jets have been extensively investigated in the last decades: on most of the experimental set-ups, a free jet issuing from a long pipe or a convergent nozzle was employed. As a matter of fact, Deo et al. (2007) [2] states that there are very few studies using a plane jet issuing from a sharp-edged orifice-plate, perhaps due to its initial and near-field flow structure being far more complex (e.g. the existence of a vena contracta). Quinn & Militzer (1988) [12] experimentally and numerically studied a turbulent air jet from a sharp-edged square slot, measuring the mean velocity along the centerline, the turbulent normal and shear stresses (by means of hot-wire anemometry) and the mean static pressure (by means of a pitot-static tube) and found a pronounced mean streamwise velocity off-center peaks in the very near field. Afterwards, Quinn (1989) [13] experimentally compared jets of air issuing from a sharp-edged elliptical and round slot and from a contoured nozzle, finding that sharp-edged slot jets have higher mean streamwise velocity decay rates than contoured nozzle jets, implying higher entrainment and better mixing. Mi et al. (2001) [9] compared mixing performances of three types of nozzle, namely a smooth contraction nozzle, a long pipe and a sharp-edged orifice, with jets of air with Reynolds number  $Re = 16,000$ , finding that the last one provides the greatest rate of mixing. In spite of this performance, they underlined that investigations on circular jets issuing from orifice plates are very limited, possibly because the initial velocity profile and the near-field flow structure are more complex, and that, consequently, further investigations were needed to quantify the link between the higher mixing rate of the orifice jet and the enhanced three-dimensionality of the initial underlying structure in round jets from sharp-edged orifice. A better mixing in a sharp-edged orifice (round and elliptical) jet rather than in a jet from contoured nozzle was found also by Quinn (2006 [14] and 2007 [15]), in his experimental investigation via hot-wire anemometry on jets of



air at  $Re \cong 180,000$ . Mi et al. (2007) [10] measured planar velocity using Particle Image Velocimetry (PIV) on a turbulent air jet ( $Re = 72,000$ ) issuing from a round sharp-edged orifice plate, focusing their efforts on the coherent structures that develop in the near field. Hence, many authors indicate that the sharp-edged orifice is the most effective exit configuration for improving mixing however, those studies were performed at very high  $Re$  in order to have unambiguous asymptotic conditions. Indeed, only few studies can be found in literature regarding low  $Re$  and/or focusing on the regime of transition to turbulence. Russ and Strykowski (1993) [16] investigated the turbulent structure in the near field of heated jets from a round nozzle as the exit conditions changed from laminar to turbulent. Malmström et al. (1997) [7] measured the streamwise velocity profiles of low-velocity jets from round nozzles of different diameters to examine the dependence of the diffusion of the jet on the outlet conditions.

All the quoted investigations were performed on simple jets, i.e. the phenomenon that develops when a fluid is released into an ambient fluid with the same density. When a fluid heavier than the ambient fluid is released upward (or, vice versa, when a lighter one is released downward), a so-called Negatively Buoyant Jet (NBj) develops. There are many practical applications involving NBjs: among the others, the discharges into the sea of brine from desalination plants (e.g. Lai & Lee 2012 [5]), the improvement of water quality by forced mixing in reservoirs, small lakes and harbors (e.g. McClimans & Eidnes 2000 [8]), the forced heating or cooling of large structures such as aircraft hangars, buildings or rooms (e.g. Baines et al. 1989 [1]), etc; see Ferrari & Querzoli (2010) [3] for a detailed list.

As, to the best of authors knowledge, the only study on NBjs from a sharp-edged orifice is Ferrari & Querzoli (2010) [3], we present here an experimental investigation on the influence of the densimetric Froude number (the most relevant non-dimensional parameter for NBjs, see chapter 2) on the statistics of velocity fields of sharp-edged orifice jets, by means of a novel non-intrusive image analysis technique, namely Feature Tracking Velocimetry (FTV).

## 2. Characteristic non-dimensional parameters

In a negatively buoyant jet the flow is driven from two sources, one of momentum and one of buoyancy: the first region of the jet is driven mostly by the momentum (so it behaves similarly to a simple jet released with the same angle); far from the outlet, there is a second region where the buoyancy acts to bend the axis down (so the jet behaves similarly to a plume) (List, 1979 [6]). The most relevant non-dimensional parameter for the classification of buoyant jets is the densimetric Froude number,  $Fr$ :

$$Fr = \frac{U_0}{\sqrt{g \frac{\rho_{DISC} - \rho_{REC}}{\rho_{REC}} D}}$$



where  $U_0$  is the mean initial jet velocity,  $g$  the gravitational acceleration,  $\rho_{\text{DISC}}$  the discharged fluid density,  $\rho_{\text{REC}}$  the receiving fluid density and  $D$  the outlet diameter.  $Fr$  has low values for heavy jets and it grows as buoyancy decreases, up to an infinite value for simple jets.

The other relevant non-dimensional parameters controlling the behavior of inclined negatively buoyant jets are the Reynolds number,  $Re = U_0 D / \nu$  ( $\nu$  is the kinematic viscosity of the discharged fluid), and the angle to the horizontal,  $\theta$ : as this last parameter controls the misalignment between the flux of buoyancy and the initial flux of momentum, a negatively buoyant jet is axisymmetric only as far as  $\theta$  is  $90^\circ$ .

### 3. Methods and materials

The experimental setup simulates a standard configuration of sea discharge, i.e. a portion of a pipe laid down the sea bottom, with orifices on its lateral wall employed as diffusers. The experiments were carried out in a 30 cm wide, 21 m long flume with glass walls, filled with water, where a solution of water, sodium-sulphate (to increase the density of the solution) and pine pollen particles (for the visualization of the jet) was released; the jet middle vertical section was lighted by a light sheet generated by a laser with a cylindrical lens. The pine pollen particles were employed to perform experiments with a non-intrusive image analysis technique, FTV (Feature Tracking Velocimetry) technique (see below). The release was in still water, to simulate a stagnant receiving body. The discharged solution came, through a pipe, from a constant head tank, supplied by a closed hydraulic circuit, to a cylindrical vessel with an orifice on its lateral wall. The experiments were performed with a constant flow rate (and high enough to have  $Re = 1500$ , larger than its critical value for the apparatus),  $Fr = 14 \div 37.2$ ,  $\theta = 65^\circ$ . A simple jet ( $Re = 1500$ ) was experimentally simulated as well for comparison.

Velocity fields were obtained, from each couple of images, using a novel algorithm, namely Feature Tracking Velocimetry (FTV), which is less sensitive to the appearance and disappearance of particles, and to high velocity gradients than classical Particle Image Velocimetry (PIV). PIV algorithms obtain fields comparing windows of successive frame on a regular grid in all the image and maximizing the correlation of the light intensity function to obtain their displacement. The idea of FTV is to compare windows only where the motion detection may be successful, that is where there are high luminosity gradients. The FTV algorithm is suitable in presence of different seeding density, for example between the jet and the external fluid, where other techniques produce significant errors, due to the non-homogeneous seeding at the boundary. The procedure of analysis consist of:

- identification of the features using the Harris corner detection (a corner is a region with high luminosity gradients along the x and y direction) (Harris & Stephens, 1988 [4]);
- ordering of the features according to their cornerness (the value of the Harris formula), and choice of the best features;

- comparison of the windows centered in the image “ $i^{\text{th}}$ ” with windows around the position of the initial feature in the image “ $i+1^{\text{th}}$ ”;
- measure of the velocity as the displacement minimizing the dissimilarity, computed using the Lorentzian estimator;
- validation of the samples with an algorithm based on a Gaussian filtering of first neighbors (define by the Delaunay triangulation).

The statistics of velocity fields are subsequently obtained, by time averaging, under the hypothesis of ergodicity.

#### 4. Results

In order to better show the different behavior of upper and lower NBJ boundaries, in Figure 1 profiles of velocity, orthogonal to the jet axis and non-dimensionalised by the axial velocity,  $U_c$ , for a jet with  $Fr = 15$  and  $\theta = 65^\circ$  and for a simple jet with the same  $Re = 1500$ . The plot shows how velocity NBJ profiles become more and more asymmetric for larger  $s/D$ . For small distances from the origin ( $s/D = 3$ ), the velocity distribution is symmetric; vice versa, going further along the axis ( $s/D = 30, 40$ ), the velocity profiles lose the symmetry and the lower region tends to widen more than the upper region. Actually, for a NBJ, at the upper boundary the buoyancy acts in the opposite direction to the momentum, allowing the full development of the Kelvin Helmholtz waves, whilst at the lower boundary the buoyancy and momentum act in the same direction, limiting the widening of the profiles.

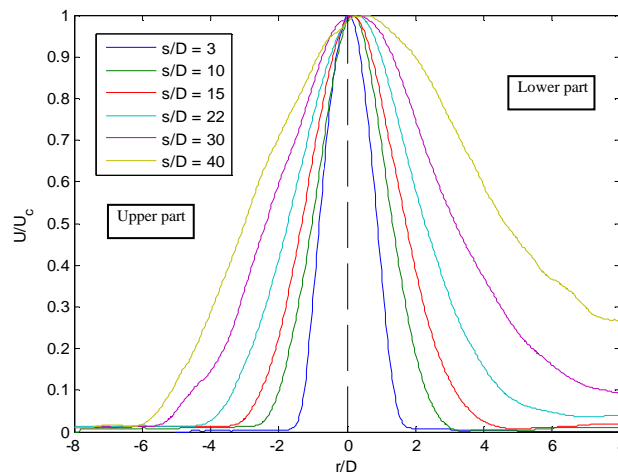


Figure 1. Profiles of velocity, orthogonal to the jet axis and non-dimensionalised by the axial velocity  $U_c$ : for a jet with  $Fr = 15$  and  $\theta = 65^\circ$ ;  $Re = 1500$ ;  $r/D$  is the orthogonal distance from the axis,  $s/D$  is the distance, along the axis, from the origin of the jet.

In Figure 2 we show the widening of a NBJ with  $Fr = 15$ ,  $\theta = 65^\circ$  and  $Re = 1500$  (coloured asterisks) and of the SJs of Quinn 2006 [14] (black rhombi for SJs issuing from a contoured nozzle, black stars for SJs issuing from a sharp-edged

orifice). It can be noted that both the NBJ upper and lower boundary grow faster than SJ boundaries. Moreover, it is confirmed that the lower part of NBJs widens more rapidly than the upper one.

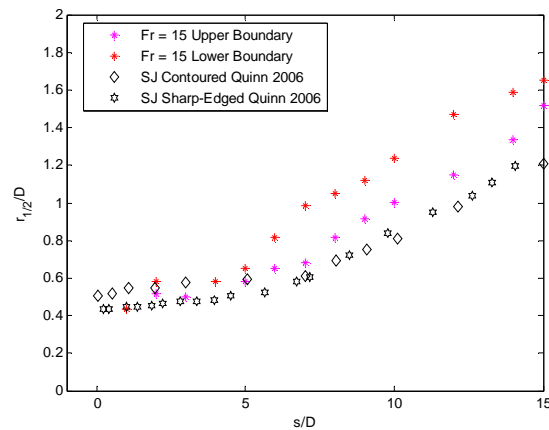


Figure 2. Widening of a NBJ with  $Fr = 15$ ,  $\theta = 65^\circ$  and  $Re = 1500$  (coloured asterisks) and of the SJs of Quinn 2006 [14] (black symbols).

In Figure 3a the Turbulent Kinetic Energy (TKE) field for a NBJ is shown. To highlight the mentioned asymmetry, in Figure 3b the profiles of TKE, orthogonal to the jet axis and non-dimensionalised with  $TKE_C$  (i.e. the axial value on the profile), are presented: there are two peaks at the jet boundaries, with different values, the highest at the upper boundary, the lowest at the lower boundary (with less intense velocity fluctuations due to buoyancy and momentum acting in the same direction). As  $s/D$  increases, the two peaks tend to become less pronounced (but always asymmetric) to finally merge into a single peak.

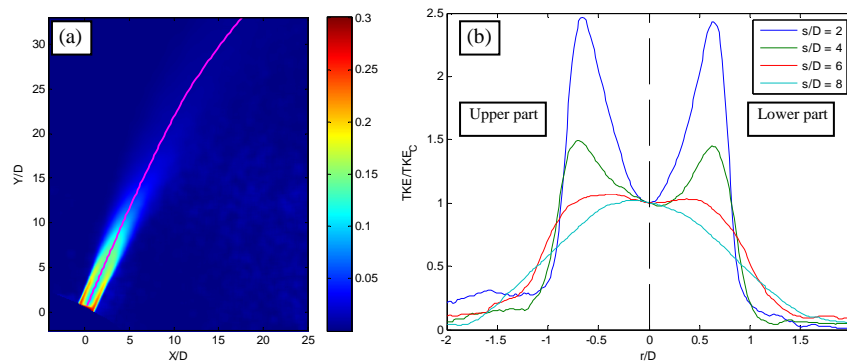


Figure 3. For a jet with  $Fr = 25$ ,  $Re = 1500$ ,  $\theta = 65^\circ$ : (a) map of the non-dimensional mean turbulent kinetic energy (TKE), non-dimensionalised with  $U_{max}^2$ , the pink line represents the jet axis (defined as the locus of maximum velocity),  $U_{max}$  is the maximum velocity value; (b) TKE/ $TKE_C$  profiles,

orthogonal to the jet axis;  $TKE_C$  is the axial value on the profile,  $r/D$  is the orthogonal distance from the axis,  $s/D$  is the distance, along the axis, from the origin of the jet.

In Figure 4, the mean streamwise centerline velocity decay is shown, for four NBJs (with different  $Fr$ ) and for the simple jet data by Quinn 2006 [14], issuing from a sharp-edged and a contoured orifice. The NBJ values have a similar trend to the sharp-edged orifice ones, starting with values larger than one due to the vena contracta effect. A dependence on  $Fr$  is not apparent on this parameter.

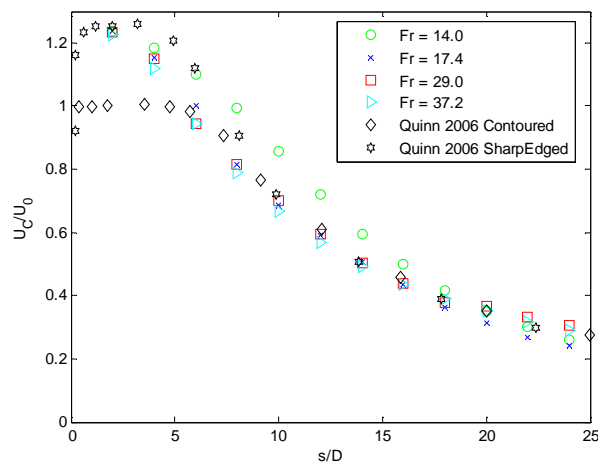


Figure 4. Mean streamwise centreline velocity decay  $U_C/U_0$ : for a jet with  $\theta = 65^\circ$ ,  $Re = 1500$  and different  $Fr$  (coloured symbols) and simple jets (Quinn 2006 [14], sharp-edged orifice, black stars, and contoured orifice, black rhombi);  $U_0$  is the mean initial jet velocity.

In Figure 5, the mean velocity profiles  $U/U_{C/2}$  are plotted versus  $r/r_{1/2}$  for four NBJs (with different  $Fr$ ) and for the simple jet experimental data by Mi 2007 [10] and for the simple jet theoretical law by Pope 2000 [11];  $r_{1/2}$  is the jet's half width, defined as the  $r$  where the velocity assumes the value of  $U_{C/2} = U_C / 2$ . This normalization tends to highlight the Gaussianity of a particular data distribution, that is, in this case, the Gaussianity of the velocity profiles. The equation of Pope is valid far from the jet origin, where the velocity profiles become self-similar:

$$\frac{U}{U_{C/2}} = \frac{1}{(1 + \alpha \eta^2)^2}, \quad \eta = \frac{r}{(s - s_0)}$$

where  $s_0$  is the virtual origin of the jet, and  $\alpha$  is a constant ( $\alpha \cong 47$ ). The NBJ values near the nozzle ( $s/D = 4$ ) follow closely the data of Mi at the same distance, showing that at a short distance from the origin the NBJs still

behave like a SJ. This is particularly true close to the jet axis whilst the tails tend to behave in a different way, possibly due to the different initial conditions: as a matter of fact, the NBJs presented here are released from a sharp-edged orifice (causing a vena-contracta effect with a sudden contraction followed by a sudden expansion) whilst the SJs of Mi issue at the end of a pipe.

Contrary to the profiles close to the origin, as the distance increases ( $s/D = 16$  and  $28$ ), the NBJ data do not follow anymore the SJ data, meaning that the NBJ velocity profiles are no more Gaussian. In particular, it is apparent how this non-Gaussianity tends to increase according to the distance from the origin. Moreover, as already shown by Figure 1 and 2, as  $s/D$  increases, the NBJ tends to be less symmetric.

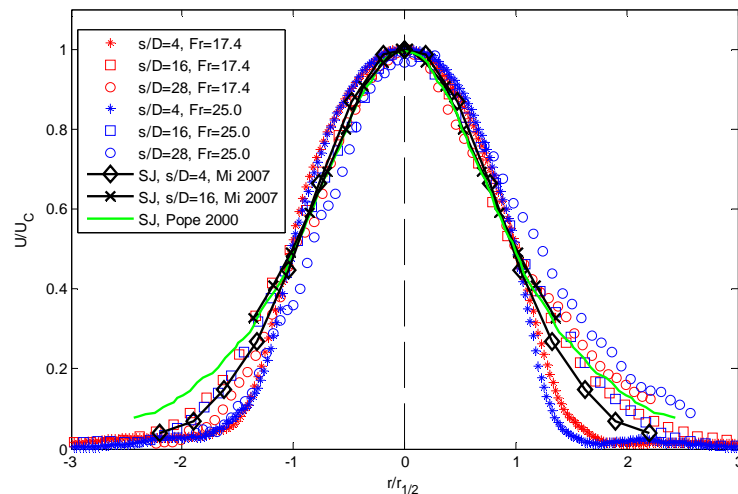


Figure 5. Mean velocity profiles  $U/U_{C/2}$ , for a jet with  $\theta = 65^\circ$ ,  $Re = 1500$  and different  $Fr$  (coloured symbols), and for simple jets (Mi 2007 [10] black lines and Pope 2000 [11] green line);  $r_{1/2}$  is the jet's half width,  $U_{C/2} = U_C / 2$ .

In Figure 6, the integral Turbulent Kinetic Energy  $TKE_{int}/U_{max}^2$  along the axis is plotted for different  $Fr$  and for a simple jet ( $Fr = \infty$ );  $U_{max}$  is the maximum velocity value and the integral is computed on profile orthogonal to the jet axis. The influence of  $Fr$  on this parameter is evident: NBJ values start always lower than simple jet ones, with an increasing distance with decreasing  $Fr$  (i.e., for an increasing buoyancy), to eventually collapse on the simple jet values as the distance from the origin increases. Moreover, the distance where the NBJ data collapse with the simple jet ones tends to increase as  $Fr$  decreases; this is justified because as  $Fr$  decreases, the buoyancy increases determining a reduction of the turbulent fluctuations.

From the analysis of the data here presented, a clear dependence of sharp-edged orifice jets on  $Fr$  arises only on the second order statistics of the velocity.

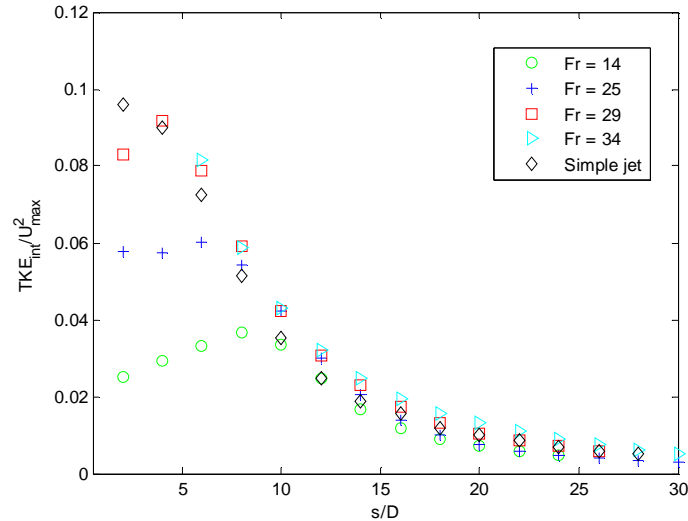


Figure 6. Integral Turbulent Kinetic Energy  $TKE_{int}/U_{max}^2$  along the jet axis, for a jet with  $\theta = 65^\circ$ ,  $Re = 1500$  and different  $Fr$  (coloured symbols), and for a simple jet (black rhombi);  $U_{max}$  is the maximum velocity value.

## 5. Conclusions

The behaviour of Negatively Buoyant Jets, released from a sharp-edged orifice, was investigated using an original non-intrusive image analysis technique to measure the velocity fields, namely Feature Tracking Velocimetry, in order to study their dependence on the densimetric Froude number. First and second order statistics of the velocity fields (velocity and turbulent kinetic energy profiles orthogonal to the jet axis, mean streamwise centreline velocity decay, and integral turbulent kinetic energy along the jet axis) were used to characterize the Negatively Buoyant Jet behaviour and their difference from simple jets. From the analysis of these data, a dependence of sharp-edged orifice jets on densimetric Froude number is evident only on the second order statistics of the velocity.

## References

1. Baines, W.D., Turner, J.S. & Campbell, I.H. Turbulent fountains in an open chamber. *Journal of Fluid Mechanics*, 212, 557-592, 1990.
2. Deo, R.C., Mi, J. & Nathan, G.J. The influence of nozzle-exit geometric profile on statistical properties of a turbulent plane jet. *Experimental Thermal and Fluid Science*, 32 (2), 545-559, 2007.
3. Ferrari, S. & Querzoli, G. Mixing and re-entrainment in a negatively buoyant jet. *Journal of Hydraulic Research*, 48(5), 632-640, 2010.
4. Harris, C. & Stephens, M. A combined corner and edge detector. In: *Proceedings of the 4<sup>th</sup> Aivey Vision Conference*, Manchester, 147-151, 1988.



5. Lai, C.C.K. & Lee, J.H.W. Mixing in inclined dense jets in stationary ambient. *Journal of Hydro-environment Research*, 6, 9-28, 2012.
6. List, E.J. Turbulent jets and plumes. In: Fisher, H.B., List, E.J., Koh, R.C.Y., Imberger, J. & Brooks, N.H. (Eds). *Mixing in inland and coastal water*, New York, USA, Academic Press, 315-389, 1979.
7. Malmström, T. G., Kirkpatrick, A. T., Christensen, B. & Knappmiller, K. D. Centreline velocity decay measurements in low-velocity axisymmetric jets. *Journal of Fluid Mechanics*, 246, 363-377, 1997.
8. McClimans, T. & Eidnes, G. Forcing nutrients to the upper layer of a fjord by a buoyant plume. *Proceedings of the 5<sup>th</sup> International Symposium on Stratified Flows*, Vancouver, 199-204, 2000.
9. Mi, J., Nathan, G.J. & Nobes, D.S. Mixing characteristics of axisymmetric free jets from a countered nozzle, an orifice plate and a pipe. *Journal of Fluids Engineering*, 123, 878-883, 2001.
10. Mi, J., Kalt, P., Nathan, G.J. & Wong, C.Y. PIV measurements of a turbulent jet issuing from round sharp-edged plate. *Experiments in Fluids*, 42, 625-637, 2007.
11. Pope, S.B. *Turbulent flows*. Cambridge University Press, 771 p, 2000.
12. Quinn, W. R. & Militzer, J. Experimental and numerical study on a turbulent free square jet. *Physics of Fluids*, 31(5), 1017-1025, 1988.
13. Quinn, W.R. On mixing in an elliptic turbulent jet. *Physics of Fluids A*, 1(10), 1716-1722, 1989.
14. Quinn, W.R. Upstream nozzle shaping effects on near field flow in round turbulent free jets. *European Journal of Mechanics B/Fluids*, 25, 279-301, 2006.
15. Quinn, W.R.. Experimental study of the near field and transition region of a free jet issuing from a sharp-edged elliptic orifice plate. *European Journal of Mechanics B/Fluids*, 26, 583-614, 2007.
16. Russ, S. & Strykowski, P. J. Turbulent structure and entrainment in heated jets: the effect of initial conditions. *Physics of Fluids A*, 5(12), 3216-3225, 1993.





# Dynamic Instabilities in Population Growth Models I: Bernoulli Randomized Modified Fibonacci Model

Maria de Fátima Brilhante<sup>1,4</sup>, Maria Ivette Gomes<sup>2,4</sup>, and Dinis Pestana<sup>3,4</sup>

<sup>1</sup> Universidade dos Açores, Ponta Delgada, Açores, Portugal  
(E-mail: [fbrilhante@uac.pt](mailto:fbrilhante@uac.pt) )

<sup>2</sup> Universidade de Lisboa, Faculdade de Ciências, DEIO, Portugal, and  
Instituto de Investigação Científica Bento da Rocha Cabral, Lisboa, Portugal  
(E-mail: [ivette.gomes@fc.ul.pt](mailto:ivette.gomes@fc.ul.pt))

<sup>3</sup> Universidade de Lisboa, Faculdade de Ciências, DEIO, Portugal, and  
Instituto de Investigação Científica Bento da Rocha Cabral, Lisboa, Portugal  
(E-mail: [dinis.pestana@fc.ul.pt](mailto:dinis.pestana@fc.ul.pt))

<sup>4</sup> CEAUL — Centro de Estatística e Aplicações da Universidade de Lisboa,  
Portugal

**Abstract.** Although Fibonacci's numbers play an important role in modeling phenomena in a wide variety of subjects, their use as descriptors of population growth has clearly been rather restricted after the introduction of the Verhulst logistic model and its numerous modifications and extensions. In fact, in the very unrealistic Fibonacci model neither population extinction nor bounded growth are possible, only quasi-exponential unbounded population growth can result. We present a modified model assuming that the number of direct offsprings of each ancestor is a Bernoulli random variable, hence with positive probability of 0 count, and thus accommodating both extinction and possible sustainable growth. We compare algebraic and numerical treatment of equations using the fixed point method in the framework of instabilities of numerical algorithms for finding roots of equations.

**Keywords:** Fibonacci model, Verhulst model, Bernoulli offsprings, branching processes, fixed point algorithm instabilities.

## 1 Introduction

Let  $N(t)$  denote the size of some population at time  $t$ . Two main issues in population dynamics deal with the probability of extinction and with the total size of the progeny of an ancestor.

Fibonacci modeled unrealistic unbounded growth, and in its scope population extinction is impossible. However, Fibonacci's numbers are still a very active research area, since they (mainly the initial numbers of the sequence) can approximate quite well counts in many natural systems, and have been applied successfully in very diverse situations and areas, namely aesthetic (the golden ratio is pervasive in all form of plastic arts, and is even used by aesthetic surgeons in beauty improvement), including for instance Lindenmayer grammars, cf. Prusinkiewicz and Hanan [11], used by Pestana [10] for an initial investigation of music composition with repetitive structures.



### 1.1 Fibonacci population growth model

Fibonacci (c. 1170 – c. 1250) in his *Liber Abaci* posed and solved a problem involving the growth of a population of rabbits based on idealized and very unrealistic assumptions. The solution, generation by generation, was a sequence of numbers  $\{F_n\}_{n \geq 0}$  later known as Fibonacci numbers, starting with  $\{0, 1\}$ , such that  $F_{n+2} = F_n + F_{n+1}$ . Using Binet’s formula

$$F_n = \frac{(1 + \sqrt{5})^n - (1 - \sqrt{5})^n}{2^n \sqrt{5}}$$

the computation of any member of the Fibonacci sequence is straightforward.

Although the wide success of Fibonacci’s sequence as an approximate model for the first few generations is still praised in many branches of Biology, the very unrealistic assumption that any couple of rabbits gives birth to exactly one couple of rabbits as offsprings, and this in each of exactly two successive mating periods, cannot accommodate important real features in population dynamics, such as sustainable growth or even population extinction, as studied successfully for instance by Lotka [8] using the more realistic sustainable growth logistic model introduced by Verhulst. In fact, rewriting  $F_{n+2} = F_n + F_{n+1} = 2F_{n+1} - F_{n-1} \implies F_{n+2} - F_{n+1} = F_{n+1} - F_{n-1}$ , the closely associated differential equation  $\frac{d}{dt} N(t) = \frac{\partial^2}{\partial t^2} N(t)$  shows that Fibonacci’s growth is approximately exponential. Indeed, we get an approximate geometric growth with ratio  $\frac{1+\sqrt{5}}{2}$ . Even for moderate values such as  $n = 11$ , say,  $F_{12} = 144 \approx F_{11} \frac{1+\sqrt{5}}{2} = 144.005$  (recall that  $\frac{1+\sqrt{5}}{2}$  is the “golden ratio” limit of  $\frac{F_{n+1}}{F_n}$ ).

### 1.2 Verhulst sustainable growth logistic model and extensions

Imposing some natural regularity conditions on  $N(t)$ , namely that  $\frac{d}{dt} N(t) = \sum_{k=0}^{\infty} A_k [N(t)]^k$ , Verhulst ([16], [17], [18]) used the second order approximation  $\frac{d}{dt} N(t) = A_1 N(t) + A_2 [N(t)]^2$ , with  $A_1 > 0$  and  $A_2 < 0$ , which can be rewritten as

$$\frac{d}{dt} N(t) = r N(t) \left[ 1 - \frac{N(t)}{K} \right], \quad (1)$$

(where  $r > 0$  is frequently interpreted as a Malthusian instantaneous growth rate parameter, whenever modeling natural breeding populations, and  $K > 0$  as the equilibrium limit size of the population) to develop a broadly successful “logistic” population growth model, much more realistic to model sustainable growth. In fact, an initial period of exponential growth if followed by moderate approximately linear growth, with exponential steep exponential moderation when limitation of natural resources (or success of predators or competing species) ultimately curb down growth to sustainable values.

Moreover, and since in many species there exist periodic mating periods, using Euler’s ideas on the interplay of differential equations and difference equations in numerical methods, the associated difference equation

$$x_{n+1} = \alpha x_n (1 - x_n), \quad (2)$$



(where it is convenient to deal with the assumption  $x_n \in [0, 1]$ ,  $n = 1, 2, \dots$ ) made his way in modeling population dynamics.

The equilibrium  $x_{n+1} = x_n$  leads to a simple second order algebraic equation with positive root  $1 - 1/\alpha$ , and to a certain extent it is surprising that anyone would care to investigate its numerical solution using the fixed point method, which indeed brings in many pathologies when a steep curve — i.e., for some values of the iterates  $|\alpha(1 - 2x_n)| > 1$  — is approximated by an horizontal straight line. This numerical investigation, apparently devoid of interest, has however been at the root of many theoretical advances when  $\alpha \notin [1, 3]$  (namely Feigenbaum bifurcations and ultimate chaotic behavior), and *a posteriori* led to many interesting breakthroughs in the understanding of population dynamics. Due to its close association with the differential equation (1), whose solution is a logistic function

$$N(t) = \frac{K N_0}{N_0 + (K - N_0) e^{-rt}},$$

the parabola  $x(1 - x)$  appearing in the discretization (2) is very often called the “logistic parabola”.

Up to a multiplicative constant, the logistic parabola is the *Beta(2, 2)* probability density function. In Aleixo *et al.* [1], and in Rocha *et al.* [12] several extensions of population growth models tied to more general *Beta(p, q)* densities have been investigated, and in Pestana *et al.* [9] the factor  $1 - x$  has been considered the linear truncation of  $-\ln x$ , so obtaining differential functions whose solution exhibits Paretian tail behaviour and ultimately extreme value models (*Gumbel*, *Fréchet* or *Weibull*) solutions for the associated differential equation  $\frac{d}{dt} N(t) = r N(t) (-\ln(N(t)))^{1+\gamma}$ . Tsoularis [15] and Waliszewski and Konarski [19] must be credited for the *Gompertz* (or *Gumbel*) solution when in the associated differential equation  $\gamma = 0$ . Tsoularis [15] is a very informative state-of-the-art on population growth models. Brilhante *et al.* ([2], [3]) provide the connection between the solution of the above extensions of the original Verhulst equation to extreme value and Rachev and Resnick [13] geo-extreme value (i.e., when the original sequence is subject to Rényi’s [14] rarefaction, equivalent in its final results to Kovalenko’s [6] and Kozubowski’s [7] geometric thinning).

### 1.3 Modified Fibonacci models

We shall discuss, using branching processes, several modifications of the Fibonacci model, so that more realistic possibilities, such as limited growth or even extinction, may occur:

1. A framework very similar to the original description posed by Fibonacci: each ancestor can produce direct offsprings only in the first two consecutive reproducing periods. However, instead of deterministically producing exactly one offspring in each reproducing epoch, the number of offsprings is a random  $X \sim \text{Bernoulli}(p)$ .



2. A simple modification, which has the advantage of affordable algebraic treatment, is to consider that the progeny (it is indifferent whether we count individuals in the case of non-sexual reproduction, or couples in the case of sexual reproduction) is a random  $Y \sim Geometric(p)$ . The hypothesis that in sexual reproduction we consider that the progeny is solely of couples, and that each of those behaves as a faithful couple, is indeed as unrealistic as what has been taken for granted as an assumption in the original Fibonacci model. But the wider variability of the number of offsprings of each ancestor at each reproducing period, with sensible choices so that the mean value  $\mathbb{E}(Y) = (1 - p)/p$  is rather small, can produce more realistic results. Observe, further, that while the Bernoulli random variable is underdispersed, i.e.  $Var(X)/\mathbb{E}(X) < 1$ , the Geometric random variable is overdispersed. So, it can accommodate more realistic wider variability.
3. An almost similar framework as the one described in item 1 is investigated explicitly assuming removing each progenitor from the system after two reproduction periods, using randomly stopped sums.

Aside from presenting models allowing for extinction and limited growth, and hence more realistic than the unlimited quasi-exponential growth of the original Fibonacci model, our aim is to compare whenever possible algebraic solutions to numerical solutions using the fixed point method. These indeed exhibit instabilities whenever the function is too steep in a neighborhood of the root we wish to calculate.

Although those instabilities are qualitatively quite different from the celebrated Feigenbaum bifurcations and ultimate chaos that the discretization of the Verhulst model brought to the limelights of the structural investigation of dynamical systems, it seems worthwhile to discuss them, since the philosophical controversy whether pathologies observed in the numerical solution of equations  $x = f(x)$  using the fixed point algorithm are an essential feature or solely an inherent consequence of instabilities to be expected when  $|f'(x)| > 1$  in the vicinity of the equation root is far from being settled.

In this first paper, we shall discuss in depth the Bernoulli randomized model described in item 1, postponing for a second part other randomizations.

## 2 Modified Randomized Fibonacci Models: Bernoulli( $p$ ) Offsprings in Each Reproduction Epoch

Let us assume that the process starts with one ancestor (single or couple, according to the reproduction characteristics of the species). In each of the two initial reproduction epochs each unit produces  $X \sim Bernoulli(p)$  offsprings, and is removed from the process after the the second reproduction epoch. On the other hand, each offspring becomes an ancestor in the next step, behaving exactly in the some fashion.

Let  $Z_1$  denote the number of units in the system in the first step of the process, i.e. exactly when the initial ancestor is removed from the system:

$$Z_1 = \begin{cases} 0 & 1 & 2 & 3 \\ (1 - p)^2 & p(1 - p)(2 - p) & 2p^2(1 - p) & p^3 \end{cases} \quad (3)$$



The probability generating function is

$$\mathcal{G}_{Z_1}(t) = (1 - p)^2 + p(1 - p)(2 - p)t + 2p^2(1 - p)t^2 + p^3t^3, \quad (4)$$

and hence the mean value, expressed as a function of  $p$ , is

$$\mathbb{E}(Z_1) = p(1 - p)(2 - p) + 4p^2(1 - p) + 3p^3, \quad (5)$$

which is greater than 1 for  $p \in (\sqrt{2} - 1, 1] \approx (0.414214, 1]$ .

If  $\mathbb{E}(Z_1) < 1$ , extinction is almost sure.

If  $\mathbb{E}(Z_1) > 1$ , defining iteratively  $x_n = \mathcal{G}_{Z_1}(x_{n-1})$ , with initial value  $x_1 = \mathbb{P}[Z_1 = 0] = (1 - p)^2$ ,  $x_n$  is the probability that the process terminates at or before the  $n$ -th generation, cf. Feller [4], Theorem p. 297.

The sequence  $\{x_n\}$  is increasing, its limit  $x \leq 1$  being the solution of the equation

$$x = \mathcal{G}_{Z_1}(x)$$

In the model at hand, the probability of extinction is therefore

$$x \equiv x_p = \min \left\{ 1, \frac{(p - 2)p^2 + \sqrt{p^3(4 - 4p + p^3)}}{2p^3} \right\}, \quad (6)$$

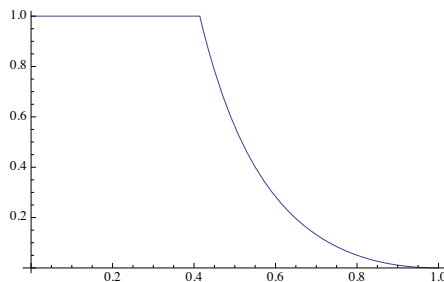


**Fig. 1.** Extinction probability  $x_p$ , in (6), as a function of  $p$  in the Bernoulli( $p$ ) offsprings randomized Fibonacci model.

On the other hand, the total number of descendants from the initial ancestor up to the  $n$ -th generation is  $Y_n = 1 + Z_1 + Z_2 + \dots + Z_n$ , where  $Z_k$  denotes the number of units in the  $k$ -th generation. Following Good [5] (an argument that inspired Feller [4], XII.5),  $R_1(t) = t\mathcal{G}(t)$  and iteratively  $R_n(t) = tR_{n-1}(t)$ , we obtain the probability generating functions for the successive generations.

This is a decreasing sequence, whose limit  $\rho(s)$  satisfies  $\rho(s) = s\mathcal{G}(\rho(s))$  and which may be found solving  $t = s\mathcal{G}(t)$ . Each coefficient  $r_k$  in the MacLaurin's expansion of  $\rho(s)$  is the probability that the total progeny consists of  $k$  elements, and therefore if  $\sum r_k = \rho(1) < 1$ , this is the probability of extinction.

The total progeny is finite whenever the expected value  $\mu = \mathbb{E}(Z_1) < 1$ . Therefore, as  $\mathbb{E}(Z_n) = \mu^n$ , it follows that the expected value of the total progeny is  $\sum_{n=0}^{\infty} \mu^n = \frac{1}{1-\mu}$ .



In this randomized Bernoulli Fibonacci modified model, from solving  $t = s\mathcal{G}(t)$  we get

$$\rho(s) = \frac{2(-p^2s + p^3s)}{3p^3s} - \frac{(1 - i\sqrt{3})A(s)}{32^{2/3} p^3s \left( (B(s) + \sqrt{4A^3(s) + B^2(s)})^{1/3} - \frac{(1 + i\sqrt{3})}{62^{1/3} p^3s} \left( (B(s) + \sqrt{4A^3(s) + B^2(s)})^{1/3} \right) \right)} \quad (7)$$

where  $A(s) = -3p^3s + (2p^4 - p^5 - p^6)s^2$ , and  $B(s) = 18(1 - p)p^5s^2 + (7p^6 - 12p^7 + 3p^8 + 2p^9)s^3$ .

Plotting the the real part of the above function  $\rho(s)$ , in (7), for  $s = 1$ , which indeed coincides with (6), we obtain a visual grasp of the probability of extinction as a function of  $p$ , exactly the one given in Fig. 1, using now a more complex definition of the function to be plotted.

Observe that the equilibrium point  $p = \rho(p)$  is 0.513376. The observation that this is approximately the proportion of male offsprings in the observed equilibrium of human reproduction is surely circumstantial, or at least we do not devise any bond tying that empirical observation.

On the other hand,  $\mu < 1$  for  $p < \sqrt{2} - 1 \approx 0.414214$ . Below, in Table 1 we register for a few values of  $p$  the expected size of the total progeny:

$p$	$\mu$	Expected size $\frac{1}{1-\mu}$
0.1	0.21	1.26582
0.2	0.44	1.78571
0.3	0.69	3.22581
0.4	0.96	25
.41421	0.99999...	99246.7

**Table 1.** Expected total progeny when  $\mu < 1$  in the modified Bernoulli randomized Fibonacci model.

### 3 Discussion and Conclusions

We now compare this analytic solution with the numerical results defining iteratively  $x_n = \mathcal{G}_{Z_1}(x_{n-1})$ , the probability that extinction does occur at or before the  $n$ -th generation, with initial value  $x_1 = \mathbb{P}[Z_1 = 0] = (1 - p)^2$ .

The successive repeated compositions of a function with itself can be computed using for instance the command “Nest” in *Mathematica*, and the corresponding evaluation at the appropriate point can then generate a list of coordinates with the command “Flatten”.

In Table 2 we illustrate the result for the choices 0.1(0.1)0.9, and also for the extreme choices 0.01 and 0.99, and finally for the equilibrium value 0.513376 (using 200 points and 300 iterated compositions of the function with itself.

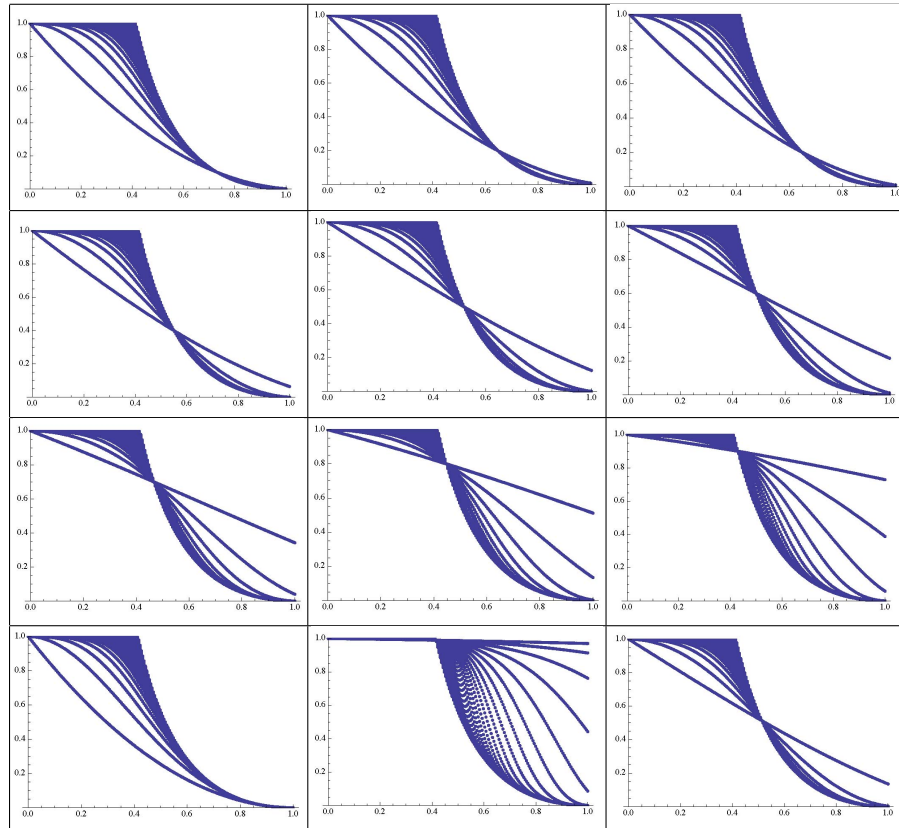


**Table 2.** Graphical representation of 300 compositions of the generating function with itself; from left to right and top to bottom, initial 0.1, 0.2, 0.3, 0.4, 0.5, 0.6, 0.7, 0.8, 0.9, 0.01, 0.99, 0.513376.

From those graphics it is obvious that the use of the fixed point method leads to instabilities, that seem quite different in nature from the Feigenbaum bifurcations encountered in the discretization of the Verhulst model and its various extensions we have mentioned. Further research is needed to interpret those pathologies in the context of dynamical models.

## References

1. Aleixo, S., Rocha, J.L., and Pestana, D., Probabilistic Methods in Dynamical Analysis: Population Growths Associated to Models Beta  $(p,q)$  with Allee Effect, in Peixoto, M. M; Pinto, A.A.; Rand, D.A.J., editors, *Dynamics, Games and Science, in Honour of Maurício Peixoto and David Rand*, vol II, Ch. 5, pages 79–95, New York, 2011, Springer Verlag.
2. Brilhante, M.F., Gomes, M.I., and Pestana, D., BetaBoop Brings in Chaos. *Chaotic Modeling and Simulation*, 1: 39–50, 2011.



3. Brillhante, M.F., Gomes, M.I., and Pestana, D., Extensions of Verhulst Model in Population Dynamics and Extremes, in Ch. Skiadas (eds) Proceedings, 5th Chaotic Modeling and Simulation International Conference, 115–122, 2012.
4. Feller, W., *An Introduction to Probability Theory and Its Applications*, vol. I, New York, 1968, Wiley.
5. Good, I.J., The number of individuals in a cascade process, *Proc. Cambridge Philos. Soc.* **45**, 360–363, 1949.
6. Kovalenko, I.N., On a class of limit distributions for rarefied flows of homogeneous events, *Lit. Mat. Sbornik* **5**, 569–573, 1965. (Translation: On the class of limit distributions for thinning streams of homogeneous events, *Selected Transl. Math. Statist. and Prob.* **9**, 75–81, 1971, Providence, Rhode Island.)
7. Kozubowski, T.J., Representation and properties of geometric stable laws, *Approximation, Probability, and Related Fields*, New York, 321–337, 1994, Plenum.
8. Lotka, A.J., *Elements of Physical Biology*, Baltimore, 1925, Williams and Wilkins Co (reprinted under the title *Elements of Mathematical Biology*, New York, 1956, Dover).
9. Pestana, D., Aleixo, S., and Rocha, J.L., Regular variation, paretian distributions, and the interplay of light and heavy tails in the fractality of asymptotic models. In C. H. Skiadas, I. Dimotikalis and C. Skiadas, editors, *Chaos Theory: Modeling, Simulation and Applications*, pages 309–316, Singapore 2011. World Scientific.
10. Pestana, P., Lindenmayer Systems and the Harmony of Fractals, *Chaotic Modeling and Simulation (CMSIM)* 1: 91–99, 2012.
11. Prusinkiewicz, P., and Hanan, J., *Lindenmayer Systems, Fractals, and Plants* (Lecture Notes in Biomathematics). Springer-Verlag, 1989.
12. Rocha, J.L., Aleixo, S., and Pestana, D., Beta(p,q)-Cantor Sets: Determinism and Randomness. In C.H. Skiadas, I. Dimotikalis and C. Skiadas (Eds.), *Chaos Theory: Modeling, Simulation and Applications*, World Scientific Books, 333–340, 2011.
13. Rachev, S.T., and Resnick, S., Max-geometric infinite divisibility and stability, *Communications in Statistics — Stochastic Models*, 7:191–218, 1991.
14. Rényi, A., A characterization of the Poisson process, *MTA Mat. Kut. Int. Kzl.* **1**, 519–527, 1956. (English translation in *Selected Papers of Alfred Rényi*, **1**, 1948–1956, P. Turán, editors, 622–279 Akadémiai Kiadó, Budapest).
15. Tsoularis, A., Analysis of logistic growth models. *Res. Lett. Inf. Math. Sci.*, vol. 2:23–46, 2001.
16. Verhulst, P.-F., Notice sur la loi que la population poursuit dans son accroissement. *Corresp. Math. Physics* 10:113–121, 1838. (easily available in [http://books.google.pt/books?id=8GsEAAAAYAAJ&printsec=frontcover&hl=pt-PT&source=gbs\\_ge\\_summary\\_r&cad=0#v=onepage&q&f=false](http://books.google.pt/books?id=8GsEAAAAYAAJ&printsec=frontcover&hl=pt-PT&source=gbs_ge_summary_r&cad=0#v=onepage&q&f=false))
17. Verhulst, P.-F., La loi de l'accroissement de la population, *Nouveaux Mémoires de l'Académie Royale des Sciences et Belles-Lettres de Bruxelles*, 18:1–42, 1845. (available at <http://gdz.sub.uni-goettingen.de/dms/load/img/>.)
18. Verhulst, P.-F., Deuxième mémoire sur la loi d'accroissement de la population. *Mémoires de l'Académie Royale des Sciences, des Lettres et des Beaux-Arts de Belgique* 20:1–32, 1847. (<http://gdz.sub.uni-goettingen.de/dms/load/img/>)
19. Waliszewski, J., and Konarski, J., A Mystery of the Gompertz Function, in G.A. Losa, D. Merlini, T. F. Nonnenmacher and E.R. Weibel, editors, *Fractals in Biology and Medicine*, Basel, 277–286, 2005, Birkhäuser.

**FCT** This research has been supported by National Funds through FCT — Fundação para a Ciência e a Tecnologia, project PEst-OE/MAT/UI0006/2011, and EXTREMA, PTDC/MAT/101736/2008.



## Extensions of the Verhulst Model, Order Statistics and Products of Independent Uniform Random Variables

Maria de Fátima Brilhante<sup>1</sup>, Maria Ivette Gomes<sup>2</sup>, and Dinis Pestana<sup>3</sup>

<sup>1</sup> Universidade dos Açores, DM, and CEAUL — Centro de Estatística e Aplicações da Universidade de Lisboa, Ponta Delgada, Portugal

(E-mail: [fbrilhante@uac.pt](mailto:fbrilhante@uac.pt) )

<sup>2</sup> Universidade de Lisboa, Faculdade de Ciências, DEIO, and CEAUL — Centro de Estatística e Aplicações da Universidade de Lisboa; and Instituto de Investigação Científica Bento da Rocha Cabral, Lisboa, Portugal

(E-mail: [ivette.gomes@fc.ul.pt](mailto:ivette.gomes@fc.ul.pt))

<sup>3</sup> Universidade de Lisboa, Faculdade de Ciências, DEIO, and CEAUL — Centro de Estatística e Aplicações da Universidade de Lisboa; and Instituto de Investigação Científica Bento da Rocha Cabral, Lisboa, Portugal

(E-mail: [dinis.pestana@fc.ul.pt](mailto:dinis.pestana@fc.ul.pt))

**Abstract.** Several extensions of the Verhulst sustainable population growth model exhibit different interesting characteristics more appropriate to deal with less controlled population dynamics. As the logistic parabola  $x(1-x)$  arising in the Verhulst differential equation is closely related to the Beta(2,2) probability density, and the retroaction factor  $1-x$  is the linear truncation of MacLaurin series of  $-\ln x$  (the growth factor  $x$  is the linear truncation of  $-\ln(1-x)$ ), in previous papers the authors introduced a more general four parameter family of probability density functions, of which the classical Beta densities are special cases. Using differential equations extending the original Verhulst, they have been able to identify combinations of parameters that lead to extreme value models, either for maxima or for minima, and also remarked that the traditional logistic model is a (geometric) extreme value model arising from geometric thinning of the original sequence. The observation that in the support  $(0,1)$  the logistic parabola  $x(1-x)$  is, up to a multiplicative factor, the product of the densities of minimum and maximum of two standard independent uniform random variables (and also the median of three independent standard uniforms), and that on the other hand  $(-\ln x)^{n-1}$  is, up to the multiplicative factor  $1/\Gamma(n)$ , the density of the product of  $n$  independent uniforms, we reexamine the ties of products and of order statistics of independent uniforms to dynamical properties of populations arising in these extensions of the Verhulst model.

**Keywords:** Extended Verhulst models, instabilities in population dynamics, products and order statistics of uniform random variables.

### 1 Extensions of the Verhulst Model

Extensions of the classical Verhulst differential equation for modeling population dynamics

$$\frac{dN(t)}{dt} = rN(t)(1 - N(t)), \quad (1)$$



where  $N(t)$  denotes the size of the population at time  $t$  and  $r > 0$  is the malthusian reproduction rate, have recently been considered.

From the fact that the logistic parabola  $x(1-x)$  arising from equation (1) is, in the support  $(0, 1)$ , closely tied to the Beta(2,2) probability density function (pdf)<sup>1</sup>, natural extensions of equation (1) using more general beta densities have been investigated by Aleixo *et al.* [1] and Pestana *et al.* [5], namely by considering the differential equation

$$\frac{dN(t)}{dt} = r(N(t))^{p-1}(1 - N(t))^{q-1}. \quad (2)$$

The normalized solution of equation (1) belongs to the family of logistic functions, which is connected to extreme value models, more precisely to max-geo-stable laws, and occurring in randomly stopped extremes schemes with geometric subordinator. On the other hand, Aleixo *et al.* [1] showed that the normalized solution of equation (2) also belongs to the class of max-geo-stable laws if  $p = 2 - \alpha$  and  $q = 2 + \alpha$  (the classical Verhulst model being the special case  $\alpha = 0$ ).

By noticing that the retroaction factor  $1 - x$  in the logistic parabola is the linear truncation of MacLaurin series of  $-\ln x$ , and that the growth factor  $x$  is the linear truncation of MacLaurin series of  $-\ln(1 - x)$ , Brillhante *et al.* [2] introduced a general four parameter family of densities, named the BeTaBoOp family, which was used to further extend equation (2) in Brillhante *et al.* [2] and [4].

**Definition.** A random variable  $X$  is said to have a BeTaBoOp( $p, q, P, Q$ ) distribution,  $p, q, P, Q > 0$ , if its pdf is

$$f(x) = kx^{p-1}(1-x)^{q-1}(-\ln(1-x))^{P-1}(-\ln x)^{Q-1}I_{(0,1)}(x), \quad (3)$$

where  $k^{-1} = \int_0^1 t^{p-1}(1-t)^{q-1}(-\ln(1-t))^{P-1}(-\ln t)^{Q-1}dt$  (Hölder's inequality guarantees that  $k^{-1} < \infty$ ).

Note that the Beta( $p, q$ ) density is the BeTaBoOp( $p, q, 1, 1$ ) density and if  $q = P = 1$ , the Betinha( $p, Q$ ) density introduced by Brillhante *et al.* [3] is obtained, where  $k = \frac{p^Q}{\Gamma(Q)}$  and  $\Gamma(\alpha) = \int_0^1 t^{\alpha-1}e^{-t}dt$  is the gamma function.

Hence, for a general discussion of growth models, it seems interesting to investigate the general differential equation

$$\frac{dN(t)}{dt} = r(N(t))^{p-1}(1 - N(t))^{q-1}[-\ln(1 - N(t))]^{P-1}(-\ln N(t))^{Q-1}, \quad (4)$$

specially for the case when some of the parameters take the value 1.

Exact solutions for equation (4) exist for some special combinations of the parameters, and when solving the corresponding difference equation

$$x_{t+1} = c(x_t)^{p-1}(1 - x_t)^{q-1}(-\ln(1 - x_t))^{P-1}(-\ln x_t)^{Q-1}$$

<sup>1</sup> A random variable  $X$  is said to have a Beta( $p, q$ ) distribution,  $p, q > 0$ , if its pdf is  $f(x) = \frac{x^{p-1}(1-x)^{q-1}}{B(p,q)}I_{(0,1)}(x)$ , where  $B(p, q) = \int_0^1 t^{p-1}(1-t)^{q-1}dt$  is the Beta function.



by the fixed point method, bifurcation and chaos are observed (see Brillhante *et al.* [2] and [4]).

## 2 Understanding population dynamics through order statistics and products of powers of uniform random variables

In section 1 we saw that the Verhulst differential equation and extensions are linked to BeTaBoOp densities. Using the fact that these densities can be expressed as functions of densities of order statistics and/or products of independent standard uniform random variables, we reexamine in this section the dynamical properties of populations described by the Verhulst model and extensions.

Let  $U_1, \dots, U_n$  be independent and identically distributed (iid) standard uniform random variables, and let  $U_n^{(*)}$  denote their product, whose pdf is

$$f_{U_n^{(*)}}(u) = \frac{(-\ln u)^{n-1}}{\Gamma(n)} I_{(0,1)}(u). \quad (5)$$

The pdf (5) is easily derived by simply noting that  $U_n^{(*)} = \exp(-V)$ , with  $V = -\sum_{i=1}^n \ln U_i = -\ln(\prod_{i=1}^n U_i) \sim \text{Gamma}(n, 1)$ . More generally,  $U_n^{\delta^{(*)}} = (\prod_{i=1}^n U_i)^\delta = \prod_{i=1}^n U_i^\delta$ ,  $\delta > 0$ , has pdf

$$f_{U_n^{\delta^{(*)}}}(u) = \frac{u^{1/\delta-1} (-\ln u)^{n-1}}{\delta^n \Gamma(n)} I_{(0,1)}(u)$$

and distribution function

$$F_{U_n^{\delta^{(*)}}}(u) = \frac{\Gamma(n, -\ln u/\delta)}{\Gamma(n)} = u^{1/\delta} \sum_{k=0}^{n-1} \frac{(-\ln u)^k}{\delta^k k!}, \quad u \in (0, 1).$$

On the other hand, let  $U_{k:n}$  denote the  $k$ -th ascending order statistic,  $k = 1, \dots, n$ , whose pdf is

$$f_{U_{k:n}}(u) = \frac{u^{k-1} (1-u)^{n-k}}{B(k, n+1-k)} I_{(0,1)}(u),$$

i.e.  $U_{k:n} \sim \text{Beta}(k, n+1-k)$ . In particular, the minimum  $U_{1:n}$  has pdf  $f_{U_{1:n}}(u) = n(1-u)^{n-1} I_{(0,1)}(u)$ , and the maximum  $U_{n:n}$  pdf  $f_{U_{n:n}}(u) = nu^{n-1} I_{(0,1)}(u)$ .

For the special case  $n = 2$ , it is obvious that  $U_1 U_2 = U_{1:2} U_{2:2} \preceq U_{1:2} \preceq U_{2:2}$ , and a similar result holds true for all  $n \in \mathbb{N}$ ,  $n > 2$ .

Thus, when  $p, q, P, Q \in \mathbb{N}$ , the pdf of the BeTaBoOp( $p, q, P, Q$ ) random variable is, up to a multiplicative factor, the product of the densities of the maximum  $U_{p:p}$  of  $p$  independent standard uniforms, of the minimum  $U_{1:q}$  of  $q$  independent standard uniform random variables, of the product  $U_P^{(*)}$  of  $P$



independent standard uniform random variables, and of  $1 - U_Q^{(*)}$ . Observe also that in the long-standing established jargon of population dynamics, the  $x^{p-1}$  and  $(-\ln(1-x))^{P-1}$  are growing factors, and  $(1-x)^{q-1}$  and  $(-\ln x)^{Q-1}$  are retroaction factors, curbing down population growth. In view of the above remarks on the connection to ascending order statistics and products of independent standard uniform random variables, we shall say that  $(-\ln x)^{\nu-1}$  is a lighter retroaction factor than  $(1-x)^{\nu-1}$ , and that  $(-\ln(1-x))^{\mu-1}$  is a heavier growth factor than  $x^{\mu-1}$ .

In view of the facts above, it is expectable that the normalized solution of the differential equation linked to the Betinha(2,2)  $\equiv$  BeTaBoOp(2,1,1,2) density, which can be obtained by replacing in (1) the retroaction factor  $1 - N(t)$  by the lighter one  $-\ln N(t)$ , will correspond to less sustainable growth.

In fact, the solution of that differential equation is the Gompertz function, that up to a multiplicative factor is the extreme value Gumbel distribution. Note that while the logistic distribution is a stable limit law for suitably linearly modified maxima of geometrically thinned sequences of iid random variables in its domain of attraction is known to be appropriate to model sustainable growth, the Gumbel distribution arises as stable limit law of suitably normalized maxima of all the random variables in its domain of attraction<sup>2</sup>, and therefore stochastically dominates the logistic solution, and is a suitable model for uncontrolled growth, such as the one observed for cells of cancer tumors.

More generally, Brillhante *et al.* [2] have shown that the normalized solution of the differential equation tied to the more general BeTaBoOp(2, 1, 1, 2 +  $\alpha$ ) density, i.e.

$$\frac{dN(t)}{dt} = rN(t)(-\ln N(t))^{1+\alpha}, \quad (6)$$

belongs to the class of extreme value laws for maxima, more precisely Gumbel if  $\alpha = 0$ , Fréchet if  $\alpha > 0$  and Weibull for maxima if  $\alpha < 0$ . Therefore, equation (6) reveals to be more appropriate than (1) to deal with less controlled population dynamics.

On the other hand, if the growth factor  $N(t)$  in (1) is replaced by  $[-\ln(1 - N(t))]^{1+\alpha}$ , we get a differential equation linked to the BeTaBoOp(1, 2, 2 +  $\alpha$ , 1) density, whose normalized solution now belongs to the class of extreme value laws for minima. Using the fact that if  $X \sim \text{BeTaBoOp}(p, q, P, Q)$ ,  $1 - X \sim \text{BeTaBoOp}(q, p, Q, P)$ , simplifies the investigations concerning the structural properties of the BeTaBoOp family, namely those related to products of uniform random variables.

Therefore, equations (1), (2) and (6) can be viewed as special cases of the more general differential equation (4) for modeling population dynamics, which embodies simultaneously two different growth patterns depicted in the growing terms  $(N(t))^{p-1}$  and  $[-\ln(1 - N(t))]^{P-1}$ , and two different environmental resources control of the growth behavior, depicted in the retroaction terms  $(1 - N(t))^{q-1}$  and  $(-\ln N(t))^{Q-1}$ .

<sup>2</sup> Note that Rachev and Resnick [6] established a connection between extreme stable laws and geometrically thinned extreme value laws, which implies, in particular, that when they have the same index — 0 in case of the Gumbel and of the logistic stable limits — they share the same domain of attraction.



We obtained explicit solutions for (4), using Mathematica, for a few special combinations of parameters, but so far only the ones connected with some form of stability and of extreme value models — either in the iid setting or in the geometrically thinned setting — seem to be suitable to characterize growth. In the sequel we shall comment on growth characteristics, in general, in terms of the order relation among parameters, and specially when all the parameters are integers.

### 3 Further comments for the special case of integer parameters

The Verhulst model is usually associated with the idea of sustainable growth. This is the case since the retroaction term  $1 - N(t)$  slows down the growth impetus  $rN(t)$ , an equilibrium often interpreted as sustainability. Another way of looking at this is to notice that the logistic parabola  $x(1 - x)$  tied to the Verhulst model is, up to a multiplicative factor, the product of the densities of the order statistics  $U_{2:2}$  and  $U_{1:2}$  — respectively, maximum and minimum of two independent standard uniform random variables. Therefore, the growth term ruled by  $U_{2:2}$  has an “equal” opposite effect exerted by the retroaction term ruled by  $U_{1:2}$ , which is curbing down the population growth to sustainable levels. On the other hand, we also have that the logistic parabola is proportional to the density of  $U_{2:3}$ , i.e. the median of three independent standard uniform random variables, thus reinforcing the idea of equilibrium.

We now amplify the above remarks to other interesting cases of the generalized Verhulst growth theory:

1. The logistic parabola generalization  $x^{p-1}(1 - x)^{q-1}$ , linked to the BeTaBoOp( $p, q, 1, 1$ )  $\equiv$  Beta( $p, q$ ) density, is:

- Proportional to the product of the densities of  $U_{p:p}$  and  $U_{1:q}$ :

Since  $U_{1:q} \preceq U_{p:p}$ , for all  $p, q \in \mathbb{N}$ , and  $U_{p:p}$  is associated with the growth term  $x^{p-1}$ , population growth is observed. However, if  $p = q$ , the retroaction term ruled by  $U_{1:p}$  will curb down the population growth to sustainable levels, since  $U_{1:p}$  and  $U_{p:p}$  are equally distant order statistics from the extremes, in the sense that they are of the type  $U_{k:n}$  and  $U_{n-k+1:n}$ . Therefore, when  $p = q$ , we may think that  $U_{1:p}$  and  $U_{p:p}$  are exerting equal opposite effects, and thus ensuring a sustainable growth. On the other hand, if  $p \neq q$ , uncontrolled population dynamics is the case.

- Or proportional to the density of  $U_{p:p+q-1}$ :

If  $p = q$ , then  $U_{p:2p-1}$  is the median of  $2p - 1$  independent standard uniform random variables, hence reinforcing the idea of sustainable growth, i.e. population equilibrium, as seen above. But if  $p \neq q$ , we are dealing with uncontrolled population dynamics, since  $U_{p:p+q-1} \preceq U_{\lfloor (p+q-1)/2 \rfloor + 1; p+q-1}$  for  $p < q$ , and  $U_{p:p+q-1} \succeq U_{\lfloor (p+q-1)/2 \rfloor + 1; p+q-1}$  for  $p > q$ , where  $U_{\lfloor (p+q-1)/2 \rfloor + 1; p+q-1}$  is the median of  $p + q - 1$  independent standard uniform random variables.



2. The expression  $x^{p-1}(-\ln x)^{Q-1}$ , linked to the BeTaBoOp( $p, 1, 1, Q$ )  $\equiv$  Betinha( $p, Q$ ) density, is:

- Proportional to the product of the densities of  $U_{p:p}$  and  $U_Q^{(*)}$ :

From the fact that  $U_Q^{(*)} \preceq U_{p:p}$ , for all  $p, Q \in \mathbb{N}$ , the growth term is again the dominant one, and consequently population growth is also observed in this setting. Now the question is whether it is possible to have here sustainable growth. The answer is no, because if we compare the two retroaction terms  $(1-x)^{Q-1}$  and  $(-\ln x)^{Q-1}$ , which are proportional to the densities of  $U_{1:Q}$  and  $U_Q^{(*)}$ , respectively, we have  $U_Q^{(*)} \preceq U_{1:Q}$ . Therefore,  $U_Q^{(*)}$  exerts a weaker control effect on population growth than  $U_{1:Q}$ , which leads necessarily to unsustainable population growth, even if  $Q = p$ .

- Or proportional to the density of  $U_Q^{1/p(*)}$ , which applies to the more general case  $p > 0$ :

Here,  $U_Q^{1/p(*)} \preceq U_Q^{(*)}$  if  $p > 1$ , and  $U_Q^{(*)} \preceq U_Q^{1/p(*)}$  if  $p < 1$ . By comparing  $U_Q^{1/p(*)}$  and  $U_Q^{(*)}$  with  $U_{1:Q}$ , which is associated with the retroaction factor  $(1-x)^{Q-1}$ , we conclude that:

- (i) for  $p > 1$ ,  $U_Q^{(*)} \preceq U_{1:Q}$ , thus revealing that  $U_Q^{1/p(*)}$  has a weaker control effect on population growth, as already unveiled above;
- (ii) for  $p < 1$ ,  $U_{1:Q} \preceq U_Q^{1/p(*)}$ , therefore showing that  $U_Q^{1/p(*)}$  has a stronger control effect on population growth.

Both cases are suitable to model unsustainable population growth.

3. The expression  $(1-x)^{q-1}(-\ln(1-x))^{P-1}$ , tied to the BeTaBoOp( $1, q, P, 1$ ) density, is proportional to the product of the densities of  $U_{1:q}$  and  $1 - U_P^{(*)}$ , associated with the retroaction and growth terms  $(1-x)^{q-1}$  and  $(-\ln(1-x))^{P-1}$ , respectively.

Since  $U_{1:q} \preceq 1 - U_P^{(*)}$  for all  $q, P \in \mathbb{N}$ , the growth factor is the dominant one, and therefore population growth will also happen. On the other hand, from the fact that  $U_{P:P} \preceq 1 - U_P^{(*)}$ , where  $U_{P:P}$  is associated with the (absent) growth term  $x^{P-1}$ , shows that in this case we have a stronger growth impetus, counteracted by growth control mechanisms influenced by  $U_{1:q}$ . As  $U_{1:q}$  exerts a stronger control effect than  $U_q^{(*)}$  would on population growth, this case is also suitable for modeling populations with unsustainable growth, as the previous one, but where a more uncontrolled population growth is observed.

Recall that Brilhante *et al.* [2] showed that the normalized solution for the differential equation linked to the BeTaBoOp( $1, 2, 2 + \alpha, 1$ ) density belongs to the class of extreme value laws for minima, which seems to be the consequence of the higher control forces needed to refrain a more uncontrolled population growth through the influence of  $U_{1:q}$ .



4. The expression  $x^{p-1}(-\ln(1-x))^{P-1}$ , tied to the BeTaBoOp( $p, 1, P, 1$ ) density, is proportional to the product of the densities of  $U_{p:p}$  and  $1 - U_P^{(*)}$ , with  $U_{p:p} \preceq 1 - U_P^{(*)}$  only if  $p \leq P$ . Thus, the growth pattern which is linked with the factor  $x^{p-1}$  is the dominant one, whenever  $p \leq P$ .

Because the growth control mechanisms are absent in this setting, the associated differential equation is ideal for modeling populations that almost surely grows to infinity, extinction being almost impossible.

5. The expression  $(1-x)^{q-1}(-\ln x)^{Q-1}$ , linked to the BeTaBoOp( $1, q, 1, Q$ ) density, is proportional to the product of densities of  $U_{1:q}$  and  $U_Q^{(*)}$ , where  $U_Q^{(*)} \preceq U_{1:q}$  if  $q \leq Q$ . Therefore, the retroaction term tied to  $(1-x)^{q-1}$  is the dominant one, whenever  $q \leq Q$ .

Given that we only have growth control factors here, the corresponding differential equation is useful for modeling populations that are almost surely doomed to extinction.

6. The expression  $(-\ln(1-x))^{P-1}(-\ln x)^{Q-1}$ , linked to the BeTaBoOp( $1, 1, P, Q$ ) density, is proportional to the product of densities of  $1 - U_P^{(*)}$  and  $U_Q^{(*)}$ , with  $U_Q^{(*)} \preceq 1 - U_P^{(*)}$  for all  $P, Q \in \mathbb{N}$ . In this setting population growth is observed, with sustainable growth occurring whenever the growth parameter  $P$  and the retroaction parameter  $Q$  are equal.

7. The expression  $x^{p-1}(1-x)^{q-1}(-\ln x)^{Q-1}$ , tied to the BeTaBoOp( $p, q, 1, Q$ ) density, is proportional to the product of the densities of  $U_{p:p}$ ,  $U_{1:q}$  and  $U_Q^{(*)}$ , with  $U_Q^{(*)} \preceq U_{1:q} \preceq U_{p:p}$  if  $q \leq Q$ . Again population growth is noticed since the dominant term is the growth term.

However, when  $p = q = Q$ ,  $U_{1:p}$  manages to “compensate” the growth effect of  $U_{p:p}$  by curbing down the population growth to sustainable levels. This action is reinforced by the other retroaction term  $(-\ln x)^{p-1}$  ruled by  $U_p^{(*)}$ . A more interesting case occurs when the growing parameter  $p$  and the retroaction parameters  $q$  and  $Q$  meet an equilibrium, in the sense that  $p = q + Q$ .

8. The expression  $x^{p-1}(1-x)^{q-1}(-\ln(1-x))^{P-1}$ , linked to the BeTaBoOp( $p, q, P, 1$ ) density, is proportional to the product of the densities of  $U_{p:p}$ ,  $U_{1:q}$  and  $1 - U_P^{(*)}$ , with  $U_{1:q} \preceq U_{p:p} \preceq 1 - U_P^{(*)}$  for  $p \leq P$ .

Uncontrolled population growth is again the case here even if  $p = q = P$ . This is so because although  $U_{1:p}$  “compensates” the effect of  $U_{p:p}$ , it does not do the same for the growth term ruled by  $1 - U_p^{(*)}$ , whose influence is stronger than  $U_{p:p}$ . However, an equilibrium is observed when the growing parameters  $p$  and  $P$  and the retroaction parameter  $q$  verify the relation  $p + P = q$ .

9. The expression  $x^{p-1}(-\ln(1-x))^{P-1}(-\ln x)^{Q-1}$ , linked to the BeTaBoOp( $p, 1, P, Q$ ) density, is proportional to the product of the densities of  $U_{p:p}$ ,  $1 - U_P^{(*)}$  and  $U_Q^{(*)}$ , with  $U_Q^{(*)} \preceq U_{p:p} \preceq 1 - U_P^{(*)}$ . In this



setting we shall have uncontrolled population growth, unless equilibrium is met, i.e. when  $p + P = Q$ .

10. The expression  $(1 - x)^{q-1}(-\ln(1 - x))^{P-1}(-\ln x)^{Q-1}$ , tied to the BeTaBoOp( $1, q, P, Q$ ) density, is proportional to the product of the densities of  $U_{1:q}$ ,  $1 - U_P^{(*)}$  and  $U_Q^{(*)}$ , where  $U_Q^{(*)} \leq U_{1:q} \leq 1 - U_P^{(*)}$ , if  $q \leq Q$ . Here we have two control mechanisms acting on population growth, with sustainability being achieved if  $P = q + Q$ .
11. The expression  $x^{p-1}(1 - x)^{q-1}(-\ln(1 - x))^{P-1}(-\ln x)^{Q-1}$ , linked to the BeTaBoOp( $p, q, P, Q$ ) density, is proportional to the product of the densities of  $U_{p:p}$ ,  $U_{1:q}$ ,  $1 - U_P^{(*)}$  and  $U_Q^{(*)}$ , where  $U_Q^{(*)} \leq U_{1:q} \leq U_{p:p} \leq 1 - U_P^{(*)}$  if  $p \leq P$  and  $q \leq Q$ .

In this setting equilibrium is observed when  $p + P = q + Q$ .

From the exposed above, we see that the generalized Verhulst theory is quite versatile in describing a wide range of population dynamics.

### Acknowledgements

This research has been supported by National Funds through FCT — Fundação para a Ciência e a Tecnologia, project PEst-OE/MAT/UI0006/2011.

### References

1. Aleixo, S., Rocha, J.L., and Pestana, D., Probabilistic Methods in Dynamical Analysis: Population Growths Associated to Models Beta (p,q) with Allee Effect, in Peixoto, M. M; Pinto, A.A.; Rand, D.A.J., editors, *Dynamics, Games and Science, in Honour of Maurício Peixoto and David Rand*, vol II, Ch. 5, pages 79–95, New York, 2011, Springer Verlag.
2. Brilhante, M.F., Gomes, M.I., and Pestana, D., BetaBoop Brings in Chaos. *Chaotic Modeling and Simulation*, 1: 39–50, 2011.
3. Brilhante, M.F., Pestana, D., and Rocha, M.L., Betices, *Bol. Soc. Port. Matemática*, 177–182, 2011.
4. Brilhante, M.F., Gomes, M.I., and Pestana, D., Extensions of Verhulst Model in Population Dynamics and Extremes, *Chaotic Modeling and Simulation*, 2(4): 575–591, 2012.
5. Pestana, D., Aleixo, S., and Rocha, J.L., Regular variation, paretian distribution, and the interplay of light and heavy tails in the fractality of asymptotic models, in Skiadas, C.H., I. Dimotikalis, I., and Skiadas, C. (eds), *Chaos Theory: Modeling, Simulation and Applications*, Singapore, 2011. World Scientific, 309-316.
6. Rachev, S.T., and Resnick, S., Max-geometric infinite divisibility and stability, *Communications in Statistics — Stochastic Models*, 7:191-218, 1991.



## Dynamic Instabilities in Population Growth Models II: Panjer Randomized Modified Fibonacci Model

Maria de Fátima Brilhante<sup>1,4</sup>, Maria Ivette Gomes<sup>2,4</sup>, Dinis Pestana<sup>3,4</sup>, and  
Maria Luísa Rocha<sup>4,5,6</sup>

- <sup>1</sup> Universidade dos Açores, Departamento de Matemática, Ponta Delgada, Açores, Portugal  
(E-mail: [fbrilhante@uac.pt](mailto:fbrilhante@uac.pt))
- <sup>2</sup> Universidade de Lisboa, Faculdade de Ciências, DEIO, Portugal, and Instituto de Investigação Científica Bento da Rocha Cabral, Lisboa, Portugal  
(E-mail: [ivette.gomes@fc.ul.pt](mailto:ivette.gomes@fc.ul.pt))
- <sup>3</sup> Universidade de Lisboa, Faculdade de Ciências, DEIO, Portugal, and Instituto de Investigação Científica Bento da Rocha Cabral, Lisboa, Portugal  
(E-mail: [dinis.pestana@fc.ul.pt](mailto:dinis.pestana@fc.ul.pt))
- <sup>4</sup> CEAUL — Centro de Estatística e Aplicações da Universidade de Lisboa, Portugal
- <sup>5</sup> Universidade dos Açores, Departamento de Economia e Gestão, Ponta Delgada, Açores, Portugal  
(E-mail: [lrocha@uac.pt](mailto:lrocha@uac.pt))
- <sup>6</sup> CEEAplA — Centro de Estudos de Economia Aplicada do Atlântico

**Abstract.** Branching processes are natural models for random population growth in many situations. Here we use basic count models whose probability mass function satisfies Panjer iteration, and investigate randomly stopped sums and collective risk when the subordinator random variable and the summands are independent and identically distributed basic count random variables.

**Keywords:** Branching processes, Panjer iteration, basic count models, collective reisk, fixed point algorithm instabilities.

### 1 Randomizing the Fibonacci Population Growth Model Via Branching Processes

Fibonacci (c. 1170 – c. 1250) in his *Liber Abaci* posed and solved a problem involving the growth of a population of rabbits based on idealized and very unrealistic assumptions. As a consequence, a population with Fibonacci's growth pattern never dies out, while we know that the total progeny of some ancestor is in many real circumstances finite, cf. for instance Lotka [10] example (p. 123–136) on the extinction of surnames, using branching processes.

Let  $\{f_n\}_{n \in \mathcal{S}_X}$  denote the probability mass function (pmf) of a discrete random variable (rv)  $X$  with support  $\mathcal{S}_X \subset \mathbb{N}$ . The corresponding probability generating function (pgf) is  $m_X(t) = E(t^X) = \sum_{n=0}^{\infty} f_n t^n$ .



If  $N$  is a discrete rv,  $X_0 = 0$  and  $X_1, X_2, \dots$  independent replicas of  $X$ , with  $N$  and  $X_k$  independent, and we define the “compound” rv  $Y = \sum_{k=0}^N X_k$ , then

$$m_Y(t) = \sum_{j \in \mathcal{S}_Y} m_X^j(t) \mathbb{P}[N = j] = m_N(m_X(t)).$$

From this, we may easily compute mean value and variance of the rv  $Y$ . An alternative designation for the concept of compounding rv’s is the concept of randomly stopped sums, which can have the advantage of explicitly indicating the type of the subordinator rv.

If in particular  $X_k$ ,  $k = 1, 2, \dots$  are independent replicas of a count rv  $X$  modeling the number of direct descendants of each individual (or each female) in the population, and we define

$$Y_0 = 1, \quad Y_1 = X_1, \quad Y_2 = \sum_{k=0}^{Y_1} X_k, \quad \dots \quad Y_{n+1} = \sum_{k=0}^{Y_n} X_k, \quad \dots$$

we may interpret  $Y_k$  as the number of direct offsprings in the  $k$ -th generation, and  $Z_n = \sum_{j=0}^n Y_j$  as the total progeny of some ancestor until the  $n$ -th generation.

Let us denote  $m(t) = m_1(t)$  the pgf of  $Y_1 \stackrel{d}{=} X$ ,  $m_n(t)$  the pgf of  $Y_n$ ; then  $m_n(t) = m(m_{n-1}(t)) = m^{\otimes(n)}(t)$ , where  $m^{\otimes(n)}$  denotes the  $n$ -fold composition of  $m$  with itself.

Following Good [5] (an argument that inspired Feller [3], XII.5),  $m_{Z_1}(t) = t m_X(t)$  and iteratively  $m_{Z_n}(t) = t m_{Z_{n-1}}(t)$ , we obtain the probability generating functions for the number of descendants up to each successive generation.

This is a decreasing sequence, whose limit  $\rho(s)$  satisfies  $\rho(s) = s m_X(\rho(s))$  and which may be found solving  $t = s m_X(t)$ . Each coefficient  $r_k$  in the MacLaurin’s expansion of  $\rho(s)$  is the probability that the total progeny consists of  $k$  elements, and therefore if  $\sum r_k = \rho(1) < 1$ , this is the probability of extinction.

$\{Y_0, Y_1, \dots\}$  is usually called a Galton–Watson branching process, or a cascade process. Simple examples of branching processes, and basic results on important problems such as extinction probability and size of a population can be found in Feller [3]. Namely, in what concerns extinction:

**Theorem 1.** *If  $\mathbb{E}(Y) = \mu \leq 1$ , the process almost surely dies out, and its expected size is  $\frac{1}{1-\mu}$  when  $\mu < 1$ , and infinite when  $\mu = 1$ . If  $\mu > 1$ , the probability  $f_n$  that the process terminates at or before the  $n$ -th generation tends to the unique root  $x < 1$  of the equation  $x = m_Y(x)$ .*

And, in what concerns the total progeny:



**Theorem 2.** Denoting  $\rho_k$  the probability that the total progeny has  $k$  individuals,

1. the extinction probability is  $\sum_{k=1}^{\infty} \rho_k$ .
2. The pgf  $\rho(s) = \sum_{k=1}^{\infty} \rho_k s^k$  is given by the unique positive root of  $t = s m_Y(t)$ , and  $\rho(s) \leq x$ .

More extensive monographies on branching processes, with deeper results, are Harris [6], Athreya and Ney [1] or Jaegers [8]. Gnedenko and Korolev [4] present interesting examples of random infinite divisibility and random stability using branching processes, and they establish necessary and sufficient conditions for the convergence of randomly stopped sums, and limit theorems for super-critical (i. e.,  $\mu = \mathbb{E}(X) > 1$ ) Galton–Watson processes.

In [2], Brilhante *et al.* investigated randomization of the Fibonacci's growth pattern modeling the individual progeny at a mating epoch using *Bernoulli*( $p$ ), and thus the progeny of the initial ancestor as

$$Z_1 = \begin{cases} 0 & 1 & 2 & 3 \\ (1-p)^2 & p(1-p)(2-p) & 2p^2(1-p) & p^3 \end{cases}$$

(since only two mating epochs are permitted to each individual).

The  $Y \sim \text{Geometric}(p)$  model for the number of direct descendants, with pmf  $\{f_n = p(1-p)^n\}_{n \in \mathbb{N}}$ , provides an algebraic simple treatment. In fact,

writing  $q = 1 - p$ ,  $m_Y(t) = \frac{p}{1-qt}$ , and

$$m_{Y_n}(t) = \begin{cases} p \frac{q^n - p^n - (q^{n-1} - p^{n-1})qt}{q^{-1}n - p^{n-1} - (q^n - p^n)qt} & p \neq q \\ \frac{n - (n-1)t}{n+1-nt} & p = q = \frac{1}{2} \end{cases}$$

is easily computed.

Both the *Bernoulli*( $p$ ) and the *Geometric*( $p$ ) pmf's satisfy the recursive expression

$$f_{n+1} = \left( a + \frac{b}{n+1} \right) f_n, \quad \forall n \geq k, \quad f_n = 0 \text{ for } 0 \leq n \leq k-1$$

(in the case of  $X \sim \text{Bernoulli}(p)$ ,  $a = \frac{p}{p-1}$  and  $b = \frac{2p}{1-p}$ , and in the case of  $X \sim \text{Geometric}(p)$ ,  $a = q$  and  $b = 0$ ). As we shall state in the following section, the above recursive expression is valid for the pmf of a broad class of rv's, known as Panjer rv's, that play an important role on the theory of collective risk. We investigate some consequences of using simple Panjer direct progeny models in branching processes.



## 2 Basic Count Models

We shall say that  $X$  is a Panjer rv if its pmf  $\{f_n\}_{n \in \mathcal{S}_X}$  satisfies the recursive expression

$$f_{n+1} = \left( a + \frac{b}{n+1} \right) f_n, \quad \forall n \geq k, \quad f_n = 0 \text{ for } 0 \leq n \leq k-1. \quad (1)$$

We denote  $Panjer(a, b, k)$  the class of all pmf's satisfying (1).

This expression has been used by several authors, with  $k = 0$ , before Panjer [11], but it was in this seminal paper that the consequences for the iterative computation of the density of the collective risk process have been established.

In fact, Panjer [11] considered only the case  $k = 0$  — for which the non degenerate types are the underdispersed binomial, the overdispersed negative binomial, and the Poisson in between —, but immediatly Sundt and Jewell [14] published the extension for  $k = 1$ , with the logarithmic and the extended negative binomial solutions.

Finally Hess *et al.* [7] defined the general class, with the recursion starting with  $k \geq 0$ , the  $f_0, \dots, f_{k-1}$  being free parameters (for  $k = 0$ ,  $f_0$  can be considered the starting jump of a hurdle process); it is also known as the class of basic count distributions, or class of basic claim distributions. For more details, cf. Rolsky *et al.* [13], Klugman *et al.* [9], and Pestana and Velosa [12].

**Theorem 3.** *Let  $\{f_n\}_{n \in \mathcal{S}_X}$  be the pmf of a non degenerate count rv  $X$ . For  $a, b \in \mathbb{R}$  the statements that follow are equivalent:*

- (a)  $\{f_n\}_{n \in \mathcal{S}_X}$  is a  $Panjer(a, b; k)$  pmf.
- (b) for  $\ell \in \mathbb{N}^+$ , the pgf  $m_X(t) = \sum_{n=0}^{\infty} f_n t^n$  satisfies the differential equations

$$(1 - at)h^{(\ell)}(t) = (\ell a + b)h^{(\ell-1)}(t) + f_k \binom{k}{\ell} \ell! t^{k-1},$$

$t \in [0, 1)$  and  $h^{(j)}(0) = 0$  for  $j \leq k-1$ .

- (c)  $m_X$  satisfies the differential equation

$$(1 - at)h^{(k+1)}(t) = ((k+1)a + b)h^{(k)}(t),$$

$t \in [0, 1)$  and  $h^{(j)}(0) = 0$  for  $j \leq k-1$ .

Further,  $Q = Panjer(a, b; k) \implies (k+1)a + b > 0$ , and on the other hand  $a + b \geq 0 \implies a < 1$  and  $a + b < 0 \implies a \leq 1$ .

From this it is easy to conclude that the Panjer class has the following non degenerate elements:



1. The *Binomial*( $\nu, p$ ),  $\nu \in \mathbb{N}^+$ ,  $p \in (0, 1)$ , which is *Panjer*( $\frac{p}{p-1}, \frac{(\nu+1)p}{1-p}, 0$ ).  
Its variation index  $\mathcal{I}(X) = \frac{\text{var}(X)}{\mathbb{E}(X)} = 1 - p < 1$ , i.e.,  $X$  is underdispersed.
2. The *Poisson*( $\mu$ ),  $\mu > 0$  is *Panjer*( $0, \mu, 0$ ). Its dispersion index is 1.
3. The overdispersed *NegativeBinomial*( $\alpha, p$ ),  $\alpha > 0$ ,  $p \in (0, 1)$ , with pmf  $\left\{ \binom{\alpha+n-1}{n} p^n (1-p)^\alpha \right\}_{n \in \mathbb{N}^+}$ , is *Panjer*( $p, (\alpha-1)p, 0$ ).
4. The *ExtendedNegativeBinomial*( $\alpha, p, k$ ),  $\alpha \in (-k, -k+1)$ ,  $p \in (0, 1)$ ,  $k \in \mathbb{N}^+$ , with pmf

$$f_n = \frac{\binom{\alpha+n-1}{n} p^n}{(1-p)^{-\alpha} - \sum_{j=0}^{k-1} \binom{\alpha+j-1}{j} p^j}, \quad n = k, k+1, \dots,$$

in the support  $\mathcal{S}_X = \{k, k+1, \dots\}$ , is *Panjer*( $p, (\alpha-1)p, k$ ). In the expression above the extended binomial coefficients  $\binom{\alpha+n-1}{n}$  are defined as  $\binom{\alpha+n-1}{n} = \binom{-\alpha}{n} = \frac{\Gamma(\alpha+n)}{\Gamma(\alpha)n!}$ .

5. The *ExtendedLogarithmic*( $p, k$ ),  $p \in (0, 1)$ ,  $k \in \mathbb{N}^+$ , with pmf

$$f_n = \frac{\frac{p^n}{\binom{n}{m}}}{\sum_{j=m}^{\infty} \frac{p^j}{\binom{j}{m}}}, \quad n = k, k+1, \dots,$$

is *Panjer*( $p, -kp, k$ ).

6. If  $X \sim \text{Panjer}(a, b, k)$ , truncating  $\{k, k+1, \dots, \ell-1\} \subset \mathcal{S}_X$  we obtain a truncated rv  $X^* \sim \text{Panjer}(a, b, \ell)$ .

The special “unit” cases *Bernoulli*( $p$ )  $\equiv$  *Binomial*( $1, p$ ), *Geometric*( $p$ )  $\equiv$  *NegativeBinomial*( $1, p$ ), *ExtendedNegativeBinomial*( $\alpha, p, 1$ ) whose pmf has the simple form  $\frac{1 - (1-qt)^{-\alpha}}{1 - p^{-\alpha}}$ ,  $t \leq \frac{1}{q}$ , and *Panjer*( $p, -p, 1$ ) or *Logarithmic*( $p$ ) (or *ExtendedLogarithmic*( $1, p$ ), with pgf  $\frac{\ln(1-pt)}{\ln(1-p)}$ ), do have specially nice properties in each of the corresponding subclasses.

In particular, *NegativeBinomial*( $\alpha, p$ ) — and hence, as a special case *Geometric*( $p$ ) — that result from a *Gamma* randomization of the *Poisson*( $\lambda$ ), i.e., an hierarchic model with  $\Lambda \sim \text{Gamma}(\alpha, 1)$  — are successfully used to



model the descendance of populations when the distribution of direct offsprings exhibits large variation, and both the the *ExtendedNegativeBinomial*( $\alpha, p, 1$ ) and *Logarithmic*( $p$ ) and the *Logarithmic*( $p$ ) distributions have been used to provide close fit to some natural populations.

In Table 1 below we summarize results, indicating also the pgf:

**Table 1.** Panjer distributions.

$X$	$a$	$b$	$k$	$m_Q(t)$
<i>Binomial</i> ( $m, p$ )	$\frac{p}{p-1}$	$\frac{(m+1)p}{1-p}$	0	$(1 - p + pt)^m$
<i>Poisson</i> ( $\mu$ )	0	$\mu$	0	$e^{\mu(t-1)}$
<i>NegativeBinomial</i> ( $\alpha, p$ )	$p$	$(\alpha - 1)p$	0	$(\frac{1-pt}{1-p})^{-\alpha}$
<i>ExtendedNegativeBinomial</i> ( $\alpha, p, k$ )	$p$	$(\alpha - 1)p$	$k$	$\frac{(1-pt)^{-\alpha} - \sum_{j=0}^{k-1} \binom{\alpha+j-1}{j} (pt)^j}{(1-p)^{-\alpha} - \sum_{j=0}^{k-1} \binom{\alpha+j-1}{j} p^j}$
<i>ExtendedLogarithmic</i> ( $p, k$ )	$p$	$-kp$	$k$	$\frac{\sum_{n=k}^{\infty} \binom{n}{k}^{-1} (pt)^n}{\sum_{n=k}^{\infty} \binom{n}{k}^{-1} p^n}$

### 3 Randomly Stopped Sums with Panjer Subordinator

The importance of the Panjer class is a consequence of the implications that the recursive expression (1) has on the recursive computation of the density of randomly stopped sums subordinated by Panjer rv's. This results from the following theorem:

**Theorem 4.** Let  $\{q_n\}_{n \in \mathbb{N}}$  be the pmf of a count distribution  $Y$ , and  $\{f_n\}_{n \in \mathbb{N}}$  denote the pmf of a claim number distribution  $X$  whose support is a subset of the positive integers, i. e.  $f_0 = 0$ . Consider the randomly stopped sum  $T = \sum_{n \in S_Y} X_n$ , with  $Y$  and the replicas  $X_n$  of  $X$  independent.

Then the following statements are equivalent:

1.  $Y \sim \text{Panjer}(a, b, k)$ ;



2. For any claim number rv  $X$  and any  $\ell \geq 1$ ,  $m_T$  satisfies the differential equation

$$(1 - a m_X(t)) h^{(\ell)}(t) = \sum_{i=1}^{\ell} \binom{\ell}{i} \left(a + b \frac{i}{\ell}\right) h^{(\ell-i)}(t) m_X^{(i)}(t) + q_k m_T^{(\ell)}(t),$$

$t \in [0, 1)$ , with the initial conditions  $h^{(j)}(0) = 0$  for  $j \leq k - 1$ .

From this, we can compute the pmf of a compound rv  $T$  with Panjer subordinator  $Y$  and count summands independent replicas of  $X$ , as defined above, by observing that for  $\ell \geq 1$

$$(1 - a m_X(t)) m_T^{(\ell)}(t) = \sum_{i=1}^{\ell} \binom{\ell}{i} \left(a + b \frac{i}{\ell}\right) m_T^{(\ell-i)}(t) m_X^{(i)}(t) + q_k [m_X^k(t)]^{(\ell)}.$$

In fact, the main consequence of Panjer's theory is the following result:

**Theorem 5.** Let  $\{q_n\}_{n \in \mathbb{N}}$  be the pmf of a count distribution  $Y$ , and  $\{f_n\}_{n \in \mathbb{N}}$  denote the pmf of a claim number distribution  $X$  whose support is a subset of the positive integers. Consider the randomly stopped sum  $T = \sum_{n \in S_Y} X_n$ , with

$Y$  and the replicas  $X_n$  of  $X$  independent. Then

$$\mathbb{P}[T = n] = g_n = \begin{cases} m_Y(m_X(0)) = m_T(f_0) & n = 0 \\ \frac{1}{1 - a f_0} \left[ \sum_{i=1}^n \left(a + b \frac{i}{n}\right) g_{n-i} f_i \right] + q_k f_n^{*k} & n \geq 1 \end{cases}$$

where  $f_n^{*k}$  stands for the  $k$ -th iterated convolution of the sequence  $\{f_n\}$  with itself.

(There exists a simple extension for the density when the summands are absolutely continuous, but it is not relevant in the context of branching processes.)

## 4 Discussion and Conclusions

With the exception of *Poisson* or of *Geometric* subordinator — i.e., of a *Panjer*(0,  $\mu$ , 0) or a *Panjer*( $p$ , 0, 0), respectively, cf. Pestana and Velosa [12] on the simplicity of these cases when compared to the complexity of others — we couldn't obtain any close expressions for the  $n$ -fold composition of the pgf for any other Panjer subordinators. Aside from those two cases, the only one for which we got more promising results has been — as predictable — the



*Logarithmic(p)*. Moreover, when the aim is to extend the Fibonacci sequence using branching randomization, in case we want to remove individuals from the population after two mating epochs, we have the extra burden of subtracting, the two rv's used being dependent.

Happily, compound pgf's are amenable to compute mean values and variances, and in what concerns the mean value we have the extra facility that the mean value of the difference is the difference of the means values, regardless whether the random variables are dependent or independent. So, it is easy to follow the process on average, and the relation of the sequence of expected values to the sequence of Fibonacci numbers simple.

The quantities of interest — extinction probability and expected total size in the supercritical case, size of the  $n$ -th generation, total size of the population up to the  $n$ -th generation, can be dealt with computationally. When the fixed point method is used to compute roots of some equation  $F(x) - x$ , numerical instabilities are a rule whenever  $F$  is too steep, and the sufficient convergence conditions are not met.

## References

1. Athreya, K. B., and Ney, P. E. *Branching processes*, New York, 2004, Dover.
2. Brillhante, M. F., Gomes, M. I., and Pestana, D. Dynamic Instabilities in Population Growth Models I: Bernoulli Randomized Modified Fibonacci Model, *Notas do CEAUL*, 2013. (Accepted to be presented at Chaos 2013, Istanbul.)
3. Feller, W. *An Introduction to Probability Theory and its Applications, I*, New York, 1968, Wiley.
4. Gnedenko, B. V., and Korolev, V. Yu. *Random Summation. Limit Theorems and Applications*, Boca Raton and New York, 1996, CRC Press.
5. Good, I.J., The number of individuals in a cascade process, *Proc. Cambridge Philos. Soc.* **45**, 360–363, 1949.
6. Harris, H. *Theory of Branching Processes*, Englewood Cliffs, 1963, Prentice-Hall.
7. Hess, K. Th., Liewald, A., and Schmidt, K. D. An Extension of Panjer's Recursion, *Astin Bulletin* **32**, 283–297, 2002.
8. Jaegers, P. *Branching Processes with Biological Applications*, London-New York-Sydney-Toronto, 1975, Wiley.
9. Klugman, S. A., Panjer, H. H., and Willmot, G. E. *Loss Models*, New York and Chichester, 1998, Wiley.
10. Lotka, A.J., *Thorie Analytique des Associations Biologiques, II*, Paris, 1939, Herman.
11. Panjer, H. H. Recursive Evaluation of a Family of Coumpound Distributions, *Astin Bulletin* **12**, 22–26, 1981.
12. Pestana, D., and Velosa, S. Extensions of Katz–Panjer Families of Discrete Distributions, *REVSTAT Statistical Journal* **2**, 145–162.
13. Rolski, T. , Schmidli, H. , Schmidt, V. , and Tengels, J. *Stochastic Processes for Insurance and Finance*, New York and Chichester, 1998, Wiley.
14. Sundt, B., and Jewell, W. S. Further Results on Recursive Evaluation of Coumpound Distributions, *Astin Bulletin* **12**, 27–39, 1981.

**FCT** This research has been supported by National Funds through FCT — Fundação para a Ciência e a Tecnologia, project PEst-OE/MAT/UI0006/2011, and PTDC/FEDER.



# Nonlinear Interdependence (S) Measures used for Exploring Chaotic Behavior in Large-Scale Neuro-Models

Dragos Calitoiu<sup>1</sup> and John Oommen<sup>1,2</sup>

<sup>1</sup> School of Computer Science, Carleton University, 1125 Colonel By Drive,  
Ottawa, ON, Canada, K1S 5B6

(E-mail: dcalitoi@scs.carleton.ca)

<sup>2</sup> University of Agder, Postboks 509, 4898 Grimstad, Norway

(E-mail: oommen@scs.carleton.ca)

**Abstract.** As the theory of nonlinear dynamics clearly shows, a state space is the natural framework in which the properties of nonlinear dynamical systems can be described and quantified. These properties may be undetectable in the time domain of the system output, e.g., in the EEG tracing. Nonlinear Interdependence, (S), proposed by Quiroga, is said to occur when the trajectories reconstructed in the phase-space of one time series, experimentally predict the evolution of the phase space trajectories of the second time series. A phase space representation may reveal the salient features of the nonlinear structure which are hidden or occluded to standard linear approaches. This measure of predictability has the advantage over linear measures, of being sensitive to interdependence between dissimilar types of activity. In this paper we present a comparison between a nonlinear measure (the Nonlinear Interdependence, S) and a linear measure (the Cross Correlation coefficient, CC). In many cases where one analyzes nonlinear signals, CC is a measure that well describes the synchronization or the desynchronization between two signals. In other cases, S is introduced in addition to CC in order to describe the nonlinear signals. This paper investigates a biologically-realistic neural network (NN) model of the piriform cortex. Our previous work studied the EEGs obtained from two components of this network. In this current work, we increase the granularity of our approach and replicate the exploration using the membrane potentials of our neurons. We thus investigate here the synchronization of these types of signals using the membrane potentials using both linear measures (i.e., CC) and nonlinear measures (i.e., S). Our results clearly prove that utilizing *both* these measures is effective in analyzing and understanding real-life chaotic systems.

**Keywords:** Chaotic Behavior, Large-scale Neuro-Models, Nonlinear Interdependence (S) Measure.

## 1 Introduction

Neuro-modeling is usually motivated by a desire to better understand specific neural circuits, particularly those whose failures could possibly trigger human illnesses. Depression, Anxiety, Schizophrenia, Alzheimer's disease, memory impairment, paralysis, Epilepsy, Multiple Sclerosis, Parkinson's disease, etc.



are areas in which intense research efforts have been (and are being) made so as to better understand and treat these conditions. In this respect, from a modeling perspective, one hypothesis is that the analysis of the *connections* between the neurons is fundamental to understanding the cause and treatment of the illness. Apart from providing a better understanding of the conditions and symptoms of a disease, such an analysis also leads to a better understanding of the development and function of the normal brain.

From the theory of nonlinear dynamics [7], we understand that nonlinear dynamical systems can be aptly and best described and quantified by a state space. This is also the natural framework to characterize its underlying phenomena. However, while their properties may be undetectable in the system's time domain output (e.g., in the EEG tracing), they can be studied in the phase space. A phase space representation may reveal the salient features of the nonlinear structure which are hidden or occluded to standard linear approaches [11]. In this context, Nonlinear Interdependence is said to occur when the trajectories reconstructed in the phase-space of one time series experimentally predict the evolution of the phase space trajectories of the second time series [10]. This measure of predictability has the advantage over linear measures, of being sensitive to the interdependence between *dissimilar* types of activity [3].

Often, in the analysis of nonlinear signals, a linear measure (the Cross Correlation coefficient, CC) is a measure that aptly describes the synchronization or the desynchronization between two signals. In other cases, the Nonlinear Interdependence, S, is introduced in addition to CC in order to describe the nonlinear signals. In this paper we present a comparison between S and CC. We shall demonstrate that whenever we are dealing with signals with a "dominant" nonlinear behavior and with a very small linear component, neither S nor CC, by themselves, can provide the same information as the pair  $\langle S, CC \rangle$ .

To demonstrate this hypothesis, we shall investigate a biologically realistic Neural Network (NN) model of the piriform cortex. In our previous work [4], we studied the EEGs obtained from two components of this network. In this current work, we increase the granularity of our approach and replicate the exploration using some previously unexplored criteria, i.e., the *membrane potentials* of our neurons. We thus investigate here the synchronization of these types of signals using the membrane potentials, wherein we utilize both a typical linear measure (i.e., CC) and a typical nonlinear measure (i.e., S). We also compare the synchronization identified between the potentials in this manner, with the one identified between the EEGs.

### 1.1 The Computational Model and the Platform: GENESIS

The computational model which we present can be viewed as a nonlinear system. Simulation of the piriform cortex requires the numerical solutions of *systems* of differential equations that describe the states of the neurons



as a function of time and space. These numerical techniques describe how the system advances the state variables of the simulation (e.g., the potential of the membrane) from time  $i$  to time  $i + 1$ , through numerical integration of the differential equations that appropriately describe the system. The computational model of the piriform cortex is treated as a loosely-coupled system of ordinary differential equations. The evaluation of a state of any neuron in the system requires only the information of the previous states from other neurons, and it can be solved for each neuron at every time step. It is well known that such equations can be solved using straightforward numerical integration techniques.

The initial architecture consists of three  $15 \times 9$  arrays of 135 nodes. Each array has only a *single* type of neuron, being either of the pyramidal cells, of the feedforward inhibitory cells ( $K^+$  mediated inhibition), or of the feedback inhibitory cells ( $Cl^-$  mediated inhibition). The array is proposed to represent the whole piriform cortex, which falls within an area of approximately  $10 \text{ mm} \times 6 \text{ mm}$ . The pyramidal cells consist of five compartments, with each compartment receiving a distinct kind of synaptic input. The inhibitory cells are modelled using the differences between the exponential functions. The model also contains 10 cells representing the excitatory input from the olfactory bulb to the cortex.

Numerous models of brain circuitry have focused on simulating the macroscopic functionality of systems containing simplified neuronal units. The increase in computational power in the last decade has permitted simulations to include models with considerable complexity, namely those comprising of *realistic* large scale NNs. The goal of a modeling phase is to generate patterns that are similar to EEGs, and to explore their possible physiological basis.

The platform for our research is the so-called GENESIS (General NEural SIMulation System)<sup>1</sup> framework [2] proposed by Bower *et al.* This simulation software was initially developed in a CALTECH (California Institute of Technology) laboratory by Wilson [13] as an extension of efforts to model the olfactory cortex. It was designed to allow for the multi-scale modelling of a single simulation system and, until now, is the only simulator possessing this capacity. Indeed, in this context, the Wilson model of the piriform cortex is generally accepted as a realistic model, since it is based on the anatomical structure, apart from which it also contains physiological characteristics of actual biological networks. The model has been cited in more than 100 refereed papers, and a review of large scale brain simulations is found in [5].

## 2 Problem of Connectivity

The problem of connectivity studied in this paper involves investigating the modification of local connectivity within the piriform cortex. More specifically, we analyze the dependence of the level of chaos as a function of the

---

<sup>1</sup> The GENESIS simulation software is free and can be downloaded from <http://www.genesis-sim.org/GENESIS/>.



density of the synapses (i.e, the number of synapses generated between the neurons). In addition, we investigate the variation of the maximum Non-linear Interdependence,  $S$ , of two sub-systems embedded in a larger system. Thus, we consider how the coupling of two interconnected sub-systems of the same underlying system would change as a function of the connectivity of the synapses. We believe that the levels of local connections between the neurons can be used as a hypothesis for the mechanism to explain underlying illnesses such as Schizophrenia.

The **Problem of Connectivity** is motivated from the following clinical considerations. In spite of intensive research conducted over the last decades and the discovery of effective medication, the cause and the mechanisms leading to Schizophrenia are still unclear. It is widely agreed that Schizophrenia is most likely based on fundamental neuronal changes of the brain. Unfortunately, physiological methodologies have not been able to contrive reliable tests beside the current assessments. Perhaps the high complexity of the human brain is what renders it vulnerable to diseases such as Schizophrenia, because animals do not develop the same types of diseases [6].

**Prior Work on the Problem of Connectivity:** In our prior research [4], we have performed modifications to the number of connections between the pyramidal neurons. By changing the connectivity, we proposed to simulate the level of pruning to be excessive or insufficient. We chose to describe the effect of pruning on the level of chaos and the degree of synchronization between the two sub-systems embedded in the piriform cortex model, using three measures: the  $LLE$ ,  $S$ , and  $CC$ . These three measures were chosen based on two hypotheses. First of all, schizophrenic symptoms, like thought disorder, hallucinations and delusions, are assumed to be dependent on the level of chaos in the brain. Secondly, the symptoms are triggered by the existence of false attractors near “good” attractors, which suggests that areas from the brain could be highly correlated in an unhealthy manner. To our knowledge, the investigation of the two theories, namely excessive and insufficient pruning, based on these three measures, is new.

The uniqueness of our research is strengthened by the fact that the pairs of signals being compared belong to the same system. Other authors [8–10], have considered two initially independent systems and partially coupled them; subsequently, they have analyzed the synchronization of the signals obtained from the two systems. In contrast to previous models that evaluate relationships between two different systems (or rather, two partially coupled systems), we have proposed a new approach where the investigation is conducted using two sub-systems which are embedded within the context of a larger system, namely, two coupled sub-systems of the same system.

## 2.1 Current Work: Problem of Connectivity

To present our current work in the right perspective, it is appropriate for us to mention how the readings and measurements are taken and recorded. Recordings from the array are averaged to produce the EEGs as below:



$$EEG(t+1) = \frac{1}{m} \sum_{i=1}^m [\Phi_i(t)], \quad (1)$$

where  $m$  is the number of electrodes, and  $\Phi_i(t)$  is the field potential depending of the output of the pyramidal neurons,  $X^p(t)$  for  $p = 1 \cdots N$ . We assume that the influence of the inhibitory neurons is marginal in the process of the EEG computation, and that it can thus be omitted.

The relation between the field potential,  $\Phi_i(t)$ , recorded from the electrode  $i$  and the output of the pyramidal neurons  $X^p(t)$  is:

$$\Phi_i(t) = \frac{1}{4\pi} \sum_{p=1}^N \frac{X^p(t)}{d_{pi}}, \quad (2)$$

where  $N$  is number of pyramidal neurons, and  $d_{pi}$  is the distance of the  $p^{th}$  pyramidal neuron from the recording site (the electrode  $i$ ).

By examining the above equations, the reader can see that the synchronization of the EEGs implies the evaluation of the *aggregated* signals, which is achieved by computing the averages of a certain number of fields (in our setting the number is 8). These fields are, in turn, obtained by weighting the membrane potentials with the inverses of the distances between the electrodes and each neuron, which is considered as a contributor in the EEG. However, prior to the averaging phase, one observes that the computational model of the piriform cortex yielded access to the raw data in and of itself, namely the *original* membrane potential of each neuron. From the perspective of understanding the efficiency of the CC and S measures, in our current work we disaggregate the signals and explore the behavior of the raw data (i.e., the membrane potentials) itself. To accomplish this for a *prima facie* study, we perform a careful selection of only *four* neurons as follows:

- i. Two of them ( $V_1$ - $V_2$ ) were involved in the previous  $EEG_1$  computation;
- ii. One of them ( $V_{135}$ ) was involved in the computation of the  $EEG_2$ ;
- iii. The last ( $V_{15}$ ) was not involved in the previous computations.

Using these selection criteria, we now investigate all the possible synchronization scenarios (i.e., the intra-EEG and the inter-EEG electrode readings).

## 2.2 The Settings

In our research, we considered two zones of the piriform cortex as depicted in Figure 1. For each zone, which was treated as a sub-system, we analyzed the artificially generated EEGs, each of them being computed with a fixed number of electrodes, and at a suitable frequency.

We considered the density of the synapses corresponding to the pyramidal neurons as a control parameter, and explored the effect of modifying the initial values suggested by the Wilson model [13]. This, in turn, involved:

1. The computation of the EEGs as function of the number of electrodes for each sub-system.

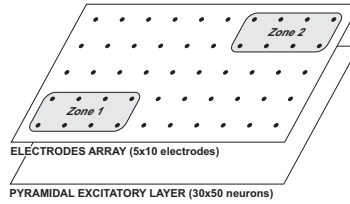


**Fig. 1.** The distribution of the electrodes in Zone1 and Zone2.

2. The determination of the optimum value for the embedding dimension for the phase space reconstruction using the FNN method *for the density of the synapses*.
3. The computation of the  $CC$  and  $S$  measures *between* the EEGs and for the membrane potentials.

### 2.3 Results for this Problem

We conducted numerous simulations over an ensemble of settings. However, we merely report here some representative results.

First of all, we mention that the time series used to describe the systems are the EEGs and membrane potentials. To obtain these, we used an array of  $n$  evenly spaced electrodes on the surface of the simulated cortex. Recordings from the array were then averaged to produce the EEGs. In our experiments, we set  $n = 50$ .

We investigated the level of chaos and the synchronization between these two zones of the piriform cortex, when the efficiency of the pruning was higher or smaller than 50%, implying that we decreased, and also increased the connectivity between the pyramidal cells. The level of connectivity was described by the maximum number of possible connections between the pyramidal neurons, where the possible values were  $p = 0.1, 0.2, 0.5, 1, 2,$  and  $10$ . The case of the healthy brain, when the efficiency of pruning is 50%, corresponds to the setting when  $p = 1$ .

For each sub-system we analyzed the artificially generated EEGs, each of them computed with 8 electrodes. We also analyzed the membrane potentials for four neurons:  $V_1$  and  $V_2$  involved in the computation of EEG1 for  $Zone_1$ ,  $V_{135}$  involved in the computation for the EEG2 for  $Zone_2$ , and  $V_{15}$  not involved in the computation of EEG1 or EEG2. The EEGs and the membrane potentials were recorded at 5,000 samples/sec for a duration of half of a second.

The first experimental step was to compute the optimum embedding dimension for each zone, using The False Nearest Neighbor (FNN) Statistics. In the interest of brevity, we will not present these results here.

To evaluate the interdependence between the artificially generated EEGs and between the membrane potentials, as mentioned earlier, we used two metrics, namely  $S$  and  $CC$ . For computing  $CC$  we used a lag which ranged

between -100 and +100. The absolute value is reported. The evolution of  $S$  and  $CC$  function of connectivity between pyramidal cells are presented in Table 1, in which we report the averages for 20 experiments, each of them conducted with a different model.

Weights	$CC_{max}$	$S(X, Y)$	EEG1 vs EEG2								
0.1	0.9678	0.2341	0.9668	0.2366	0.9680	0.2439	0.9692	0.246	0.5005	0.2396	
0.5	0.6600	0.1094	0.6539	0.1117	0.7300	0.212	0.8032	0.2170	0.6204	0.2870	
1	0.1386	0.0797	0.2111	0.0671	0.1380	0.0823	0.1872	0.0680	0.2227	0.1112	
1.5	0.1439	0.0234	0.1419	0.0215	0.2526	0.0390	0.2158	0.0330	0.2524	0.2607	

**Table 1.** Nonlinear Interdependence ( $S$ ) and maximum Cross Correlation Coefficient ( $CC_{max}$ ) for membrane potentials ( $V_1-V_{15}$ ,  $V_2-V_{15}$ ,  $V_1-V_{135}$ , and  $V_2-V_{135}$ ) and for EEG1 and EEG2 function of the value of the connectivity between the pyramidal cells.

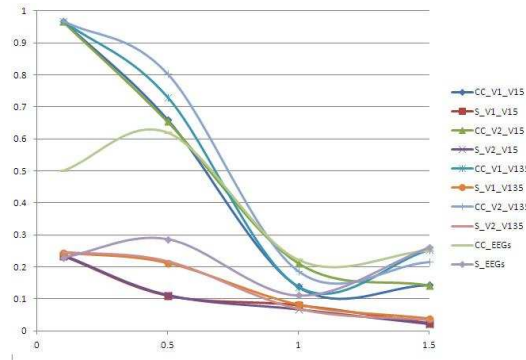


**Fig. 2.** The evolution of  $S(X|Y)$  and  $CC$  as a function of the level of connectivity between the neurons (see Table 1.)

## 2.4 Discussion of Results

Table 1 and Figure 2 are used for analyzing the two behaviors, namely that of increasing and decreasing the connectivity levels. Table 1 contains the averages of the  $CC$  and  $S$  measures computed with membrane potentials (the first 8 columns) and the averages computed with the EEG signals (reported earlier in [4]). The reader can see that the computation used to obtain the EEG affects the ranges of the  $CC$  and  $S$  measures, namely it decreases the ranges, compared to the ranges of the  $CC$  and  $S$  measures computed with the membrane potentials. To be more specific, the  $CC$  ranges are 0.8306 for the membrane potentials and 0.3977 for the EEGs, while the  $S$  measure ranges are 0.2245 for the membrane potentials and 0.1758 for the EEGs.



With regard to the degree of synchronization represented by the Nonlinear Interdependence  $S$ , only a decrease in the connectivity leads to a consistent modification, again as displayed in Figure 2.

### 3 Conclusions

The analysis of the two behaviors, namely that of increasing and decreasing the connectivity levels, reveals that both of them determine a decrease in the level of chaos in the system, as seen in Figure 2.

From these observations, we can conclude that whenever we are dealing with signals with a “dominant” nonlinear behavior and with a very small linear component, neither  $S$  nor  $CC$ , by themselves, can provide the same information as the pair  $(S, CC)$ .

### References

- 1.J. Arnold, P. Grassberger, K. Lehnertz, and C. E. Elger. A robust method for detecting interdependences: application to intracranially recorded EEG. *Physica D*, 134:419–430, 1999.
- 2.J.M. Bower and D. Beeman. The Book of GENESIS. Springer TELOS, 1998.
- 3.M. Breakspear and J. R. Terry. Topographic orientation of nonlinear interdependence in multichannel human EEG. *Neuroimage*, 16:822–835, 2002.
- 4.D. Calitoiu, B.J. Oommen, and D. Nussbaum. Large scale neuro-modeling for understanding and explaining some brain-related chaotic behavior. *Simulation: Transactions of the Society for Modeling and Simulation International*, 88:1316–1337, 2012.
- 5.H. deGaris, S. Chen, B. Goertzel, and R. Lian. A world survey of artificial brain projects, Part I: Large-scale brain simulations. *Neurocomputing*, 74:3–29,2010.
- 6.A. Fell. The Disorder Mind. *UC Davis Magazine*, 19:1–7, 2001.
- 7.A. V. Holden. *Chaos - Nonlinear Science: Theory and Applications*. Manchester University Press, 1986.
- 8.L. M. Pecora. Synchronization conditions and desynchronizing patterns in coupled limited-cycle and chaotic systems. *Physical Review E*, 58:347–360, 1998.
- 9.R. Q. Quiroga, J. Arnold, and P. Grassberger. Learning driver-response relationships from synchronization patterns. *Physical Review E*, 61:5142–5148, 2000.
- 10.S. F. Schiff, P. So, and T. Chang. Detecting dynamical interdependence and generalized synchrony through mutual prediction in a neural ensemble. *Physical Review E*, 54:6708–6724, 1996.
- 11.C. J. Stam. Nonlinear dynamical analysis of EEG and MEG. Review of an emerging field. *Clinical Neurophysiology*, 116:2266–2301, 2005.
- 12.M. Wilson and J. M. Bower. A computer simulation of olfactory cortex with functional implications for storage and retrieval of olfactory information. *Neural Information Processing Systems*, edited by D. Anderson, American Institute of Physics, New York, 114–126, 1988.
- 13.M. Wilson and J.M. Bower. The simulation of large-scale neural networks. *Methods in Neuronal Modelling: From Synapses to Networks*, edited by C. Koch and I. Segev, Cambridge, MA: MIT Press, 291–334, 1989.



## EOG Based Eye Movement Controlled Human Machine Interface

Chetan S, Shivaputra

Department of Electronics & Communication Engineering, Dr Ambedkar  
Institute of Technology, Bengaluru, India  
E-mail: [chetans31@gmail.com](mailto:chetans31@gmail.com)

**Abstract:** Bio-based human computer interface (HCI) has the potential to enable severely disabled people to drive computers directly by bioelectricity rather than by physical means. A study on the group of persons with severe disabilities shows that many of them have the ability to control their eye movements, which could be used to develop new human computer interface systems to help them communicate with other persons or control some special instruments.

There is some work done on Human Computer Interface using the mathematical morphology to process the signal. This requires costly Laptop or DSP chip which makes the entire system costly. So, the objective is to reduce the cost and the complexity of the existing system by using a low cost Graphical LCD and a Microcontroller. Thus, the system would become affordable by all. This Human Machine Interface, which can be controlled using EOG Signals and final output is to be used to move cursor on the graphic display which has several buttons and each button is clicked by blinking the eyes which activates corresponding appliance or action. RF interface is provided between acquisition/processing part and application so that it's easy to handle and easy to install in homes and hospitals

**Keywords:** Human computer interface, EOG, eye movement.

### 1. Electro-Oculography (EOG) Principle

Electro-oculography (EOG) is a new technology of placing electrodes on user's forehead around the eyes to record eye movements. EOG is a very small electrical potential that can be detected using electrodes. Compared with the EEG, EOG signals have the characteristics as follows: the amplitude is relatively high (15-200 $\mu$ V), the relationship between EOG and eye movements is linear, and the waveform is easy to detect.

#### A. Anatomy of Eye

The main features visible at the front of the eye are shown in Figure 1. The lens, directly behind the pupil, focuses light coming in through the opening in the center of the eye, the pupil, onto the light sensitive tissue at the back of the eye, the retina. The iris is the colored part of the eye and it controls the amount of light that can enter the eye by changing the size of the pupil, contracting the pupil in bright light and expanding the pupil in darker conditions. The pupil has very different reflectance properties than the surrounding iris and usually appears black in normal lighting conditions. Light rays entering through the pupil first pass through the cornea, the clear tissue covering the front of the eye. The cornea and vitreous fluid in the eye bend and refract this light. The conjunctiva is a membrane that lines the eyelids and covers the sclera, the white

part of the eye. The boundary between the iris and the sclera is known as the limbus, and is often used in eye tracking.

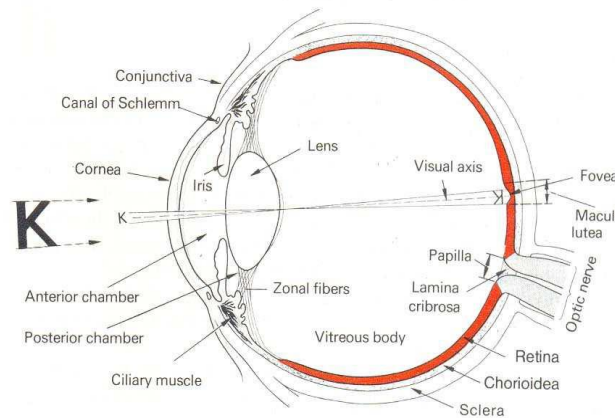


Figure 1

The light rays falling on the retina cause chemical changes in the photosensitive cells of the retina. These cells convert the light rays to electrical impulses which are transmitted to the brain via the optic nerve. There are two types of photosensitive cells in the retina, cones and rods. The rods are extremely sensitive to light allowing the eye to respond to light in dimly lit environments. They do not distinguish between colors, however, and have low visual acuity, or attention to detail. The cones are much less responsive to light but have a much higher visual acuity. Different cones respond to different wavelengths of light, enabling color vision. The fovea is an area of the retina of particular importance. It is a dip in the retina directly opposite the lens and is densely packed with cone cells, allowing humans to see fine detail, such as small print. The human eye is capable of moving in a number of different manners to observe, read or examine the world in front of them.

## 2. The Electro-Oculogram

The electro oculogram (EOG) is the electrical signal produced by the potential difference between the retina and the cornea of the eye. This difference is due to the large presence of electrically active nerves in the retina compared to the front of the eye. Many experiments show that the corneal part is a positive pole and the retina part is a negative pole in the eyeball. Eye movement will respectively generates voltage up to 16uV and 14uV per 1° in horizontal and vertical way. The typical EOG waveforms generated by eye movements are shown in Figure 2.

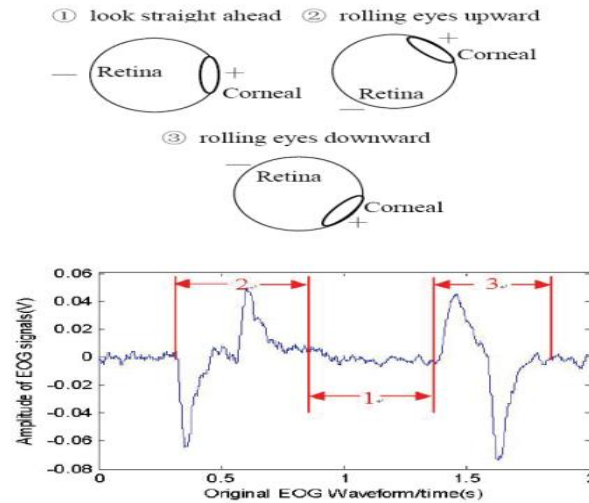


Figure 2

In Figure 2, positive or negative pulses will be generated when the eyes rolling upward or downward. The amplitude of pulse will be increased with the increment of rolling angle, and the width of the positive (negative) pulse is proportional to the duration of the eyeball rolling process.

### 3. Methodology

In our HCI system, four to five electrodes are employed to attain the EOG signals. Figure 3 shows the electrode placement.

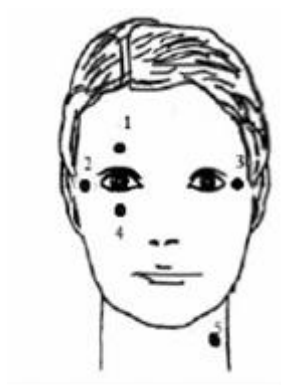


Figure 3

Electrodes 1 & 4 for detecting vertical movement, 2 & 3 for detecting horizontal movement and 5 is for reference(can be omitted or place at forehead). Blink detection is by separate algorithm based on EOG signals

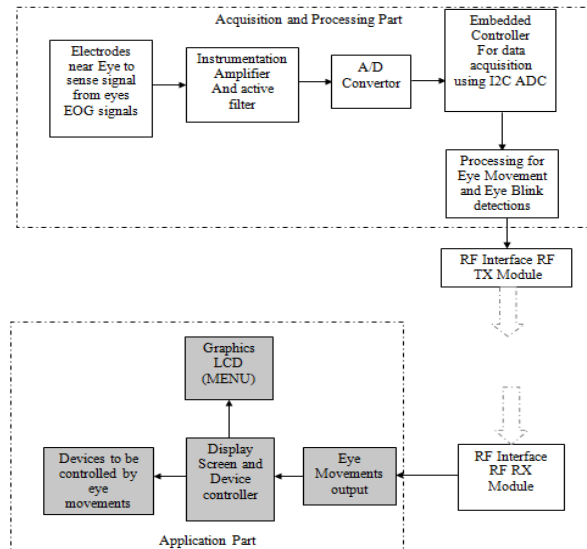


Figure 4

## 4. Acquisition Part

### A. Electrodes:

The Ag-AgCl electrodes will pick up signals which corresponds to eye movements signals mixed with some others signals which are noise and the noise is filtered at later stages

### B. Instrumentation Amplifier:

Signals from electrodes are received and sent to Instrumentation Amplifier which is a type of differential amplifier that has been outfitted with input buffers, which eliminate the need for input impedance matching and thus make the amplifier particularly suitable for use in measurement and test equipment. Instrumentation amplifier with very low DC offset, low drift, low noise, very high open-loop gain, very high common-mode rejection ratio, and very high input impedances is used for great accuracy and stability of the circuit. AD620 a precision Instrumentation amplifier is used here

### C. Active Filters and Gain Blocks:

Opamp based Active low pass filters are used so that only eye signals are going further in the circuit, cutoff frequency for this filter is 20Hz-40Hz. And high pass filter is used to block DC and frequencies up to 0.1-0.3Hz. These filters and gain blocks are implemented using LM324 Opamp.

### D. Analog to Digital Converter:

Final amplified and filtered analog output is converted into Digital signal using I2C Based 4 channel A2D convertor-PCF8591 to save space as ADC0808 is little bigger in size.

### E. Acquisition and processing microcontroller:

This is 8051 class of microcontroller and it has to acquire signals from A/D convertor for both chains up-down electrode chain and left-right electrode chain. As our microcontroller is fast and powerful we will process the signal here itself and transmit final eye move outputs to application part wirelessly.

Commands sent:

- CL: Right eye movement
- CR: Left eye movement
- CU: Up eye movement
- CD: Down eye movement
- BL: Blinking of eye

*F. RF Transmitter:*

Here we can use 315/433 MHz Transmitter modules along with HT640 Encoder to send eye movement commands to the application part.

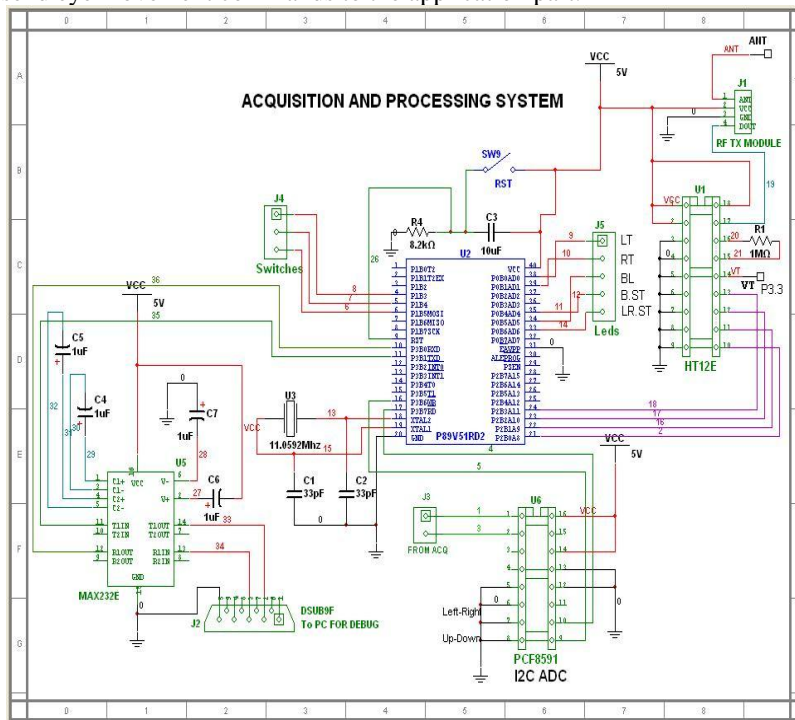


Figure 5

**5. Application Part**

*A. RF Receiver:*

Wireless signals transmitted by the acquisition part are received in this section, here 315/433MHz Rx modules along with HT648 decoder is used. Output of RF receiver goes to application part directly.

*B. Display and appliance controller:*

This is a again a microcontroller which receives eye movements signals (R L U D B) as described above via UART interface.

We use P89V51RD2 from NXP (Philips), this microcontroller is connected to Graphic LCD which displays Cursor and 4 buttons

1. TV
2. FAN
3. Lights
4. Alarm

Using eye movements a cursor is controlled and using blink click operation is done, each Button is toggle button i.e. if appliance is on it will become off and vice versa. But alarm button is different when clicked an On-off alarm is generated to call assistance. And assistant has to come and reset the alarm. Now this controller is also connected to relay board so button action is converted into relays getting switch off and on. And hence appliances are getting turned on and off.

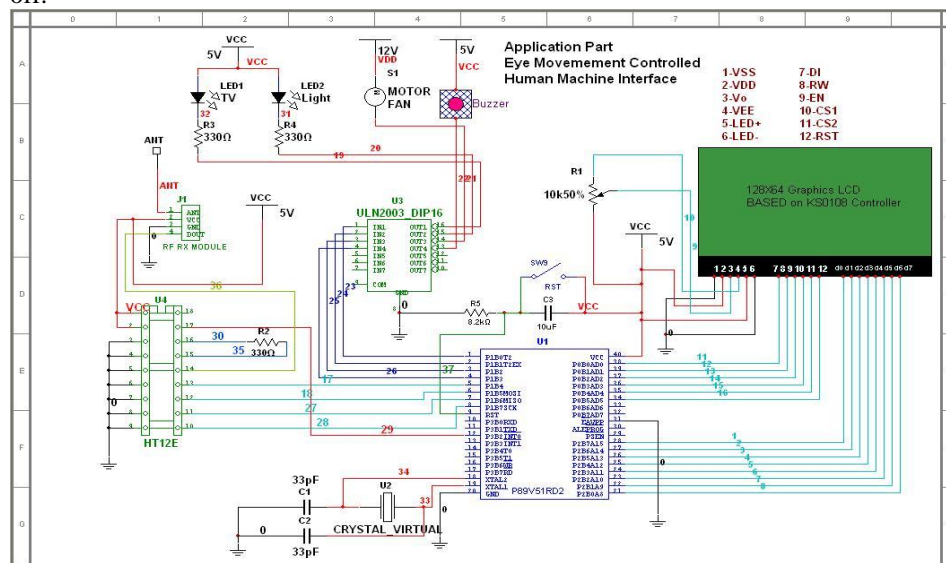


Figure 6

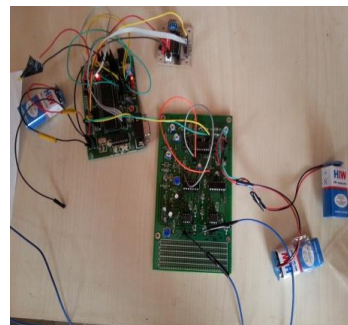
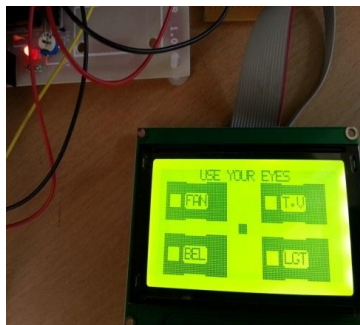
## 6. Advantages of the EOG over other methods

- The EOG typically has a larger range than visual methods which are constrained for large vertical rotations where the cornea and iris tend to disappear behind the eyelid. Angular deviations of up to 80° can be recorded along both the horizontal and vertical planes of rotation using electrooculography.
- The reflective properties of ocular structures used to calculate eye position in visual methods are linear only for a restricted range, compared to the EOG where the voltage difference is essentially linearly related to the angle of gaze for ±30° and to the sine of the angle for ±30° to ±60°.
- The EOG has the advantage that the signal recorded is the actual eyeball position with respect to the head. Thus for systems designed to measure relative eyeball position to control switches (e.g. looking

- up, down, left and right could translate to four separate switch presses) head movements will not hinder accurate recording.
- Unlike techniques such as the magnetic search coil technique, EOG recordings do not require anything to be fixed to the eye which might cause discomfort or interfere with normal vision. EOG recording only requires three electrodes (for one channel recording), or five electrodes (for two channel recording), which are affixed externally to the skin.
  - In visual methods, measurements may be interfered with by scratches on the cornea or by contact lenses. Bifocal glasses and hard contact lenses seem to cause particular problems for these systems. EOG measurements are not affected by these obstacles.
  - EOG based recordings are typically cheaper than visual methods, as they can be made with some relatively inexpensive electrodes, some form of data acquisition card and appropriate software.
  - The EOG can be used to record eye movement patterns when the eye is closed, for example during sleep. Visual methods require the eye to remain open to know where the eye is positioned relative to the head, whereas an attenuated version of the EOG signal is still present when the eye is closed.

## 7. Result

The microcontroller P89V5RD2 in both acquisition end and at the receiver end is programmed using C. The observed result is that the list of appliances that can be controlled and a cursor is displayed on the LCD graphical display. The cursor can be moved up, right, left and down by the eye movements and the appliances could be controlled by blinking the eyes without using the hands. The minimum time interval between two operations is 5seconds.



## Acknowledgement

The authors would like to thank the Principal, Management, SPFU and NPIU for sponsoring the authors to present the paper in the International Conference CHAOS 2013 under the World Bank Funded Project TEQIP-2.



## References

1. A portable wireless eye movement-controlled Human-Computer Interface for the Disabled by Xiaoxiang Zheng, Xin Li, Jun Liu, Weidong Chen, Yaoyao Hao
2. D. A. Robinson, "A method of measuring eye movement using a scleral search coil in a magnetic field," *IEEE Trans Biomed Eng.*, vol.10, pp. 137-45, 1963.
3. R. S. Rimmel, "An Inexpensive Eye Movement Monitor Using the Scleral Search Coil Technique," *Biomedical Engineering, IEEE Transactions on*, vol. BME-31, pp. 388-390, 1984.
4. J. R. LaCourse and F. C. Hludik, Jr., "An eye movement communication-control system for the disabled," *IEEE Trans. Biomed. Eng.*, vol. 37, pp. 1215-1220, 1990.
5. Y. Kenji, H. Junichi, and M. Michio, "Development of EOG-Based Communication System Controlled by Eight-Directional Eye Movements," in *Engineering in Medicine and Biology Society, 2006.EMBS '06. 28th Annual International Conference of the IEEE*, 2006, pp. 2574-2577.
6. R. Barea, L. Boquete, M. Mazo, and E. Lopez, "System for assisted mobility using eye movements based on electrooculography," *Neural Systems and Rehabilitation Engineering, IEEE Transactions on*, vol. 10, pp. 209-218, 2002.
7. S. P. Liversedge and J. M. Findlay. Saccadic eye movements and cognition. *Trends in Cognitive Sciences*, 4(1):6-14, 2000.
8. J. M. Henderson. Human gaze control during real-world scene perception. *Trends in Cognitive Sciences*, 7(11):498-504, 2003.
9. D. Melcher and E. Kowler. Visual scene memory and the guidance of saccadic eye movements. *Vision Research*, 41(25-26):3597-3611, 2001.
10. M. M. Chun. Contextual cueing of visual attention. *Trends in Cognitive Sciences*, 4(5):170-178, 2000.



## Efficient Transport Management System (ETMS) Using ARM Processor

Shivaputra, Chetan S

Dr Ambedkar Institute of Technology, Bangalore, India  
E-mail: [putrauvce@gmail.com](mailto:putrauvce@gmail.com)

**Abstract:** The utilization of RFID cards in the field of asset tracking, manufacturing, supply chain management, retailing, security and access control other far reaching applications and with the implementation of advanced ARM series processors in almost every consumer application specific systems, advanced features associated with these systems mark a milestone in the development. The vulnerability and the adaptability of an advanced system as such which involves the embedment of ARM processors and the RFID cards in the system without any hindrance and any mis-utilization of the resources are in more demand. The paper deals with the accesses of the entry for the user/commuter into the bus in a pre-defined path using a RFID card, which the user has to scan during the in and out of the bus, due for which the user will be accessing their pre-paid account and there happens to be a reduction in the usage of paper. It has got a wide variety of applications and can be designed for any security or access control system. In this paper, the design and development of the electronic system, in which the user can just use the card to get into the bus and also inform about his balance left in his card is being appreciated. The system is user-friendly with easy accessibility for each and every user/commuter, system also allows the user/commuter to gain entry into the bus, system also monitors the proper utilization of the resources without any mis-utilizations.

The paper focuses on the development of system and the necessary hardware components required, along with its proper implementation details.

**Keywords:** ARM(Advanced RISC Machines) processor; Keil  $\mu$ Vision Compiler; LCD(Liquid Crystal Display); RFID.

### 1. Introduction

With the increased misutilization of the public transport resources such as the illegal usage of tickets and daily tickets and passes, and also with the wastage of the available natural resources such as paper in the form of tickets, we thought of overcoming these hurdles by constructing a system that is eco-friendly; thus reducing the usage of the usage of the natural resources such as the paper as the user/commuter here handling or accessing or interacting with this system uses a RFID card which as long durability and user –friendly system; can be easily accessed by the user/commuter at any real time.

This system has a basic feature thus enabling securized/ authenticated entry into the bus and also the checking of the proper utilization of the resources without any hampering/misutilization/tampering of the resources. This is a



versatile autonomous system which follows a predefined path and allows the user to access the system in an economic and efficient way.

## 2. PRESENT WORK

Every user/commuter will be having a pre-paid account to which the access is enabled with the help of the RFID cards. These cards will be read with the help of the RFID Readers when the user of the system scans his/her card.

The user will then be logged in into his/her account whose database will be certainly maintained in a database management system, from which the details of the user is retrieved. The door of the bus opens and the passenger enters into the bus. During the exit of the passenger he/she has to again scan the card and the door of the bus opens up for the exit of the passenger.

The respective amount will be deducted from their account upon the scanning of their card during their exit from the bus. The heart of the system is the ARM processor which is responsible for the entire processing and the vigilance of the proper working of the entire system. The series of ARM processor used here is ARM7TDMI, bearing the required suitable features.

A display remains to be the guide to process the functioning of the system, that displays the user details with the remaining balance in his/her card and the validity of the card, after which the door of the bus is made to open with the help of a stepper motor and as the passenger/user/commuter enters the bus the door of the bus closes, and the process is to be repeated for the next and the other users/commuters in the queue to gain entry into the bus. If the amount in the account of the user/commuter is low or if the user/commuter is trying to access the system with a fake RFID card or a wrong card then the door of the bus is not opened but there is the howling of the alarm alerting both the user/commuter as well as the driver of the bus.

## 3. RELATED WORKS

With the development and the design of the system, the major drawbacks of the previous existing protocols and the systems that consisted of the processors other than ARM series of processors, motivated in developing such a system.

“The performance of the system components can be improved by optimizing the performance of every component in the system”, as quoted by L. Ruiz-Garcia , P. Barreiro , J.I. Robla [3] in their paper “Performance of ZigBee-Based wireless sensor nodes for real-time monitoring systems”, “Radio Frequency can have data rates of up to 450kbps, which provides very fast rates for data transfer while Bluetooth offers only 250kbps, and the security of the data and its integration as compared with that of Radio frequency, is much more open to interception and attacks” as quoted in the seminar report of “BLUETOOTH” [1] and the disadvantages of the previous protocols existing prior to that of the RFID makes us to adopt to the utilization and the implementation of RFID and its clear applications in our *work*.

“The amount of interrupt latency, the support of the modules by the kernels, Operating systems, addressing modes and register sets, are the few drawbacks that hinders the performance rates of the predecessor processors of ARM”, as



interpreted by Thomas Wiedemann in his paper “How fast can Computers React?” [2], stands as a support and substantiates the use of the more advanced and adorable series of processor, ARM processors that accommodate nearly about 75% of today’s all consumer goods to every 32-bit RISC CPUs, in our work.

And as per the advantages that have been stated with respect to our work and with these the ideas for an efficient system to govern the entire process of accessing and security in local transport facilities with the increased rate of misutilization of the resources as such by a lot lead us through this work. To mention few, below are the disadvantages of the previous protocols i.e. of Zigbee and Bluetooth that existed before the evolution of RFID;

- Market for Zigbee and Bluetooth is WPAN and whereas for the RFID its WSN (Wireless Sensor Network)
- Data Rate is of standard 20-250kbps for Zigbee and 1Mbps for Bluetooth whereas for RFID its 2.48kbps (slow speed data at 13.56MHz) and 423kbps (high speed data at 13.56MHz)
- Range is 1-75+ for Zigbee and 1-10+ for Bluetooth whereas for RFID its 1.5m-100m
- Has the key attributes of both Zigbee and Bluetooth i.e. cost effective, low power and convenience.
- Transmission technology of Zigbee is DSSS and that for Bluetooth is FHSS whereas that for the RFID is ASK(bi-phase modulation), FSK and PSK.
- Power: 0dbm for Zigbee; 0/20dbm for Bluetooth and 0.1w-2w (800MHz) for RFID
- Topology: 64000 devices (nodes) for Zigbee and max of 8 devices point-to-multipoint, whereas for RFID its ‘N’ point-to-multipoint devices.

#### **4. TECHNOLOGY**

##### *a. ARM PROCESSOR*

The ARM7TDMI[4] is a member of the Advanced RISC Machines (ARM) family of general purpose 32-bit microprocessors, which offer high performance for very low power consumption and price. The ARM architecture is based on Reduced Instruction Set Computer (RISC) principles, and the instruction set and related decode mechanism are much simpler than those of micro-programmed Complex Instruction Set Computers. This simplicity results in a high instruction throughput and impressive real-time interrupt response from a small and cost-effective chip. Pipelining is employed so that all parts of the processing and memory systems can operate continuously.



The ARM7TDMI processor employs a unique architectural strategy known as THUMB, which makes it ideally suited to high-volume applications with memory restrictions, or applications where code density is an issue.

The major advantage of a 32-bit (ARM) architecture over a 16-bit architecture is its ability to manipulate 32-bit integers with single instructions, and to address a large address space efficiently. When processing 32-bit data, a 16-bit architecture will take at least two instructions to perform the same task as a single ARM instruction. THUMB also has a major advantage over other 32-bit architectures with 16-bit instructions. This is the ability to switch back to full ARM code and execute at full speed. Thus critical loops for applications such as

- Fast interrupts
- DSP algorithms

can be coded using the full ARM instruction set, and linked with THUMB code. The overhead of switching from THUMB code to ARM code is folded into subroutine entry time. Various portions of a system can be optimised for speed or for code density by switching between THUMB and ARM execution.

The code density with respect to this processor family is in the range of about 75% while that for ARM9 is about 35%. The ARM7TDMI processor is associated with the Von-Neumann Architecture whereas the latter is of Harvard Architecture. The particularity for this paper is satisfied with the features of ARM7TDMI.

#### *b. KEIL $\mu$ VISION COMPILER*

The Keil Development Tools are designed for the professional software developer; however programmers of all levels can use them to get the most out of the embedded microcontroller architectures that are supported. Tools developed by Keil are distributed in several packages and configurations, dependent on the architecture.

**MDK-ARM:** Microcontroller Development Kit, for several ARM7, ARM9, and Cortex-Mx based devices

In addition to the software packages, Keil offers a variety of evaluation boards, USB-JTAG adapters, emulators, and third-party tools, which completes the range of products.

#### *c. LCD (Liquid Crystal Display)*

The LCD is accessed as matrix 5 x 8 dots that include cursor. It also has a built-in controller (KS 0066 or Equivalent). The LCD is powered up with the help of a + 5V power supply (Also available for + 3V). This is also characterized with 1/16 duty cycle. Note that the +4.2V for LED or the Negative Voltage (N.V.) is



optional for +3V power supply. The LEDs can be driven by pin 1, pin 2, pin 15, pin 16 or A and K. FFC and FFC connector is for LCD-020M004B only.

*d. RFID (Radio Frequency Identification)*

RFID systems consist of three components in two combinations: a transceiver (transmitter/receiver) and antenna are usually combined as an RFID reader. A Transponder (transmitter/responder) and antenna are combined to make an RFID tag. An RFID tag is read when the reader emits a radio signal that activates the transponder, which sends data back to the transceiver.

There are two types of transponders, which correlate to the two major types of RFID tags.

- *Passive* transponders and RFID tags have no energy source of their own, relying on the energy given off by the reader for the power to respond. Cheaper, passive RFID tags are the most likely to be used for consumer goods.
  
- An *active* transponder or tag has an internal power source, which it uses to generate a signal in response to a reader. Active transponders are more expensive than passive ones. They can communicate over miles like ordinary radio communications. They are commonly used in navigation systems for commercial and private aircraft.

*CHIPS AND DATA*

The RFID tag stores data on a tiny computer chip. The cheapest and most common chip will be the read-only chip, which is likely to carry only a serial number. More expensive “read-write” chips allow new information to be added to the tag or written over existing information when the tag is within range of a reader.

Writeable chips will be useful in some specialized applications such as maintaining maintenance records for vehicles or appliances, but they are more expensive than read-only chips and impractical for tracking less expensive items.

**5. IMPLEMENTATION DETAILS**

The source code for the application of the system is developed in Embedded C language implemented in Keil  $\mu$ Vision4[5] IDE. The basic design of the basic combinational circuit is implemented in Cadence OrCAD Lite 16.5[7]. System architecture is realized in a development environment with its development done virtually using Proteus ISIS 7[5]. The layout of the entire system will be minimized, in comparison with the previous system.



## 6. SYSTEM ARCHITECTURE

The RFID reads the tag through the antenna provided and the data is communicated through the MAX232 IC, where the RS232 signal is converted into TTL logic signals via UART.

The MAX563 IC on the ARM development board receives these input signals and transmit it to the LPC2148 controller of the ARM and the display is enabled through the ports P1.16 to P1.23 i.e the data lines through which the data is sent to the display to be displayed.

- P0.15 is set for the buzzer/alarm.
- The driver ULN2003 communicates with the ARM through the ports P0.4 to P0.7. This controls the rotation of the stepper motor thus indicating the opening and the closing of the door of the bus.
- IC UM91215B represents the DTMF encoder which encodes the sinusoidal tone generated when an individual key on the DTMF keypad is pressed.
- This encoded data is decoded by using the DTMF decoder IC MT8870 which sends the signal respective of that key in the DTMF keypad to the LPC2148 controller of the ARM for the processing.
- A supply of +12V for the stepper motor to run and +5V for the DTMF keypad and the DTMF decoder is required.

## 7 CONCLUSION

The BUS TICKETING USING PRE-PAID CARDS was realized using the ARM processor(LPC2148 controller)with a Stepper Motor for the opening and the closing of the door of the bus and an HD44780U LCD display to guide through the process of accessing the entry with the help of an RFID card. When the power of the entire circuit was turned on and the unique RFID card was scanned, then the ARM processor process the data stored within the card of the user and allows the user to access the entry into the bus through the correct procedures and the correct inputs given by the user. When the entire process is done with this the ARM processor then commands the Stepper Motor to rotate thus indicating the opening of the door of the bus, as it rotates to an angle of 45°.

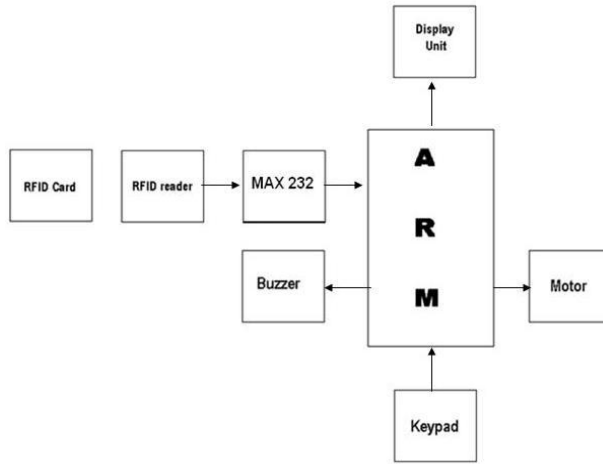


Figure 2. Block Diagram of the system (for demo purpose keypad is used)

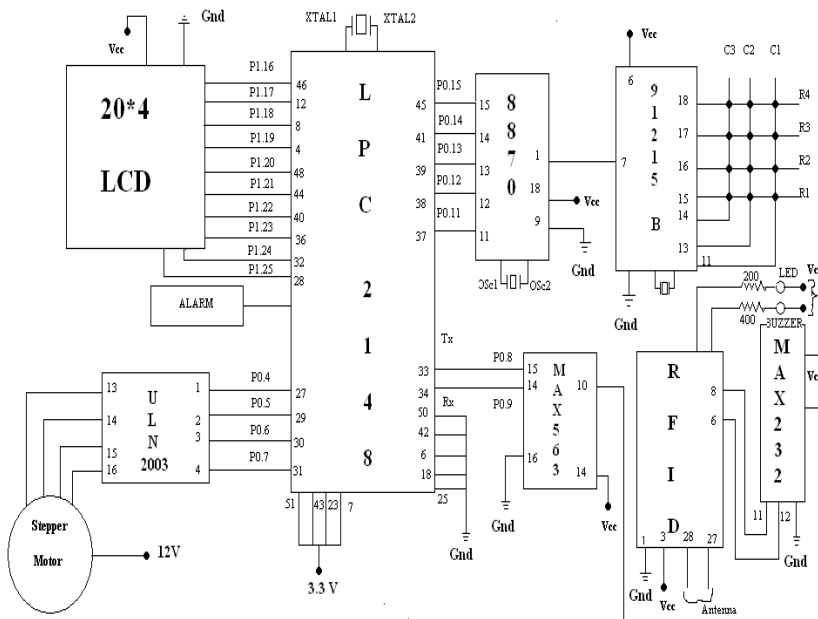


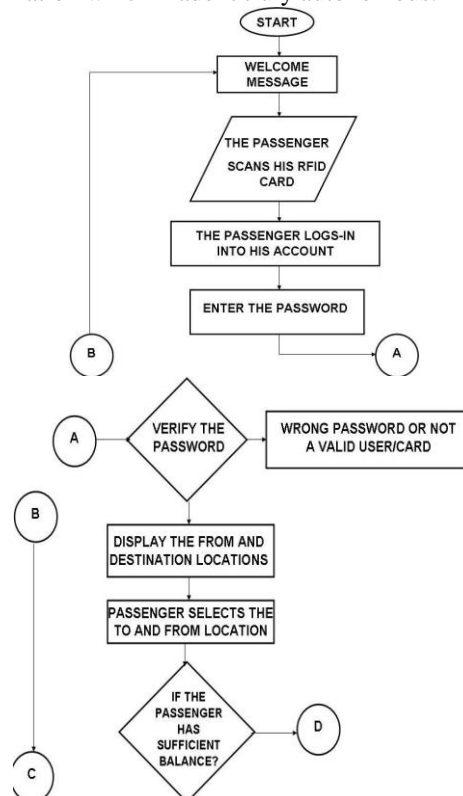
Figure 3. Circuit Diagram of the system (keypad is used only for the demo purpose)

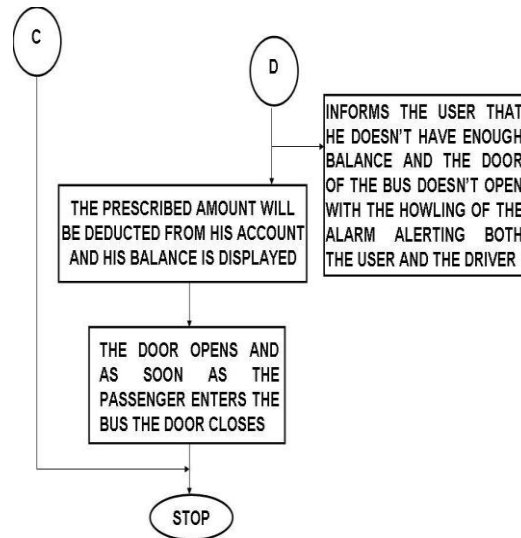


## 7. RESULTS

Once done with the programming, and burn the compiled program into the controller as explained above, we could test the following results on from the system designed and could achieve nearly 80% of the output through this system which includes the following results:

- The autonomous system followed the pre-defined path smoothly.
- It scanned the user/passenger RFID card and the processing was done successfully by the ARM7TDMI processor with the controller LPC2148 and displayed the proper messages after its scanning to the system.
- After the user/passenger entered or selected the from and destination locations from the list displayed, using the DTMF Keypad(This keyboard facility was for the demo purpose), the door of the bus opens and this is done with the help of the stepper motor, with its successful running.
- The alarm/buzzer also worked perfectly when the user didn't had the appropriate balance.
- All the components in the system worked completely in synchronization which made it truly autonomous.





## REFERENCES

- [1]. McCartney, "New Vehicle Security Assessment -A Practical Insurance Approach", European Convention on Security and Detection, May 1995, pp.239-243.
- [2]. .lie Yang, William Kunz, and Xilin Chen, "A PDA-Based Face Recognition System", Proceeding of Applications of Computer Vision in IEEE Workshop, 2002, pp. 1-5.
- [3] Kushal. K. S, Chetan. S, Shivaputra "Design and Implementation of A Smart AuTomated OUT-ward (SAT OUT)System using ARM processor for Aircrafts", Proceeding of Fourth International Conference on Computational Intelligence and Communication Networks in IEEE, 2012, pp 463-467
- [4]David Seal, Addison-Weasley, "ARM Architecture Reference Manual".
- [5]"DTMF Encoder UM9121XXX series", Article by United Microelectronics.
- [6]Steve Furber, "ARM System-on-chip Architecture", Second edition.
- [7]"RFID Tags and Privacy: How Bar-Codes-On-Steroids Are Really a 98- Lb. Weakling", Article by Jim Harper
- [8] "RFID: Innovative Silicon IDIC Solutions", by ATMEL
- [9] Nios II Software Developer's Handbook





## On the Quantitative Aspects of the Asymmetry Coefficients as Indicators of Order and Chaos

Dumitru D. Deleanu

Maritime University of Constanta, Romania  
E-mail: dumitru.deleanu@yahoo.com

**Abstract:** Recently, a simple, very fast and easy to compute qualitative indicator of the chaotic or ordered nature of orbits in dynamical systems was proposed by Waz et al (2009), the so-called “Asymmetry coefficients”. The indicator has been obtained from an analysis of the statistical behavior of an ensemble derived from the time dependence of selected quantities characterizing the system’s motion. It was found that for an ordered orbit the indicator converges to zero while for a chaotic orbit no sign of convergence can be observed. Using the Henon-Heiles Hamiltonian system and the Smaller Alignment Index method, in our paper we proposed a numerical criterion in order to quantify the results obtained by the “Asymmetry coefficients” method. This criterion helped us to define threshold values between regularity and chaoticity and to construct detailed phase-space portraits, where the ordered and chaotic regions are clearly distinguished. Additionally, exploiting the rapidity of the method, we showed how it can be used to identify “sticky” orbits or tiny regions of order and chaos.

**Keywords:** asymmetry coefficients, ordered and chaotic orbits, hamiltonian systems.

### 1. Introduction

A long-standing fundamental issue in nonlinear dynamics is to determine whether an orbit is regular or chaotic. This distinction is of great interest because in the case of regular orbits we have predictability in time whereas for chaotic orbits we are unable to predict the time evolution of the dynamical system after a short time period. There are many methods and indicators for chaotic motions. The well-known are the phase space method, the time series method, bifurcation diagram, the Poincare section of surface, Frequency-map analysis, Lyapunov characteristic exponents, and most recently the Fast Lyapunov indicator, the 0-1 test, the Dynamic Lyapunov indicator, and the Smaller alignment Index [1-6]. However, none of the methods has the merits to be beyond any doubt. Most of them, especially the so-called “traditional” tools, work hard in systems with many degrees of freedom, where phase space visualization is no longer easily accessible. The recent tools seem to be more efficient and faster than the older ones, but each of them has its weak points. This is the reason that motivates the researchers in the field to search better methods.

In 2009, Waz et al. proposed an alternative, very simple and related to the observational data, statistical indicator of chaos [7]. In their approach the values of a time dependent function describing the studied motion are recorded in a sequence of time intervals and each of these recordings are considered statistical distributions. Then, the “asymmetry coefficients” of these distributions are



defined and their behavior for ordered and chaotic orbits is analyzed. Their qualitative indicator was applied only in the simple case of the damped driven pendulum. In present paper we have attempted to improve their work by proposing a numerical criterion associated to asymmetry coefficients, which helped us to reveal the detailed structure of the dynamics in the phase space of the Henon-Heiles Hamiltonian system.

The organization of rest of the paper is as follows. Section 2 contains that information strictly required for understanding the “Asymmetry coefficients” and SALI methods. All calculations and numerical results are given in Section 3. The final remarks and conclusions are presented in Section 4.

## 2. Description of methods

For the sake of completeness let us briefly recall the definition of the “Asymmetry coefficients” and of the “Smaller Alignment Index (SALI)” and their behavior for regular and chaotic orbits. The interested reader can consult [7, 8] to have a more detailed description of the methods.

### 2.1. Method of the Asymmetry Coefficients

Let  $X(t)$  be a function characterizing the motion we are going to analyze. Usually, in practical applications,  $X(t)$  is known as a part of the solution of a differential system of equations or from experimental measurements, so its values are given in a discrete set of points  $\{X_i\}$ . Let us define a time series  $X_k(t) = \{X(t), t \in (T_0, T_{f_k}) / k = 1, 2, \dots, K\}$  with a fixed  $T_0$  and  $T_{f_1} < T_{f_2} < \dots < T_{f_K}$ . The terms of the series are treated as statistical distributions. The starting time  $T_0$  and the final one  $T_{f_K}$  denote the beginning and the end of the  $k$ -th distribution  $X_k(t)$ .

The asymmetry coefficients of the discrete  $k$ -th distribution  $X_k$  are defined as

$$A_q(k, N_k) = S(k, N_k) \cdot \sum_{i=1}^{N_k} \left( X_{t_i^k} + c \right) \left[ \frac{t_i^k - M_1(k, N_k)}{\sqrt{M_2(k, N_k) - M_1^2(k, N_k)}} \right]^q$$

$$S(k, N_k) = \left[ \sum_{i=1}^{N_k} \left( X_{t_i^k} + c \right) \right]^{-1} \quad (1)$$

$$M_n(k, N_k) = S(k, N_k) \cdot \sum_{i=1}^{N_k} \left( X_{t_i^k} + c \right) \cdot \left( t_i^k \right)^n, \quad n \in \{1, 2\}$$

$q = 2j + 1, j = 1, 2, 3, \dots$  and  $c$  is a constant.  $N_k$  is the number of points in the  $k$ -th distribution, i.e.  $t_i^k = \tau_i, i = 1, 2, \dots, N_k, k = 1, 2, \dots, K$ , with  $t_1^k = T_0$ ,



$t_{N_k}^k = T_{f_k}$ ,  $N_1 < N_2 < \dots < N_K$ . Since  $T_0$  is the same for all  $k$ , the length of the  $k$ -th distribution is proportional to  $N_k$ .

Waz et al shown that the qualitative results are the same for all  $c$  chosen so  $X_k(t) + c \geq 0$ . Using the damped driven pendulum, they demonstrated that for a periodic motion the asymmetry coefficients approach zero while  $T_f$  approaches infinity. For a chaotic orbit no regular asymptotic behaviour was observed. It results a qualitative indicator regarding the nature of an orbit. We proceeded one step further by introducing a quantitative criterion. Calculating for about one thousand orbits the maximum value of  $|A_q|$ ,  $q = 3, 5, 7$  when  $t \in [500 s, 1000 s]$ , we proposed for every asymmetry coefficient a threshold value between regularity and chaoticity, as Section 3 will demonstrate.

## 2.2. Method of the Smaller Alignment Index

Consider a  $n$ - dimensional phase-space of a dynamical system and an orbit in that space. In order to determine if this orbit is ordered or chaotic we follow the evolution in time of two different initial deviation vectors  $\xi_1(0), \xi_2(0)$ . In every time step, we compute the parallel/ anti-parallel alignment index (ALI),

$$d_-(t) = \left\| \frac{\xi_1(t)}{\|\xi_1(t)\|} - \frac{\xi_2(t)}{\|\xi_2(t)\|} \right\| \quad \text{and} \quad d_+(t) = \left\| \frac{\xi_1(t)}{\|\xi_1(t)\|} + \frac{\xi_2(t)}{\|\xi_2(t)\|} \right\|, \quad \text{where } \|\cdot\| \text{ denotes}$$

the Euclidean norm of a vector. The Smaller Alignment Index (SALI) is defined as the minimum value of the above alignment indices at any point in time

$$SALI(t) = \min(d_-(t), d_+(t)) \quad (2)$$

Skokos shows that the two deviation vectors tend to coincide or become opposite for chaotic orbits, i.e. the SALI tends to zero. For ordered orbits, which lie on a torus, the two deviation vectors eventually become tangent to the torus, but in general converge to different directions, so the SALI does not tend to zero. Its values fluctuate around a positive value.

## 3. Numerical results

We consider the two degrees of freedom Henon-Heiles Hamiltonian

$$H_2(x, y, p_x, p_y) = \frac{1}{2}(p_x^2 + p_y^2) + \frac{1}{2}(x^2 + y^2) + x^2 y - \frac{1}{3}y^3 \quad (3)$$

where  $x, y$ , and  $p_x, p_y$  are the coordinate and conjugate moments respectively.

The equations of motion derived from the Hamiltonian are

$$\dot{x} = \frac{\partial H}{\partial p_x} = p_x, \quad \dot{y} = \frac{\partial H}{\partial p_y} = p_y \quad (4a)$$

$$\dot{p}_x = -\frac{\partial H}{\partial x} = -x - 2xy \quad , \quad \dot{p}_y = -\frac{\partial H}{\partial y} = -y - x^2 + y^2 \quad (4b)$$

and yields solutions (orbits) of the system evolving in a four dimensional phase space. In our study we keep the value of the Hamiltonian fixed at  $H_2 = 0.125$ .

We consider first two representative orbits: an ordered (quasi-periodic) orbit with initial conditions  $(x, y, p_x, p_y) = (0.0, 0.55, 0.2417, 0.0)$  and a chaotic orbit with initial conditions  $(x, y, p_x, p_y) = (0.0, -0.016, 0.49974, 0.0)$ .

Figure 1a shows the Poincare surface of section (PSS) of the two orbits defined by  $x = 0, p_x \geq 0$ . The points of the ordered orbit (blue points) form a set of smooth curves while the points of the chaotic orbit (red points) appear randomly scattered. The  $\log_{10}(SALI)$  of the ordered orbit (blue line in Figure 1b) fluctuates around 0.05, indicating the regular character of the orbit, while the  $\log_{10}(SALI)$  of the chaotic orbit (red line in Figure 1b) falls abruptly reaching the limit of the accuracy of the computer precision ( $10^{-16}$ ) after about 1700 time units.

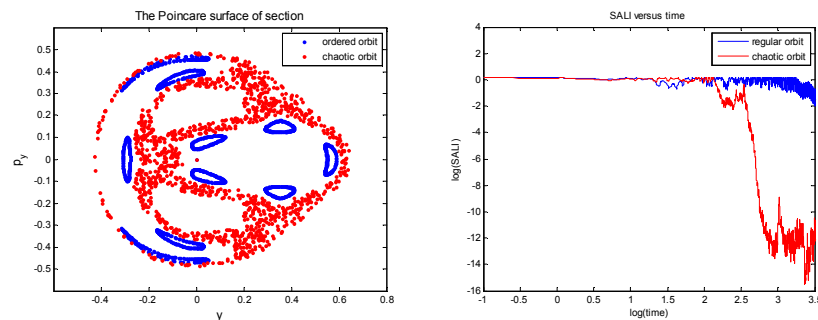


Fig.1. a) The PSS of an ordered orbit (blue points) and a chaotic orbit (red points); b) The time evolution of the SALI for the same orbits

The calculations of the asymmetry coefficients have been performed in equidistant points of the time interval  $t \in [0s, 4000s]$ . The origin of each distribution corresponds to the initial time  $T_0 = 0$  whereas the final points of the distributions have been selected as  $T_{f_k} = 0.2k, k = 1, 2, \dots, 20000$ . The time step on each interval was equal to 0.02 s and  $c$  was taken as  $-\min X_k(t)$ . In addition,  $X(t) = x(t)$ .

Figure 2 depicts the asymmetry coefficients  $A_q, q = 3, 5, 7$  as function of time. For the periodic orbit (blue lines) the coefficients  $A_q$  converge to 0, after a

short transition period (about 300s). A irregular behaviour of  $A_q$  could be seen for the chaotic orbit (red lines). As it was proved in [8], the qualitative results are the same for all  $c$  that satisfy the condition  $X_k(t) + c \geq 0$ , for all  $t$ , and for any other component of the dynamical system (here,  $y$ ,  $p_x$  or  $p_y$ ).

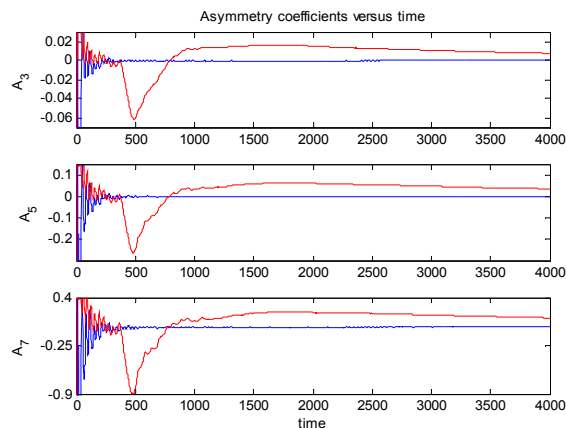


Fig. 2. The asymmetry coefficients  $A_q$ ,  $q = 3, 5, 7$  for the ordered orbit (blue lines) and for the chaotic orbit (red lines) discussed in Figure 1

In order to present the effectiveness of the quantitative indicator proposed in Section 2 (the maximum value of  $|A_q|$ ,  $q = 3, 5, 7$  when  $t \in [500 s, 1000 s]$ , hereafter noted by  $\max|A_q|$ ) in detecting regions of chaos and order we computed it for a large grid of equally distributed initial conditions on the axis of PSS ( $y, p_y$ ) of the Henon-Heiles system. To do this, we chose 440 initial conditions on the line  $p_y = 0$  of the PSS, between  $y = -0.43$  and  $y = 0.67$  with step  $\Delta y = 0.0025$ , and 400 initial conditions on the semi-line  $y = 0, p_y > 0$  (because of symmetry) of the PSS, between  $p_y = 0$  and  $p_y = 0.5$  with step  $\Delta p_y = 0.00125$ . Figure 3 shows the SALI values for these orbits. The running time for every orbit was  $T = 1,000$  time units. We assigned a coloured circle to every individual initial condition according to the value of the SALI: if it was smaller than  $10^{-8}$  the circle was coloured red (the orbit is chaotic beyond any doubt). If  $\text{SALI} \in [10^{-8}, 10^{-4})$  the circle was coloured yellow (the orbit is probably “sticky” chaotic) and finally, if  $\text{SALI} \in [10^{-4}, 2)$  it was coloured bleu (the orbit is ordered). To clear up the nature of the orbits

having  $SALI \in [10^{-8}, 10^{-4})$  and to verify if the running time  $T = 1,000$  time units is sufficient for asymmetry coefficients to reveal the type of the orbits we computed the  $\max|A_q|, q = 3, 5, 7$  for  $T = 1,000$  and  $T = 4,000$ , respectively. The results for  $\max|A_7|$  only are presented in Figure 4 (for semi-line  $y = 0, p_y > 0$ ) and Figure 5 (for line  $p_y = 0$ ).

There are some observations that are worth mentioning. Firstly, the CPU time needed to obtain the results plotted in Figure 3 was twenty times greater than for the results depicted in Figures 4a and 5a. Secondly, comparing Figure 3 with Figures 4b and 5b a similitude between them is easy to observe. In fact, every orbit with  $\max|A_7| \geq 0.1$  has  $SALI \leq 10^{-4}$  (therefore is chaotic) and all orbits having  $\max|A_7| < 0.1$  are characterized by  $SALI > 10^{-4}$  (they are ordered). Finally, we point out that a too short running time (here,  $T = 1,000$ ) might give erroneous results concerning the “sticky” orbits.

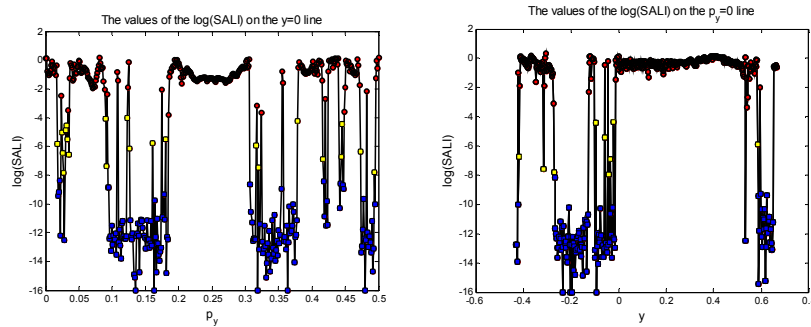


Fig. 3. The SALI values for initial conditions chosen on the semi-line  $y = 0, p_y > 0$  (left panel) and on the line  $p_y = 0$  (right panel)

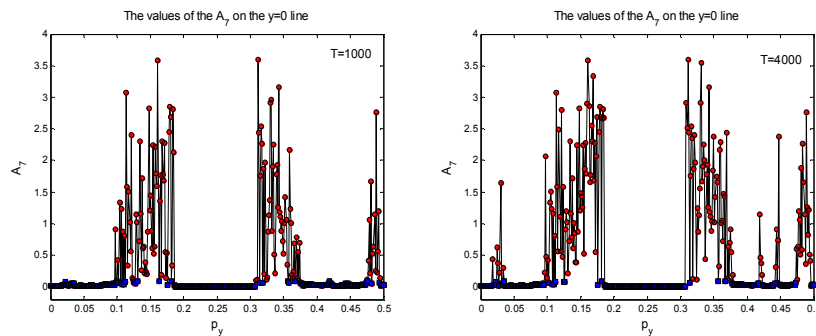


Fig. 4. The  $\max|A_7|$  values for initial conditions chosen on the semi-line  $y = 0, p_y > 0$  ( $T=1,000$  - left panel;  $T=4,000$  - right panel)

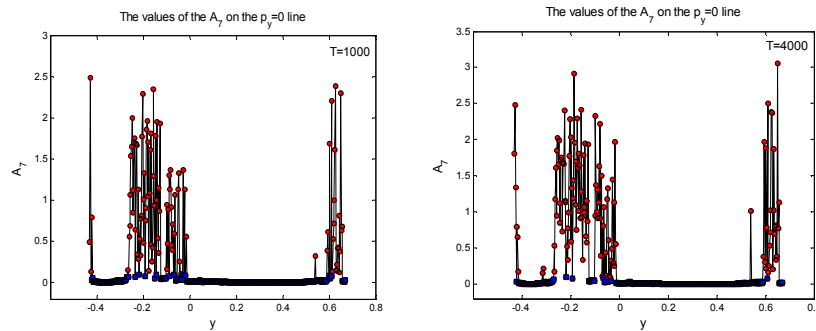


Fig. 5. The  $\max|A_7|$  values for initial conditions chosen on the line  $p_y = 0$  (T=1,000 - left panel; T=4,000 - right panel)

The same remarks are valid for the others asymmetry coefficients,  $A_3$  and  $A_5$ . We propose as threshold values between regularity and chaoticity the value 0.005 for  $\max|A_3|$  and 0.025 for  $\max|A_5|$ .

Let us now return to the “sticky” orbits that make the difference between the two panels of Figures 4 and 5. In order to illustrate the capability of the asymmetry coefficients to identify these kinds of orbits we considered a set of three orbits with very closely initial conditions on the axis  $p_y = 0$  and computed the coefficient  $A_7$  for T=12,000 time units. Figures 6 and 7 present our findings. When T=4,000 time units, one can see that the PSSs of these orbits are practically indistinguishable and indicate ordered orbits. The first visible deviations from these smooth curves appeared for  $T \cong 5,000$  time units, as Figure 7 shown. When T=12,000 time units two of these orbits clearly entered in the chaotic sea, while the third remained ordered.

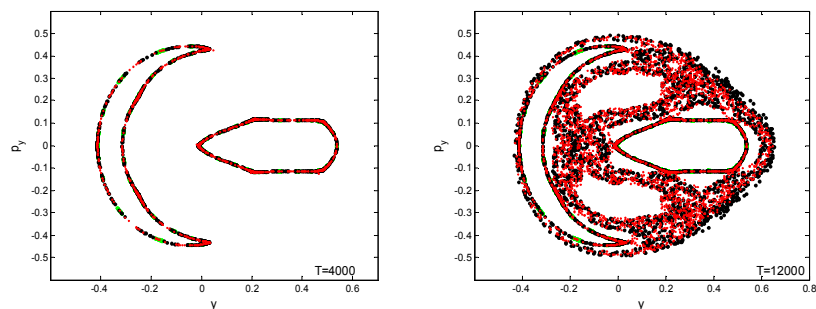


Fig. 6. The PSS of an ordered orbit (green points) and two “sticky” orbits (black and red points); T=4,000 – left panel, T=12,000 – right panel

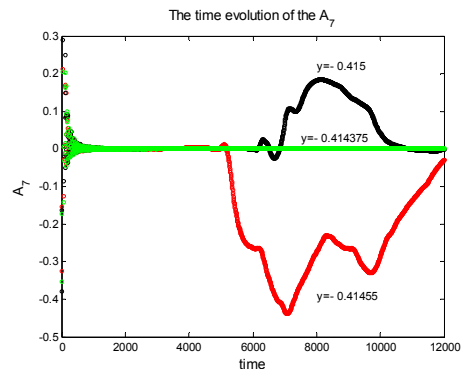


Fig. 7. The asymmetry coefficient  $A_7$  for the ordered orbit (green line) and for the “sticky” orbits (black and red lines) discussed in Figure 6

### 3. Conclusions

In this paper we have illustrated the capability of the “Asymmetry coefficients” method in distinguishing between order and chaos in Henon-Heiles Hamiltonian system. Besides the fact that our calculations have validated the qualitative results obtained by Waz et al, we proposed a numerical criterion in order to quantify these results. Exploiting the rapidity of the method, we constructed detailed phase-space portraits and defined threshold values between regularity and chaoticity. Additionally, we showed how it can be used to identify “sticky” orbits or tiny regions of order and chaos.

### References

1. G.L. Baker, J.P. Gollub, Chaotic Dynamics: An Introduction, *Cambridge University Press, New York*, 1990.
2. C. Froeschle, E. Lega, R. Gonczi, Fast Lyapunov Indicator. Application to asteroidal motion, *Celest. Mech. Dyn. Astron.*, vol. 67, 41-62, 1997.
3. G.A. Gottwald, I.A. Melbourne, A new test for chaos in deterministic systems, *Proc. Roy. Soc. London*, vol. 460, 603-611, 2004.
4. N. Maffione, L. Darriba, P. Cincotta, C. Giordano, A comparison of different indicators of chaos based on the deviation vectors, *Celest. Mech. Dyn. Astron.*, vol. 111, 285-307, 2011.
5. Z. Sandor, B. Erdi, A. Szell, B. Funk, The Relative Lyapunov Indicator: an efficient method of chaos detection, *Celest. Mech. Dyn. Astron.*, vol. 90, 127-138, 2004.
6. A. Wolfe, B. Swift, H.L. Swenney, J.A. Vastano, Determining Lyapunov exponents from a time series, *Physica D* 16, 285-317, 1985.
7. Ch. Skokos, Alignment indices: a new, simple method for determining the ordered or chaotic nature of orbits, *J. Phys. A: Math. Gen.*, vol. 34, 10029-10043, 2001.
8. P. Waz, D.D. Waz, Asymmetry coefficients as indicators of chaos, *Acta Physica Polonica*, vol. 116, 987-991, 2009.



## Wavelet Analysis of the Human Brain Lability to Reproduce the External Rhythm

Olga E. Dick

Pavlov Institute of Physiology of Russian Academy of Science, St. Petersburg, Russia

E-mail: [glazov.holo@mail.ioffe.ru](mailto:glazov.holo@mail.ioffe.ru)

**Abstract:** The task is to evaluate the differences in the human brain lability involving its opportunity to forget or reproduce the external rhythm for patients with neural disorders connected with disruptions of the thalamo-cortical or stem-cortical links. For solving the task the EEG segments before, during and after periodic light stimulation are examined by the wavelet transform method. The degree of the human brain lability is estimated by changing in the maximums of the global wavelet spectra and by the coefficients of reproduction and holding the rhythm. Maximal reproduction of the external frequency is observed in the ranges specific for the both groups of the patients. For the patients with stem-cortical disruptions the all parameters essentially differ from the parameters obtained for the patients with thalamo-cortical disorders. Thus, the study demonstrates the possibility of the wavelet analysis to estimate quantitatively the human brain lability of perception of light stimuli.

**Keywords:** EEG, Wavelet transform, Reproduction of external rhythm.

### 1. Introduction

Bioelectrical activity of the human brain recorded from the head surface as electroencephalography time series (EEG) during solving the complex imaginary and real visual-motor tasks or during awake and various sleep stages in healthy state exhibits nonstationary, chaotic and multifractal dynamics [1, 2, 3]. The comparative analysis of the dynamics in EEG patterns of normal and pathological brain activities is one of the tools of elucidation of the degree the brain seizures [4, 5] and estimation of the efficiency of the drug or psychological treatment [6]. Photostimulation, that is the light stimulation of the given frequency, is one of the functional probes applied for determining of the human brain lability to reproduce or to reject the suggested rhythm [7]. The degree of such lability characterizes the level of nerve excitability and can classify persons for whom drugs hyperactivating the nervous system are unsuitable due to their own hyperexcitability.

The aim of the work is to evaluate the differences in the potentialities of the human brain to forget or reproduce the external light rhythm for patients with chronic pain complaints rather resistant to medicinal treatment. These patients can be divided into two groups accordingly to the classification connected with the disruptions on the thalamic level or on the brain-stem level that leads as a rule to changing the thalamo-cortical links in the first case and the stem-cortical links in the second case [8]. It results to the significant suppression of the alpha component prevailing for the healthy persons and the emergence of the theta



activity or occurrence of polymorphous small amplitude activity, that is, to essential deviation from the healthy EEG patterns.

## 2. Experimental procedure

The scalp EEG data were recorded with Ag/AgCl electrodes from 10 healthy subjects and 16 patients with neural impairments connected with chronic pain complaints. Signals of reproducing the light rhythm propagate symmetrically and have maximal amplitude in the occipital lobes of the human brain, that is why the data were collected with electrodes placed at the occipital O1, O2, Oz sites. The recordings were obtained for three states: before the light rhythmic stimulation (the interval  $[0, t_A]$ ), during it (the interval  $[t_A, t_B]$ ) and during relaxation (the interval  $[t_B, t_K]$ ) with eyes closed. The duration of each interval was 20 seconds. The data were sampled at a rate 256 samples/sec with a resolution of 12 bits/sample. Then the data were digitally filtered using 1–30 Hz band pass filter. After repeated recordings 60 non-artifact segments of equal duration were randomly chosen from the sets: “before stimulus”, “during stimulus” and “during relaxation”.

## 3. Estimation of the global energy of the EEG segment

To estimate the global energy of EEG segment we applied the continuous wavelet transform of a time series  $x(t)$ :

$$W(a, t_0) = \frac{1}{a} \int_{-\infty}^{+\infty} x(t) \psi^* \left( \frac{t - t_0}{a} \right) dt,$$

where  $a$  and  $t_0$  are the scale and space parameters,  $\psi((t - t_0)/a)$  is the wavelet function obtained from the basic wavelet  $\psi(t)$  by scaling and shifting along the time, symbol \* means the complex conjugate. As the basic wavelet we use the complex Morlet wavelet:

$$\psi(t) = D \exp(-0.5t^2) [\exp(-i\omega_0 t) - \exp(-0.5\omega_0^2)],$$

$$D = \frac{\pi^{-1/4}}{\sqrt{1 - 2 \exp(-0.75\omega_0^2) + \exp(-\omega_0^2)}}.$$

The value  $\omega_0 = 2\pi$  gives the simple relation between the scale  $a$  and frequency  $f$ :  $f = 1/a$ .

The square of the modulus  $|W(f, t_0)|^2$  characterizes the instantaneous distribution of energy over frequencies at the time  $t_0$ , that is, the local spectrum of the signal energy.



The value 
$$E(f) = \int_{t_1}^{t_2} |W(f, t_0)|^2 dt_0$$

describes the global wavelet spectrum, i.e., the integral of energy distribution over frequency range on the interval  $[t_1, t_2]$ .

The value

$$E(t_0) = \int_{f_1}^{f_2} |W(f, t_0)|^2 df$$

represents the integral of energy distribution over time shifts in the frequency range  $[f_1, f_2]$ .

#### 4. The light time series

The light time series limited on the interval  $[t_A, t_B]$  was described as a sequence of  $k$  Gauss impulses following each other with frequency  $f_C$  equal to 4, 6, 8, 10, or 16, 20 Hz. The each impulse had the width  $r_0 = 10$  ms. The centres of the impulses were in points

$$t_{0i} = t_A + i / f_C, \quad i = 0, \dots, k-1,$$

where  $t_A$  is the time of switching of the light series, that is the time of the beginning of the first impulse in the sequence.

Thus, the light stimulus can be described as

$$p(t) = \sum_{i=0}^{k-1} \frac{0.5}{r_0 \sqrt{\pi}} \exp\left(-\frac{(t-t_{0i})^2}{4r_0^2}\right).$$

The continuous wavelet transform of the light time series  $p(t)$  can be calculated in the form:

$$W(f, t_0) = \frac{Df}{\sqrt{s}} \exp\left(-\frac{z^2 + 2(\omega_0 f r_0)^2}{2s}\right) \left[ \exp\left(-\frac{i\omega_0 z}{s}\right) - \exp\left(-\frac{i\omega_0^2}{2s}\right) \right],$$

where  $s = 1 + 2(fr_0)^2$ ,  $z = f(t-t_0)$  is non-dimensional time measured from time  $t_0$ .

#### 5. Estimation of the coefficients of reproduction and holding the rhythm

Let  $E_{X1}(\Delta f)$  and  $E_{X2}(\Delta f)$  be the global wavelet spectra of the EEG time series in the frequency range  $\Delta f$  over the intervals  $[0, t_A]$  and  $[t_A, t_B]$ , i.e. before and during photostimulation.

The reproduction coefficient of the suggested rhythm can be estimated as the ratio of the maximum of the global spectrum during the light time series to the maximum of the global spectrum before photostimulation:

$$k_R(\Delta f) = \max E_{X2}(\Delta f) / \max E_{X1}(\Delta f).$$

If the frequency value corresponding to the  $\max E_{X2}(\Delta f)$  does not coincide with the light time series frequency  $f_C$  then there is no reproduction of the rhythm in the range  $\Delta f = f_C \pm \Delta$ , where  $\Delta = 0.5$  Hz. The larger  $k_R(\Delta f)$  value, the better the reproduction of the suggested rhythm.

Let us  $E_X(t)$  and  $E_P(t)$  denote the normalized integral distributions of energies of the EEG and light time series in the frequency range  $[f_1, f_2]$ :

$$E_X(t) = E_X(t) / \max E_X(t) \text{ and } E_P(t) = E_P(t) / \max E_P(t).$$

Examples of the normalized integral distributions  $E_X(t)$  and  $E_P(t)$  for  $f_C = 4$  Hz are given in Fig. 1.

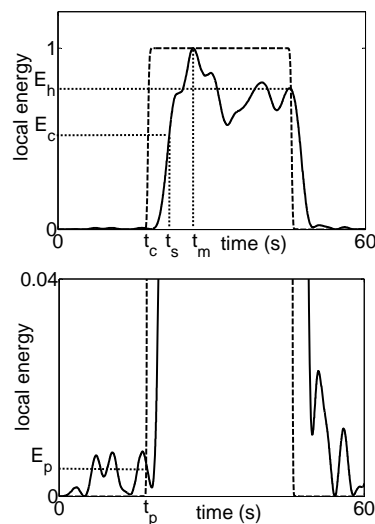


Fig. 1. The normalized energy distributions of the EEG time series (solid line) and the light time series (dashed line). The lower figure is represented in the enhanced scale to see the point  $(t_p, E_p)$  of intersection of the integrals  $E_X(t)$  and  $E_P(t)$ .

The integrals  $E_X(t)$  and  $E_P(t)$  cross each other in two points  $(t_p, E_p)$  and  $(t_h, E_h)$  after switching on and switching off the light time series.

The value  $E_h$  is taken as the coefficient of holding the suggested rhythm;

$$k_H(\Delta f) = E_h(\Delta f).$$



The smaller the value, the more badly the rhythm of photostimulation is kept by the human brain.

### **6. Estimation of the time of remembering the external rhythm and the delay time of the brain response on the rhythm**

If the EEG response on the light time series reaches the maximal value at the moment  $t_m$ , then the difference

$$T_R(\Delta f) = t_m(\Delta f) - t_p(\Delta f)$$

can characterize the time of remembering the rhythm. The smaller the value, the faster the brain begins to generate the external frequency.

The delay time of the EEG response from the moment of switching on the light time series can be estimated as

$$T_D(\Delta f) = t_s(\Delta f) - t_c(\Delta f),$$

where  $t_c$  is the moment when the condition

$$E_C(\Delta f) = 0.5 (1 - E_p(\Delta f))$$

is satisfied.

### **7. Results and discussion**

The examples of global wavelet spectra of EEG for the healthy subject and patients with changes in the stem-cortical or thalamo-cortical links in two functional states, namely, before and during the light stimulation are given in Fig. 2.

The spectra calculated in the broad frequency range [2, 20] Hz differ by the width as well as by the position and value of maximum. In the rest state with closed eyes the EEG time series of a healthy person is characterized by narrow frequency interval [8, 16] Hz and the large value of the global energy, maximum of which is equal to  $5 \cdot 10^4 \mu V^2$ .

The disruptions of neuronal links on the brain-stem level are exhibited in the form of polymorphous activity of the smaller amplitude and broaden frequency range [0, 12] Hz.

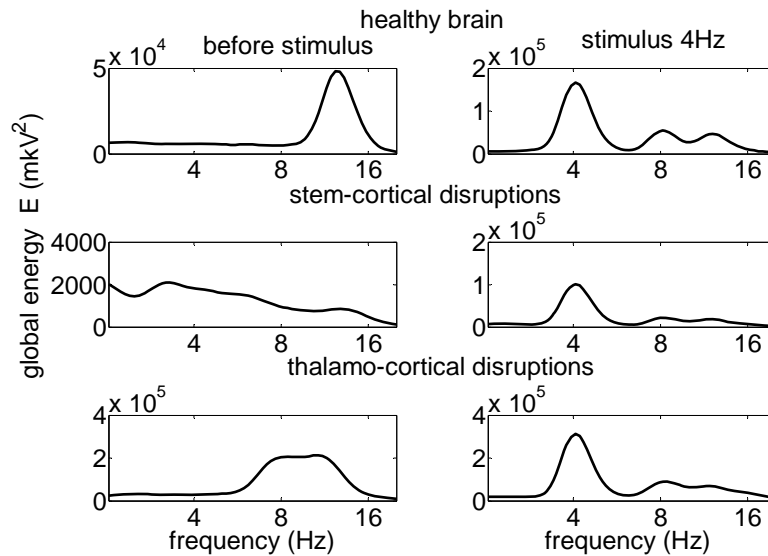


Fig.2. Examples of global wavelet spectra of EEG for the healthy subject and two groups of patients before and during the light time series of  $f_c = 4$  Hz.

The maximal global energy is 10 times less than the value obtained for the healthy person.

The thalamo-cortical disruptions are manifested by the extended spectrum in the frequency interval [6, 14] Hz and the significant increase (almost in 10 times) as compared with the maximum of the global spectrum for the healthy brain and in 100 times in comparison with the global energy for the stem-cortical disruptions.

The light stimulus of frequency 4 Hz leads to the emergence of the detectable maximums in all the considered cases. The value of the global energy increases in 4 times for the healthy subject and in 1.5 times for the patient with thalamo-cortical disorders. This value grows in almost 100 times for the patient with stem-cortical defects.

The occurrence of the visible maximum of the global energy at the frequency of the external stimulus means the good reproduction of the suggested rhythm. Reproduction of the external rhythm is observed for all the subjects and the frequencies 4, 6, 8, 10 and 12 Hz and only for the healthy and persons with thalamo-cortical disruptions at 16 and 20 Hz.

The coefficients of reproduction ( $k_R(\Delta f)$ ) and holding ( $k_H(\Delta f)$ ) the rhythm estimated by the wavelet spectra are given in the Table 1.



The time of remembering the rhythm ( $T_R$  ( $\Delta f$ )) and the delay time of the EEG response from the moment of switching on the light time series ( $T_D$  ( $\Delta f$ )) are represented also in the Table 1.

$f_C = 4$ Hz				
	$k_R$	$k_H$	$T_R$ (s)	$T_D$ (s)
healthy	4.2±0.6	0.52±0.06	11.1±1.2	1.9±0.4
group 1	95±5	0.85±0.07	6.2±0.8	0.9±0.2
group 2	2.1±0.4	0.49±0.05	12.5±1.7	1.5±0.3
$f_C = 10$ Hz				
healthy	6.1±0.7	0.95±0.09	0.9±0.2	0.3±0.11
group 1	2.1±1.3	0.41±0.05	13.2±1.3	2.1±0.5
group 2	5.3±0.6	0.69±0.07	1.5±0.4	0.5±0.1
$f_C = 16$ Hz				
healthy	4.5±0.4	0.81±0.07	5.3±0.4	1.1±0.3
group 1	there is no reproduction of the rhythm			
group 2	3.7±0.3	0.77±0.06	7.1±0.8	2.1±0.5

Table 1. The comparison of the mean values averaged over 10 healthy subjects and 8 persons in each group of patients. The site is Qz. The patients with the thalamo – cortical disruptions are denoted as “group 1” and patients with the stem – cortical defects are depicted as” group 2”.

For each frequency of the light time series ( $f_C$ ) the both coefficients of reproduction and holding the rhythm are largest for the subjects who have the eigen oscillations at this frequency in the rest state.

The time of remembering the rhythm and delay of the EEG response from the moment of switching on the light time series are smallest in the presence of eigen oscillations. These times grow in the non-specific frequency range.

The spectra of the patients of two groups differ by four considered parameters. The stem – cortical defects are characterized by the absence of the external rhythm reproduction at frequencies larger than 16 Hz and the fast maintenance of the rhythm in the range [2, 6] Hz.

The EEG time series of the patients with the thalamo–cortical disruptions have the large eigen oscillations in the interval [6, 14] Hz and larger values of both coefficients  $k_R$  and  $k_H$  and smaller times  $T_R$  and  $T_D$  comparing with the EEG of the first group.

## Conclusion

The work supports that the human brain is a rather stable dynamic system and rearranges slowly on external rhythm of non-specified frequency range. The parameters found from the wavelet spectra give an opportunity to evaluate quantitatively the brain lability of perception of the light time series.



These parameters can help to estimate the nerve excitability level of a subject for the purpose of the appropriate drug treatment, that is, to exclude the drug administration hyperactivating the nervous system for patients with the enhanced personal excitability in the rest state.

### Acknowledgements

The author is thankful to Dr. I. A. Svyatogor for her help with EEG recordings.

### References

1. D. Popivanov, et. al. Multifractality of decomposed EEG during imaginary and real visual-motor tracking. *Biological Cybernetics* 94: 149-156, 2006.
2. M. A. Qianli, et al. A new measure to characterize multifractality of sleep electroencephalogram. *Chinese Science Bulletin* 51: 3059-3064, 2006.
3. A. M. Wink, et al. Monofractal and multifractal dynamics of low frequency endogenous brain oscillations in functional MRI. *Human Brain Mapping* 29: 791-801, 2008.
4. M. Nurujjaman, R. Narayanan and A. N. Sekar Iyengar. Comparative study of nonlinear properties of EEG signals of normal persons and epileptic patients. *Nonlinear Biomedical Physics* 3: 6-11, 2009.
5. G. E. Polychronaki, P.Y. Ktonas, S. Gatzonis, et. al. Comparison of fractal dimension estimation algorithms for epileptic seizure onset detection. *J. Neural Engineering* 7: 60-78, 2010.
6. O. E. Dick, I. A. Svyatogor. Potentialities of the wavelet and multifractal techniques to evaluate changes in the functional state of the human brain. *Neurocomputing* 82: 207-215, 2012.
7. S.V. Bozhokin. Wavelet analysis of dynamics of reproducing and forgetting the rhythms of photostimulation for nonstationary EEG. *J. Technical Physics* 80: 16-24, 2010 (in Russian).
8. O. E. Dick, I. A. Svyatogor. V. A. Ishinova, et al. Fractal characteristics of the functional state of the brain in patients with anxious phobic disorders. *Human physiology* 38: 249 -254, 2012.



## Competition of Scenarios of Transition to Chaos in Plasma – Experiment and Theoretical Modeling

Dan G. Dimitriu<sup>1</sup> and Maricel Agop<sup>2</sup>

<sup>1</sup>Faculty of Physics, “Alexandru Ioan Cuza” University, Iasi, Romania

<sup>2</sup>Department of Physics, “Gh. Asachi” Technical University, Iasi, Romania

E-mail: [dimitriu@uaic.ro](mailto:dimitriu@uaic.ro)

**Abstract:** We report on theoretical modeling of the competition of three scenarios of transition to chaos in plasma: by intermittencies, by cascade of sub-harmonic bifurcation and by quasi-periodicity (Ruelle-Takens scenario). This phenomenon was experimentally observed in plasma in connection with the dynamics of a fireball, by analyzing the time series of the oscillations of the current collected by the exciting electrode. By considering that the plasma's particles move on continuous but non-differentiable curves, *i.e.* on fractal curves, and applying the full and fractional revivals formalism, we developed a theoretical model, based on the scale relativity theory, able to explain the experimental results.

**Keywords:** Chaotic modeling, Intermittency, Quasi-periodicity, Sub-harmonic bifurcation.

### 1. Introduction

Plasma is a strong nonlinear dynamic system with many degrees of freedom, very favorable for development of instabilities and transition from ordered to chaotic states. Thus, a large variety of scenarios of transition to chaos were experimentally observed in plasma systems: intermittencies [1,2], period doubling (Feigenbaum scenario) [3,4], quasi-periodicity (Ruelle-Takens scenario) [5,6], or cascade of sub-harmonic bifurcations [7,8]. In many experimental situations, the transition to chaos of the plasma system state was associated to the nonlinear dynamics of a complex space charge structure developed in plasma in form of a fireball [2,8]. Fireball are intense luminous almost spherical structures in plasma, consisting of a positive inner core (ion-enriched plasma) confined by an electrical double layer [9,10]. Fireballs can be created in front of a positively biased electrode immersed into plasma, up to a threshold value of the applied potential. At higher values of the voltage on the electrode, the fireball passes into a dynamic state, consisting of periodic disruptions and re-aggregations of it, giving rise to oscillations of the current collected by the electrode [10].

In a series of articles [11-13], Pae and Hahn reported on a new phenomenon called attractor competing, consisting of coexistence of several dynamical states with the same initial conditions in a narrow region of the parameter space. The results were obtained by numerical simulation of the plasma dynamics in a modified Pierce-type diode. The observed attractors include chaotic attractors, so that three scenarios of transition to chaos were identified in the simulated time series: intermittency, period doubling cascade and quasi-periodicity. This



phenomenon was later explained as a noise-driven dynamical switch between attractors, occurring due to the noise fluctuations inside a system near the fractal basin boundaries [14].

Here we report on experimental results showing the competition of three scenarios of transition to chaos (intermittency, quasi-periodicity and cascade of sub-harmonic bifurcations) in a plasma system in which a fireball exists in dynamic state. The phenomenon was identified by analysis the time series of the oscillations of the current collected by the exciting electrode, the voltage applied on it being used as control parameter.

To explain the experimental results, a theoretical model based on the scale relativity theory [15,16] was build. Due to the collisions, the plasma particles (electrons, ions and neutrals) move on continuous but non-differentiable curves, i.e. fractal curves. Thus, in the scale relativity theory the space becomes fractal. As effect on the motion (in standard space), the Newton's fundamental equation of dynamics transforms into a Schrödinger like equation. Thus, equivalence between the formalism of the fractal hydrodynamics and the one of the Schrödinger like equation is obtained. The potential applied on the electrode is modeled as a one-dimensional square well. The different criteria of evolution to chaos are obtained by applying the full and fractional revivals formalism [17]. The full and fractional revivals of a speed scalar potential in the infinite square well occurs when a speed scalar potential evolves in time to a state that can be described as a collection of spatially distributed sub-speed scalar potentials that each closely reproduces the initial speed scalar potential shape. The results obtained from this theoretical model are found in good agreement with the experimental ones.

## 2. Experimental results

The experiments were performed in a hot-cathode plasma diode, under the following experimental conditions: argon pressure  $p = 7 \times 10^{-3}$  mbar, plasma density  $n_{pl} \cong 10^8 - 10^9$  cm<sup>-3</sup>. Plasma was driven away from equilibrium by gradually increasing the voltage applied to a tantalum disk electrode with 1 cm diameter, immersed into plasma. By increasing the voltage applied on this electrode, at a critical value ( $V_E = 85$  V), a luminous fireball suddenly appears in front of the electrode. The fireball is in dynamic state, fact emphasized by the oscillations of the current collected by the electrode (see Fig. 1(i)), with a frequency of about 6.7 kHz. Fig. 1(ii) shows the fast Fourier transform (FFT) spectrum of these current oscillations. Further increase of the voltage applied on the electrode lead to the appearance of intermittencies up to the critical value  $V_E = 101$  V (see Figs. 1(iii)-1(iv)). The intermittencies appear more and more frequently with the increase of the voltage on the electrode, the oscillation frequency being embedded in a broadband noise (see Figs. 1(v)-1(viii)). For a new critical value of the applied voltage,  $V_E = 107$  V, small-amplitude oscillations with a frequency of about 14 kHz replace the intermittent ones (see Figs. 1(ix)-1(x)). For a small interval of applied voltage values, the large-amplitude oscillations are stabilized (the intermittencies disappear) with a frequency of about 7 kHz, i.e. half of the frequency of the small-amplitude

oscillations (see Figs. 1(xi)-1(xii)). Starting with  $V_E = 109$  V, only the small-amplitude oscillations of the current are present (see Figs. 1(xiii)-1(xiv)). For  $V_E = 112$  V sub-harmonic bifurcations appear in the dynamics of the plasma system, being identified in the FFT spectrum of the current oscillations, where the sub-harmonics  $f_0/3$  and  $2f_0/3$  of the fundamental frequency are present (see Figs. 1(xv)-1(xvi)). For  $V_E = 113$  V a transition to chaos through quasi-periodicity

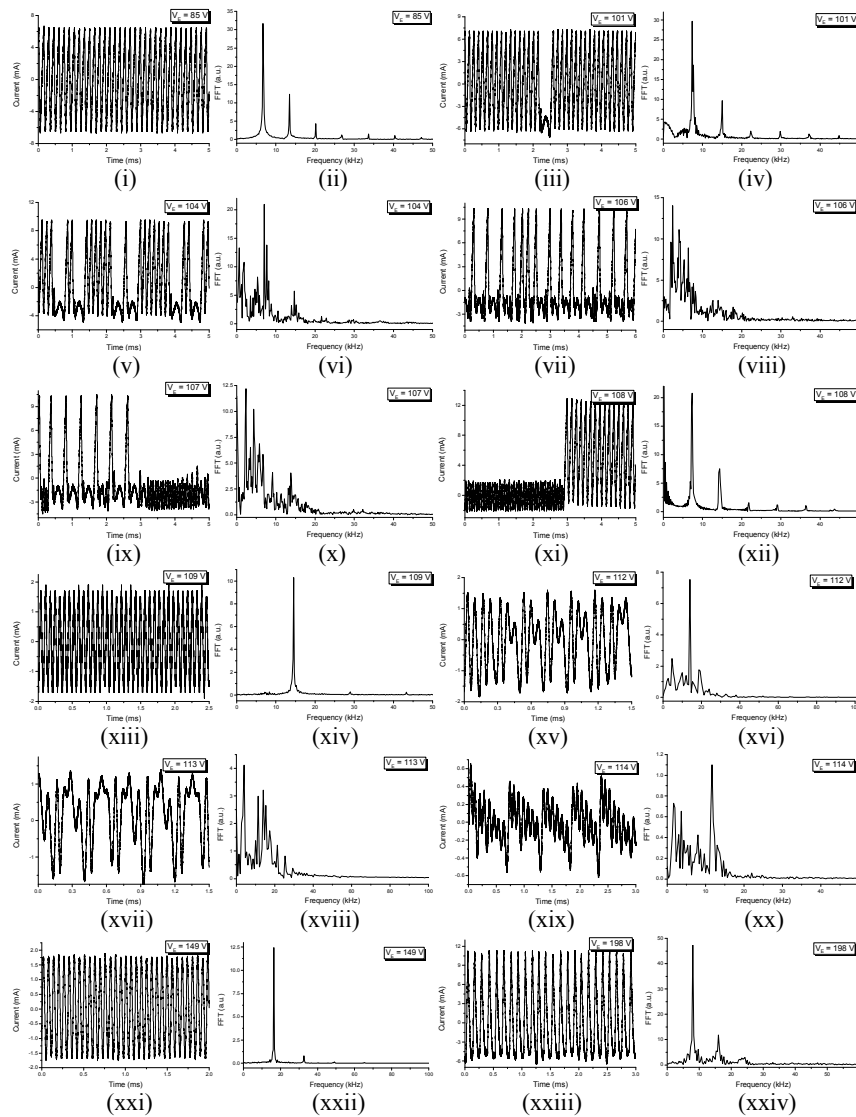


Fig. 1. Time series of the oscillations of the current collected by the electrode E (left column) and their FFT's (right column), for different values of the applied voltage.



being again identified in the FFT spectrum of the current oscillations, where several peaks corresponding to incommensurate frequencies are present (see Figs. 1(xvii)-1(xviii)). Immediately after this, for  $V_E = 114$  V the sub-harmonic bifurcations re-appear, the peaks corresponding to  $kf_0/7$ , with  $k = 1-6$ , being this time observed in the FFT spectrum of the current oscillations (see Figs. 1(xix)-1(xx)). For the critical value  $V_E = 149$  V all the sub-harmonics are eliminated, almost harmonic oscillations being recorded, with a frequency of about 16.4 kHz (see Figs. 1(xxi)-1(xxii)). From now, by increasing the voltage applied on the electrode, only a decrease of the oscillation frequency was observed (about 8 kHz for  $V_E = 198$  V), together with an increase of the oscillation nonlinearity (the amplitudes of the superior harmonic increase) (see Figs. 1(xxiii)-1(xxiv)).

### 3. Theoretical model

Once accepted that the plasma particles move on continuous but non-differentiable curves (due to the collisions), some consequences of non-differentiability by scale relativity theory are evident [15,16,18]:

- i) physical quantities that describe the discharge plasma dynamics are fractal functions, i.e. functions dependent on both spatial coordinates and time, as well as on the scale resolution;
- ii) the dynamics of the plasma discharge are described by the fractal operator  $\hat{d}/dt$  [18]

$$\frac{\hat{d}}{dt} = \frac{\partial}{\partial t} + \hat{\mathbf{V}} \cdot \nabla - i \frac{\lambda^2}{\tau} \left( \frac{dt}{\tau} \right)^{(2/D_F)-1} \Delta$$

where  $\hat{\mathbf{V}} = \mathbf{V}_D + i\mathbf{V}_F$  is the complex velocity,  $\mathbf{V}_D$  is the differentiable and resolution scale independent velocity,  $\mathbf{V}_F$  is the non-differentiable and resolution scale independent velocity,  $\hat{\mathbf{V}} \cdot \nabla$  is the convective term,  $\frac{\lambda^2}{\tau} \left( \frac{dt}{\tau} \right)^{(2/D_F)-1} \Delta$  is the dissipative term,  $D_F$  is the fractal dimension of the movement curve,  $\lambda$  is the Debye length,  $\tau$  is the inverse of the plasma pulsation and  $\frac{\lambda^2}{\tau} = D$  is the Nottale coefficient specific to the fractal – non-fractal transition [15,16].

Applying the fractal operator to the complex speed and accepting a generalized Newton's principle (a generalization of Nottale's principle of scale covariance [15,16] in the form

$$\frac{\hat{d}\hat{\mathbf{V}}}{dt} = -\nabla U$$



we obtain the geodesics equation

$$\frac{d\hat{\mathbf{V}}}{dt} = \frac{\partial\hat{\mathbf{V}}}{\partial t} + (\hat{\mathbf{V}} \cdot \nabla)\hat{\mathbf{V}} - i \frac{\lambda^2}{\tau} \left(\frac{dt}{\tau}\right)^{(2/D_F)-1} \Delta\hat{\mathbf{V}} + \nabla U = 0$$

where  $U$  is an external scalar potential. This equation is a Navier-Stokes type equation. If the dissipative term is neglected, then we obtain [19]:

$$\frac{d\hat{\mathbf{V}}}{dt} = \frac{\partial\hat{\mathbf{V}}}{\partial t} + (\hat{\mathbf{V}} \cdot \nabla)\hat{\mathbf{V}} - \frac{\sqrt{2}}{3} \frac{x^3}{2} \left(\frac{dt}{\tau}\right)^{(3/D_F)-1} \hat{\mathbf{V}}^3 \hat{\mathbf{V}} = 0$$

In the one-dimensional case, by supposing that the density of states is constant, the solution of this equation in normalized coordinates takes the form:

$$\mathbf{V} = \bar{\mathbf{V}} + 2a \left( \frac{E(s)}{K(s)} - 1 \right) \mathbf{V} + 2acn^2 [\alpha(\xi - M\tau); s]$$

where  $\mathbf{V}$  is the normalized speed field,  $E(s)$  and  $K(s)$  are the elliptic integrals of the first and second order of  $s$  modulus,  $cn$  is the Jacobi's elliptic function of  $s$  modulus,  $\bar{\mathbf{V}}$  is the mean normalized speed,  $a$  is an amplitude,  $\xi$  is the normalized spatial coordinate,  $\tau$  is the normalized temporal coordinate,  $M$  is the Mach number and  $\alpha$  is a coefficient depending on  $a$ . Thus, the dynamics in plasma run through cnoidal modes of the speed field. By choosing  $s \in [0,1]$  we distinguish different degenerescences of cnoidal modes: harmonic package for  $s \rightarrow 0$ , package of solitons for  $s \rightarrow 1$ , soliton for  $s = 1$ , or mixed modes. By choosing the right running plane for the plasma dynamics, according to the method described in [19] we can obtain intermitencies.

For irrotational motions of the plasma particles ( $\nabla \times \hat{\mathbf{V}} = 0$ ,  $\nabla \times \mathbf{V}_D = 0$ ,  $\nabla \times \mathbf{V}_F = 0$ ) we can choose  $\hat{\mathbf{V}}$  of the form

$$\hat{\mathbf{V}} = -i \frac{\lambda^2}{\tau} \left(\frac{dt}{\tau}\right)^{(2/D_F)-1} \nabla \ln \psi$$

where  $\phi = \ln \psi$  is the speed scalar potential. By using the method described in [18], it results

$$\frac{d\hat{\mathbf{V}}}{dt} = -i \frac{\lambda^2}{\tau} \left(\frac{dt}{\tau}\right)^{(2/D_F)-1} \nabla \left[ \frac{\partial \ln \psi}{\partial t} - i \frac{\lambda^2}{\tau} \left(\frac{dt}{\tau}\right)^{(2/D_F)-1} \frac{\nabla \psi}{\psi} + U \right] = 0$$



This equation can be integrated and yields

$$\frac{\lambda^4}{\tau^2} \left( \frac{dt}{\tau} \right)^{(4/D_F)-2} \Delta \psi + i \frac{\lambda^2}{\tau} \left( \frac{dt}{\tau} \right)^{(2/D_F)-1} \frac{\partial \psi}{\partial t} - \frac{U}{2} \psi = 0$$

up to an arbitrary phase factor which may be set to zero by a suitable choice of the phase of  $\psi$ . This last relation is a Schrödinger type equation.

Let us consider that the potential applied on the electrode immersed into plasma simulates a one-dimensional square well. After solving the time-dependent Schrödinger type equation according to the method described in [17], we obtain the discrete eigenvalues

$$E_n = 2m_0 \mathcal{D} \left( \frac{n\pi}{a} \right)^2, \quad \mathcal{D} = \frac{\lambda^2}{\tau} \left( \frac{dt}{\tau} \right)^{(2/D_F)-1}$$

and the eigenfunctions

$$\phi_n = \begin{cases} \left( \frac{2}{a} \right)^{1/2} \sin \left( \frac{n\pi x}{a} \right), & n \text{ even } |x| \leq \frac{a}{2} \\ \left( \frac{2}{a} \right)^{1/2} \cos \left( \frac{n\pi x}{a} \right), & n \text{ odd } |x| \leq \frac{a}{2} \end{cases}$$

where  $a$  is the well's width and  $m_0$  is the rest mass of the fluid particle. Some time scales of a speed potential evolution are contained in the coefficients of the Taylor series of the quantized energy levels  $E_n$  around the main energy  $E_{\bar{n}}$

$$E_n = E_{\bar{n}} + 4\pi m_0 \mathcal{D} \left[ \frac{n - \bar{n}}{T_\alpha} + \frac{(n - \bar{n})^2}{T_\beta} + \dots \right]$$

when often the zero of energy is shifted to remove the  $E_{\bar{n}}$  term. Taking into account the discrete eigenvalues in the form

$$E_n = E_1 n^2 = E_1 \bar{n}^2 + 2E_1 \bar{n} (n - \bar{n}) + E_1 (n - \bar{n})^2$$

we relate

$$T_\alpha = \frac{2\pi m_0 \mathcal{D}}{\bar{n} E_1}, \quad T_\beta = \frac{4\pi m_0 \mathcal{D}}{E_1}$$



We note that the time scale  $T_\beta$  does not depend on the mean energy level  $\bar{n}$ . This will provide us with a “universal” time scale for describing the speed potential evolution, which does not depend on the particle average energy. We write the particle’s speed scalar potential in the infinite square well for  $t = 0$  as  $\psi(x, t = 0) = \psi_i(x)$ . We expand this speed scalar potential using the energy eigenstate basis

$$\psi_i(x) = \sum_{n=1}^{\infty} C_n \phi_n(x) \text{ with } C_n = \int_{-\infty}^{+\infty} \phi_n(x) \psi_i(x) dx$$

Using the time scale  $T_\beta$ , the time evolution in the energy eigenbasis found from Schrödinger type equation is

$$\psi(x, t) = \sum_n \exp \left[ -2\pi i \left( \frac{t}{T_\beta} \right) n^2 \right] C_n \phi_n(x)$$

Now, the full and fractional revivals formalism may be applied. Full and fractional revivals of a speed scalar potential in the infinite square well occur when the speed scalar potential evolves in time to a state that can be described as a collection of spatially distributed sub-speed scalar potentials that each closely reproduces the initial speed scalar potential shape [17]. Therefore, the full and fractional revivals of the speed scalar potential in the infinite square well implies either

$$\psi(x, t = t_0 + 2^k T_\beta) = \psi(x, t = t_0) \text{ or } \psi \left( x, t = t_0 + \frac{p}{q} T_\beta \right) = \psi(x, t = t_0)$$

for any time  $t_0$  and  $k, p, q$  integers. In any of the situations above, either for  $t = T(F) = 2^k T_\beta$  or for  $t = T(SH) = \frac{p}{q} T_\beta$ , we can introduce Reynolds type criterions [20]. Then, through  $T(F)/T_\beta = 2^k$  it is formally simulated the criterion of evolution to chaos via Feigenbaum mechanism, while through  $T(SH)/T_\beta = p/q$  with  $p < q$  the criterion of evolution to chaos via a cascade of sub-harmonic bifurcations.

#### 4. Conclusions

A theoretical model based on the scale relativity theory was developed in order to explain the competition of different scenarios of transition to chaos, experimentally observed in plasma in connection to the nonlinear dynamics of a



fireball. The results obtained from this model are in good agreement with the experimental ones.

## References

1. P. Y. Cheung, S. Donovan and A. Y. Wong. Observations of intermittent chaos in plasmas, *Phys Rev Lett* 61:1360-1363, 1988.
2. S. Chiriac, D. G. Dimitriu and M. Sanduloviciu. Type I intermittency related to the spatiotemporal dynamics of double layers and ion-acoustic instabilities in plasma. *Phys Plasmas* 14:072309, 2007.
3. J. Qin et al. Chaos and bifurcations in periodic windows observed in plasmas. *Phys Rev Lett* 63:163-166, 1989.
4. R. Timm and A. Piel. Hysteresis and transition to chaos in a thermionic plasma discharge. *Contrib Plasma Phys* 32:599-611, 1992.
5. W. Ding et al. Quasiperiodic transition to chaos in a plasma. *Phys Rev Lett* 70:170-173, 1993.
6. V. Igochine et al. Transition from quasiperiodicity to chaos just before sawtooth crash in the ASDEX Upgrade tokamak. *Nucl Fusion* 48:062001, 2008.
7. A. Atipo, G. Bonhomme and T. Pierre. Ionization waves: from stability to chaos and turbulence. *Eur Phys J D* 19:79-87, 2002.
8. M. Agop et al. Experimental and theoretical evidence of the chaotic dynamics of complex structures. *Phys Scripta* 87:045501, 2013.
9. S. D. Baalrud, B. Longmier and N. Hershkowitz. Equilibrium states of anodic double layers. *Plasma Source Sci Technol* 18:035002, 2009.
10. O. Niclescu et al. Experimental and theoretical investigations of a plasma fireball dynamics. *Phys Plasmas* 17:042305, 2010.
11. K. H. Pae and S. J. Hahn. Self-oscillation and chaos in positive-bias plasma diodes. *J Phys Soc Japan* 71:2169-2173, 2002.
12. S. J. Hahn and K. H. Pae. Competing multistability in a plasma diode. *Phys Plasmas* 10:314-316, 2003.
13. K. H. Pae and S. J. Hahn. Multistability and chaos in a plasma diode. *J Korean Phys Soc* 42:S994-S999, 2003.
14. J. T. Seo, K. H. Pae and S. J. Hahn. Noise-driven multistability in a plasma diode. *Phys Plasmas* 11:5364-5367, 2004.
15. L. Nottale. *Fractal Space-Time and Microphysics: Towards a Theory of Scale Relativity*, World Scientific, Singapore, 1993.
16. L. Nottale. *Scale Relativity and Fractal Space-Time. A New Approach to Unifying Relativity and Quantum Mechanics*, Imperial College Press, London, 2011.
17. D. L. Aronstein and C. R. Stroud. Fractional wave-function revivals in the infinite square well. *Phys Rev A* 55:4526-4537, 1997.
18. M. Agop et al. Implications of an extended fractal hydrodynamic model. *Eur Phys J D* 56:405-419, 2010.
19. E. S. Bacaita et al. Nonlinearities in drug release process from polymeric microparticles: long-time-scale behaviour. *J Appl Math.* 2012:653720, 2012.
20. L. Landau and E. M. Lifshitz. *Fluid Mechanics* 2<sup>nd</sup> edition, Butterworth-Heinemann, Oxford, 1987.